CYRIC

ANNUAL REPORT

1995

(January 1995 - December 1995)

CYCLOTRON AND RADIOISOTOPE CENTER
TOHOKU UNIVERSITY

PREFACE

In this sixteenth issue of the CYRIC Annual Report, we summarize the activities for research and development and results of training for radioisotope safe-treatment at Cyclotron and Radioisotope Center, Tohoku University during the calendar year 1995.

In 1995 research programs in various fields such as nuclear physics, nuclear chemistry, solid state physics and element analyses by PIXE and activation were carried out, and radioisotopes were produced for use in engineering, biology and medicine. At the same time several facility improvements have been carried out. A total of 3500 hours of the cyclotron beam was delivered for the scheduled researches, while 50 hours for research and development for the accelerator and related facilities. It should be noted here that a two weeks long unscheduled shut-down occurred in this year due to the break down of the RF power supply device, while unscheduled shut-down so far experienced by the last year was limited to a few percents of the total beam time used. In almost 70% of the beam time, protons were accelerated for nuclear physics and short-lived radioisotopes for medical and other studies, in 15% deuteron beams for the same purposes, while in 7% ^{4}He beams for material and solid state physics. Heavier ions such as ^{13}C and ^{15}N have been accelerated as well for some limited works.

It is plausible to note that studies with PIXE technique have been carried out by using electro-static accelerator, installed at FNL (Fast Neutron Laboratory) in Graduate School of Technology, Tohoku University, under the scientific tie up between CYRIC and FNL. Indeed, more than six groups are running under this project.

During 1995, 522 of staff members and students of Tohoku University were trained at this Center in the beginner's course of safe handling of radiation and radioisotopes, while 254 staff members and students in the "x-ray course". In addition, a new course of safe handling of radiation from a SOR (Synchrotron Orbital Radiation) has been opened, and 38 of staff members and students of Tohoku University were trained.

On 20 and 21 Nov. 1995, the annual conference of CYRIC was held. A symposium related to 3-Dimensional Positron Emission tomography (3D-PET) was set as the special session of this conference celebrating accomplishment of the PET system. In addition to the 33 orally presented contribution papers in the conference, four lectures including two invited talks by Professor Sugishita of Tokyo University, and by Dr. Uemura of Research Institute for Brain and Blood Vessels-AKITA were given in the symposium.

As so far been mentioned in the last issues, the present Model 680 AVF cyclotron with K= 50 MeV is becoming less powerful both qualitatively and quantitatively from the view points of progress of science and activities of Tohoku University. Some people may require more energetic and/or high-intense beams including those of heavy nuclide or even of unstable nuclei. Others expect that polarized and unpolarized intense neutron beams may promise further fruitful researches for physics and technology.

On the other hand, deterioration of the present AVF cyclotron is evident, an example for which is the break down of the RF power supply. It is of crucial importance to replace the cyclotron by a new one with higher specifications to maintain the present activities in CYRIC. We are planning and requiring the budget to replace the present K=50 MeV AVF cyclotron with K=130 MeV AVF cyclotron equipped with high-intensity negative ion-source together with ECR heavy-ion and polarized-ion sources. A number of projects as following are presented;

(1) Nuclear Physics by Polarized Neutron
(2) Search of New-element and Super-unstable Nuclide by Heavy Ion Beam
(3) Labeled Compound Synthesis of Medium-heavy Positron Emitter
(4) Diagnostic of Heat and Brain Diseases, and Cancer
(5) Brain Research by Positron Nuclear Medicine
(6) Cancer Therapy by Epi-thermal Neutron and Boron Compound

We are very grateful to Tohoku University and to the Ministry of Education, Science, Sports and Culture for their continuous support.

January 1996

Hikonojo ORIHARA

Director
Cyclotron and Radioisotope Center
Tohoku University

EDITORS:

Hikonojo	*ORIHARA*
Manabu	*FUJIOKA*
Tatsuo	*IDO*
Takashi	*NAKAMURA*
Masatoshi	*ITOH*

WORD PROCESSED BY

Yu-ko YAMASHITA

CONTENTS

I. PHYSICS AND TECHNOLOGY

II. CHEMISTRY

III. MEDICINE AND BIOLOGY (Basic)

IV. MEDICINE AND BIOLOGY (Clinical)

V. HEALTH PHYSICS

I. PHYSICS AND TECHNOLOGY

I. 1. Shell-Model and Distorted-Wave Analysis for the (p, n) Reactions on ^{6,7}Li at 35 MeV

Orihara H., Terakawa A., Yun C. C., Itoh K., Yamamoto A., Teramoto Y., Matsumura N., Nakagawa T., Ishii K** and Ohnuma H.****

Cyclotron and Radioisotope center, Tohoku University
*Faculty of Science, Tohoku University**
*Faculty of Engineering, Tohoku University***
*Department of Physics, Tokyo Institute of Technology, Tokyo 152****

Because of their simple structure consisting of ^{4}He plus two or three nucleons, the mass 6 and 7 systems provide a good place to explore the effective nucleon-nucleon interaction through, for example, charge-exchange scattering. ^{6}Li nucleus is only the odd-odd target which provides a strong $1^+ \rightarrow 0^+$ GT-like transition in a pure manner for scattering experiments, while such $\Delta J = 1$ GT-contribution involved in the $3/2^- \rightarrow 3/2^-$ and $3/2^- \rightarrow 1/2^-$ transitions in mass-7 nuclei plays a dominant role for spin-isospin excitation in these nuclei. A number of experiments have been reported concerning nucleon and electron scattering, as well as charge-exchange reaction on ^{6,7}Li[1-4]. Moreover, there should be interesting higher excited states, for which two or three neucleons are excited through a different type of spin-isospin excitation.

From the view points of effective nucleon-nucleon interaction between particles or particle-hole in such a simple system, it is significant to extend scattering experiments over high-lying states whereas no reliable data have not yet reported for the transitions leading to the first excited state in ^{6}Be and higher spin states in ^{7}Be. Recently, Petrovich and his collaborators have reported[5] consistent folding model description of nucleon elastic, inelastic and charge-exchange scattering from ^{6,7}Li at 25-50 MeV.

In this report we discuss firstly the experimental results for the (p, n) reactions on ^{6,7}Li(p, n)^{6,7}Be at 35 Mev, then perform a shell model study with presently available effective nucleon-nucleon interactions testing how the observrd level structure is reproduced, finaly we compare the experimental and calculated cross sections.

The experiment was carried out using a 35 MeV proton beam from the AVF cyclotron and the time-of-flight facilities[6] at the Cyclotron and Radioisotope Center at Tohoku University. A beam swinger system was used to measure angular distributions of emitted neutrons between 0° and 110° (lab). The target was a metallic foil of enriched ^{6,7}Li prepared by rolling. The thickness and enrichment of the target were, respectively, 2.0 mg/cm^2 and 99.9%.

Neutrons were detected by an array of twelve detectors, which were located at 44.3 m from the target and contained a total of 23.2 liters of NE213 scintillator. The detector efficiencies were obtained from Monte Carlo calculations for monoenergetic neutrons with $E_n \leq 34$ MeV. Absolute detector efficiencies were also measured by counting neutrons from the ^{7}Li(p, n)^{7}Be reaction and comparing its yield with the absolute neutron fluence determined by activation. They were in good agreement with the Monte Carlo calculations. Overall time resolution was typically 1.3 ns corresponding to 200 keV for the most energetic neutrons. Errors in the absolute scale of the cross sections were estimated to be less than 15%, and those for the excitation energy were ±15keV. Further experimental details have been given in a previous report$^{7)}$.

Figures 1(a) and 1(b) illustrate sample neutron excitation energy spectra taken for the (p, n) reactions on ^{6}Li and ^{7}Li, respectively. Lines in the figure are results of peak-fitting. With the reported width of 1.16 MeV$^{8)}$ for the first excited state in ^{6}Be, consistent peak-fitting results have been obtained over the angles measured. As for the ^{7}Be case, two peaks are analyzed for neutrons leading to the particle unbound 4.570 ($7/2^-$) and 7.0 MeV states, the latter of which may be a composite peak consisting of those to 6.73 ($5/2^-$) and 7.21 MeV ($5/2^-$) states. The width of the 4.570-MeV state is seen to be narrower than the present experimental energy resolution of 200 keV, while that for the composite peak is ~1.0 MeV.

Predicted level diagrams are compared in Fig. 2. Shell model calculations over p- and full sd-shells have been carried out with the code OXBASH$^{9)}$ by adopting three types of effective interactions: namely, PM3Y: Michigan 3-range-Yukawa by Bertsch et al$^{10)}$, PWY by Warburton$^{11)}$, and CKPOT by Kohen and Kurath$^{12)}$. As seen in the figure, the experimental level diagram for ^{6,7}Be is resonably reproduced by shell model calculations among which that for M3Y, by which microscopic DWBA calculation is performed as described later on, gives the best fit results for both nuclrei.

In Figs. 3 through 8, illustrared are experimental and theoretical angular distributions of neutrons leading to the ground and first excited states in ^{6}Be, and those for neutrons corresponding to the four peaks in ^{7}Be. The data are compared with the DW results calculated by the computer code DWBA-74$^{13)}$, which includes knock-on exchange effects in an exact manner. Note that fully antisymmetrized calculations are made in the present DW analysis, in which non-normal parity terms such as $\Delta J(\Delta L, \Delta S) = 1(1, 0)$ for the $0^+ \rightarrow 1^+$ transition also contribute to the cross section. They indeed play important roles in some cases. Optical potential parameters of Becchetti and Greenlees$^{14)}$ are used for the entrance channel. Those for the exit channel were self-consistent potential parameters derived by Carlson et al$^{15)}$. The effective nucleon-nucleon interactions used in the present DW analysis are those by Bertsch et al. (M3Y)$^{10)}$. Sensitivity of such calculations to the optical-potential parameters is elaborated in Ref. [13].

The angular distribution for $1^+ \rightarrow 0^+$ neutrons leading to the ground state in ^{6}Be is illustrated in Fig. 3 together with theoretical prediction. This transition corresponds to the strong analog ^{6}He(β)^{6}Be, $0^+ \rightarrow 1^+$ beta-decay which have a log*ft* value of 2.9. Due to the statistical factor for initial and final spin values, (p, n) cross section are reduced, however, cross section magnitudes a^{6}Li(p, n) ^{6}Be reaction at $E_p = 30.2$ MeV. For comparison purpose, cross sections are plotted as functions of linear momentum transfer q(fm^{-1}). Their calculation is based on more realistic, complex, density-dependent interaction of JLM[16)], being different from M3Y interaction by spin-dependent, central components. Their calculations overestimated experimental results by a factor of 1.6, whereas our present calculation reproduces the measurements absolutely so long as data at small angles are concerned. It is noticeable as well that two calculations are quite reasonable as compared in the figure as functions of q. Figure 4 shows results for the $1^+ \rightarrow 2^+$ transition in the ^{6}Li(p, n) ^{6}Be reaction, where the cross section is a additive sum over $\Delta J = 1$, 2 and 3. It is remarkable that both cross section magnitudes are absolutely fitted, and the angular shape is reproduced reasonably. Among the three J-transfer values, the $\Delta J = 2$ component may contain predominantly the $\Delta L(\Delta L, \Delta S) = 1(2,1)$ spin-quadrupole contribution as seen in its angular distribution shape.

Results of experimental and theoretical sdudies for the ^{7}Li(p, n) ^{7}Be reaction are displayed in Figs 5 through 8, in which transitions to $3/2^-$ and $1/2^-$ ground and 1st-excited states are absolutely fitted, though angular distributions are rather poorly reproduced. The angular distribution for the $3/2^- \rightarrow 7/2^-$ transition have been firstly analyzed by using one-body-transition-density by OXBASH. Cross section magnitudes are almost reasonably explained by incoherent sum over $\Delta J = 2$ and 3 components. Note that $\Delta J = 4$ and 5 components vanish identically due to limitted model space.

We have carried out further study to higher states. Two $5/2^-$ states are reported at 6.73 and 7.21 MeV in ^{7}Be, though they have too broad level-widths to be observed as separated peaks. Indeed, the shell model predicts two $5/2^-$ states as shown in Fig 2. Thus, these two are analyzed all together as illustrated in Fig. 8. One of the interesting points in the present analysis is the $\Delta J = 1$ GT-like component involved in the $3/2^- \rightarrow 5/2^-$ transitions, where 1(0,1) contribution is dominant for the higher $5/2^-$ states as seen in Fig. 8. An important $3/2^- \rightarrow 5/2^-$, $\Delta J = 1$ transition has been discussed concerning the ^{71}Ga(ν, e) ^{71}Ge reaction, whether 0.175-MeV, 5/2- state in ^{71}Ge play a sizable role for solar neutrino absorption.

In summary, angular distributions of neutrons leading to the high-lying states in ^{6,7}Be have been measured for the (p, n) reactions on ^{6,7}Li. Measured cross section were analyzed by microscopic DW theory, where transition amplitudes by recent shell-model theory were utilized. Almost all data were reproduced absolutely by calculations. For the $1^+ \rightarrow 2^+$ transition in the ^{6}Li(p, n) ^{6}Be reaction, $\Delta L(\Delta L, \Delta S) = 1(2,1)$ spin-quadrupole contribution was found to play an important role, while in the ^{7}Li(p, n) ^{7}Be reaction, (p, n) cross sections were firstly analyzed by DW theory. An example of the $3/2^{-} \rightarrow 5/2^{-}$, $\Delta J = 1$, GT-like transition was presented.

References

1) Batty C. J. et al., Nucl. Phys. **A120** (1968) 297.
2) Rapaport J. et al., Phys. Rev. **C41** (1990) 1920.
3) Glover C. W. et al., Phys. Rev. **C41** (1990) 2487.
4) Glover C. W. et al., Phys. Rev. **C43** (1991) 1664.
5) Petrovich F. et al., Nucl. Phys. **A563** (1993) 387.
6) Orihara H. and Murakami T., Nucl. Instrum. Methods **181** (1981) 15.
7) Orihara H. et al., Nucl. Instrum. Methods **A257** (198 7) 189.
8) Firestone R. B., *Table of Isotopes* 1996.
9) The shell model code OXBASH, Echegoyen A. E., National Superconducting Cyclotron Laboratory Report No. 524 (1984).
10) Bertsch G., Borysowics J., McManus H. and Love W. G., Nucl. Phys. **A284** (1977) 399.
11) Warburton and Brown G., Phys. Rev. **C44** (1991) 233.
12) Kohen S. and Kurath D., Nucl. Phys. **A101** (1967)1.
13) Schaeffer R. and Raynal J., unpublished.
14) Becchetti F. D. and Greenlees G. W., Phys. Rev. **182** (1969) 1190.
15) Carlson J. D.,Zafiratos C. D. and Lind D. A., Nucl. Phys. **A249** (1975) 29.
16) Jeukenne J. P., Lejeune A., and Mahaux C., Phys. Rev. **C16** (1977) 80.
17) Orihara H. et al., Phys. Rev. Lett. **51** (1983) 1328.

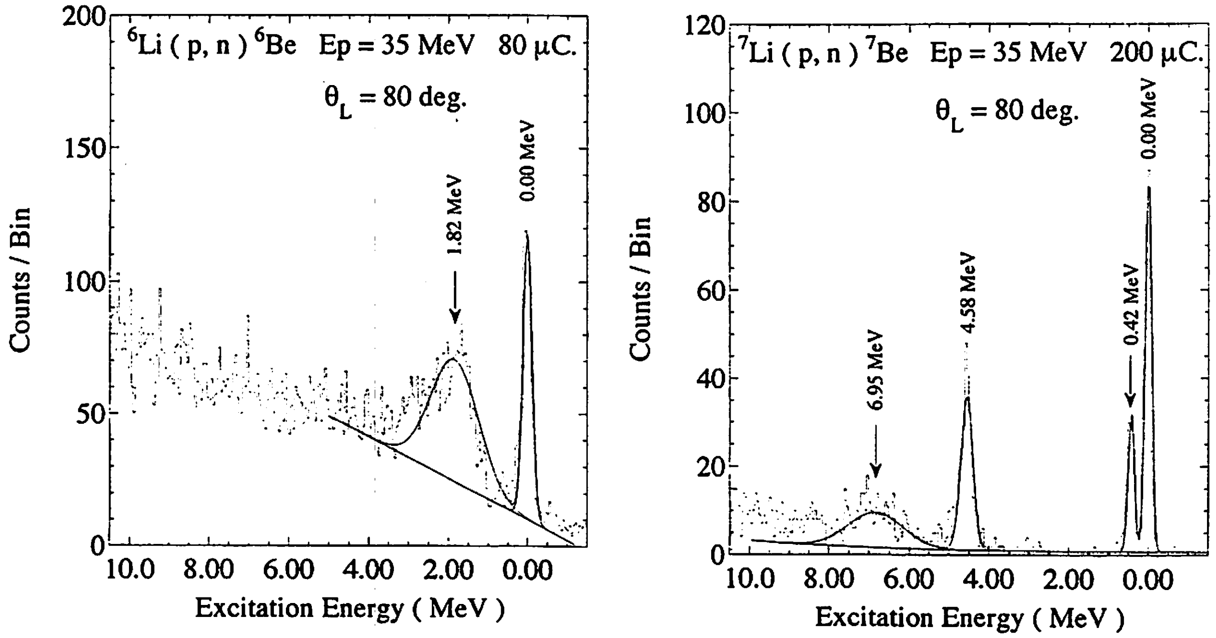

Fig. 1. A sample excitation energy spectrum from the ^{6,7}Li(p, n) ^{6,7}Be reaction taken at 25° with a flight path of 44.3 m. Energy per bin is 25 keV.

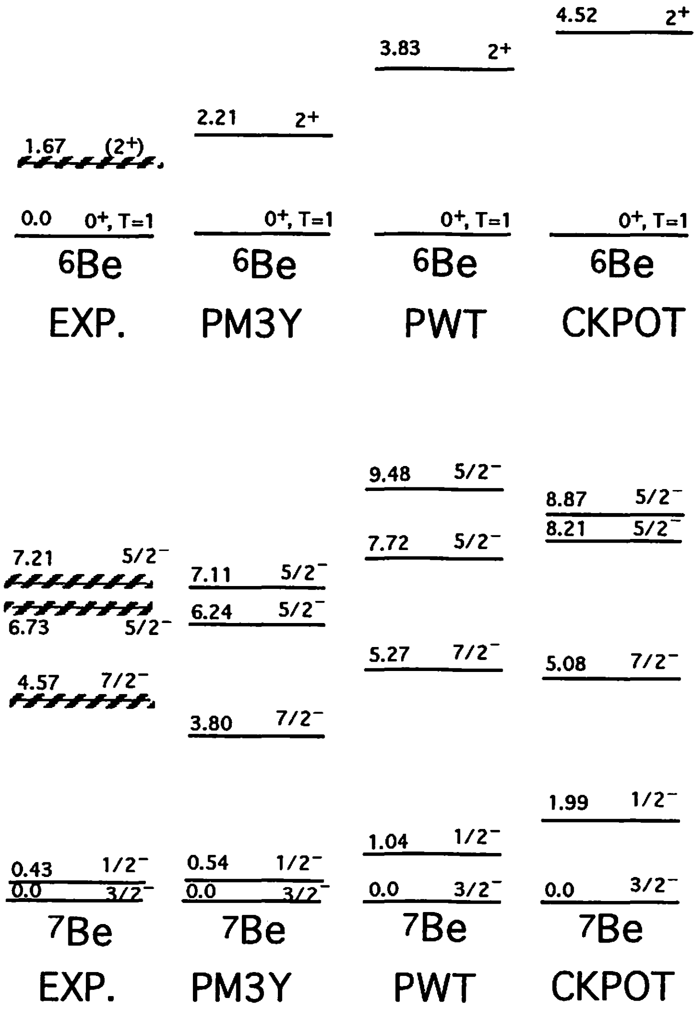

Fig. 2. Experimental and calculated level diagrams of ^{6}Be and ^{7}Be.

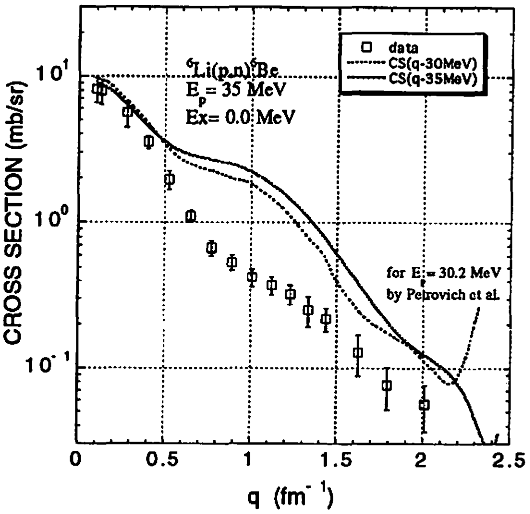

Fig. 3. Differential cross sections for neutrons leading to the ground state of ^{6}Be.

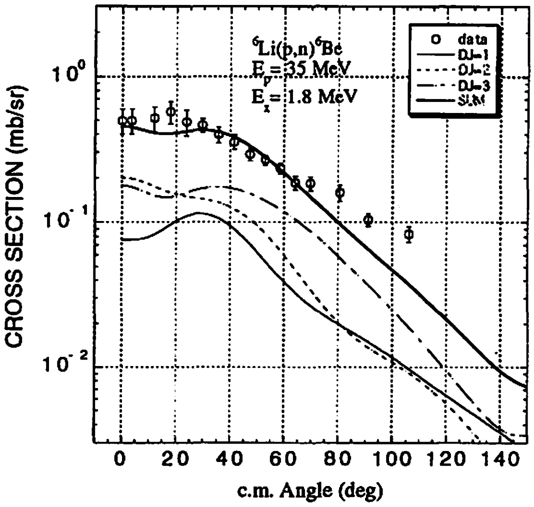

Fig. 4. Differential cross sections for neutrons leading to the 1st excited state in ^{6}Be.

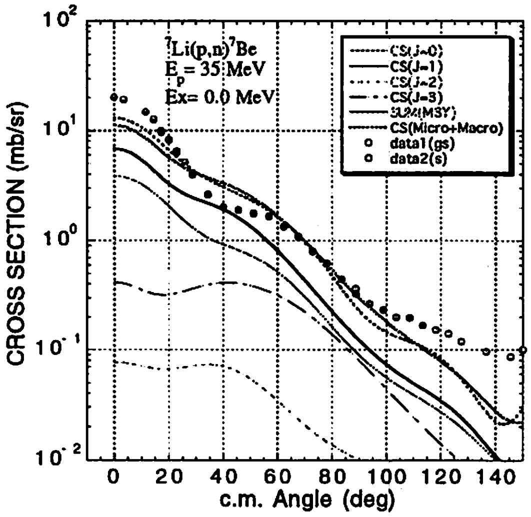

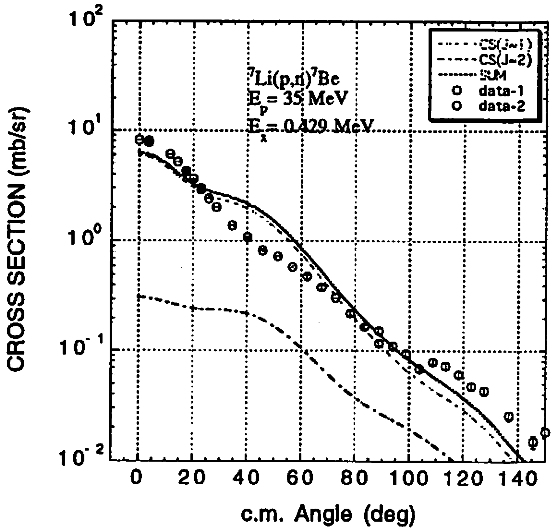

Fig. 5. Differential cross sections for neutrons leading to the ground state of ^{7}Be.

Fig. 6. Differential cross sections for neutrons leading to the 1st excited state of ^{7}Be.

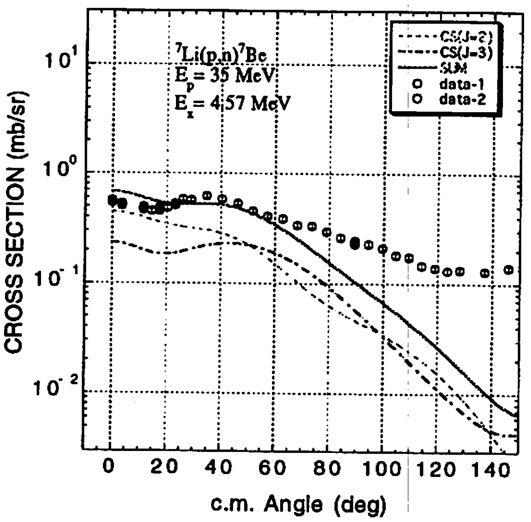

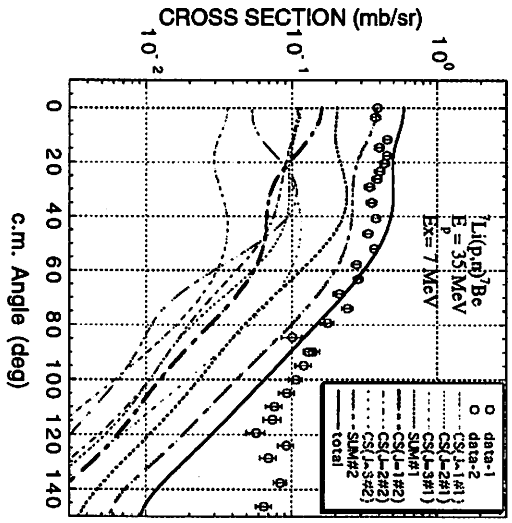

Fig. 7. Differential cross sections for neutrons leading to the 4.57-MeV state in ^{7}Be.

Fig. 8. Differential cross sections for neutrons leading to the 7-MeV states in ^{7}Be.

I. 2. High Energy γ-ray Production from Be, C, Al Targets by 50-MeV α-particle bombardment

Yamamoto A., Ishii K., Hosaka M.**, Terakawa A., Guan Z., Itoh K.,*
Yun C. C., Teramoto Y., Matsumura N., and Orihara H.

Cyclotron and Radioisotope center, Tohoku University
*Department of Nuclear engineering, Tohoku University**
*UVSOR, Institute of Molecular Science***

Introduction

A main process for the production of high energy γ-rays in nuclear reactions is bremsstrahlung by the nuclear forces. It is supposed that there are two bremsstrahlung processes: i. e. nucleon-nucleon bremsstrahlung and potential bremsstrahlung. Nucleon-nucleon bremsstrahlung is produced by the collision between a nucleon in the projectile-nucleus and that in the target-nucleus[1,2] The potential bremsstrahlung, on the other hand, takes place when the projectile (or target) is suddenly accelerated as a "lump" at the nuclear surface[3,4]. Namely, γ -rays by the potential bremsstrahlung is produced by the motion of all nucleons in the projectile or the target nucleus. As such, γ -rays as high as the kinematical maximum energy are expected to be produced by the latter process. Moreover, in the case that the projectile or the target nucleus consists of too many nucleons, the potential bremsstrahlung cannot be achieved as well.

Hosaka et al. have shown that the theory of the potential bremsstrahlung could explain well the high energy γ -rays produced by 65-MeV ^{3}He bombardments[5]. Our present purpose is to study the potential bremsstrahlung for four particle system observing the bremsstrahlung for α particles.

Experiment and results

The experiment was performed with a 50-MeV α beams from the AVF cyclotron at CYRIC, Tohoku University. The target thicknesses were 18.5, 11.3, and 27.0 mg/cm^2 for ^{9}Be, ^{12}C and ^{27}Al, respectively. The γ -rays were detected with a set of seven hexagonal BaF_2 scintillators placed at 50cm from the target. Solid angles were defined to be 7.85msr with a Pb collimator. The backgrounds which consist of neutrons and cosmic-rays were significantly reduced by the use of the TOF technique with the fast component of light signals from the BaF_2 scintillator. Angular distributions of γ -rays were measured between 35° to 144° in the laboratory system. The energy resolution (FWHM) was about 9%.

The energy spectra and angular distributions of high energy γ -rays are shown in Figs. 1-6. In the angular distributions, the differential cross sections are integrated over the photon energies above 30MeV. The γ-rays up to the kinematical maximum energy was observed for all targets. The angular distributions for the E_γ >30MeV cases in laboratory frame show a dominant forward peak. Among them, the result of the ^{12}C target is interesting, since the intensity of γ -rays takes the minimum value at 90°.

Theory

The one-dimensional formula for the probability of potential bremsstrahlung[3-5] is expressed as:

$$\frac{d^2P}{d\omega d\Omega} = \frac{\alpha\omega}{(2\pi)^2}\frac{m^2}{p_i p_i}\sum_{\hat{\varepsilon}_k}^{2}\left|\int dz\,\psi_i^*(z)\,e^{k_z z}\frac{\vec{p}}{m}\cdot\hat{\varepsilon}_k\psi_f(z)\right|^2,$$

where ψ_i and ψ_f are initial and final wave functions, respectively, for the projectiles in the Woods-Saxon potential given by:

$$V(z) = \frac{V_0}{1+\exp\left(-\frac{z}{a_0}\right)}.$$

We treat the potential depth V_0 and the effective Q-value S as parameters for the potential bremsstrahlung, while we use the diffuseness a_0 and the nuclear radius r_0 taken from a global optical potential set[6]. The differential cross section per unit solid-angle and unit photon-energy is obtained by integrating over the impact parameter b and the azimuthal angle φ. i.e.:

$$\frac{d^2\sigma}{d\omega d\Omega} = \int_0^{b_{max}} b\,db\int_0^{2\pi} d\varphi\frac{d^2p}{d\omega d\Omega}.$$

The potential bremsstrahlung must be taken into account for both the projectile and the target nucleus. Then, the T-matrix of Eq.(1) is modified as follows:

$$T_{if} = \int dr\,\psi_i^*(r)\left\{\frac{Z_p}{m_p+m_t}F_p(k)e^{ik_z\frac{m_t}{m_p+m_t}r}\hat{\varepsilon}_k\cdot p_r - \frac{Z_t}{m_p+m_t}F_t(k)e^{-ik_z\frac{m_p}{m_p+m_t}r}\hat{\varepsilon}_k\cdot p_r\right\}\psi_f(r).$$

The factor Fp(k) (Ft(k)) is a probability which shows that all nucleons of the projectile nucleus (the target nucleus) behave as one particle for photon emission. We fixed Fp(k)=1 considering that the incident α particle has no structure, and parameterize Ft(k) with a real value between 0 and 1.

Discussion

In Figs 1-6, the γ-ray spectra and the angular distributions are shown together with the calculations for the potential bremsstrahlung. The theoretical cross sections are folded with a response function of the detector for the purpose of comparison with experiment. It is seen from these figures that the predictions of the potential bremsstrahlung reproduce well the experimental spectra in the photon energy region higher than 30MeV. Especially, the theoretical prediction of angular distribution is in good agreement with the experimental result for ^{12}C. The potential parameters were obtained by fitting the theoretical cross sections to the experimental ones in the γ-ray energy spectra at 90°, and they are listed in Table 1. The values of S_0 in the table show the experimental Q-values[7]. The values of V_0 are larger than those for optical potential[8] for all targets investigated. Namely, the projectile which causes bremsstrahlung receives much more strong attractive forces than in the case of elastic scattering by which optical potential parameters have been determined.

It is supposed that S should be smaller than S_0 because the projectile in the final state keeps a same internal structure, like a cluster, as that of the initial state in the process of potential bremsstrahlung. S would show the Q-value of a α-cluster state against a ground state in which a nucleus is reconstructed with the projectile and the target.

In contrast with the small values of Ft(k) of about 0.3 obtained for Be and Al targets, the value for C is 0.9. Thus, while the target nucleus of Be or Al rarely emit photons, the target nucleus of C emits photons as well as the projectile does. This discrepancy might be related to the α-cluster like nuclear structure.

References

1) Bauer W., Bertsch G. F., Cassing W., and Mosel U., Phys. Rev. C**34** (1986) 2127.
2) Cassing W., Metag V., Mosel U., and Niita K., Phys. Rep. **188** (1990) 363.
3) Nakayama K. and Bertsch G. F., Phys. Rev. C**34** (1986) 2190.
4) Nakayama K. and Bertsch G. F., Phys. Rev. C**36** (1987) 1848.
5) Hosaka Met al., "High energy γ-ray production from Be, C, and Al target by 65MeV ^{3}He bombardment". submitted to Phys. Rev. C.
6) Nolte M., Machner H., and Bojowald J. , Phys, Rev. C**36** (1987) 1312.
7) Keller K. A., Lange J., and Munzel H., Q-value and Excitation function of Nuclear Reactions, Part a Q-value (Springer-Verlag, Berlin-Heiderberg-New York, (1973).
8) Perey C. M. and Perey F. G., Atomic Data and Nuclear Data Tables **17** (1976) 1.

Table 1. The fitting results of parameters.

Targets	S_0(MeV)	S(MeV)	V_0(MeV)	Ft(k)
^{9}Be	10.6	10.0	-209	0.33
^{12}C	7.2	3.4	-343	0.94
^{27}Al	9.7	3.1	-219	0.30

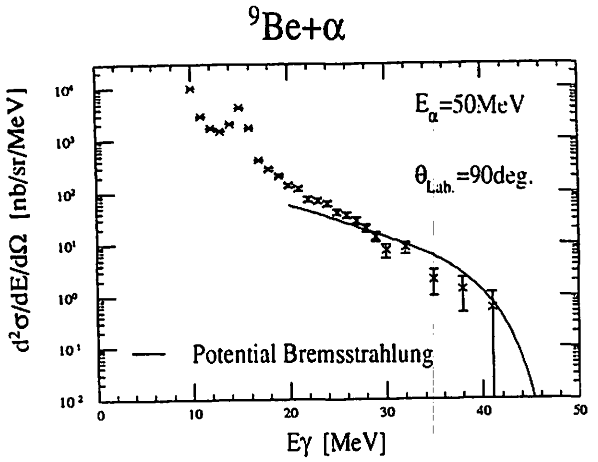

Fig. 1. Spectre of α+⁹Be.

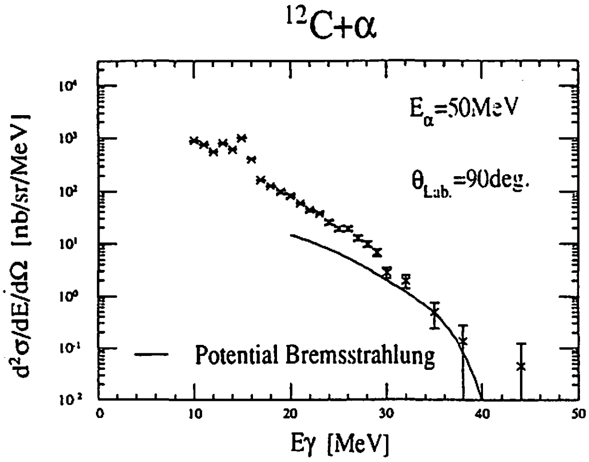

Fig. 2. Spectre of α+¹²C.

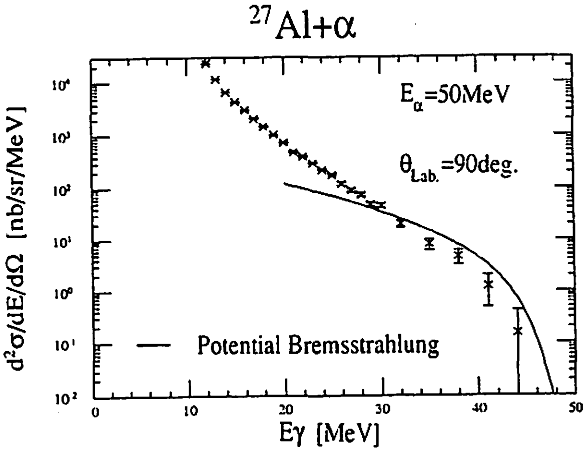

Fig. 3. Spectre of α+²⁷Al.

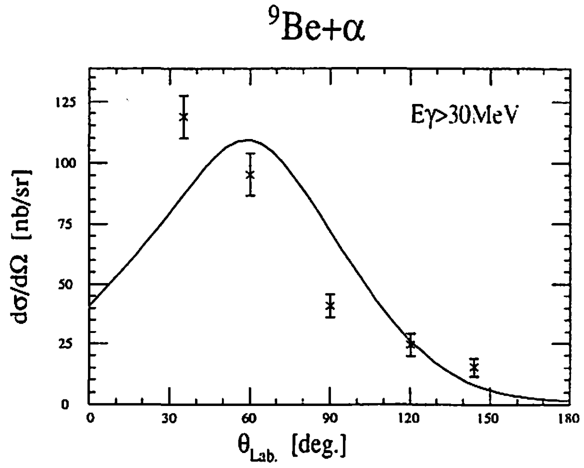

Fig. 4. Angular disstribution of α+⁹Be.

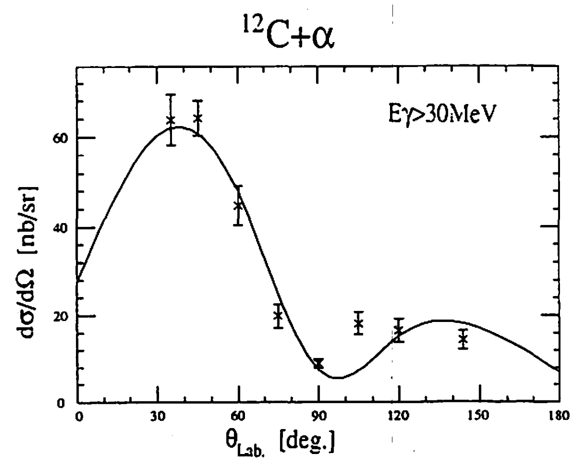

Fig. 5. Angular disstribution of α+¹²C.

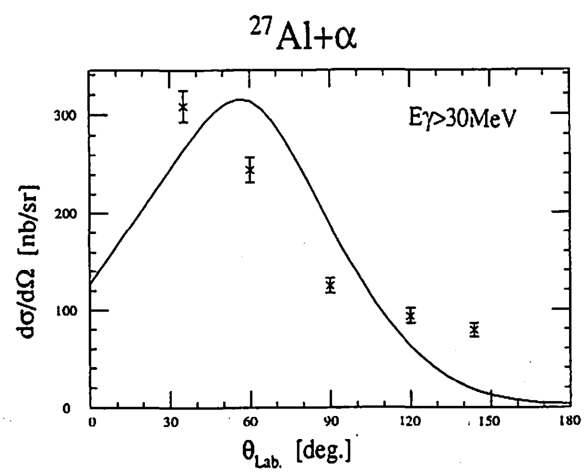

Fig. 6. Angular disstribution of α+²⁷Al.

I. 3. Total Reaction Cross Section and Forward Glory Scattering in Heavy Ion Collisions

Yamaya T., Ishiyama H., Yamazaki A., Tojima J., Katoh M., Kotajima K., Suzuki K.*, Fujioka M.**, and Shinozuka T**.*

Department of Physics, Tohoku University
*Depaetment of Nuclear Enginerring, Tohoku University**
*Cyclotron and Radioisotope Center, Tohoku University***

The possibility of a model independent determination of the total reaction cross sections were experimentally shown by the measurements forward glory phenomena at extremely forward angles in the heavy-ion elastic scattering.

The observations of glory scattering in molecular and atomic collisions have been successful. In the nuclear collisions, an existence of forward glory phenomena has theoretically been predicted by many theorests$^{1-4)}$, and the many data have been analyzed to deduce the forward glory phenomena in the nuclear collisions$^{5-10)}$.
However these data are synthetic, i.e the angular distributions measured in a limitted angular range which is not involve the forward angles.

Elastic cross sections in a foward angular range up to θ_{Lab} =1.6° have been measured at E/A=1~2 MeV $^{11-12)}$ in the ^{12}C + ^{12}C scattering system, and an possibility of observation of the forward glory in the nuclear collision have been shown from the experimental data. However, the ^{12}C + ^{12}C system in this energy region should be considered appreciable effects of resonances for the total reaction cross sections or the nuclear scattering amplitudes.

The forward glory for the scattering system of ^{12}C, ^{15}N, ^{16}O+ ^{28}Si have been observed at the energies E/A=4~5 MeV$^{13)}$ in a forward angular range up to 1.2°. However, the measurements in such a limitted angle range are not enough for the purpose to deduce the high precise total reaction cross sections or the nuclear amplitudes at θ =0°.

In the present work, the measurements of elastic differential cross sections were extended to the forward angular region up to 0.6° for the scattering systems, ^{12}C, ^{13}C, ^{15}N and ^{16}O on ^{28}Si. The result of the precise experiments showed undoubted oscillations and undulating envelope shape in the sum-of-differences cross sections(SOD), as shown in Fig.1.

For the measurements at extremely forward angles(θ = 0.6°~4.0°), a trapezoidal scattering chamber was designed and installed downstream a large scattering chamber. A distance between the target position and a defined slit of the detector system was 1599mm.

The detector system consists of two 25 μ m totally depleted silicon detectors and a 240 μ m position-sensitive silicon detector. The telescope was mounted by a thin tantalum plate with three slit apertures of 0.4 × 2 mm^2 in front of the ΔE detectors. Each slit aperture was defined solid angles of 3.1×10^{-7} sr. and the differential angles of $\Delta\theta$ =0.014° assuming a point beam spot on the target. The accuracy of angle setting was 5×10^{-4} degree. Four solid-state detectors were symmetrically situated with respect to the beam axis, to monitor the deflection of the beam intensity distribution in the beam spot. These monitor detectors were symmetrically placed on a circle with a small corn angle of θ_{lab} =1.1° with the incident beam axis. This monitor system was movable on the scattering plane and an accuracy of absolute scattering angles was 0.02°. The absolute scattering angles was determined by measureing the symmetry of the slight small deflective patterns on the Rutherford scattering yields with the beam axis. Differences between yields at symmetrical points are within pm 0.0003°. The beam was doubly collimated to a spot diameter less than 0.4mm on the target. The target was a self-supporting natural Si metal of 180 μ g/cm^2 thickness.

The contributions from the target contaminations have to be taken into account in order to keep the resulting error small. We found a contaminate material of about 3.7×10^{-3}% in the Si target which is estimated a mass number of near A=180, it may be Au, from the elastically scattered energy spectra at the large angles.

As the physical effects for the elastic scattering data at very forward angles, the multiple scattering, the electron screening and vacuum polarization should be considered. The effects of the first and second terms were negligible for the data at angles larger than 0.2° at least. However, the effect of the third term was taken into account for the data.

The sum-of-differences (SOD) cross sections were calculated using the measured angular distribution. The resulting function $\sigma_{SOD}(\theta_0)$ were renormalyzed as the median of the upper and lower envelopes of $\sigma_{SOD}(\theta_0)$ became a horizontal line. These $\sigma_{SOD}(\theta_0)$ functions exhibt a certain osillation at small angles. The additional fingerprint for a forward glory is an undulating envelope of the oscillating σ_{SOD} function $|f_N(\theta_0)| = f_N(0)J_0(l_g \sin\theta)$ as predicted by the semiclassical scattering theory, which the envelope of the oscillation part behaves like the Bessel function $J_0(l_g \sin\theta)$ if a forward nuclear glory exist. The $\sigma_{SOD}(\theta_0)$ obtained from data are compared in Fig.1 with the $J_0(l_g\sin\theta)$ function caluculated with glory angular momenta of l_g =30, 30, 40, and 45 for ^{12}C, ^{13}C, ^{15}N and ^{16}O projectile nuclei, respectively. These glory angular momenta correspond to the grazing angular momenta, respectively. In Table 1, the values of the total reaction cross sections sigma σ_R are listed together with the $|f_N(0)|$ and the glory angular momenta.

References

1) Holdman J. T. Holdeman and Theler R. M., Phys. Rev. Lett. **14** (1965) 81.
2) Marty C., Z. Phys. A **309** (1983),261; Z. Phys. A **322** (1985) 499.
3) Hussein M. S. et al., Phy. Lett. **114B** (1982) 1.
4) Hussein M. S., Phys. Lett. **127B** (1983) 165.
5) Oeschler H. et al., Nucl. Phys. **A325** (1979) 463.
6) Hussein M. S. et al., Phys. Rev. Lett. **52** (1984) 511.
7) BarretteJ. and Alamanos N., Phy. Lett. 153B, **208** (1985); Nucl.Phys. **A441** (1985) 733.
8) Hnizdo V., Phys. Lett. **167B** (1986) 26.
9) Lipperheido R. H., Nucl. Phys. **A469** (1987) 190.
10) Villari A. C. C. et al., Nucl. Pfys. **A501** (1989) 605.
11) Ostrowski A. N. et al., Phys. Lett. **B232** (1989) 46.
12) Ostrowski A. N. et al., Phy. Rev. **C44** (1991) 2082.
13) Yamaya T. et al., Proc. of 3rd-IN2P3-RIKEN Symposium on Heavy Ion Collision, Kawagoe, Saitama, Oct. 1994. pp23-33.
14) Yamaya T. et al., Phys. Rev. **C37** (1988) 2585.

Table 1. Results from the SOD analyses.

projectiles	SOD (mb)	OMP (mb)
^{12}C	1490±50	1510±300
^{13}C	2090±80	1960±390
^{15}N	1650±50	1906±380
^{16}O	1600±30	1520±304

In the Table 2 the total reaction cross sections obtained from the SOD methode are compared with the results from the optical model potential analyses$^{14)}$.

Table 2. Comparison between the reaction cross sections deduced from the SOD and OMP analyses.

projectiles E_{lab}(MeV)	^{12}C 65	^{13}C 60	^{15}N 85	^{16}O 75
wave number k (fm^{-1})	4.28	4.17	5.08	4.83
coulomb parameters η	5.68	6.16	6.26	8.14
total reaction cross sections σ_R (mb)	1490±50	2090±80	1650±50	1600±30
nuclear scattering amplitudes |f(0)| (fm)	10±2	21±4	48±20	35±5

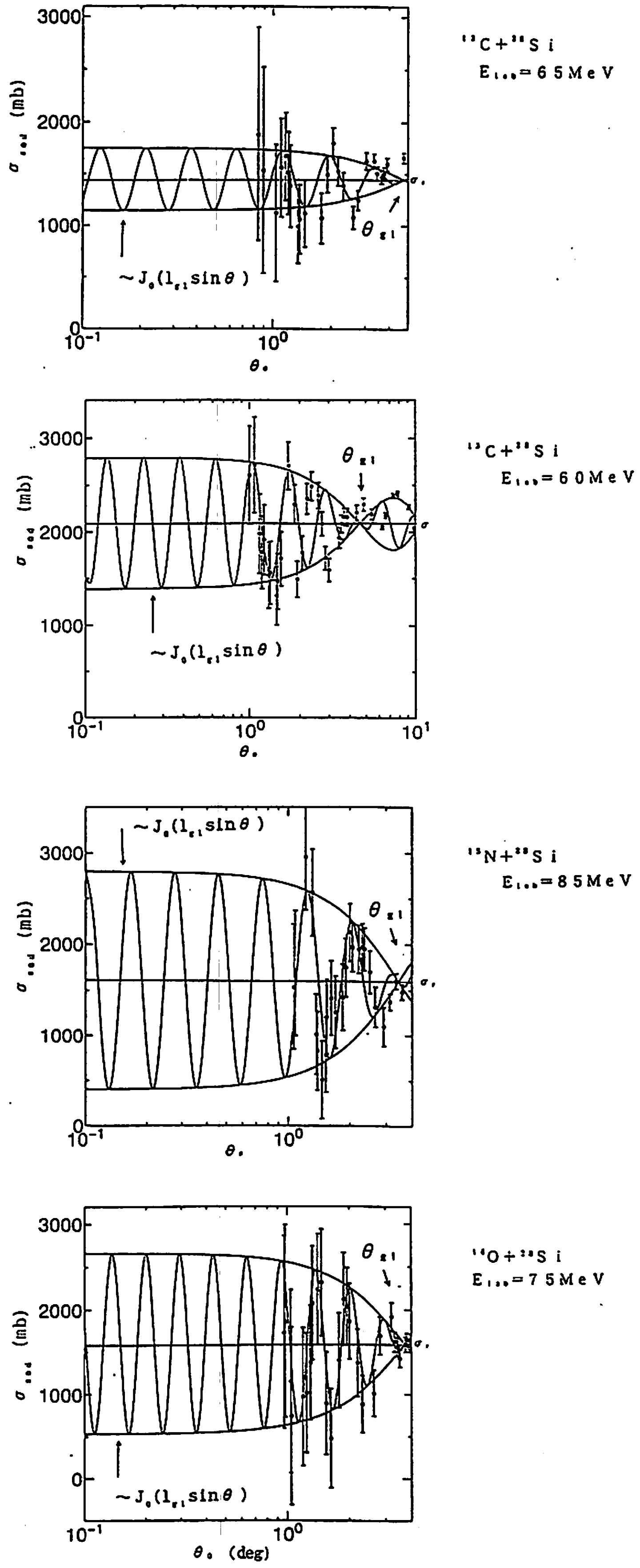

Fig. 1 The Sum of differences cross sections $\sigma_{SOD}(\theta_0)$ obtained from the present data.
Solid curves are the results of the χ^2 fit. The holizontal lines give the total reaction cross sections σ_R as obtained from χ^2 fit.

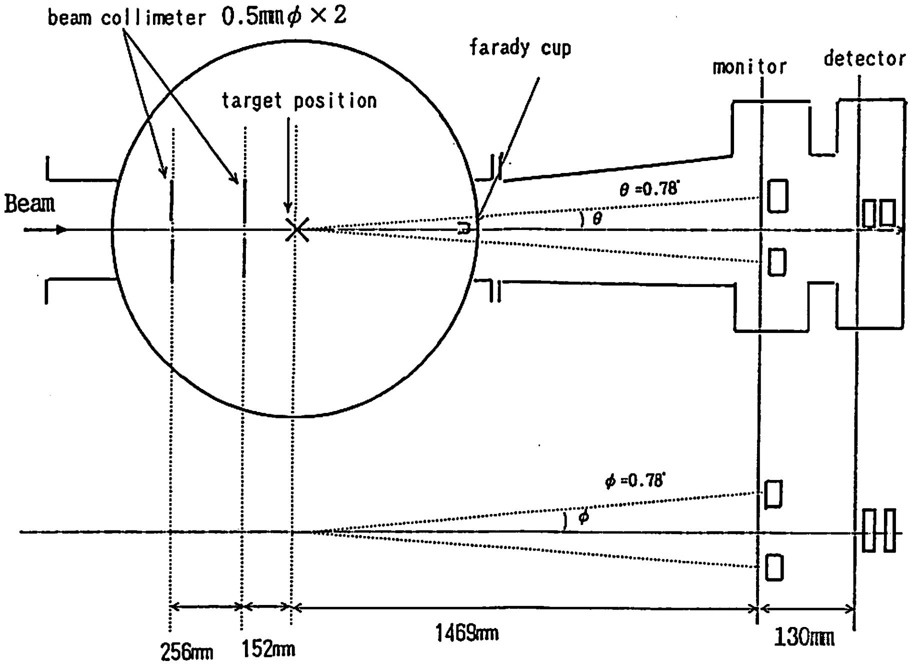

Fig. 2 Trapezoidal scattering chamber for the measurments at exteremely forward angles.

I. 4. Measurement of Neutron Spallation Cross Sections of ^{12}C, ^{27}Al and ^{209}Bi

Kim E., Nakamura T., Konno A., Imamura M., Nakao N.*, Shibata T.*,*
*Uwamino Y.**, Nakanishi N.**, Tanaka Su***.*

Cyclotron and Radioisotope Center, Tohoku Uninersity
*Institute for Nuclear Study, University of Tokyo**
*Institute of Physical and Chemical Research***
*Japan Atomic Energy Research Institute****

At present, a demand for neutron reaction data is world-wide increasing from the view points of intense neutron source of material study, induced radioactivity and shielding design of high energy accelerators. Neverthless, neutron reaction data in the energy range above 20MeV are very poor and no evaluated data file exists at present. In this study, we measured the neutron spallation cross sections using quasi-monoenergetic p-^{7}Li neutrons in the energy range of 20MeV to 210MeV. The irradiation experiments were performed at four cyclotron facilities of 1) INS of Univ of Tokyo, 2) CYRIC of Tohoku Univ, 3)TIARA of JAERI, and 4)RIKEN.

The ^{7}Li targets of 2 to 10 mm thicknesses were bombared by proton beams of 20 to 210MeV energies which were extracted from these cyclotrons. The neutrons produced in the forward direction from the target were transported through the collimator for sample irradiation and the proton beams passed through the target were swept out by the magnet to the beam dump. The neutron spectra were measured with the TOF method using an organic liquid scintillator. The absolute neutron fluence of the monoenergetic peak was determined with the PRT(Proton Recoil counter Telescope) at TIARA, and with the Li activation method to detect the ^{7}Be activity from the ^{7}Li(p,n)^{7}Be reaction at INS, CYRIC and RIKEN. The irradiation samples are ^{12}C, ^{27}Al and ^{209}Bi. The sizes of the samples are 20mm to 80 mm and thickness are 0.6 mm to 10.8 mm. Irradiation time consisted of short irradiation time (1 to 2 hours below E_p = 120MeV, 30 min above E_p = 120MeV) and long irradiation time (about 20 hours) by considering the half lives of produced nuclei. The gamma-ray activities of irradiated samples were counted by using a Ge detecter. The carbon samples were put into an aluminum case to absorb the positron energy from ^{11}C nuclei produced by the ^{12}C(n,2n)^{11}C reaction, since the annihilation gamma rays of 511keV were measured with the Ge detecter. The peak efficiency of the Ge detecter was obtained from the mixed standard source and the self absorption of samples was calculated with the PEAK code$^{1)}$ and the EGS4 code$^{2)}$.

The reaction rates of identified radioisotopes were obtained by analyzing gamma-ray spectra after corrected for the peak efficiency, sum-coincidence and self-absorption effects, also for the beam current fluctuation during sample irradiation. The spallation cross section data were obtainded from the neutron spectra and the reaction rates.

From the obtained cross sections, Fig.1 and 2 exemplify the cross section values of ^{209}Bi(n,4n)^{206}Bi to ^{209}Bi(n,10n)^{200}Bi, ^{12}C(n,2n) ^{11}C reactions. The cross section data of ^{209}Bi(n,xn)$^{210-x}$Bi reactions were compared with the ENDF/B-VI high energy file data calculated with the ALICE code$^{3)}$. Our experimental results are the first experimental data and are generally in good agreement with them except for ^{209}Bi(n,9n)^{201}Bi. A big discrepancy, about a factor of 4, between our experiment and ENDF/B-VI may come from the uncertainty of the decay scheme of ^{201}Bi, where we assumed the 100% branching ratio of 628keV gamma rays from the first excited state to the ground state. If this ratio is 25%, then our data well agree with the ENDF/B-VI. Our cross section data of ^{12}C(n,2n)^{11}C shown in Fig. 2 are lower in the peak region around 40MeV than the ENDF/B-VI high energy file data, but much higher than the ENDF/B-VI data above 60MeV. Our results below 40MeV show good agreement with the Brill's data$^{4)}$. Our first experimental data above 40MeV show almost a constant value of 20mbarn, which revealed that the ENDF/B-VI data of ^{12}C(n,2n)^{11}C reaction may be inaccurate.

References

1) Nakamura T., and Suzuki T., Monte Carlo Calculation of Peak Efficiencies of Ge(Li) and Pure Ge Detecter to Voluminal Sources and Comparison with Environmental Radioactivity Measurement. Nucl. Instr. and Meth. **205, 211** (1983).
2) Nelson W. R., Hirayama H., and Rogers D. W. O, SLAC-265.
3) Blann M., CODE ALICE/89, private communication (1989).
4) Brill O. D., N. A. Vlasov, S. P. Kalinin and L. S. Sokolov, Cross Section of the (n,2n) Reaction in C^{12}, N^{14},O^{16} and F^{19} in the Energy Interval 10-37MeV, DOK 136, Inst. Atom Energy I.V., Kurchatova, Moscow, **55** (1961).

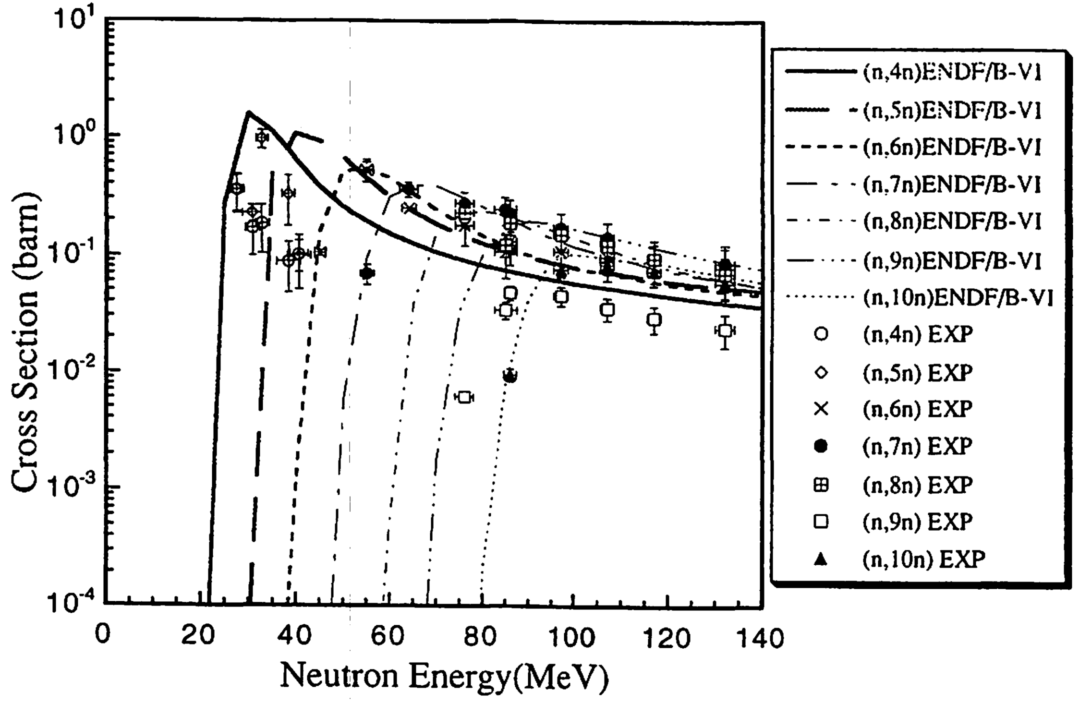

Fig. 1 Cross sesction data of ^{209}Bi(n,xn) $^{210-x}$Bi reaction compared with ENDF/B-VI.

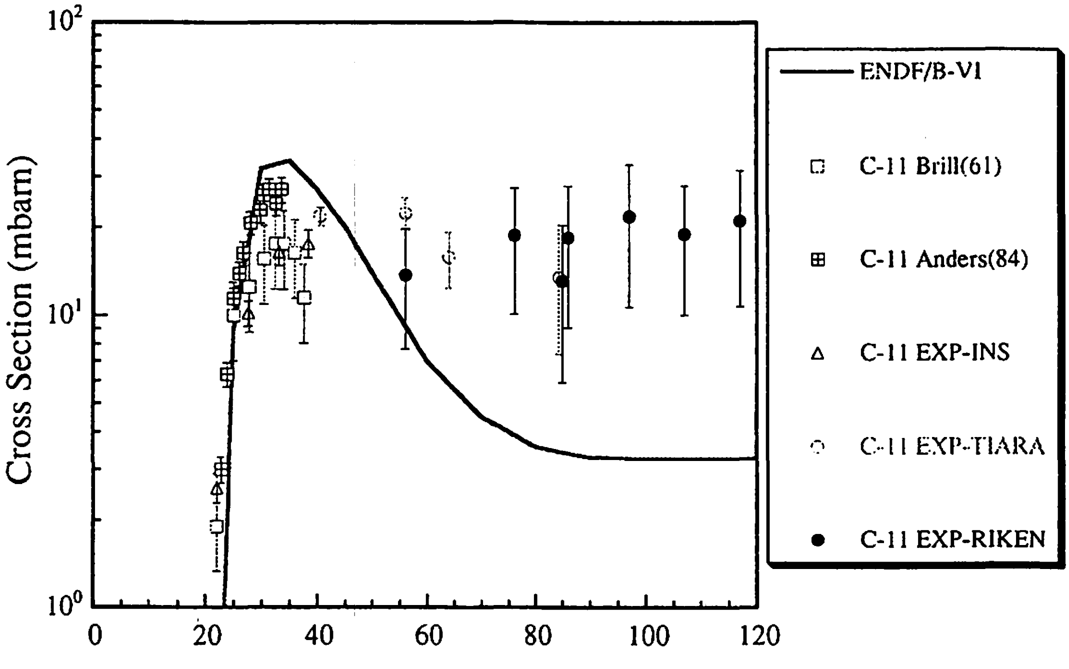

Fig. 2 Cross sesction data of ^{12}C(n,2n) ^{11}C reaction compared with ENDF/B-VI.

I. 5. Single Particle States in the ^{49}Sc Nuclus

*Hino T., Tohei T.****, Nakagawa T., Fujii Y., Aizawa T., Orihara H.*,Terakawa A.*, Guan Z.*, Yun C. C.*, Ito K.*,Teramoto Y.*, Yamamoto A.*, Matsumura N.*, Ishii K.**, Abe K.**, Narita A.***, Suehiro T.**** and Ohnuma H.******

Department of Physics, Tohoku University
*Cyclotron and Radioisotope Center, Tohoku University **
*Department of Nuclear Engineering, Tohoku University ***
*Department of Information Science, Hirosaki University ****
*Tohoku Institute of Technology *****
*Department of Physics, Tokyo Institute of Technology ******

One nucleon transfer reactions, like (^{3}He,d), (d,^{3}He), (d,p), (d,n), etc. have provided a good place to explore the single particle strength in a nucleus, while their deduced values suffer from ambiguities due to those for the choice of optical potential parameters applied in the distorted-wave Born-approximation (DWBA) analysis and/or for the treatment of the reaction mechanism involved. As for the proton single-particle strength, the (^{3}He,d) reaction has mainly used for this purpose because of its experimental reliabilities comparing with that of the (d,n) reaction, though the former is more complicate in the choices of optical potential parameters and theoretical treatment of reaction mechanism. Recently, there have been new progresses in calculation with large shell-model spaces over the 1f2p-shell region[1,2]. In order to test the validity of such shell-model predictions, one nucleon transfer, like (d,p) and (d,n) reactions, are expected to present very useful tools.

We have systematically studied sd proton-shells via the (d,n) reaction using the CYRIC time-of-flight (TOF) facility. In recent years, the ^{40,42,44}Ca + one proton systems, which are located in the edge of the fp-shell region, have been investigated[3,4]. We have also carried out the experiments of the ^{40,42,44,48}Ca(d,p) reactions with the same deuteron-bombarding energy of 25MeV to study the ^{40,42,44,48}Ca + one neutron systems[5]. All Ca isotopes have the Z = 20 closed proton shell and ^{40,48}Ca have neutron closed-shell as well at N = 20 and 28. Therefore, systematic investigations of the Ca isotope plus one nucleon systems are very interesting, not only for testing shell model predictions but also for observing mass dependence of nuclear structures. It is expected that the results of experiments accomplished with the same bombarding energy may bring less ambiguities in the DWBA analyses.

For the study of single particle states in ^{49}Sc, the measurements of the ^{48}Ca(^{3}He,d) ^{49}Sc reaction have been mainly done in many previous works. Iwasaki et al. carried out the

^{48}Ca(d,n)^{49}Sc experiment with bombarding energy 20MeV and reported spectroscopic factors for various states in ^{49}Sc up to about 7MeV in excitation energy[6)]. Our purposes are to obtain spectroscopic information for higher excited states in ^{49}Sc with better statistical conditions through the ^{48}Ca(d,n)^{49}Sc reaction, and to reduce ambiguities for the spectroscopic factors by systematic analyses.

Experiments were carried out with 25MeV deuteron beam from the CYRIC AVF cyclotron. The target was a 1.6mg/cm^2 thick and isotopically 97.8% enriched self-supporting foil of ^{48}Ca prepared by evapolation. Energies of emitted neutrons were measured by a TOF technique with a 44m long flight pass. For the neutron detection, liquid scintillator NE213 was used. It was contained in four 50cm(W)$*$10cm(H) $*$5cm(D) rectangular cases and eight 20.3cm ϕ, 5cm(D) cylindrical cases, which led to the solid angle of 0.233msr and the effective efficiency of 2.9%. Angular distributions of differential cross sections were measured between θ_L=0deg to 80deg using a beam-swinger system.

Angular distributions of differential cross sections for 36 states were obtained in the excitation energy range from the ground state up to 15MeV. Achieved energy resolutions for the states were 220-280keV. Figure 1 shows an energy spectrum obtained at θ_L=25deg. The zero-range DWBA code DWUCK4[7)] was employed to obtain theoretical differential cross sections. As a deuteron optical potential was used an adiabatic potential[8)] obtained from Becchetti and Greenlees's potential[9)] for a proton and Carlson et al.[10)] for a neutron. The corrections for finite range and non-locality were contained in the present DWBA calculation[11,12)]. Figure 2 shows typical angular distributions and the results of the DWBA calculation, which well reproduce the experimental data, and Table 1 shows spectroscopic factors obtained for each states, comparing with the results of Iwasaki et al. One could see they are well agree with each other.

Excitation energy distributions of single particle strengths for each shell in ^{49}Sc are presented in Fig. 3. A few states with stronger strengths and many weak-strength states appear for the $1f_{7/2}$ and $2p_{3/2}$ orbits, which are the nearest shells outside the Z = 20 proton core. While only a few states with strong amplitudes can be seen for the $2p_{3/2}$, $2p_{1/2}$, and $1f_{5/2}$ orbits of ^{49}Ca, which are the nearest shells outside the N = 28 neutron core, in our (d,p) experiment with the same incident energy. On the other hand, 2s1d hole strengths are observed in ^{49}Sc, whereas 2s1d or $1f_{7/2}$ hole strengths in ^{49}Ca can't be seen almost. These facts indicate qualitatively that the $1d_{3/2}$ proton closed core should be less inert than that of $1f_{7/2}$ neutron.

Sum rules for the obtained spectroscopic factors of ^{49}Sc are presented in Fig. 4, with those of ^{49}Ca. It is noticed that sums of the spectroscopic factors for the fp-shells of ^{49}Sc exceed largely their shell model sum-rule limits. This seems to be owed to the results of the DWBA calculations with the present adiabatic potential parameters used for the ^{48}Ca(d,n) reaction. The DWBA calculations using the same optical potential parameter systematics have resulted in success for the (d,n) reactions on the other Ca targets and the (d,p) reactions on all Ca targets at the same deuteron energy. These facts suggest a new systematic analysis with consistency through the (d,n) and (d,p) reactions on every Ca isotope should be found.

References

1) Richter W. A., Van Der Merwe M. G. and Brown B. A., Nucl. Phys. **A579** (1994) 173.
2) Richter W. A., Van Der Merwe M. G. and Brown B. A., Nucl. Phys. **A586** (1995) 445.
3) Mori S., M. thesis, Tohoku University (1988).
4) Narita A. et al., CYRIC Annual Report (1991)23.
5) Narita A., M. thesis, Tohoku University(1990).
6) Iwasaki Y., Galonsky A. and Weber D. J., Phys. Rev. C **22** (1980)456.
7) Kunz P. D., DWBA code DWUCK4, unpublished.
8) Johnson R. C. and Soper P. J. R., Phys. Rev. C **1** (1970) 976.
9) Becchetti F. D. and Gleenlees G. W., Phys. Rev. **192** (1969) 1190.
10) Carlson J. D., Zafiratos C. D. and Lind D. A., Nucl. Phys. **A249** (1979) 15.
11) Buttle P. J. A. and Goldfarb L. J. B., Proc. Phys. Soc. **83** (1964) 701.
12) Perey F. G. and Buck B., Nucl. Phys. **32** (1962) 353.

Table 1. Spectroscopic factors obtained from the ^{48}Ca(d,n)^{49}Sc reaction, together with the previous work.

		Present work E_d=25MeV					Iwasaki et al.[6] E_d=20MeV			
No.	E_x(MeV)	l	j^π	C^2S			E_x(MeV)	l	j^π	C^2S
1	0.00	3	$\frac{7}{2}^-$	1.75			0.000	3	$\frac{7}{2}^-$	1.73
2	2.25	0+2	$\frac{1}{2}^+$	0.04						
3			$\frac{3}{2}^+$	0.06						
4	3.08	1	$\frac{3}{2}^-$	0.81			3.093	1	$\frac{3}{2}^-$	0.76
5	3.80	3	$\frac{7}{2}^-$	0.13			3.821	3	$\frac{5}{2}^-$	0.20
6	4.07	3	$\frac{5}{2}^-$	0.31			4.082	3	$\frac{5}{2}^-$	0.28
7	4.33	3	$(\frac{5}{2}^-)$	0.09			4.341	3	$\frac{5}{2}^-$	0.10
8	4.49	1	$\frac{1}{2}^-$	0.81			4.507	1	$\frac{1}{2}^-$	0.32
9	4.76	1+3	$(\frac{1}{2}^-)$	0.04	$(\frac{3}{2}^-)$	0.02	4.756	3	$\frac{5}{2}^-$	0.19
10			$\frac{5}{2}^-$	0.20						
11	5.07	1+3	$(\frac{1}{2}^-)$	0.18	$(\frac{3}{2}^-)$	0.09	5.035	1	$\frac{1}{2}^-$	0.18
12			$(\frac{5}{2}^-)$	0.48			5.100	3	$\frac{5}{2}^-$	0.48
13	5.37	2+3	$(\frac{3}{2}^+)$	0.05			5.392	3	$\frac{5}{2}^-$	0.22
14			$(\frac{5}{2}^-)$	0.17						
15	5.67	1	$(\frac{1}{2}^-)$	0.37	$(\frac{3}{2}^-)$	0.18	5.686	1	$\frac{1}{2}^-$	0.33
16	5.85	1	$(\frac{1}{2}^-)$	0.07	$(\frac{3}{2}^-)$	0.03	5.836	1	$\frac{1}{2}^-$	0.06
17	6.52	1+4	$(\frac{1}{2}^-)$	0.05	$(\frac{3}{2}^-)$	0.02				
18			$(\frac{7}{2}^+)$	0.05	$(\frac{9}{2}^+)$	0.02				
19	6.80	1+3	$(\frac{1}{2}^-)$	0.15	$(\frac{3}{2}^-)$	0.08	6.836	1	$\frac{1}{2}^-$	0.13
20			$\frac{5}{2}^-$	0.04						
21	7.07	1+4	$\frac{1}{2}^-$	0.13			7.081	1	$\frac{1}{2}^-$	0.07
22			$(\frac{7}{2}^+)$	0.10	$(\frac{9}{2}^+)$	0.05				
23	7.33	1+3	$(\frac{1}{2}^-)$	0.11	$(\frac{3}{2}^-)$	0.06				
24			$(\frac{5}{2}^-)$	0.06						
25	7.52	1+3	$(\frac{1}{2}^-)$	0.06	$(\frac{3}{2}^-)$	0.03				
26			$(\frac{5}{2}^-)$	0.16						
27	7.83	1	$(\frac{1}{2}^-)$	0.33	$(\frac{3}{2}^-)$	0.17				
28	8.07	1+4	$(\frac{1}{2}^-)$	0.16	$(\frac{3}{2}^-)$	0.09				
29			$(\frac{7}{2}^+)$	0.09	$(\frac{9}{2}^+)$	0.04				
30	8.34	1	$(\frac{1}{2}^-)$	0.15	$(\frac{3}{2}^-)$	0.08				
31	8.90	2	$(\frac{3}{2}^+)$	0.05	$(\frac{5}{2}^+)$	0.03				
32	9.98	1+3	$(\frac{1}{2}^-)$	0.12	$(\frac{3}{2}^-)$	0.07				
33			$(\frac{5}{2}^-)$	0.07						
34	11.59	1	$\frac{3}{2}^-$	0.29						
35	15.59	3+4	$\frac{5}{2}^-$	0.17						
36			$\frac{9}{2}^+$	0.04						

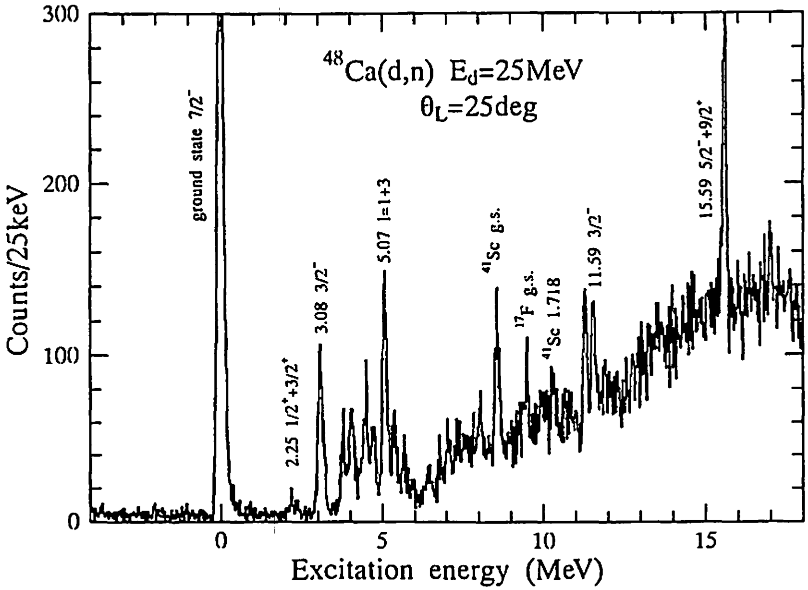

Fig. 1. An energy spectrum obtained from the ^{48}Ca(d,n)^{49}Sc reaction at θ_L=25deg.

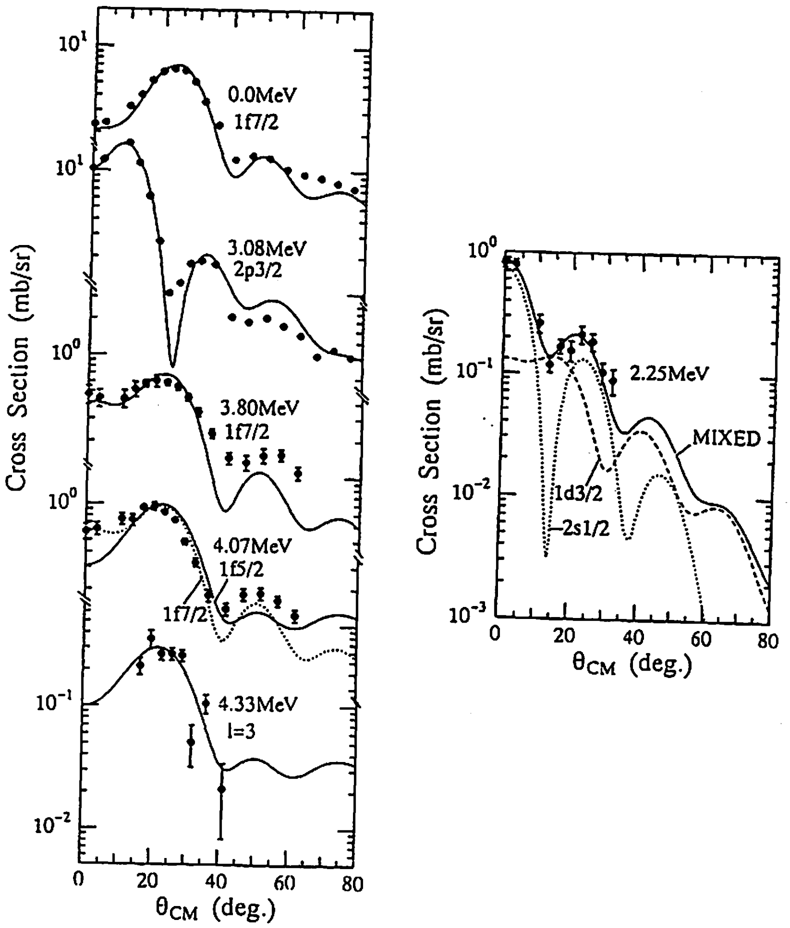

Fig. 2. Typical angular distributions of the differential cross section for the ^{48}Ca(d,n) ^{49}Sc reaction at E_d=25MeV. The curves show DWBA predictions which are normalized to experimental data.

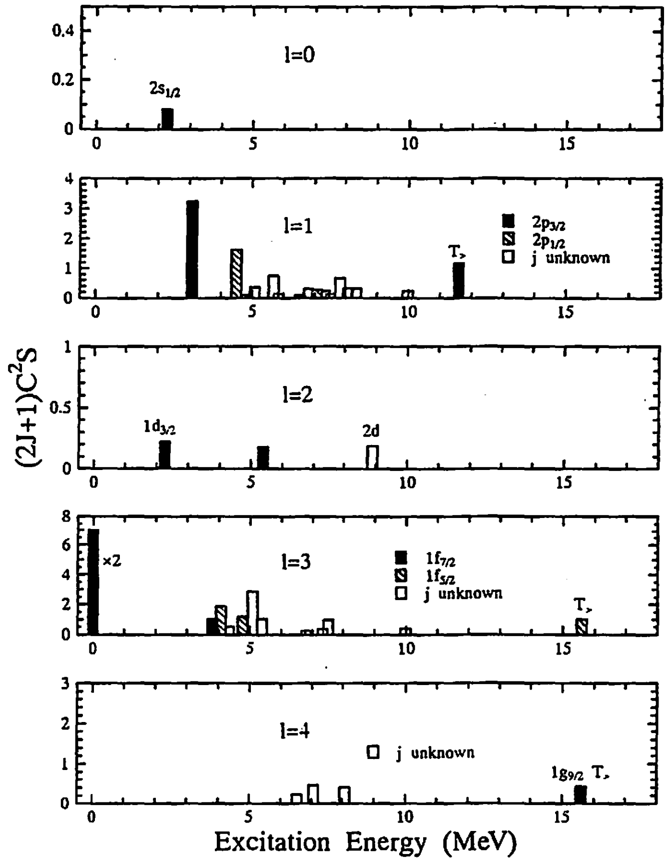

Fig. 3. Excitation energy distributions of single particle strengths for each orbits in ^{49}Sc.

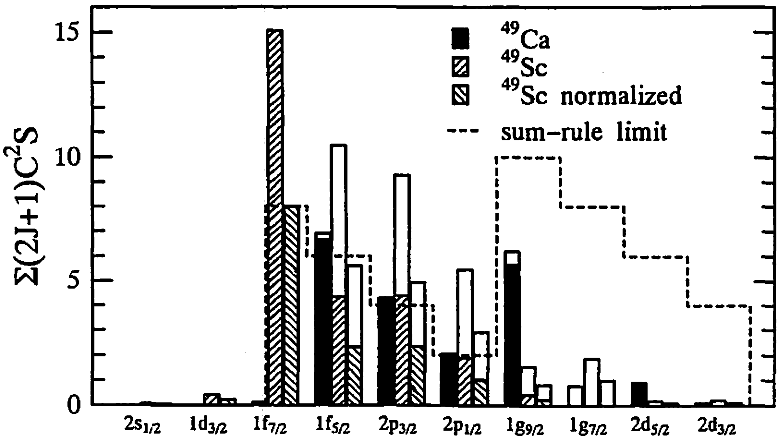

Fig. 4. Sum rule for obtained spectroscopic factors of ^{49}Sc(fore diagonal), together with those of ^{49}Ca(filled) at E_d=25MeV. Summed spectroscopic factors which are obtained by normalizing the sum of the $1f_{7/2}$ strengths to its shell model sum-rule limit are also presented(back diagonal). White bars indicate additional strengths if j-unknown states are assumed to belong to corresponding orbits.

I. 6. Study of Neutron-Rich N = 50 Nuclei

Watanabe A., Shinozuka T., Fujita M., Kanai Y.**, Kohda T., and Fujioka M.**

Department of Physics, Tohoku University
*CYRIC, Tohoku University**
*Department of Nuclear Engineering, Tohoku University***

Various nuclear models were proposed to understand nuclear structure. A large number of experimental data have shown that nuclei with neutron or proton number 2, 4, 8, 20, 50, 82 and 126 are unusually stable. Mayer and Jensen et al. proposed the shell model with assumption of a spin-orbit force and explained those magic numbers.

In recent years more and more nuclei far from stability are being studied. The problem if these unstable nuclei have shell structure is of great interest. ^{84}As has proton number $Z = 33$ and neutron number $N = 51$, and one can directly chech the effect of $N = 50$ shell by measureing the Q_β value of ^{84}As → ^{84}Se.

Since the experimental data about the decay of ^{84}As were not enough, there were following questions; one is about the presence of isomer. Kratz et al. reported two isomers with half-lives of 5.5 sec and 0.65 sec. On the other hand, Hoff et al. recently determined the half-life to be 4.5 sec, but did not confirm a shorter isomer.

The other question is about the Q_β value of ^{84}As → ^{84}Se. Estimation by Wapstra et al. and calculations by nine different semi-empirical mass formulas give Q_β value ranging from 9.4 to 11.0 MeV. Experimental Q_β value by Gill and Rudstam, however, are 6.8 - 7.2 MeV and are in disagreement with the values derived from systematics.

We report on a direct mesurement of the Q_β value and half-life of ^{84}As, and compare them with the values already reported.

^{84}As was produced in 25 MeV proton-induced fission of ^{232}Th and was mass-separated by IGISOL. The ion beam was implanted onto the aluminumized mylar tape. The tape was moved periodically to reduce background of daughter activities.

The half-life of ^{84}As was measured with a 155cc HPGe detector using a P-chopper to cut down neutron background. Sorting the γ-time list data by ^{84}As γ ray gates, the half-life of ^{84}As was determined to be 3.24 ± 0.26 sec, and the above mentioned 0.65 sec isomer was not detected.

For the measurement of the Q_β value of ^{84}As a LEPS and a 234cc HPGe detector were used and β-γ-time list data were collected. The data were analyzed by gating on the ^{84}As

1455 keV γ ray peak and its Compton region. The projected β spectrum was replotted by Kurie analysis to determine the end-point energy. We obtained 7.66 ± 0.88 MeV for the end-point energy. Adding 1.455 MeV to this value 9.12± 0.88 MeV for the Q_β of ^{84}As is obtained.

Two neutron separation energy of ^{84}As is deduced to be 12.910± 0.88 MeV from the present Q_β value. S_{2n} estimated by Wapstra et al. indicates the presence of $N = 50$ shell. However, the experimental values by Gill and Rudstam are in disagreement with the systematic trend and they underestimate the $N = 50$ shell gap. On the other hand our S_{2n} is consistent with the value of Wapstra et al. and supports the systematic trend.

Since the yield of ^{84}As was small (≤10 atoms/sec), our result has large errors. It is expected to improve IGISOL for further study.

References

1) Kratz J. V., Franz H., Kaffrell N. and Hermann G., Nucl. Phys. **A250** (1975)13.
2) Hoff P., Ekström B. and Omtvedt J. P., Z.Phys. **338** (1991) 285.
3) Wapstra A. H. and Audi G., Nucl.Phys. **A432** (1985) 1.
4) Houstein P. E., At.Data Nucl.Data Tables **39** (1988) 185.
5) Gill R. L., Phys. Rev **C50** (1994) 2612.

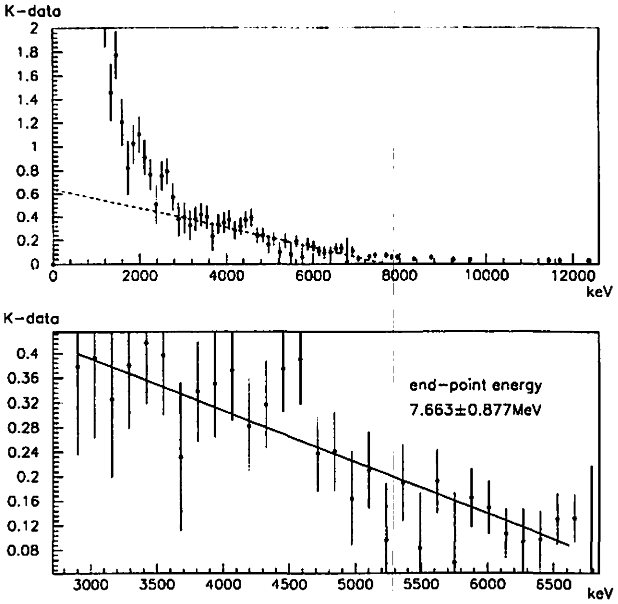

Fig. 1. Kurie-plot of β spectrum for ^{84}As.

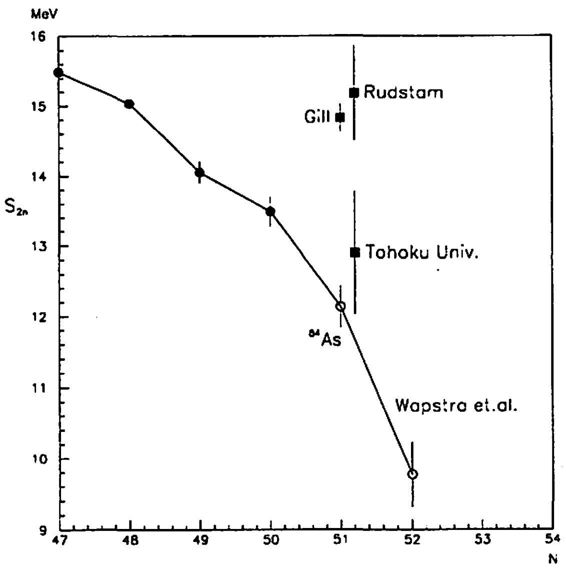

Fig. 2. Behavior of S_{2n} near ^{84}As.

I. 7. Branching Ratio of the Direct Proton Decay from the Isobaric Analog State Populated by the ^{208}Pb(p,n) ^{208}Bi Reaction

Terakawa A., Yun C. C., Itoh K., Yamamoto A., Teramoto Y., Matsumura N.,
Fujii Y., Hino T*., Aizawa T*., Nakagawa T.*, Ishii K.** and Orihara H.*

Cyclotron and Radioisotope center, Tohoku University
*Faculty of Science, Tohoku University**
*Faculty of Engineering, Tohoku University***

Studies of the decay property for giant resonances following charge-exchange reactions limited to a few cases, especially for the (p,n) reaction, no reliable data has been reported due to experimental difficulties encountered with measuring neutrons and decay protons with a sufficient efficiency, and with reasonable resolution. As such, the (^{3}He,t) reaction has been the good candidate to explore proton decay of the isobaric analog state (IAS) and/or giant Gamow-Teller resonance (GTR). Hofmann and his collaborators[1)] have reported total and escape widths of IAS in even-*A* Pm isotopes through ^{A}Nd(^{3}He,t$\bar{\mathrm{p}}$) $^{A\text{-}1}$Nd reactions at an bombarding energy of 75 MeV. At an intermediate energy (≥ 100 MeV), where spin-flip GTR is dominant at small momentum transfer, Akimune et al.[2)] have performed measurement for microscopic structure of the GTR in ^{208}Bi with the ^{208}Pb(^{3}He,t$\bar{\mathrm{p}}$)^{207}Pb reaction

Because of the larger Coulomb displacement energy, an isobaric analog states (IAS) is located in a heavier nucleus at a high enough excitation energy above particle-decay threshold energy. It has been found that such an IAS has a noticeable level width of several hundred keV. It is natural to described the width Γ of an IAS as a sum of the escape width $\Gamma^{\uparrow}$ and the spreading width $\Gamma^{\downarrow}$□as:

$$\Gamma = \Gamma^{\uparrow} + \Gamma^{\downarrow}. \qquad (1)$$

The escape width consists of those by the isospin-allowed proton decays into the neutron-hole states in the daughter nucleus, since the decay channels through heavier particles-emission are severely inhibited by the Coulomb barrier. On the other hand, the spreading width is speculated to be due to the Coulomb interaction which gives rise to the isospin-mixing between the IAS(T_0) and near-by lying T_0 -1 states (T_0: isospin of the parent nucleus). Moreover, isospin mixing would lead to the isospin-forbidden neutron decay in the final stage of the damping process of the IAS. Thus, in contrast to decay of GTR, that of IAS is of paticular interest since knowledge of the spreading width and neutron decay provide good candidates to study isospin-mixing interactions. Furthermore, the recent measurement of neutron-decay for the IAS in ^{208}Bi has shown$^{3)}$ that the neutron-decay branch accounts for the all missing decay width other than that of the proton decay, and thus one can derive the spreading width of the IAS by subtracting the proton escape width from the total width following Eq.(1).

In this report, we present the result of the proton-decay measurement for the IAS in ^{208}Bi through the ^{208}Pb$(p,n)^{208}$Bi reaction as a feasibility tests of the neutron-proton coincidence measurement at the CYRIC TOF Facility$^{4)}$. A diagram for these processes is illustrated in Fig. 1. The physical motivation of this study is to deduce the IAS proton-decay branch by which information about the microscopic structure of the IAS may be obtained. Furthermore, it is aimed to obtain isospin-impurity information on the IAS wave function, as well, from the spreading width which is indirectly deduced according to Eq. (1) with both the proton escape and the total widths

The experiment was performed using a 35 MeV momentum-analyzed proton beams obtained from the AVF cyclotron at CYRIC, Tohoku University. The target used was a 99.9 % isotopically-enriched self-supporting foil of ^{208}Pb. The target thickness was 27.6 mg/cm^2. Neutrons were detected with four neutron detectors containing the NE213 liquid scintillator located at the flight length of 12m. The size of each detector was 20.5 cm in diameter and 5 cm in length along the neutron-flight direction. The effective solid angle for the neutron detection was 0.53 msr. The beam swinger system was set for the 0-degree measurement of emitted neutrons, while the beam was bent downstream of the target by a cleaning magnet, and stopped by the Faraday cup located after the magnet.

Decay protons were detected in coincidence with neutrons using a SSD-telescope of Si surface-barrier type mounted at the length of 8 cm from the target, and at $\theta_p = 135$ degree relative to the beam direction. The SSD-telescope consisted of ΔE (250μm thick), E (1000μm thick) and veto counters with a 100 mm^2 active surface area. The veto detector was used to reject energetic protons scattered at backward angles. The solid angle for the proton detection was 15.6 msr. The experimental setup for the present measurement is illustrated in Fig. 2.

Figure 3 shows a part of the inclusive neutron spectrum of the ^{208}Pb$(p,n)^{208}$Bi reaction. The IAS is strongly populated at E_x = 15.17 MeV in ^{208}Bi$^{5)}$, while the Gamow-Teller resonance$^{5)}$ [GTR, E_x = 15.6 MeV, Γ = 3.72MeV$^{2)}$] is not clearly identified in this bombarding energy. Thus, the proton decay of the GTR would not contribute to the present neutron-proton coincidence measurement for the IAS. A time spectrum of the coincidence events, measured with the neutrons as start and with the protons as stop, has displayed the

The energy spectrum of the decay protons from the IAS is shown in Fig. 4. The low-lying neutron-hole states in ^{207}Pb have been populated via the direct proton decay from the particle-hole configuration of the IAS. The proton energy resolution was about 700 keV, in which main part was due to energy losses in the rather thick target presently used.

Since the IAS is excited via the $L = 0$ transition, the proton emission from the IAS may be assumed to be isotropic. The branching ratio of the proton decay is obtained with the singles and coincidence double differential cross sections :

$$\frac{\Gamma_p^{\uparrow}}{\Gamma} = \frac{\Sigma \Gamma_{pi}^{\uparrow}}{\Gamma}, \qquad (2)$$

where

$$\Gamma_{pi}^{\uparrow} = \int \frac{d^2\sigma_{pi}}{d\Omega_n d\Omega_p} d\Omega_p = 4\pi \frac{d^2\sigma_{pi}}{d\Omega_n d\Omega_p}, \qquad (3)$$

and

$$\Gamma = \frac{d\sigma}{d\Omega_n}. \qquad (4)$$

The partial and total proton branching ratios measured in the present experiment are listed in Table 1, together with the results of the previous works$^{2,6)}$ and the theoretical calculation$^{6)}$. The obtained proton-branch of (57 ± 21)% reproduces well the earlier data$^{2,6)}$. When both the proton emission energies and the neutron spectroscopic factors for the one-neutron removal from the parent nucleus are taken into account in the calculation$^{7)}$, theoretical prediction using an effective force of the Skyrme type has given good accounts as well for the present observation.

The remaining decay branch of about 40% would be attributed to the neutron decay which accounts for the spreading width. Indeed, the above value is in consistent with neutron-decay branch of (37 ± 3)% determined by the recent measurement for isospin-forbidden neutron-decay.

In summary, the direct measurement of the proton decay from the IAS in ^{208}Bi was performed by means of the neutron-proton coincidence experiment through the (p,n) reaction at 35 MeV. The branching ratio for the proton decay of the IAS has been determined to be (57 ± 21)%, which is in consistent with the previous results within the statistical error.

References

1) Hofmann H. J. ey al., Nucl. Phys. **A433** (1985) 181.
2) Akimune H. et al., Phys. Rev. C **52** (1995) 604.3)
3) Bordewijk J. A. et al., Nucl. Phys. **A574** (1995) 453.
4) Orihara H. et al., Nucl. Instr. Meth. **A257** (1987) 189.
5) Nishihara S. et al., Phys. Lett. **106B** (1985) 369 and references there in.
6) Gaarde C. et al., Phys. Rev. Lett. **46** (1981) 902.
7) Colò G. et al., Phys. Rev. C **50** (1994) 1496.

Table 1. Branching ratios Γ_{pi}/Γ for the decay of the IAS in ^{208}Pb into the neutron-hole states in ^{207}Pb.

E_x in ^{207}Pb (MeV)	neutron hole states $n\ell j^{-1}$	Expt. $\Gamma^{\uparrow}_{pi}/\Gamma$ a	b	c	Theor.[d] $\Gamma^{\uparrow}_{pi}/\Gamma$
g.s.	$3p^{-1}_{1/2}$	0.20 ± 0.07	0.22 ± 0.03	0.22 ± 0.03	0.237
0.570	$2f^{-1}_{5/2}$	incl. $3p^{-1}_{3/2}$	0.11 ± 0.03	incl. $3p^{-1}_{3/2}$	0.061
0.898	$3p^{-1}_{3/2}$	0.28 ± 0.08	0.26 ± 0.03	0.34 ± 0.06	0.196
1.633	$1i^{-1}_{13/2}$	incl. $2f^{-1}_{7/2}$		-	0.010
2.340	$2f^{-1}_{7/2}$	0.09 ± 0.06	0.014 ± 0.002	0.015 ± 0.007	$< 10^{-3}$
3.413	$1h^{-1}_{9/2}$	-		-	$< 10^{-3}$
$\Sigma\Gamma^{\uparrow}_{pi}/\Gamma$		0.57 ± 0.21	0.60 ± 0.09	0.58 ± 0.09	0.504

[a] Present expt.

[b] Reference [6]. (^{3}He, t) reaction at 81 MeV.

[c] Reference [2]. (^{3}He, t) reaction at 450 MeV.

[d] Reference [7].

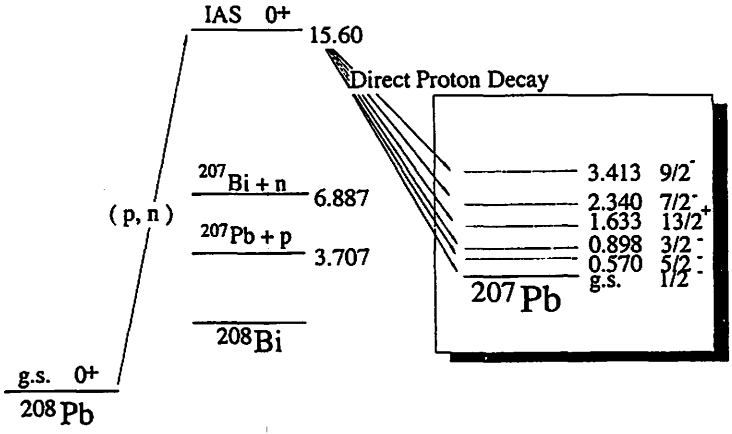

Fig. 1. Diagram of the ^{208}Pb($p,n_{IAS}\,p$)^{207}Pb reaction.

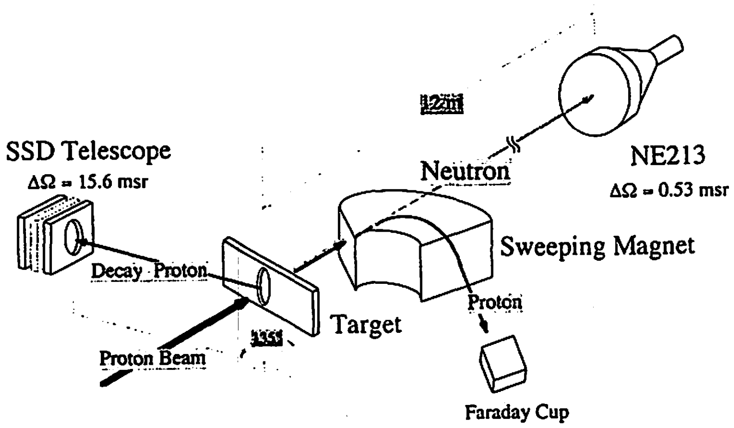

Fig. 2. Experimental set-up for the ($p,n_{IAS}\,p$) reaction.

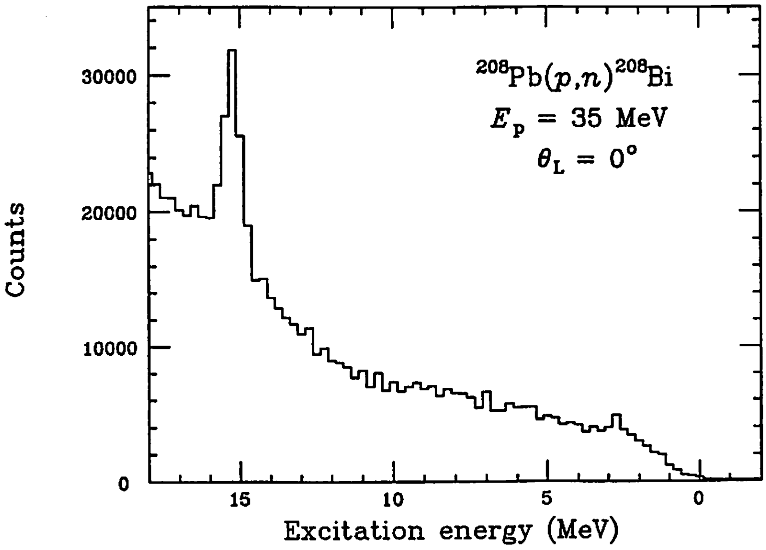

Fig. 3. Inclusive neutron spectrum of the ^{208}Pb(p,n_l) ^{207}Pb reaction at 35 MeV.

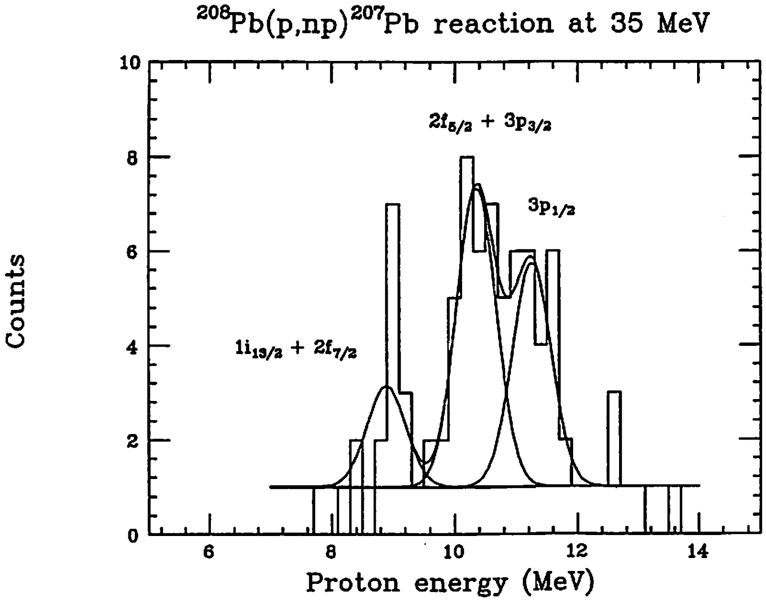

Fig. 4. Energy spectrum of the protons from the IAS in ^{208}Bi into the low-lying neutron-hole states in ^{207}Pb.

I. 8. TRIM Calculation of Distribution of Ions Implanted to Fe (AMU=1-210) and Si (AMU=1-10) in the Energy Range of ISOL (10-60keV)

Hanada, R

Institute for Materials Research, Tohoku University

Introduction

This note reports results of TRIM calculation for ions distribution (ions range, ions concentration and radiation damage) when ions are implanted to Fe and Si using the isotope separator on line (ISOL) at CYRIC. This is the continuation of the work reported in CYRIC report-1994 by the present author[1)], where the above described values have been calculated for ions with the atomic mass unit (AMU) above 10 for Si host. In this report, the calculations are extended to ions with the AMU below 10 (H, D(^{2}H), T(^{3}H), ^{3}He, ^{4}He, ^{7}Li and ^{10}B) for Si host and for ions with the AMU between 1-210 (H-Bi) for Fe host.

Results

The method of the calculation is exactly the same with those reported in Ref. 1. Fig. 1 shows a result of TRIM calculation for ^{111}In implanted to Fe host at the energy of 40keV to define the values shown in the following figures.

Fig. 2 shows the maximum ion concentrations in Si in the unit of (atoms/cm^3)/(atoms /cm^2) in the left and in the unit of (no. of atoms/no. of Si atoms) in the right ordinate. Here the implantation energy is taken as a parameter.

Since the main purpose of the present calculation is to determine the optimum implantaion energy for the maximum overlap with the PAC probe ^{111}In, the implantation energy was limited below 30keV for light ions.

In Fig. 2 as well as in Fig. 3 and 4, it is noteworthy that hydrogen isotopes (^{1}H, ^{2}H and ^{3}H) show different behaviors in the distribution and radiation damage. This is reasonable since the higher momentum of ^{3}H results in the larger range, larger straggling and hence lower ion concentration than those for ^{1}H at the same implantation energy. Also a higher transferred energy to the host atom results in the higher damage. Also when the ^{3}H(Z=1) values are compared with those for ^{3}He(Z=2), jumps are noticed in the calculated values. This is also reasonable since the higher Z value results in the higher energy loss and hence smaller range, straggling and larger ion concentration for ^{3}He than ^{3}H.

Figs. 5 through 7 show the results of the same calculation for Fe host for ions with the AMU between 1 and 209. The similar isotope effects described above are noticed also in the Fe case. The result in Fig. 6 reveals that the implantation energy of ^{1}H should be at the order of 1 keV to obtain the maximum overlap with 40keV ^{111}In. Such a low energy is not available for the ISOL at the CYRIC and so some other method of hydrogen introduction must be employed for hydrogen study in Fe by PAC using ^{111}In probe. An example of such a work, using an electrolytic method for H introduction, is reported in this volume.

Acknowledgement

This work is supported by a Grant-in Aid for Scientific Research on Priority Area from the Ministry of Education, Science and Culture of Japan.

References

1) Hanada, R : CYRIC Annual Report-1994, p39 (1995).

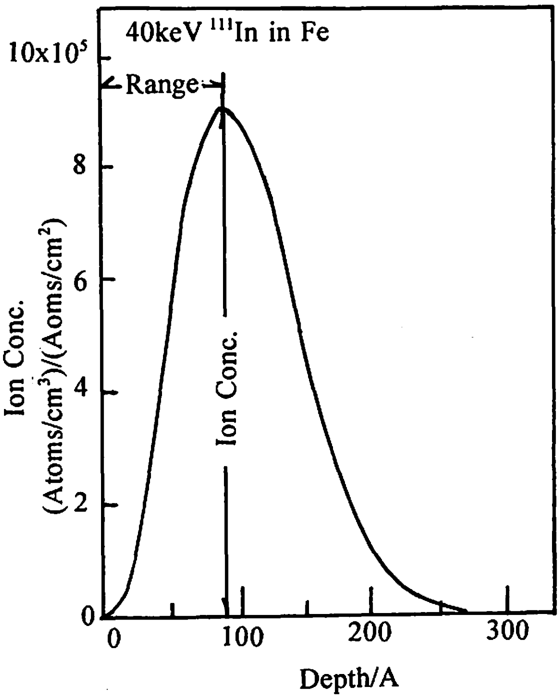

Fig. 1 40keV ^{111}In distribution in Fe host. Refer to Range and Ion Conc. in Fig. 2-7.

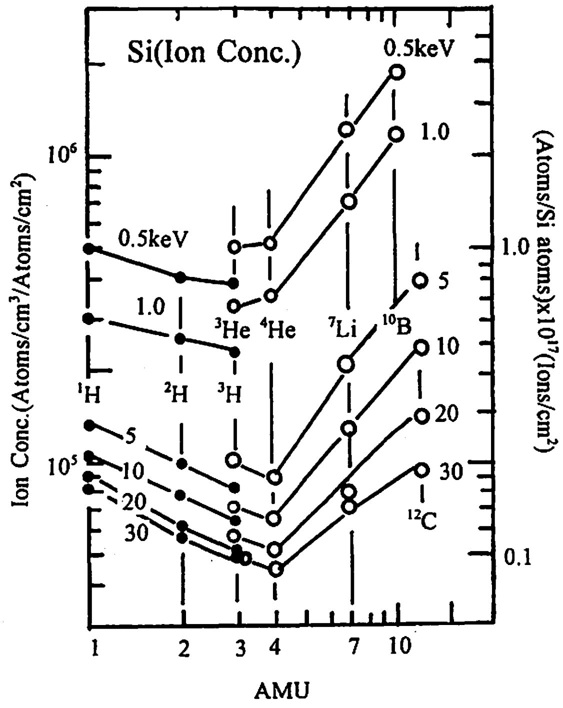

Fig. 2 Ions(AMU=1-12) concentration in Si. Implantation energy as a parameter.

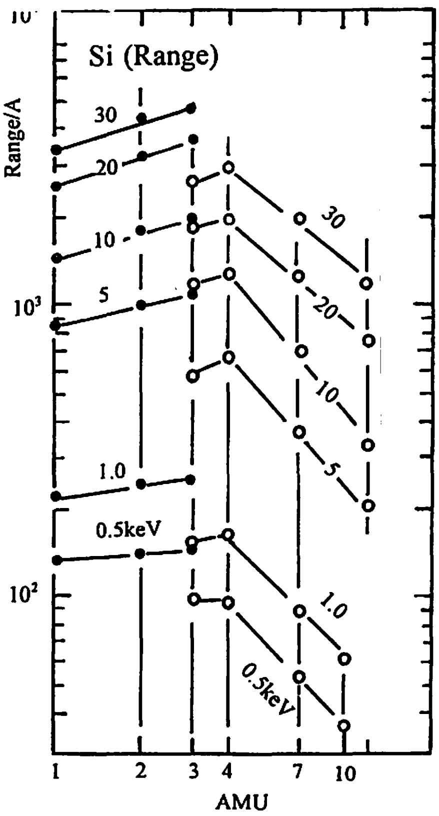

Fig. 3 Ion range in Si for ions (AMU=1-12).

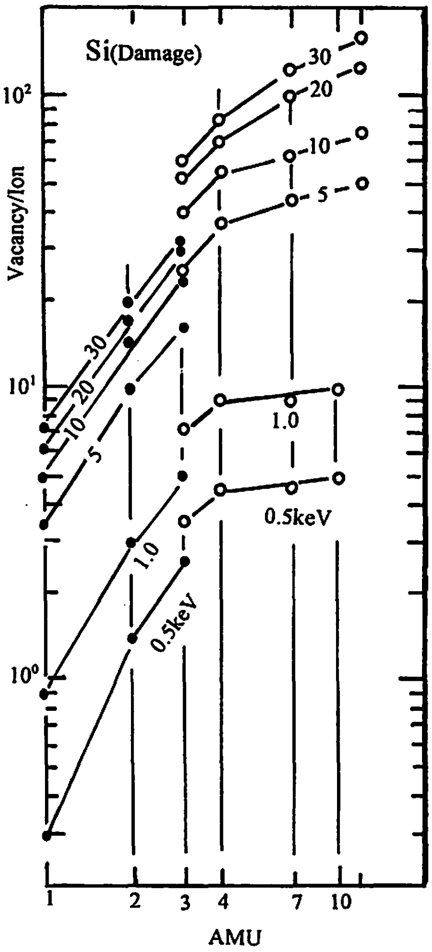

Fig.4 Damage in Si. E_d=20eV and Kinchin-Pease model are assumed.

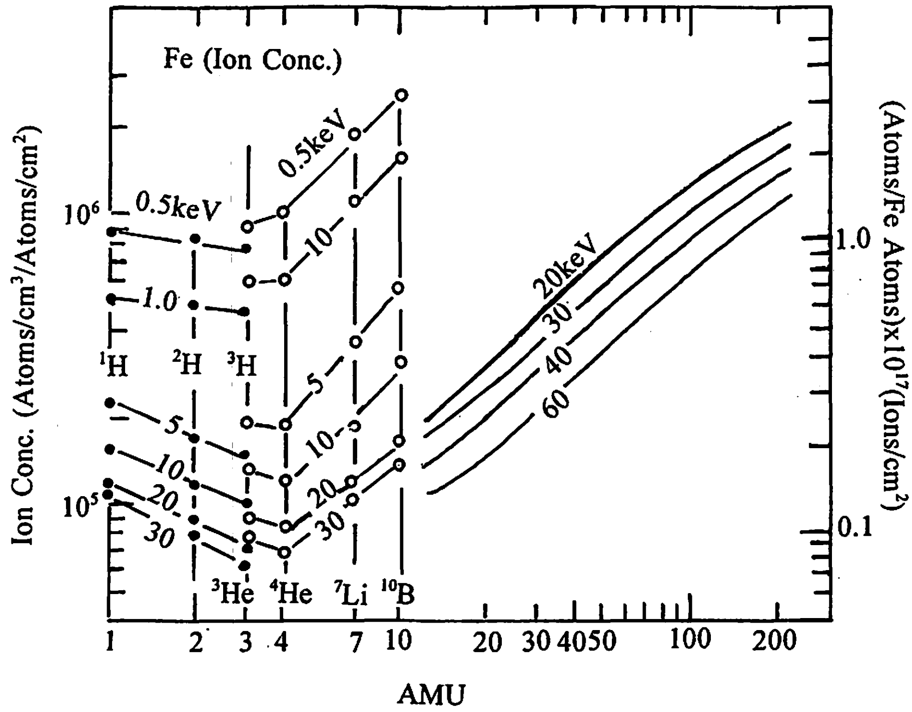

Fig. 5 Ions concentration in Fe. AMU=1-210. E=0.5-60keV.

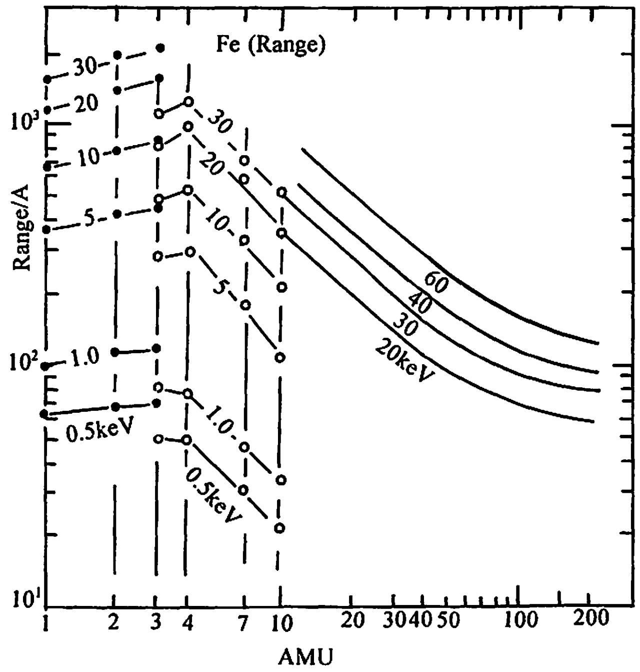

Fig. 6 Ion range in Fe.

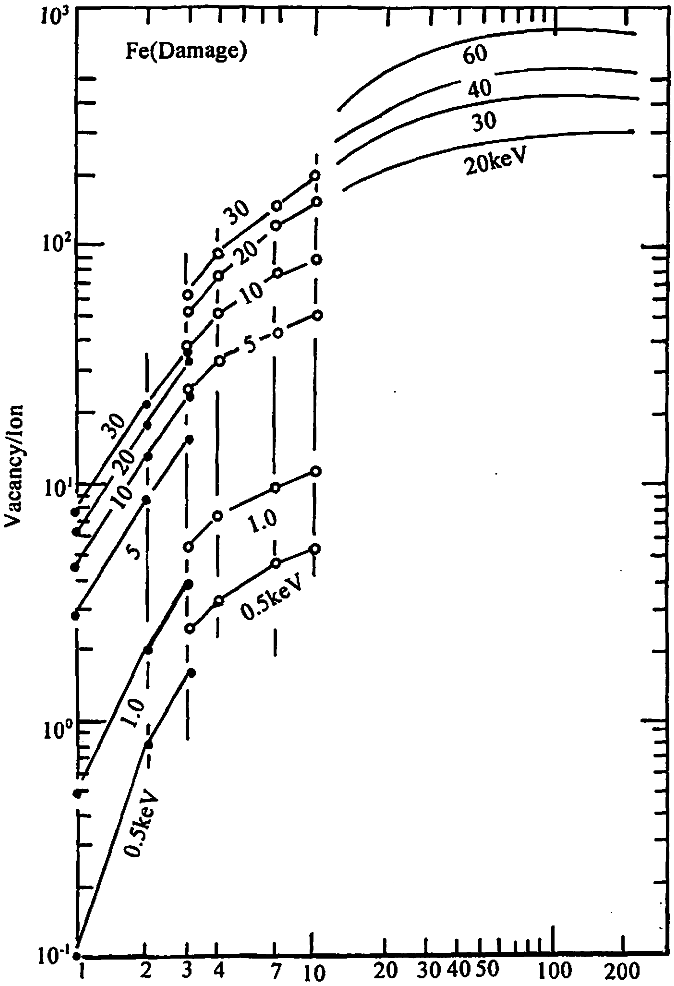

Fig. 7 Damage in Fe. E_d=20eV and Kinchin-Pease model are assumed.

I. 9. PAC Study of Recovery of Fe Implanted by ^{111}In

Hanada, R.

Institute for Materials Research, Tohoku University

Introduction

This note reports a result of annealing experiments on pure Fe, which was implanted by ^{111}In for the PAC spectroscopy. The purposes of the experiments are ; (1) to search for a possible vacancy trapping to the probe ^{111}In at around 200°C, where one school claims that the vacancy migration takes place at 200°C in contrast to other schools proposals of at 200°K. (2) to determine the optimum annealing temperature where the substitutional component in the PAC spectrum shows the maximum amplitude. This is necessary if one wishes to use the ^{111}In implanted Fe specimen for other experiments. Namely it is necessary to remove the damage introduced by the implantation as much as possible to avoid possible complication by the presence of damage in the further experiment. One example of such a study for hydrogen in Fe is reported in a separate paper in this volume.

For these purposes, a finer annealing schedule of 60°C/30min was employed in the present compared with the ones previously reported$^{1)}$.

The progress in our implantation procedure, namely, a higher ^{111}In implanted activity, has made it possible to measure about 10 PAC spectra with a reasonably high counts (5×10^4 at $t = 0$) within a reasonably short time.

Experimental procedure

Fe specimens are quasi-single crystals ($5\times18\times0.5\text{mm}^3$) with small islands made from high purity Johnson Matthey rods. The orientation of the crystal, however,are not specified yet. The ^{111}In implantation was done at RT with the energy of 40keV and found to be completed within 1 hr by monitoring the electrical current of ^{115}In of which known amount was intentionally added to the ion source. By knowing the amount and integrating the current of ^{115}In, the In implantation efficiency (implanted/charged to ion source) was found 0.5%, which is comparable with those by others.

PAC spectrum was measured at RT or at 77°K without any external magnetic field by a three detectors set up. The spectrum was converted to Fourier spectrum by a FFT program using the 1st 2^8 points.(0-200ns). The annealing was done in an UHV of 10^{-7} Torr.

Experimental Results and Discussion

Fig. 1 shows the PAC spectra for Fe during an isochronal run between RT and 400°C and Fig. 2 for the corresponding Fourier spectra. The rotation pattern with the period of 11.2 ns in Fig. 1 has been known as due to ^{111}In at the substitutional site without trapping any defects. This component is observed as the prominent Fourier component at 560Mrads^{-1} in Fig. 2 (S-component). Fig. 3 shows the amplitude of the S component as a function of the annealing temperature together with results of other runs. All experimental results show a monotonous increase of the amplitude up to 400°C. Namely, some part of implanted ^{111}In are out of the sight in the PAC spectrum right after the implantation and yet brought to S site as the annealing proceeds. Since the 40keV ^{111}In produces about 350 frenkel pairs per one incident ion near the range of ^{111}In (see a report on TRIM calculation for Fe in this volume), it is very likely some part of them are trapped to the probe, most likely in forms of clusters. At present no detail can be inferred on the nature of the defect clusters from the experimental results, since no clear Fourier component other than the S component is observed in Fig. 2. However it can be concluded that they are unstable to anneal out between RT and 400°C leaving ^{111}In in S site to give the S component growth.

No decrease of the S amplitude is observed near 200°C. This indicates either that (1). vacancy migration has been completed below RT as has been proposed or (2) no attractive interaction is present between ^{111}In and the lattice vacancy in Fe. The former is likely since a NMR/ON$^{2)}$ or a PAD$^{3)}$ experiment has revealed that the vacancy migration takes place below RT or at 200°K.

Although not shown here, the annealing above 400°C has revealed that the amplitude of S component decreases again and almost vanishes at 700°C$^{1)}$. So we conclude that 400°C is the optimum annealing temperature to obtain the maximum S site population for ^{111}In in Fe. This result is utilized in an experiment reported in a separate paper for H in Fe.

Acknowledgement

This work is supported by a Grant-in Aid for Scientific Research for Priority Area from the Ministry of Education, Science and Culture of Japan.

References

1) Hanada R. CYRIC Annual Report-1994, **p49** (1995).
2) Visser D. et al., Phys. Rev. Letter, **41** (1978) 882
3) Mahnke H. -E. Hyp. Int. **61** (1990) 1247.

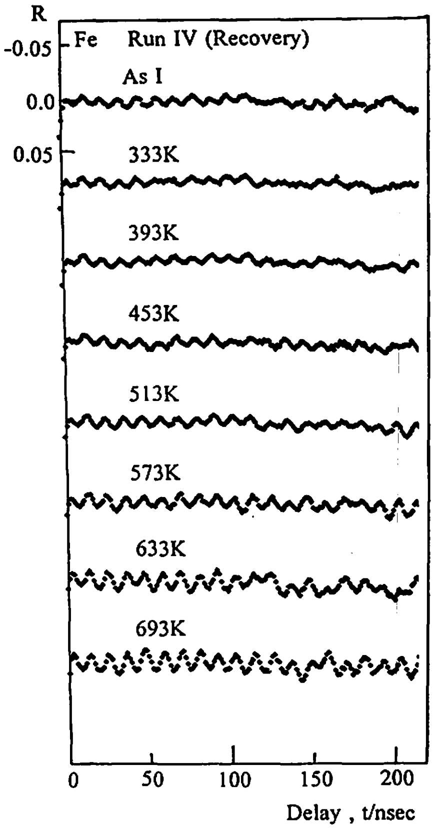

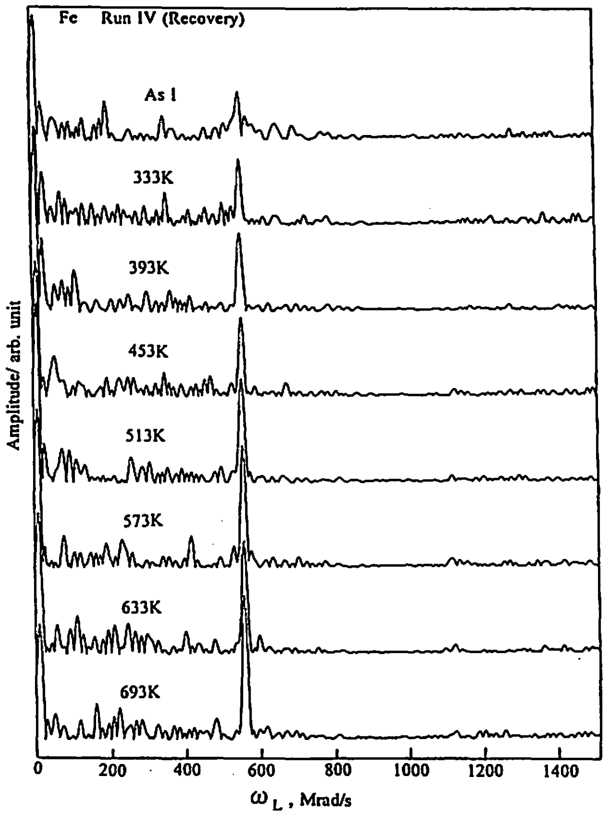

Fig. 1 PAC spectra for ^{111}In implanted Fe. Isochronal annealing (60°C/30min.) in UHV.

Fig. 2 Fourier spectra for Fig .1.

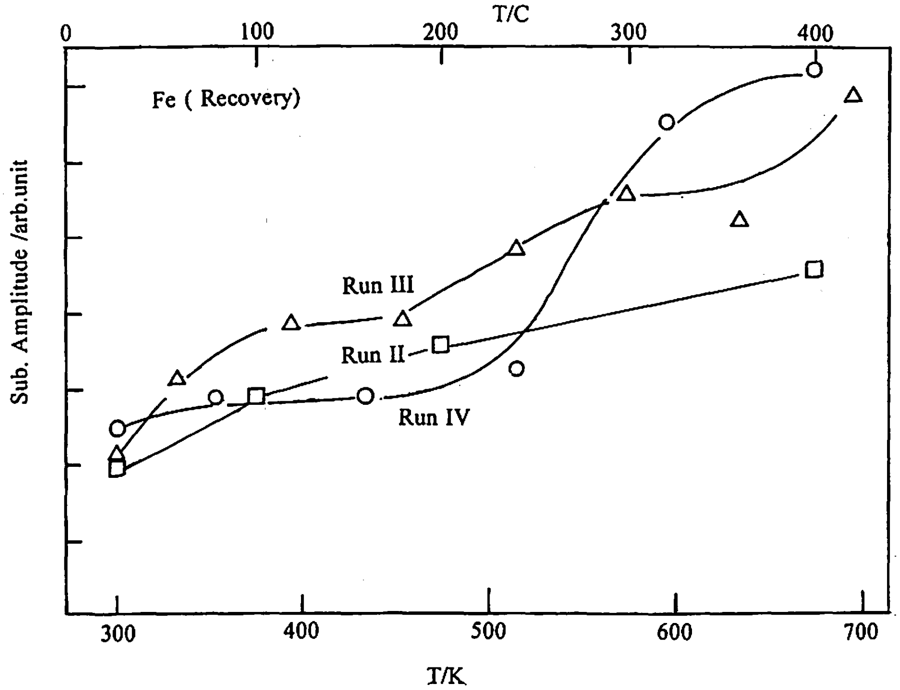

Fig. 3 S-amplitude as a function of annealing temperature. 3 independent runs.

I. 10. Effects of Hydrogen Charging on the PAC Spectrum of Fe

Hanada, R

Institute for Materials Research,Tohoku University

Introduction

Hydrogen in Fe has been one of the most important subjects in the field of materials science. This is because that hydrogen in Fe has been known to cause hydrogen embrittlement which results in disastrous destruction of artificial buildings or structures. Although many phenomenological or practical researches have been reported on the subject, researches to investigate the microscopic state of hydrogen in Fe have been scarce. The low solid solubility of hydrogen (H) in Fe prevents to apply the modern experimental methods as NMR, INS, RBS, channeling et cet.

In this paper, we report an experimental result of PAC spectrum measurements on Fe given by a hydrogen charging treatment. Since the concentration of the PAC probe ^{111}In is extremely low(1ppb-1ppm) even when it is implanted to a high radioactivity level, the small amount of H might be detected if they are trapped to the probe.

Although no conclusive theory exists for the H embrittlement in Fe, some school prefer so called "decohesion theory" to others. Namely the electrons donated by H fill up the Fe d-band near the Fermi surface, namely, the anti-bonding state, thus weakening the bonding between Fe atoms. This decohesion theory that can be traced back to Zener's work$^{1)}$ is still in effect even at the present time. Apart from the fact no quantitative discussion exists how the "weakened bonding" is related to the embrittlement phenomena, the band filing model is too naive in the present day where results of detailed theoretical calculations are available on the electronic structure of impurities in ferromagnetic materials as Fe or Ni$^{2)}$. For instance, these new calculations have revealed that the rigid band model, which is the basis of the d-band filling model, is completely wrong for H in Fe.

Since the PAC probes in Fe measure the hyperfine field (H_f) at the nuclei, namely, the difference of the up spins and down spins electron concentration at the nuclei, some effect can be expected in H_f if H modifies the electronic structure of Fe lattice. This may relate the embrittlement phenomena with the recent theoretical works on the electronic structure change of Fe host upon impurities doping.

Experimental

The specimens used, the method of the implantation and the annealing treatment are exactly the same with those described in a report in this volume for the Fe recovery study. As has been described in that report, the annealing at 400°C for 0.5-1hr is the most optimum treatment to obtain the maximum substitutional (S) component after the implantation. So all the specimens used in the present were given this treatment prior to any H experiment.

After the annealing at 400°C, the specimen was dipped in 0.1N H_2SO_4 with a small amount of an As compound and electrolytically charged with the specimen as the cathode and a Pt wire as the anode. It is believed that part of H ions arriving at the Fe surface diffuse into Fe bulk as an ion in the electrolytic method. Arsenic has been known as a poison to enhance the H uptake by preventing the H ions recombination to H_2 molecule at the surface.

The current density was typically 5-50mA/cm^2 and the duration was varied between 30min to 10 hrs.

After the treatment , PAC spectrum was measured at RT or 77°K. This procedure was repeated several times to follow the amplitude change in the substitutional site component (S) in the PAC spectrum. No external magnetic field was applied during the measurement.

Result and discussion

Fig. 1 shows the PAC spectra by ^{111}In for Fe during the hydrogenation treatment as above. After the annealing at 420°C without any H treatment, The PAC spectrum shows a maximum amplitude(top). With the 1st H treatment with the indicated current and the time duration, the amplitude shows a trend of a reduction. This trend proceeds with the increasing H treatment duration, which can be seen more clearly in Fig.2 where the corresponding Fourier spectra are shown. The S amplitude at 560Mrad^{-1} gradually decreases with the total electrolytic charge deposited on the Fe specimen. Also the angular frequency at 77°K is noted to shift to a higher frequency than that at RT. This is due to a higher H_f at 77°K than that at RT, which is normally observed in ferromagnetic materials.

Fig. 3 summarizes the S amplitude reduction as a function of the charge density (current/cm^2 times duration) for 4 independent runs and all experimental results show a reproducible reduction of the S amplitude with the charge density.

With the reduction of the S amplitude, several components with the frequencies below that of the S are found to develop. However their frequency positions varies for each charging treatment and so no unique assignment ,for instance as H- ^{111}In pair, is possible for the components at present. Possibility is that H clusters with different size are formed around the probe ^{111}In giving rise to the H_f reduction, of which size increases with the increasing H concentration giving further H_f reduction. Indeed a trend is observed that the population of the lower frequency component increases with the H charge density.

Although the above discussion is based on an *apriori* assumption that the H charging treatment introduces H in Fe and the H causes the PAC spectrum change, this has never been proved experimentally yet. First, the H concentration in the specimen after the treatment has not been measured yet and so the H cluster model as above is still a hypothesis. Second, Fe is notorious for the active chemical reactivity with the external environment ,as oxidation, and so some chemical reaction other than H introduction is possibly taking place during the H treatment which may cause the PAC spectrum change. This is especially so for our implanted specimens, where most of ^{111}In are present close to the surface (100A).

Further experiments are now in progress for H in Fe by PAC spectroscopy.

Acknowledgement

This work is supported by a Grant-in Aid for Scientific Research on Priority Area from the Ministry of Education, Science and Culture of Japan.

References

1) Zener C. Trans. AIME, (1955) 619.
Troiano A. R., Trans. ASM **52** (1960) 54.
2) H. Akai et al., Progress of Theoretical Physics suppl **No101** (1990) 11.

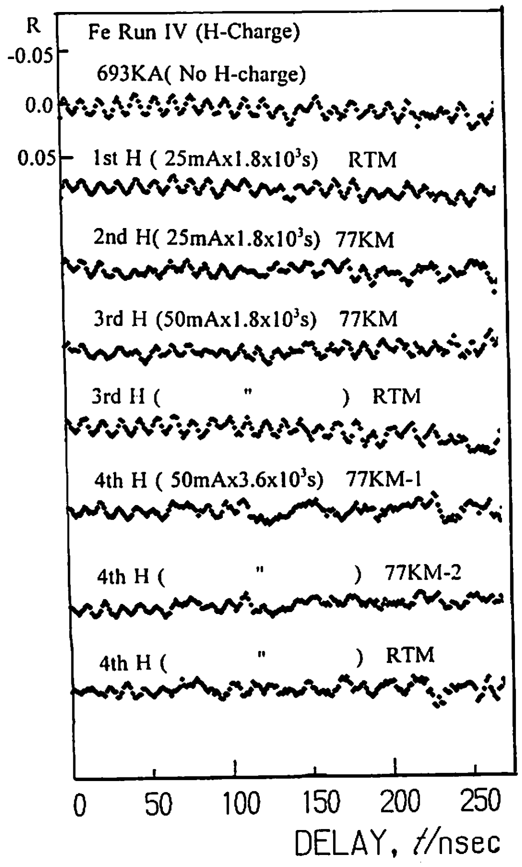

Fig. 1 PAC spectra by ^{111}In in Fe.

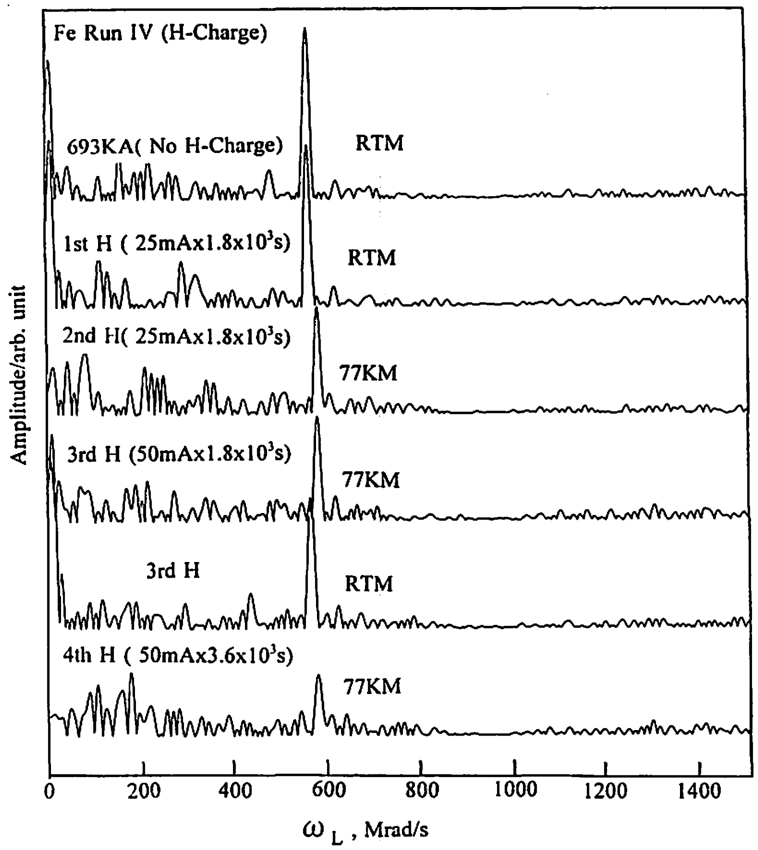

Fig. 2 Fourier spectra for Fig.1.

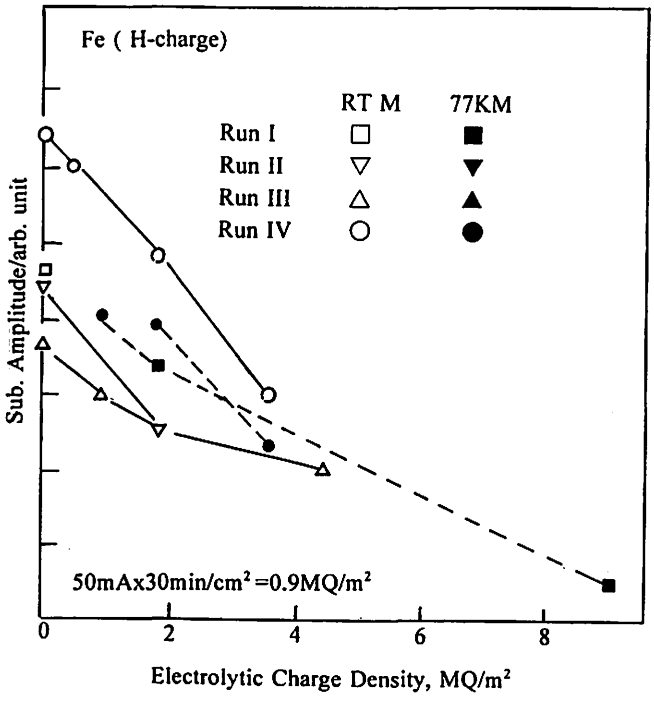

Fig. 3 S amplitude as a function of electrolytic charge density (current times duration) 4 independent runs.

I. 11. PAC Study of Si with Fe Impurities Doped by Implantation or Diffusion

Hanada, R

Institute for Materials Research, Tohoku University

Introduction

Fe impurity in Si has been a subject of Mössbauer spectroscopic study for a long time since ^{57}Fe is the best nuclear probe for the spectroscopy. Also in Si industries, Fe has been known as one of the impurities to cause deterioration in electronic devices. It forms a deep trap to form a recombination center thus reducing the effective carrier concentrations. In this report a result of PAC spectroscopy for Si doped by Fe impurity will be described. Here, Si specimens were given either by Fe impurity implantation or by diffusion treatment. A part of the results has been reported in1).

Experimental

N-type Si specimens were implanted by Fe ions at a energy of 40keV to various doses. Since no high Fe ion beam current was obtained with a metallic Fe in the ion source (Dan-Fysik 910 type), an Fe chloride ($FeCl_2$) was used as the source material to obtain a reasonably high ^{56}Fe beam. This chloride method was found to work for several low vapor pressure elements as Cu, Sn, Zr, Ag and probably can be applied to others.

For the case of diffusion doping, Si specimens were annealed in a vacuum with a high purity Fe powder at 900°C for several hrs and cooled fast to RT by removing the furnace. It is not known, however, the cooling rate is high enough to freeze in the Fe atom in an isolated impurity in Si lattice.

Subsequently these specimens were implanted with 40keV ^{111}In and PAC spectrum was measured at RT after the isochronal annealing in a vacuum. Since Fe impurity has been known to migrate at low temperature ($E_M = 0.68eV$)2), the isochronal annealing was started from a low temperature.

Result

Fig. 1 shows the PAC spectrum for Si to which Fe impurity was implanted. Fig. 2 shows the spectrum for Si given by the Fe diffusion treatment.

Although very small in magnitude, a PAC rotation pattern is noted in Fig. 1 after the annealing at 463-673°K which gradually fades out after the annealing above 773°K. A similar pattern with the almost same period with that in Fig. 1 is noted in Fig. 2 for the diffusion treated specimen.

One possible cause of the pattern is the formation of Fe-In pair although the formation of Fe precipitates with ^{111}In in them is an another possibility. The latter will be discussed in terms of the reported results of ^{57}Fe Mössbauer spectroscopy in Si.

Discussion

The CEMS for ^{57}Fe implanted Si have revealed that a doublet is observed near v=0mm/s in the as implanted state$^{3)}$. The doublet was interpreted as caused by a quadrupole interactions and the formation of Fe dimer (a pair of Fe atom) is responsible for the interaction. Namely the arrival of single Fe atom to the probe Fe atom breaks the cubic symmetry of Si lattice thus giving rise to a finite electric field gradient. Upon annealing above 600C the splitting is narrowed, which is interpreted as due to a formation of silicides (precipitates). So if one applies this model to our case of the implanted Si, no precipitates are present after the implantation and so the formation of the Fe-In pair upon the annealing may be concluded as the cause of the PAC rotation pattern below 673°K.

However a recent "in beam" Mössbauer spectroscopy for ^{57}Fe in Si$^{4)}$ has revealed a similar doublet. Since the ^{57}Fe concentration is extremely low in the "in beam" case, the formation of Fe dimer or precipitates is almost negligible in the experiment. So the doublet was interpreted as due to" a strongly disturbed environment", namely, a radiation damaged state which is created by the probe itself (correlated damage).

The values of the quadrupole splitting and the corresponding EFG's for these ^{57}Fe spectroscopy are summarized in Table 1 together with a ^{57}Co result$^{5)}$. Here V_{zz}'s are obtained using an expression for the quadrupole splitting, $(1/4)eQV_{zz}$, with a known quadrupole moment of I=3/2 state of ^{57}Fe. If this value for ^{57}Fe is assumed to be felt by ^{111}In also, the frequency of PAC spectrum should becomes as high as 7 Grads^{-1}, far above the observed value of 355 Mrads^{-1}. So the EFG due to "a strongly disturbed environment" can not account for the present PAC result. This argument, however, assumes that the EFG felt by ^{111}In is the same with that felt by ^{57}Fe which, however, may not be justified.

A fast quenching experiment or the implantation at lower temperature will be necessary to obtain a clearer information on the state of Fe in Si.

Acknowledgement

This work is supported by a Grant in Aid for scientific Research in a Priority Area from the Ministry of Education, Science and Culture of Japan.

References

1) Hanada R. et a., Mat. Sci Forum **196-201** (1995) 1369.
2) Takahashi H. et al., Mat. Sci. Forum **83-87** (1992) 155.
3) Sawicki B. D. et al., in "Mössbauer Spectroscopy II" ed by U. Gonser, Springer (1981).
4) Schwalbach P. et al., Phys. Rev. Letters, **64** (1990) 1274.
5) G. M. Langouche et al., Phys. Rev. Letters **53** (1984) 1364.

Table 1. Quadrupole doublet after ^{57}Fe Implantarion in Si and the corresponding V_{zz} (EFG).

Probe	Q.S/mms^{-1}	Vzz/10^{16}Vcm^{-2}	proposed species	Author
^{57}Fe	0.785	3.9	Fe-dimer	Sawicki et al
	0.43	2.1	β - FeSi$_2$	Sawicki et al
^{57}Fe(in beam)	0.84	4.2	disturbed environmt	Schwalbach et al
^{57}Co(^{57}Fe)	3.16	15.7	^{57}Co-dimer	Langouche
	0.465	2.3	disturbed environmt	Langouche et al

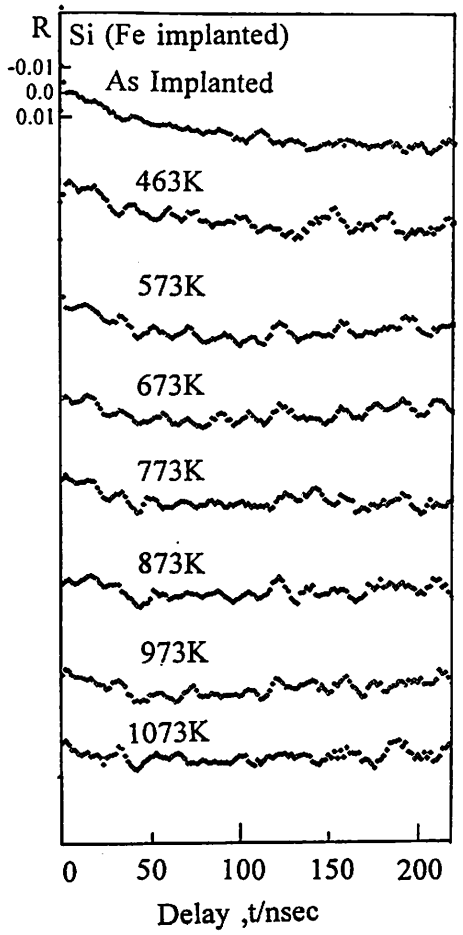

Fig. 1 PAC spectrum by ^{111}In in Fe ions implanted Si.

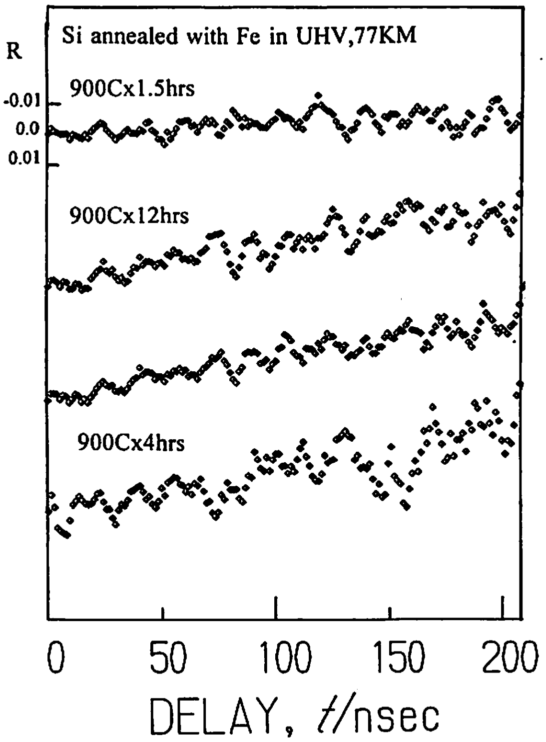

Fig. 2 PAC spectrum in Si annealed with Fe powder at 900°C. After the treatment, ^{111}In was implanted.

I. 12. Conversion Electron Mössbauer Spectroscopy(CEMS) of Impurities Implanted Fe.

Hanada, R

Institute for Materials Research, Tohoku University

CEMS is a powerful tool to study microscopic structure of materials surface layers, of which ranges are between 100 and 4000A from the surface of Fe host. Namely, the conversion electrons (6.3keV) in this range can reach to the surface to be detected by a proper electron counter with carrying information on the structures through hyperfine interactions. This range is comparable with those of ions implanted to Fe host in the energy range of the ISOL(10-60keV). So CEMS enables us to study the effects of ion implantation on Fe host.

Here, we have implanted several impurities to Fe host with the natural ^{57}Fe abundance(2.2%) and CEMS measurement has been performed to develop the method or to find a proper dose of impurities implantation.

Experimental

Several impurities ions (Ag, N and CO) were implanted to high purity Fe specimens ($20\times20\times0.25mm^3$) to a dose of up to $2\times10^{17}/cm^2$ with a proper energy. Since the extraction efficiencies for light ions were found poor for low implantation energies (below 20keV), a higher implantation energies were chosen to obtain a high current rather than to obtain a maximum overlap with the range of the conversion electron. For the range of implanted ion , see a separate report in this volume on TRIM calculation results on Fe host.

The BSD-2400 from Austin was used as the counter with He-3% butane (Q gas) as the counting gas. The Mossbauer source was 25 mCi ^{57}Co/Rh. Since no clear 6.3keV peak was observed in the energy spectrum, the SCA settings were determined in a try and error manner to obtain the maximum S/N ratio.

All the implantation and measurements were done at RT.

Results and Discussion

Fig. 1 shows the CEM spectra for CO (top), Ag (2nd top) and N (bottom two) implanted Fe to a dose as indicated together with pure Fe (center).

All spectra show six emission lines that correspond to Fe atoms in the ferromagnetic phase without any disturbance. Namely, most of Fe atoms are in the substitutional site with no defects or impurities at their 1st or 2nd neighbor sites even after impurities implantation. However, if the spectra are examined closely, implantation effects are noted in N or CO implanted cases.

For the case of N implanted Fe, the spectra show a bulge near 0mm/s of which magnitude increases with the N ion dose. This indicates that a paramagnetic phase is formed by the implantation in the ferromagnetic host phase. This paramagnetic line is present at almost the same position with that of the paramagnetic austenite phase in N alloyed and quenched specimens$^{1)}$. The present results shows, therefore, N implantation causes a phase transformation of α phase (bcc ferromagnetic lattice, ferrite) into a γ phase(fcc paramagnetic lattice, austenite) at RT. No fast cooling from a high temperature, which is inevitable for N-alloyed specimens to obtain the γ phase at RT, is necessary in the present implantation case.

The result for the CO implanted specimen, several bulges (-1.5, 0 and 1.5 mm/s) are noted. Although both C and O ions are implanted by CO ion implantation, the positions of these emission lines are different from those of C-alloyed specimens. Therefore it is likely these lines are caused by O. Although O is an important impurity elements in Fe, almost no study has been reported to examine it as an isolated point defect. This is because the attempts to make an O-Fe alloy by a thermodynamic method end up with the formation of oxides. So the present method of the implantation gives a possibility to prepare an Fe-O alloys where O is present as an isolated defect. Further experiment is now in progress using O or O_2 ions.

For the case Ag implanted Fe, the spectrum is almost the same with that of pure Fe. This indicates either the dose of Ag implantation is too low for the spectrum affected or the implanted Ag ions precipitate to form aggregates. Ag and Fe are known to be immiscible and hence the latter possibility is likely. So if the temperature of the implantation is low enough for Ag ions not to migrate, Fe-Ag alloys, which can not be prepared by usual metallurgical method, may possibly be synthesized by the implantation method. New ion source which provides a higher beam current of Ag or other elements will be required to synthesize new alloys in a reasonably short time.

Acknowledgement

This work is supported by a Grant in Aid for Scientific Research on a priority Area from the Ministry of Education, Science and Culture of Japan.

References

1) Gielen P. M. et al., Acta Met. **15** (1967) 49.

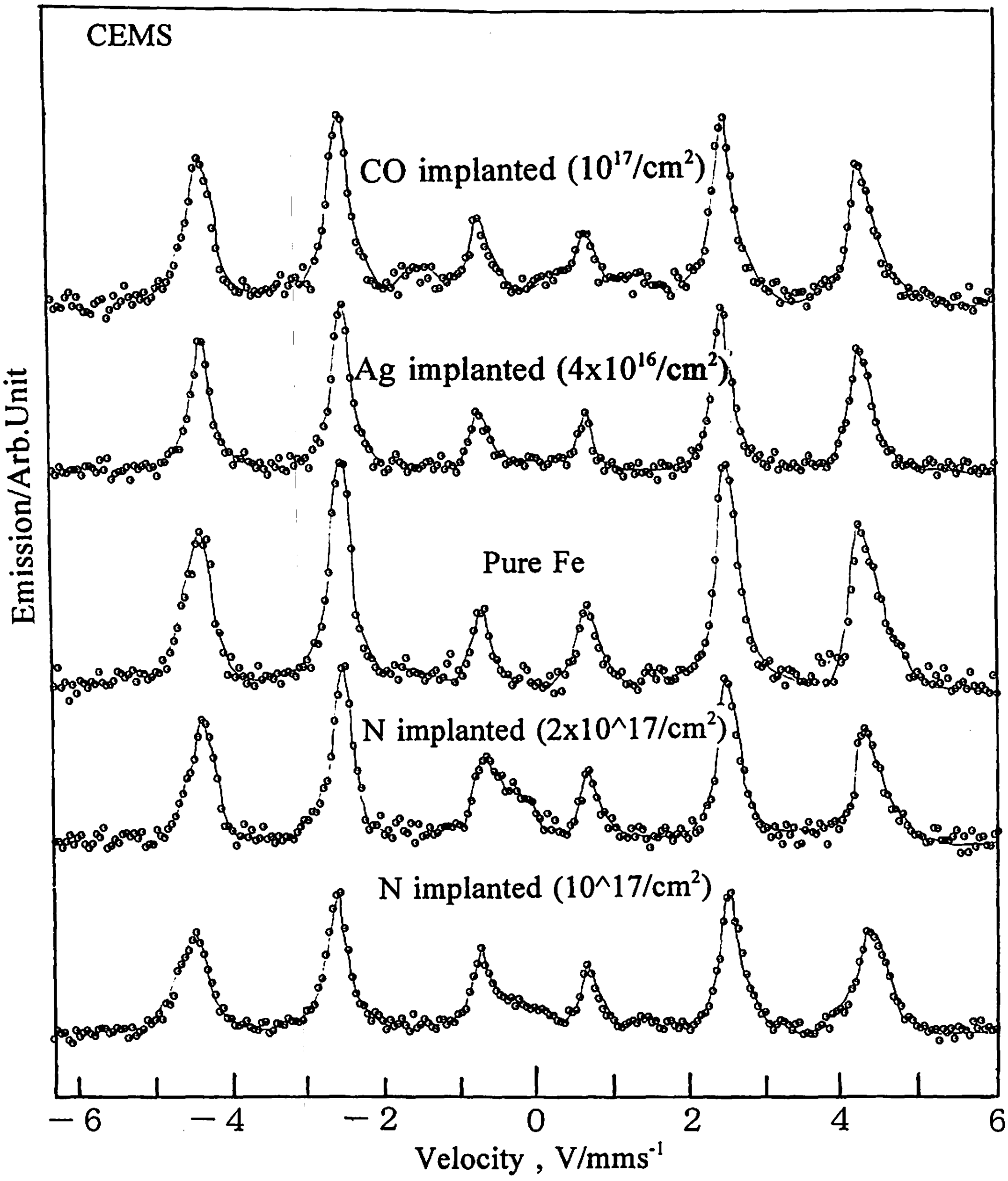

Fig. 1 CEMS for Fe implanted by nitrogen(N), carbon-monoxide(CO) and Ag ions.
CEMS for pure Fe is also shown for comparison.
(For pure Fe, shorter measurement time than others)

I. 13. Performance of a Parallel Plate Avalanche Counter(PPAC) for Emission Mössbauer Spectroscopy.

Hanada, R

Institute for Materials Research, Tohoku University

Introduction

For the case of emission Mössbauer spectroscopy, where the probe activity is in a specimen, there are several ways of configurations for the spectroscopy. Namely, the specimen and the counter (for instance a conventional proportional counter) are fixed and the absorber(for instance stainless steel foil) between them are given the Mössbauer velocity modulation. If this configuration is used in an "in beam" Mössbauer spectroscopy, where an high energy ion beams are incident on an Fe specimen, the high background of γ or X-rays chokes the counter to perform the spectroscopy almost impossible. To overcome the difficulty, Weyer has constructed a counter which is sensitive only to the resonance γ ray and not to others[1]. The key of his counter is the use of ^{57}Fe enriched stainless steel foil as the electrode, which emits conversion electrons only when the resonance absorption takes place. Since He is selected as the counting gas, the counter is sensitive to the electron and not to γ or X-rays. So, the spectroscopy can be performed with a reasonably low background even in the "in-beam" case.

Since an "in beam" Mössbauer spectroscopy was started with Nasu group in CYRIC, a counter of this type was constructed and tested, of which results will be described in the followings.

Experimental

Fig. 1 shows the counter which was hand made with the ^{57}Fe enriched stainless steel as the anode and an aluminized mylar as the cathode. The total weight of the counter is 7gr which is light enough for the K-3 linear motor (Austin) for the Mössbauer velocity modulation. The counting gas is Q-gas which is a mixture of He and butane (3%). Different from the usual configuration, the Mössbauer source (25mCi ^{57}Co/Rh) was fixed and the counter itself was given the velocity modulation. The output of the counter was recorded as the function of the modulation velocity.

Results and Discussion

Fig. 2 shows a typical emission spectrum for the ^{57}Fe in the stainless steel by ^{57}Co in Rh matrix. One notes a high S/N ratio of 2000%, which is typical for this kind of resonance counter. The absorption width(FWHM) is 0.4 mm/s, which is also a typical value for a stainless steel foil. So the counter should give a good spectrum if used other source specimens or in "in beam" experiment.

Further testing is now in progress for the "in beam" spectroscopy.

Acknowledgement

The author is indebted for CYRIC Research Program Committee for the financial support. This work is supported by a Grant in Aid for Scientific Research on a Priority Area from the Ministry of Education, Science and Culture of Japan.

Reference

1) Weyer. G. in "Mössbauer Effect Methodology Vol.10" ed. by Gruverman I. I. pub. by Plenum Press (1976).

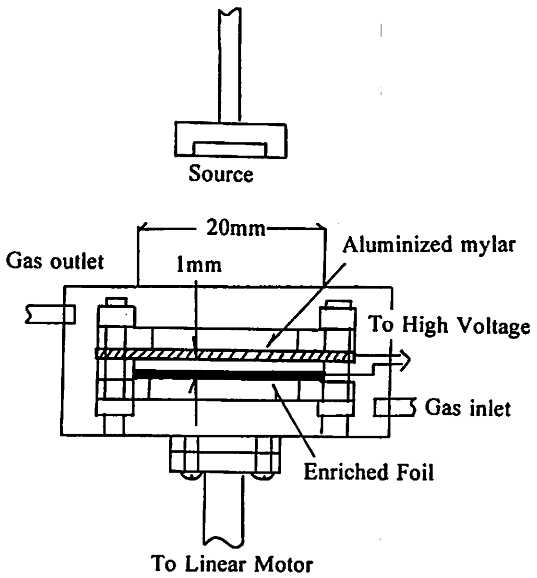

Fig. 1 The PPAC used in the present.

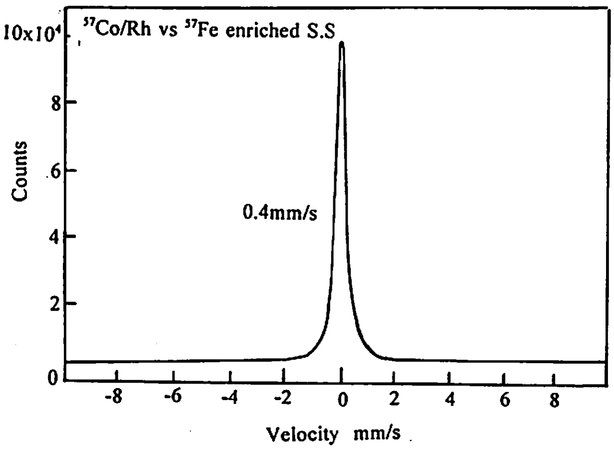

Fig. 2 An emission spectrum by the counter. 6 hrs measuring time.

I. 14. Effects of Helium on Mechanical Properties of Structural Materials for Nuclear Reactors

Hasegawa A., Abe K. and Satou M.
Department of Nuclear Engineering, Tohoku University

Introduction

Materials in nuclear reactors including fission reactors and fusion reactor are exposed by high energy neutron irradiation. The neutron irradiation produce lattice defects and transmutation atoms in the materials by atomic collision or nuclear reactions to atoms in materials. Helium is one of transmutation elements and the solubility of helium in materials is so small that helium precipitates as bubbles in the matrix and on grainboundaries. Behavior of lattice defects are strongly influenced by the helium, too.

Degradation of material performance by the transmutation helium such as mechanical property change and dimension change are very important material issues in nuclear reactor engineering1). For example, complex of helium and lattice defect (void) in the matrix cause swelling and hardening, and helium bubbles on grainboundary cause irradiation embrittlement. The effects of helium depend on materials, alloying elements and irradiation conditions such as irradiation temperature. We have been studying the helium effects on mechanical properties of various materials using helium implantation method with a cyclotron in CYRIC2,3). This report will show some recent results of helium effects in zirconium alloys(Zircaloys) and vanadium(V) alloys. Zircaloys are fuel cladding materials of light water reactors and V alloys are one of candidate structural materials of fusion reactors.

Results

Helium effects on Zirconium Alloys

Helium effects on tensile properties of Zr, Zircaloy-2(Zry-2) and Zircaloy-4(Zry-4) were examined using miniature tensile specimens of 0.15mmt thickness. Two heat treatment conditions were used to examine grain size effect. The grain sizes of heat-treated at 853K for 3600s samples were 20μm, 4μm and 7μm and that of heat-treated at 1053K for 3600s samples were 40μm, 7μm and 16μm respectively. Helium was implanted up to 100appm at room temperature by cyclotron in CYRIC using energy degrader to obtain uniform helium depth distribution in a specimen2,3). The energy of helium ion beam was 36MeV. Displacement damage induced by the helium implantation was about 0.03dpa. After the implantation, tensile tests were carried out from room temperature to 1073K.

Results of tensile test are shown in fig.1 and fig.2. The increase in yield stress was observed in the three materials after the implantation. The decrease in elongation was observed at all the test temperatures. The maximum reduction of 70% of un-implanted condition was observed in the case of pure Zr tested at 1073K. Grainboundary embrittlement at higher temperatures, which had been observed in typical austenitic steels[2)] was not observed. The results suggest that enough helium bubbles could not grow at grainboundary in zirconium and zircaloys.

Helium effects on Vanadium alloys

Helium effects on tensile properties of pure V and V-5Ti-5Cr-1Si-Al-Y alloy were examined using miniature tensile specimens of 0.25mmt thickness. The specimens were heat-treated at 1173K for 1800s and at 1373K for 3600s respectively. After the heat treatments the grain sizes were 30μm and 20μm respectively. Implanted helium concentration was 50appm. Helium implantation technique and post implantation tests were as the same as that of zirconium alloys.

The results of tensile tests are shown in fig.3 and fig.4. The increase in yield stress after implantation was observed in the two materials but the yield stress increase of V-5Ti-5Cr-1Si-Al-Y was smaller than that of pure V. The elongation behavior was more complicated than that of Zr alloys. In the case of V-5Ti-5Cr-1Si-Al-Y alloy, decrease of elongation after implantation became lager with increasing test temperature, but elongation change by implantation of pure V depends on test temperature. Grainboundary fracture surface was only observed in helium implanted V-5Ti-5Cr-1Si-Al-Y alloy tested above 723K. In the case of pure V, grainboundary fracture surface was not observed in this test conditions. The mechanism of these fracture behavior of helium implanted samples is in progress.

References

1) Mansur L. K. and Grossbeck M.L., J.Nucl.Mater. vol.155-157, pp.130-147 (1988).
2) Hasegawa A. et al., JCSTEA 7th symposium on Materials for Advanced Energy Systems & Fission and Fusion Engineering, pp359-362, (1994).
3) Masuyama T. et al. Proc. of the Int. Conf. on Evolution in Beam Applications, Takasaki, Japan Nov.5-8, 1991, pp729-733.

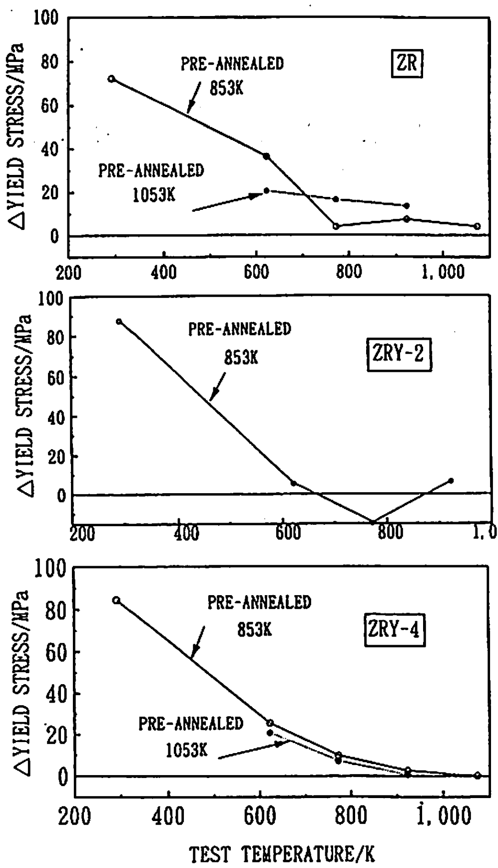

Fig. 1. Temperature dependence on yield stress increase of Zr and Zircaloy by helium implantation.

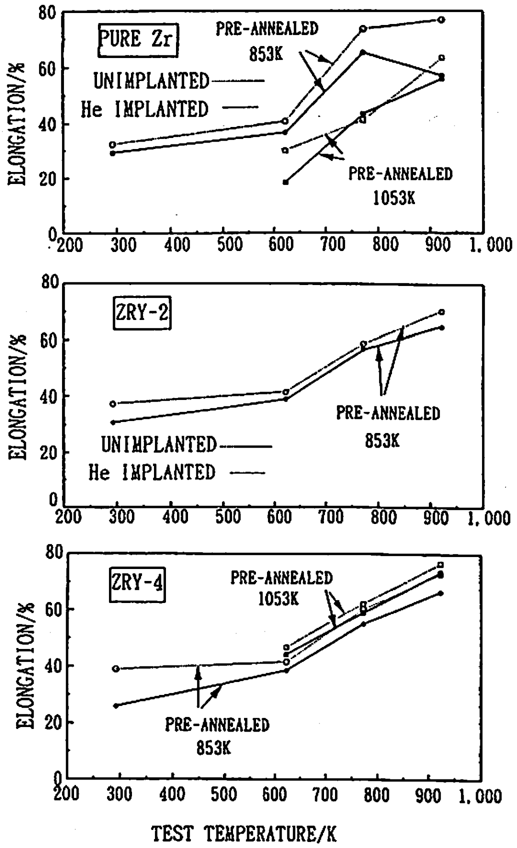

Fig. 2. Temperature dependence on total elongation of Zr and Zircaloys.

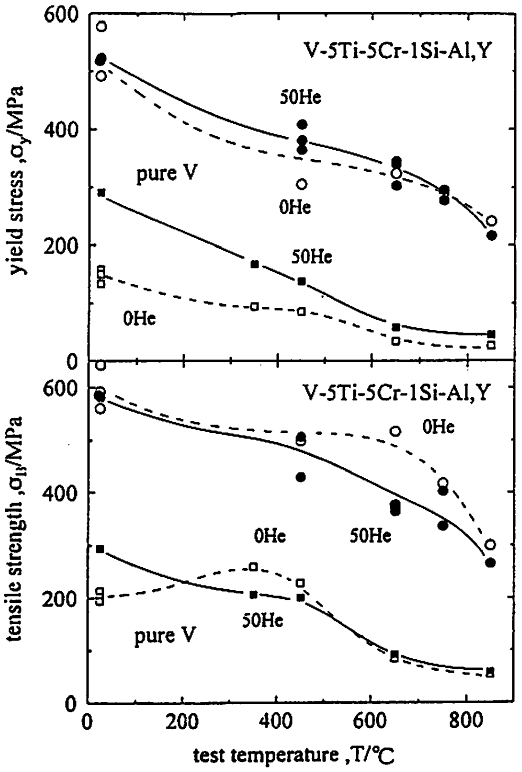

Fig. 3. Temperature dependence on yield stress and ultimate tensile strength of V and V alloy by helium implantation.

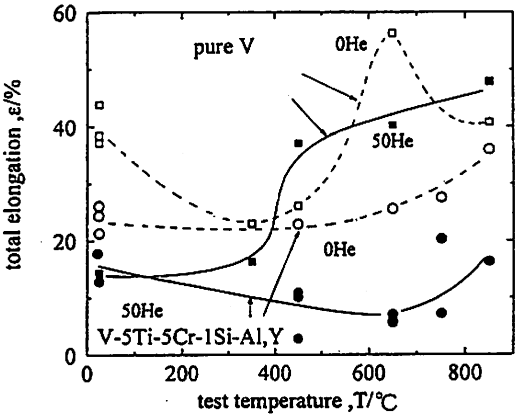

Fig. 4. Temperature dependence on total elongation of V and V alloy.

I. 15. A Weak-Coupling Approach to the Least-Squares Method

Fujioka M.

Cyclotron and Radioisotope Center, Tohoku University

Using an explicit expression of inversion of a symmetric matrix the "coupling" between two sets of parameters in the least-squares method is studied, and the result of weak-coupling limit given.

The least-squares method (LSM) is very popular and convenient in many fields for data analysis$^{1)}$. In the following we formulate a least-squares method in which N_p parameters are divided into two qroups of N_1 and N_2 parameters, and especially consider the case of "weak-coupling" limit; $N_1 + N_2 = N_p$. We follow the vector-matrix way of description of ref. 2). We assume a linear LSM.

We use the following notations:

y	: column vector of measurements at N_m points.
p	: column vector of N_p parameters.
F	: N_m x N_p matrix of fitting functions.
$W(y)$	: N_m x N_m weight matrix of measurements equal to the inverse of error matrix of measurement $E(y)^{-1}$; $E(y) \equiv <\delta y \delta y^T>$, where ^{T} denotes transposition.
E (p)	: N_p x N_p error matrix of parameters $\equiv$ $<\delta y \delta y^T>$.

The outcome of LSM is written as

$$\left.\begin{array}{l} p = A^{-1}F^TW(y)y, \text{ where } A \equiv F^TW(y)F, \text{ and} \\ \qquad E(p) = A^{-1}. \end{array}\right\} \tag{1}$$

When we divide the N_p parameters into two qroups of N_1 and N_2 parameters and "partially" conduct LSM, we have for p_1

$$\left.\begin{array}{l} p_1^{(1)} = A_1^{-1}F_1^TW(y)y, \text{ where } A_1 = F_1^TW(y)F_1, \text{ and} \\ \qquad E(p_1^{(1)}) = A_1^{-1}; \text{ for } F_1 \text{ see eq. (5) below.} \end{array}\right\} \tag{2}$$

The corresponding relations hold for $p_2^{(2)}$; the indexes $^{(1)}$ and $^{(2)}$ indicate that the LSM was performed independently within the parameter sets 1 and 2, respectively.

Now we formulate the relationship of "partial" and "whole" LSM's by using an expression of inversion of a symmetric matrix:

$$A \equiv \begin{pmatrix} A_1 & \alpha \\ \alpha^T & A_2 \end{pmatrix}, \text{ both } A_1 \text{ and } A_2 \text{ being symmetric.} \tag{3}$$

Then we have as seen by direct computation:

$$A^{-1} = \begin{pmatrix} (A_1 - \alpha A_2^{-1}\alpha^T)^{-1} & -A_1^{-1}\alpha(A_2 - \alpha^T A_1^{-1}\alpha)^{-1} \\ -A_2^{-1}\alpha^T(A_1 - \alpha A_2^{-1}\alpha^T)^{-1} & (A_2 - \alpha^T A_1^{-1}\alpha)^{-1} \end{pmatrix}$$

$$= \begin{pmatrix} (A_1 - \alpha A_2^{-1}\alpha^T)^{-1} & -(A_2 - \alpha^T A_1^{-1}\alpha)^{-1}\alpha A_2^{-1} \\ -(A_2 - \alpha^T A_1^{-1}\alpha)^{-1}\alpha^T A_1^{-1} & (A_2 - \alpha^T A_1^{-1}\alpha)^{-1} \end{pmatrix}. \tag{4}$$

The symmetricity of A^{-1} is implicitly contained in eq. (4); suffice it to see that

$$(1 - \alpha A_2^{-1}\alpha^T A_1^{-1})\alpha = (A_1 - \alpha A_2^{-1}\alpha^T) A_1^{-1}\alpha$$
$$= \alpha(1 - A_2^{-1}\alpha^T A_1^{-1}\alpha) = \alpha A_2^{-1}(A_2 - \alpha^T A_1\alpha),$$

which when multiplied by

$$(A_1 - \alpha A_2^{-1}\alpha^T)^{-1} \text{ and } (A_2 - \alpha^T A_1^{-1}\alpha)^{-1}$$

from left and right, respectively, give

$$A_1^{-1}\alpha(A_2 - \alpha^T A_1^{-1}\alpha)^{-1} = (A_1 - \alpha A_2^{-1}\alpha^T)^{-1}\alpha A_2^{-1} = [A_2^{-1}\alpha^T(A_1 - \alpha A_2^{-1}\alpha^T)^{-1}]^T,$$

etc. ; QED.

Let us apply eq. (4) to the whole LSM:

$$F = (F_1 \ F_2) \text{ and } A = \begin{pmatrix} F_1^T W(y) F_1 & F_1^T W(y) F_2 \\ F_2^T W(y) F_1 & F_2^T W(y) F_2 \end{pmatrix}. \tag{5}$$

We note that F_1 is N_m x N_1 and F_2 is N_m x N_2 composing F of N_m x N_p. From eqs. (3) and (5) we identify A_1 with $F_1{}^T W(y) F_1$, A_2 with $F_2{}^T W(y) F_2$ and α with $F_1{}^T W(y) F_2$, respectively. Therefore, we have:

$$p \equiv \begin{pmatrix} p_1 \\ p_2 \end{pmatrix} = A^{-1} F^T W(y) y = \begin{pmatrix} (A_1 - \alpha A_2^{-1}\alpha^T)^{-1} & (F_1^T - \alpha A_2^{-1} F_2^T) \\ (A_2 - \alpha^T A_1^{-1}\alpha)^{-1} & (F_2^T - \alpha^T A_1^{-1} F_1^T) \end{pmatrix} \cdot W(y) y. \tag{6}$$

Eq. (6) shows generally the relation or the "coupling" between p_1 and p_2. At this point we focus our attention to p_1 and see the "perturbation" from p_2 for the case of "weak coupling" i. e. for $|\alpha| \ll 1$. Then we have:

$$\Delta p_1 \equiv p_1^{(1)} - p_1 = A_1^{-1}\alpha A_2^{-1} F_2^T W(y) y + \cdots\cdots, \tag{7}$$

and, similarly for $E(p)$:

$$E(p) = A^{-1} \equiv \begin{pmatrix} E(p)^{(11)} & (E(p)^{(12)} \\ E(p)^{(21)} & E(p)^{22} \end{pmatrix}, \tag{8}$$

from which we have:

$$\Delta E(\hat{p}_1) \equiv E(\hat{p}_1^{(1)}) - E(\hat{p}_1) \equiv A_1^{-1} - E(\hat{p})^{(11)} = A_1^{-1}\alpha A_2^{-1}\alpha^{T} A_1^{-1} + \cdots . \tag{9}$$

We conclude; when we divide the parametrers in a LSM into two sets of parameters such that the coupling term $\alpha \equiv F_1^{T}W(y)F_2$ be small, the error of fitted parameters and their variance of one group committed by neglecting the other is to the first and the second orders of magnitude of the "strength of the cougling", respectively.

Since eqs. (4) through (6) are themselves exact, they might also be utilized for studying the effects of changing the number of parameters in a LSM and, further, to study the optimum number of parameters for the corresponding (i. e., when the population is given as a multidimensional normal distribution having the error (covariance) matrix of $E(y)$) problem of MLM (Maximum-Likelifood Method) under the regime of AIC (Akaike's Information Criterion)$^{3)}$.

References

1) Andou H, The history of the least-sqaures method (Modern Mathematics Publ. Co.,Tokyo, 1995), in Japanese.
2) Frodesen A. G. et al., Probility and statistics in particle physics (Universitetsforlaget, Oslo, 1979).
3) Akaike H., IEEE Trans. Automat. Contr. AC-19 (1974) 716.

I. 16. A Note on the Paraxial Expansion of Cylindrically Symmetric Magnetic Field

Fujioka M. and Honma T.

Cyclotron and Radioistope Center, TohokuUniversity

For the sake of convenience a brief derivation and the general expansion formulas are qiven for the magnetic field around the symmetry axis in terms of $B_z(z)$ defined on the axis.

Axially symmetric magnetic field $\vec{B}(r,z)$ is determind once the field distribution along the axis $B_z(0,z) \equiv B(z)$ is given. This fact is utilized for the magnetic field off axis e. g. in a lens-type beta-ray spectrometer 1) or in the central hole through the cyclotron yoke. 2) Since the formula in ref. (1) is limited and not referenced we briefly derive the full formulas in the following.

The magnetic flux density $\vec{B}$ must fulfill the following we—take the cylindrical coordinates (r, ϕ, z):

$$\mathrm{div}\vec{B} = r^{-1}\partial_r r B_r + \partial_z B_z = 0. \qquad (1)$$

$$\mathrm{rot}\vec{B} = 0 \Rightarrow \partial_r B_r - \partial_z B_z = 0. \qquad (2)$$

It is noted that $B_\phi \equiv 0$ and that $\vec{B}$ does not depend on ϕ. Operating ∂_z on (1) and using (2) one obtains

$$(r^{-1}\partial_r r \partial_r + \partial_z^2)B_z \equiv \Delta B_z. \qquad (3)$$

On the other hand, operating∂_r on (1) and using (2) gives

$$(\partial_r r^{-1}\partial_r r + \partial_z^2)B_r \equiv \Delta' B_r\,. \qquad (4)$$

Note the difference of Δ and Δ'.

Let us begin with $B_z(r, z)$: putting for brevity

$$B_z(r,z) = \sum_{n=0} f_n(z) r^n\,, \qquad (5)$$

which when substituted in (3) gives ($^{(n)}$ denotes nth differentiation)

$$
\begin{aligned}
\Delta B_z = \sum_{n=0} (n^2 r^{n-2} f_n + r^2 f_n^{(2)}) \\
= f_0^{(2)} + r^{-1} f_1 + r f_1^{(2)} + 4 f_2 + r^2 f_2^{(2)} + 9 r f_3 + r^3 f_3^{(2)} \\
+ 16 r^2 f_4 + r^4 f_4^{(2)} + 25 r^3 f_5 + r^5 f_5^{(2)} + \cdots\cdots = 0,
\end{aligned}
$$

which by equating term by term gives a series of relations.

$$f_1 = 0,\ f_0^{(2)} + 4f_2 = 0,\ 9f_3 + f_1^{(2)} = 0,\ 16f_4 + f_2^{(2)} = 0,\ 25f_5 + f_3^{(2)} = 0,\ \cdots\cdots$$

i. e. :

$$
\begin{aligned}
f_1 = f_3 = f_5 \cdots\cdots = 0,\ f_2 = -(1/4) f_0^{(2)},\ f_4 = -(1/16) f_2^{(2)} \\
= (1/64) f_0^{(4)},\ \cdots\cdots
\end{aligned}
$$

Since f_0 (z) is just $B_z(0, z) \equiv B(z)$ itself, one gets

$$B_z(r,z) = B(z) - (1/4)B^{(2)}(z)r^2 + (1/64)B^{(4)}(z)r^4 \cdots\cdots \tag{6}$$

By inspection we have a general formula:

$$\boxed{B_z(r,z) = B(z) - (1/2^2)B^{(2)}(z)r^2 + (1/2^2 4^2)B^{(4)}(z)r^4 - (1/2^2 4^2 6^2)B^{(6)}(z)r^6 \cdots .} \tag{7}$$

In a completely similar fashion we get;

$$\boxed{\begin{aligned} B_r(r,z) = -(1/2)B^{(1)}(z)r + (1/2^2 4)B^{(3)}(z)r^3 \\ -(1/2^2 4^2 6)B^{(5)}(z)r^5 + (1/2^2 4^2 6^2 8)B^{(7)}(z)r^7 \cdots\cdots . \end{aligned}} \tag{8}$$

Eqs. (7) and (8) are the required result; the general term is easy to identify.

References

1) Siegbahn K., in α -, β - , and γ - Ray Spectroscopy Vol. 1 (1966, North-Holland) p. 147.
2) Honma T. et al, Proc. 9th Symp. Accelerator Sci. and Tech. , Aug. 25-27, KEK, Tsukuba, 1993, p. 300.

I. 17. Field Properties of a Small Dipole Magnet Utilizing 4-Pairs of Permanent-Magnets

Honma T., Fujioka M., and Shinozuka T.

Cyclotron and Radioisotope Center, Tohoku University

A new type of small dipole magnet utilizing 4-pairs of cylindrical permanent magnets has been designed. By the use of 4-pairs of permanent magnets the anti-symmetry terms of the vertical field component in the horizontal mid-plane can be completely eliminated over the whole range of field strength, resulting in a better field uniformity as a dipole magnet.

Introduction

Advantages of using permanent magnets in accelerator instruments are that to be expected to provide a very high field in a limited available space and should be operated easily where its using in a high voltage terminal because of being the lack of electric power for maintaining the field and cooling system.

Previously we proposed and manufactured a proto-type permanent-magnet dipole[1) (PMD) utilizing 3-pairs of cylindrical permanent-magnet rods. However, a small quantity of quadrupole component remained due to its anti-symmetry terms of vertical field distribution in the horizontal mid-plane. It is practically impossible to eliminate the anti-symmetry terms with the PMD consisting of 3-pairs of magnet. Therefor, a better configuration was searched to correct the field distribution. In this paper we present a new assembly of dipole magnet[2) PMDII, which have 4-pairs of cylindrical permanent-magnet rods, and discuss the field properties of the PMDII by using the two-dimensional permanent magnet code PANDIRA[3).

Magnet Layout and Field Properties

The PMDII has been designed to have the almost same dimentions as the PMD except for the rod diameter and its assembly. A cross sectional layout of the PMDII with 4-pairs of rods (8-permanent magnets) is shown in Fig. 1. The magnetic field in the working area can be changed by rotating the rods, where each adjacent rods are rotated in the opposite direction to obtain the symmetric field distributions for the configulation of 4-pairs of rods. Figure 2 shows the calculated field inhomogeneity distributed in the horizontal mid-plane as a function of the rotation angle of θ = 30°,60° and 80.5°, where the value of θ = 80.5° gives the maximum field strength in the PMD II. As can be seen in Fig. 2, symmetrical field distributions are obtained, and they do not depend strongly upon the rod rotation angle θ. For the present design of shims the maximum field inhomogeneity over the region of ±2.0 cm amounts to 0.05%. Figure 3 shows the field distribution in the various planes of y = 0.0 (mid-plane), 0.4, 0.8 and 1.2 cm for the rotation angle of $\theta = 60°$, where the field inhomogeneities are represented as the ratio $[\{B_y(y)-B_y(0)\}/B_y(0)]$ similarly as in Fig. 2. As is clear in the figure, the field distributions over the whole y-plane have a good symmetry. The maximum field inhomogeneity in the working area amounts to about 0.15%.

The field strength at the center of the magnet calculated by the code as a function of the rotation angle θ is shown in Fig. 4. A maximum field strength of 3.56 kG was predicted. One should note that the maximum field strength emerges not at the rotation angle of 90° but at 80.5°, corresponding to the result that the zero-field occurs not at $\theta = 0°$ but at $\theta = -9.5°$; otherwise the field strength depends upon the rotation angle of the rods like a function of sin θ (see in Fig. 4).

The PMDII has special advantage of field unuformity in the vertical field distributions due to the fact that the quadrupole components over the whole range of field strength are completely eliminated by the symmetry of the configuration. This type of magnet can be conveniently used as a dipole magnet elsewhere in beam handling systems.

References

1) Honma T., et al., Nucl. Instr. and Method, **A361** (1995) 13-20.
2) Honma T., et al., Proc. 14th Int. Conf. Cycltron and their Applications (Cape Town, 1995) to be published.
3) Menzel M. T. and Stokes H. K., User's Guide for the POISSON/ SUPERFISH Group codes, Los AlamosNational Laboratory Rept. LA-UR-87-115, Jan. (1987).

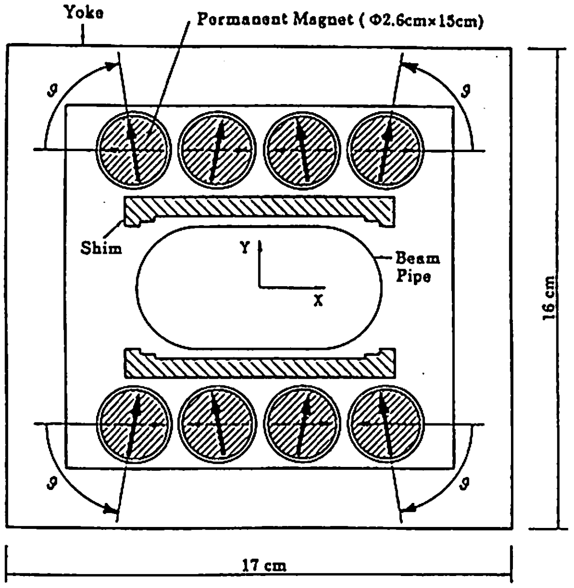

Fig. 1. Cross section of a newly proposed permanent magnet dipole (PMDII). Solid arrows indicate direction of magnetization of permanent magnet rods with arbitrary rotation angle of θ, and broken arrows show $\theta = 0°$

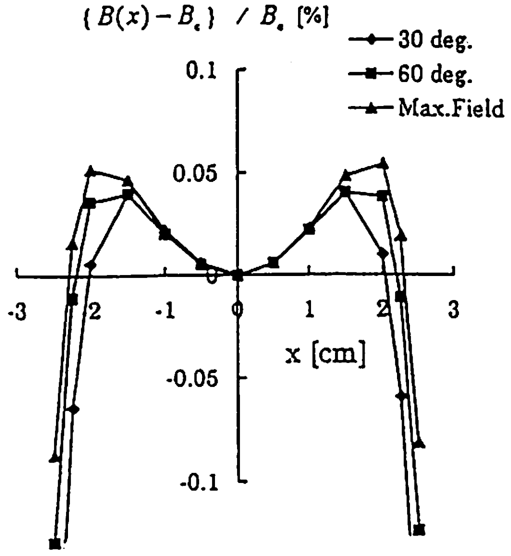

Fig. 2. Inhomogeneities of magnet field in horizontal mid-plane for rotation angles of 30° and 60°, and for the maximum field strength.

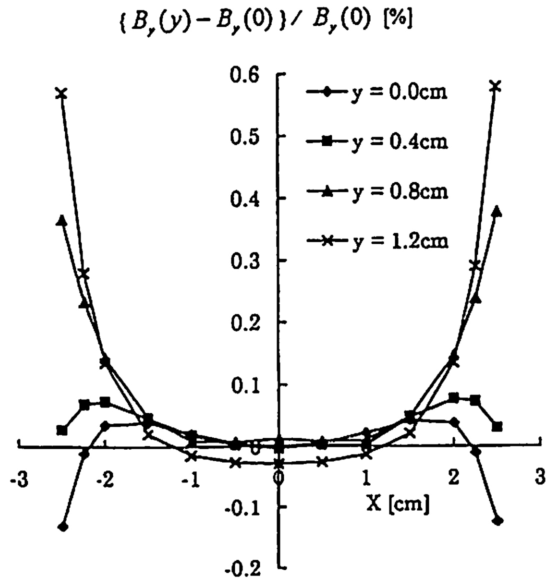

Fig. 3. Field inhomogeneities on various planes perpendicular to the y-axis.

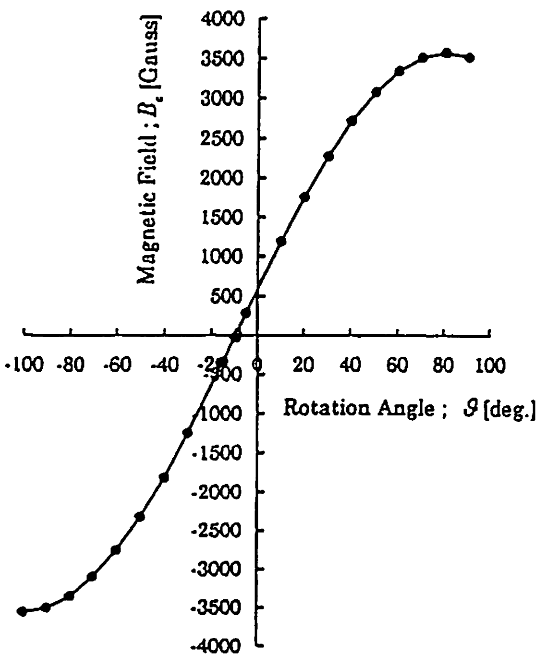

Fig. 4. Calculated magnetic field strength B_C at the center of the dipole magnet as a function of rotation angle θ using PANDIRA. Solid circles indicate points of calculation.

I. 18. Annealing Effects of Au-Si Nuclear Detectors Irradiated by 10 MeV α-Rays

*Ohba K., Mito A., Wakamatsu M., Shoji T., Hiratate Y., Tohei T. and Ishii K.**

Department of Electronics, Tohoku Institute of Technology
*Department of Quantum Science and Energy Engineering, Tohoku University**

Introduction

The effects of radiation damages produced by charged particles have so far been reported in Si nuclear detectors[1-5]. These radiation damages cause serious deterioration in semiconductor detectors.

In the previous report[5], we discussed degadiation characteristics of the Au-Si nuclear detectors irradiated by 10 MeV α-rays.

In this report, we discuss annealing effects of Au-Si nuclear detectors irradiated by 10 MeV α-rays. This annealing is performed in order to recover the characteristics of the damaged detectors.

Experimental

The Au-Si surface barrier nuclear detectors used in this study were fabricated from phosphorus doped n-type Si wafer with a carrier concentration of $\sim 10^{12}$ cm^{-3}(2 kΩ-cm) and thickness of 400 μm. The process of the detector fabrication was described in detail in the previous work[5].

The detectors were irradiated with 10 MeV α-rays by using the cyclotron of Tohoku University. The irradiation doses were up to $\sim 10^{11}$n/cm^2.

Recovery of the radiation damaged detectors was carried out by the thermal annealing method. The annealing was performed in an atomosphere of Ar gas at a temperature of 150°C for an 1 hour.

The characteristics of the detectors before and after irradiation, and after annealing were studied by I-V(current-voltage), C-V(capacitance-voltage), counting response to ^{241}Am α-rays(5.48 MeV) and DLTS(deep level transient spectroscopy)[6] measurements.

Results and Discussion

As shown in Fig. 1, after irradiation the reverse currents increased due to the carrier generation through the defect-states introduced in the depletion layer of the detector. By annealing, the reverse currents decrease and approach to the currents before irradiotion.

In the C-V characteristics, we could not observed obvious changes between the irradiated detectos and the annealed ones.

In Fig. 2, counting response of the detector to ^{241}Am α-particles at 30 V bias is shown, before and after irradiation, and after annealing. After irradiation, the peak position shifts toward the lower channel numbers, but by annealing the peak position tends to return to the before irradiation position. The FWHM of the spectrum before irradiation is 54 keV, but becomes 94.5 keV after irradiation and 57.4 keV after annealing.

In the DLTS measurements, an only one energy level is obviously observed at 0.39 eV below the conduction band edge. By annealing the defect density of this level is reduced to about 1/2 as compared with the density before annealing.

From these measurements, it is seen that the perfomances of the detectors are degraded by the irradiation of 10 MeV α-rays and are moderately recovered by annealing. However, in order to aim at complete recovery of the degraded detectors by the irradiation, it is thought that improvements of the annealing methods are necessary.

Acknowledgment

The authors wish to thank to the staff members of CYRIC for operating the cyclotron.

References

1) Coleman J. A. et al., IEEE Trans. Nucl. Sci. NS-**15** (1968) 363.
2) Chisaka H., JPN. J. Appl. Phys. **12** (1973) 439.
3) Kraner H. W., IEEE Trans. Nucl. Sci. **NS-29** (1982) 1088.
4) Ohba K. et al., IEEE Trans. Nucl. Sci. **NS-30** (1983) 371.
5) Ohba K. et al., CYRIC Annual Report 1994, P72.
6) Lang D. V., J. Appl. Phys. **45** (1974) 3023.

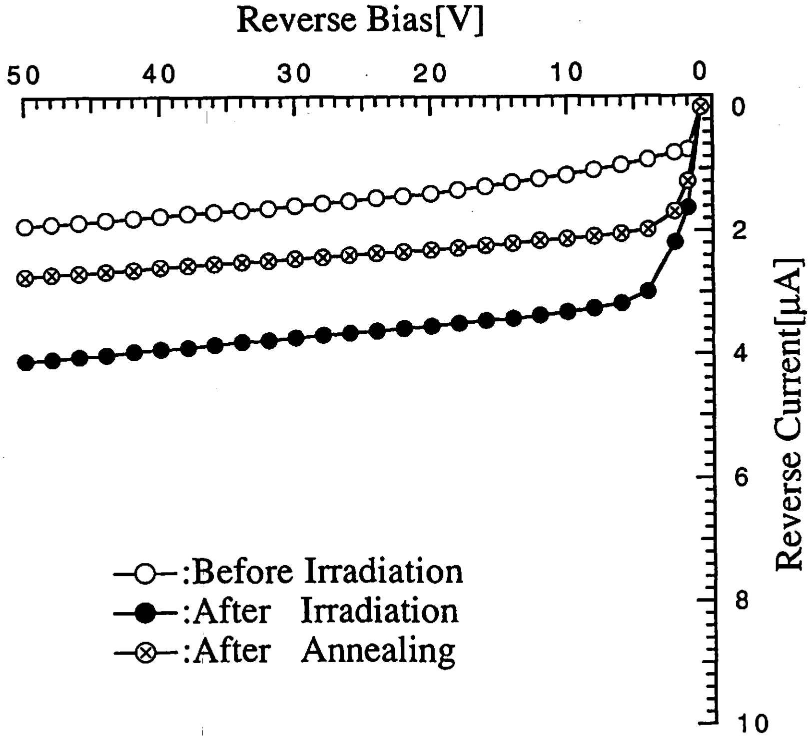

Fig. 1. Current-voltage characteristics before and after irradiation with 10 MeV α-rays, and after annealing.

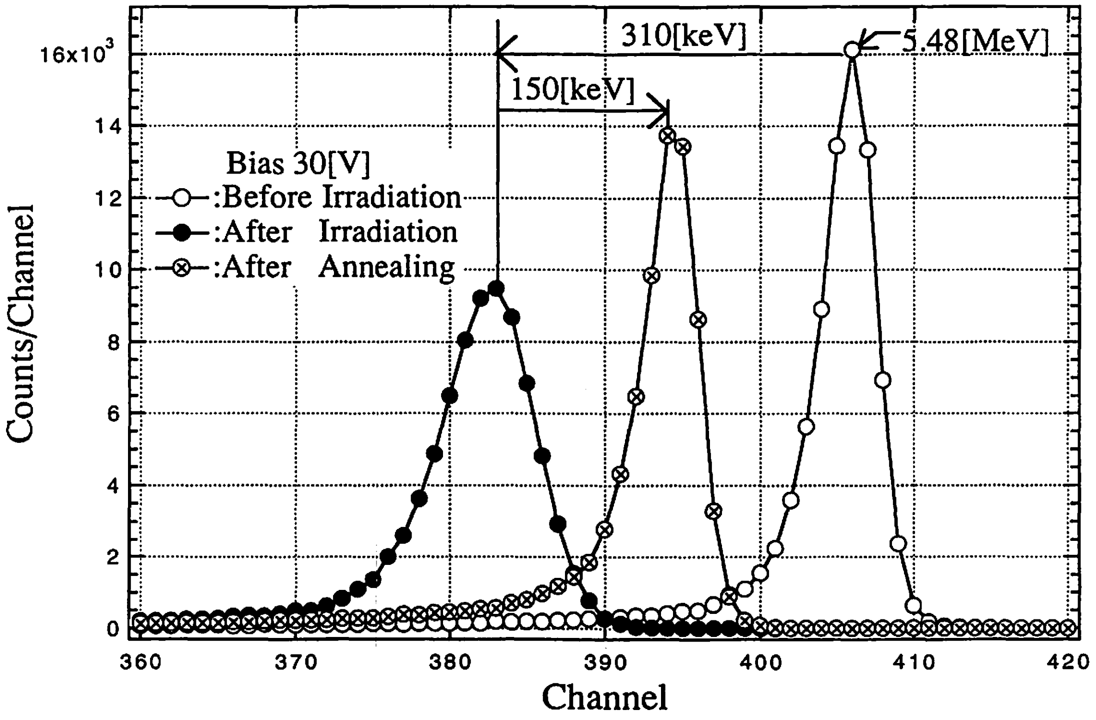

Fig. 2. Counting response to ^{241}Am α-rays(5.48 MeV) before and after irradiation, and after annealing.

I. 19. Characteristics of a High-Purity Germanium Detector

Tsubota H., Miyase H., Maeda K., Suda T., Toyofuku A., and Endo T.

Department of Physics, Graduate School of Science, Tohoku University

A High-purity germanium (HPGe) semiconductor has been used as a detector of charged particles with a good energy resolution$^{1)}$. This detector has excellnet properties for storage and operating. When not operating at liquid nitrogen tenperature, this detector can be stored at room temperature. This is very useful to the user. The energy resolution of the HPGe detector is also so good for charged particles as well as for gamma ray that a more compact measurement system than a magnetic spectrometer can be made with a good energy resolution. However there are some flaws which are unfavorable to the user. Firstly it is difficult to obtain a large volume detector, and the maximum energy of the particles to be measured is also liumited by the size of the detector. Then the characteristics of a large HPGe detector has reported very few. It is important to obtain information so the large HPGe detector for the experimental study with the high energy resolution using this detector. Secondly the gerumanium semiconductor is very sensitive to a gamma ray and is used as the detector with a high efficiency for the gamma ray. This property of the HPGe detector makes the user difficult to measure particles in a strong gamma ray environment.

In this paper the experimental results for the dependence of the energy resolution on the incident proton intensity and the influence of the background environment to the large HPGe detector, that is the possibility to use this detector in the experimental room V of CYRIC, are reported.

The experimental arrangement is shown in Fig. 1. A target of Au(0.46 mg/cm^2) set in a scattering chamber was irradiated by protons (of energies of 35 MeV) from the cyclotron. The Au target was held with a 1 mm thick Al holder. The scattered protons were detected with the HPGe detector (Σurisys Measure, EDGP 2800-35-R, 2800mm^2 × 35mmt) set in a vacuum chamber at 35 degrees with respect to the incident proton beam. It is expected that the beam shape at the target position is broad in the horizontal plane$^{2)}$. In order to avoid the effect from the beam shape a slit (2mm gap, 2mm thick stainless steel) was set in front of the detector as shown in Fig. 2. The scattered proton has an energy uncertainty of about 2 keV by this slit gap. During measurement, the detector was kept at liquid nitrogen temperature in the vacuum chamber (about 10^{-6} Pa). The vacuum chamber was shielded with concrete blocks and paraffin blocks for the backgrounds from a Farady cup.

A typical energy spectrum of the scattered protons by the Au target is shown in Fig. 3. On can see several conspicuous peaks other than an elastic scattering peak at 35 MeV of the protoon energy (E_p) in the spectrum. The 32.5MeV peak seems due to the broaden protons horizontally which passed through the Al target holder and lost the energy in the holder. The 11 keV peak is protons passed through the stainless steel slit in front of the detector, which indicates also the incident beam wideness at the target. In this measurement the electric signals from the detector were discriminated at about 7 MeV. The part lower than about 10 Mev in the spectrum includes noises mainlly. This spectrum was measured with the proton intensity of 0.6nA and counting rate of 13.2 (counts/sec). The spectrum shows a clear elastic peak and indicates the possibility to use this large HPGe detector for study inelastic protons in the energy region above 14 keV under a more suitable shield for backgrounds. A serious pile-up by backgrounds of X-rays fron target was expected, and pointed out with emphasis[2)] the difficulty of the particle measurement using the HPGe detector at CYRIC. But such pile-ups are not found in the spectrum. The proton measurement with the beam intensity of 2.8 μA was also made. The spectrum shows also similar result to that with 0.6 nA except a small pile up.

Dependence of the energy resolution on the counting rate was measured, and the result (full widths at half maximum) is shown in Fig. 4, where errors are not shown. The figure does not show a notable dependence of the resolution on the counting rate. The average resolution is about 0.3 keV. The specification sheet for this detector gives 2.04 kev at 1332 kev gamma ray. Assuming the same resolution, we expect the resolution of 0.05 MeV at 35 keV for protons. For the Ge(Li) detector 15 Kev at 44 MeV protons has been reported[3)]. The presnt result is larger than the expected one and that for the Ge(Li) detector condideably in sprite of the clear proton energy spectrum. The present resolution seems to indecate the incident bram uncertainty.

The above resolts show that: (1) The presnt HPGe detector has a good energy resolution for protons as well as gamma ray, and the resolution for the proton detection is better than 0.3%. (2) Protons in the energy region above E_p = 14 MeV can be detected without a serious backgroud of X-Rays from tne target, gamma rays of the neutron caputure by the around materials, especially Faraday cup, and electrical noises. This indicates that the experimental environment of the experimental room is bery good and the experiment using the present large HPGe can be made for proton detection with a good energy resolutioon. We can plan the measurement of protons using HPGe detectors. For other charged particles the detector test will be made in future.

The authors would like to thank professor H. Orihara for his kindness to give us a chance of this experiment. They also thank Mr. A. Yamamoto for his helpful advice and assistance during this experiment.

references

1) D. L. Friesel et al., Nucl. Instr. and Meth. **207** (1983) 403.
R. H. Pehl, P. Luke and D. L. Friesel Nucl. Instr. and Meth. **A242** (1985) 103. and references in these papers.
2) K. Ishii, Private communications.
3) G. Riepe, D. Ptotic and J. Reich, Nucl. Instr. and Meth. **124** (1975) 527

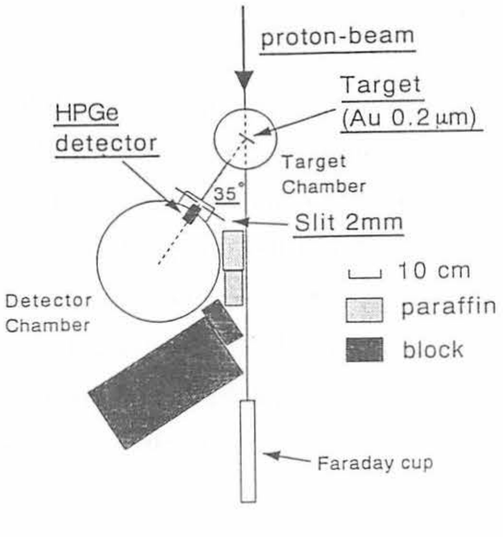

Fig. 1..Experimental arrangement.

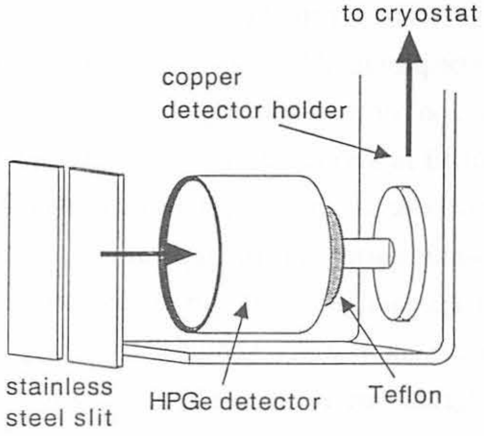

Fig. 2 The detector setting in the chamber.

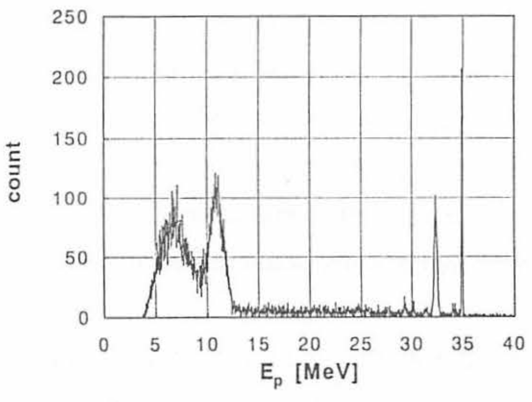

Fig. 3 Typical energy spectrum of protons scattered by the Au target at 35°.

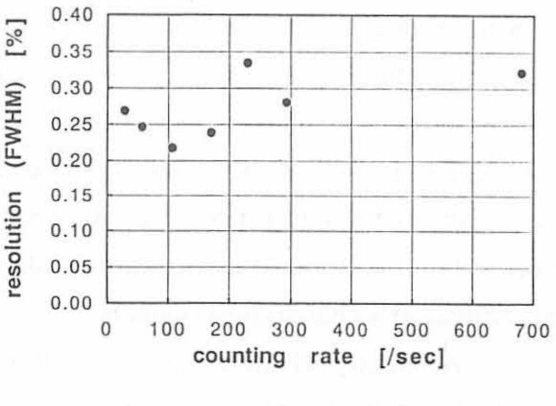

Fig. 4 The relation between energy resolution and counting rate.

I. 20. Development of The RF Separator for The Secondary Beam from The Incident Particles

Suzuki K., Kotajima K., Fujisawa M., Tanaka M., Minemoto K., Yamaya T., Ishiyama H.*, Yamazaki A.*, Katoh M.*, Tojima J.*, Shinozuka T.**, and Fujioka M.***

Department of Nuclear Engineering, Tohoku University
*Department of Physics, Tohoku University**
*Cyclotron and Radioisotope Center, Tohoku University***

The kinematically focused secondary beams of neutrons and some unstable nuclides can be provided by using the heavy ion induced reactions on light nuclei, the $^{1}H(^{13}C,n)^{13}N$ reaction for example. By counting unstable particles produced in the reaction, the yield of the emitted neutrons can be estimated as standard neutron field. From a technological point of view, one of the important facts which severely influence upon the counting yield of the unstable particles is the separation from the incident beam. In this work, the radio-frequency (RF) separator[1,2] was chosen and built up as a device for the α-beam separation, and practical performance was examined by using 14.5 MeV beam. Through the measurements of deflected angle of α-beam on various delay time for the separator RF timing from the cyclotron RF timing, it was confirmed that the RF separator was driven correctly.

Introduction

The kinematically focused secondary beams can be produced by utilizing the endoenergetic Heavy Ion (HI) induced reactions on light nuclei[3]. We could have obtained focused beams of neutron[4] and some radioactive nuclides[5] from the $^{1}H(^{13}C,n)^{13}N$ and $^{1}H(^{15}N,n)^{15}O$ reactions at Tohoku University Cyclotron and Radioisotope Center (CYRIC). Counting radioactive particles created in the reaction makes it possible that the intensity of this focused neutron beam is estimated absolutely. The secondary beam must be separated from the incident HI beam before detection, because the incident particles are still more than the secondary by millions times. We had used the dipole magnet for the separation, however it is impossible that the secondary beam is identified from inelastically scattered particle whose momentum per charge (p/q) is equal.

A velocity selection (time of flight selection in other words) is aimed by using the RF separator for the present work, not only a p/q selection with the dipole magnet. In using this separator behind the magnet, the incident beam is supposed to be rejected by the magnet, and in the second place, the RF separator will deflect radioactive particles and inelastically scattered particles in the different directions because of different TOF from the target to the electrodes of the separator. Between the electrodes high voltage is supplied by amplifying the RF signal that is provided from the synthesizer driving the cyclotron.

Design of the RF separator

Threshold energy of ^{1}H (^{13}C, ^{13}n) N reaction is 41.75 MeV, so incident energy of $^{13}C^{4+}$ ion should be 47 MeV taken into account energy loss at the window of the gas-target to obtain well-focused secondary beams. In this case radio-frequency operating cyclotron is 24.8 MHz and energy of ^{13}N is 26.9 - 28.4 MeV that is to say velocity of 2.00 - 2.05 cm/nsec. So $^{13}C^{6+}$ with velocity of 1.71- 1.76 cm/nsec cannot be thrown out by the magnetic field for selection of $^{13}N^{7+}$. In order to kick the ^{13}C in the different direction from ^{13}N, the RF separator should be established at the distance of 2.45 m from the target, because half the periodic time of the RF is 20.2 nsec.

The block diagram of the RF separator is shown in Fig. 1. The RF signal driving cyclotron is divided for the separator to synchronize the phase of the electric field and the pulsed beam from the cyclotron. We can control the amplitude and phase of the RF signal for the separator with the synthesizer and nano-second delay generator, respectively.

The amplitude- and phase-controlled signal is fed into the high voltage generating stage consisting of a driver, an RF power amplifier and a tank circuit. The tank circuit is composed of three variable capacitors whose capacitance is variable from 30 to 150 pF and three inductors. The capacitors in the output side are connected in series. The inductors in the output side consist of two coils in series, each constructed from a 5 mm diameter copper tube to form a 3.5 turn coil of 60 mm diameter and 60 mm long. The inductors in the input and output sides are arranged coaxially to be supported by a cross-structured acryl. The inductance of these coils is determined experimentally because of the stray capacity. The optimum tuning point is found by minimizing the voltage standing wave ratio through adjustment of three variable capacitors. 10 kV of peak to peak voltage was measured for an input power of 40 W by a 1000:1 high voltage probe. Therefore the Q-factor of this tank circuit is larger than 75. It should be noted that a probe is a large Q-dump load, viz a lower power might be sufficient to obtain 10 kV peak to peak voltage without a probe.

The electrodes consist of parallel oxygen-free copper plates, 20 cm long by 4 cm wide with 2.0 cm spacing. They are supported by four high voltage vacuum feed-throughs withstanding a voltage of 12 kV DC inside the beam duct.

Suppose that a particle with mass of m, velocity of v_L and charge of q gets vertically into the electric field V/d by RF voltage $V = V_0 \sin 2\pi f(t + t_0)$ at the time $t = 0$. When this particle runs across the field for longitudinal distance of L, the transverse component of velocity v_T is

$$
\begin{aligned}
v_T &= \int_0^{L/v_L} \frac{q V_0}{m d} \sin 2\pi f\left(t+t_0\right) dt \\
&= \frac{q V_0}{2\pi f m d}\left\{\cos 2\pi f t_0 - \cos 2\pi f\left(\frac{L}{v_L}+t_0\right)\right\}
\end{aligned}
\qquad (1)
$$

and the transverse position y is given as follows :

$$
\begin{aligned}
y &= \int_0^{L/v_L} \frac{q V_0}{2\pi f m d}\left\{\cos 2\pi f t_0 - \cos 2\pi f\left(t+t_0\right)\right\} dt \\
&= \frac{q V_0}{2\pi f m d}\left\{\frac{L}{v_L}\cos 2\pi f t_0 + \frac{1}{2\pi f}\sin 2\pi f t_0 - \frac{1}{2\pi f}\sin 2\pi f\left(\frac{L}{v_L}+t_0\right)\right\}
\end{aligned}
$$

$$(2)$$

Therefore the transverse position Y on the slit position at the flight pass length D distance from the end of the electric field is expressed as

$$
Y = y + \frac{v_T}{v_L} D. \qquad (3)
$$

Experimental Procedures and Results

The practical performance of this RF separator thus prepared was examined by using 14.5-MeV α particle beam from CYRIC AVF cyclotron. The experimental setup is illustrated in Fig. 2. Then the radio-frequency is 24.783 MHz nearly equal in case of the acceleration of 47-MeV $^{13}C^{4+}$.

At first the α-beam deflected in half the side was measured on various delay time of RF high voltage from the cyclotron RF timing, and its result is shown in Fig. 3. Intensity of α particle was measured as beam-current by Faraday cup behind the slit and normalized with counts of α particles scattered at the Al target. This result shows that the beam was transported in bunches and the deflection of beam depends on the difference in the phase on arrival times of beam. The large spot size of beam is supposed to be the reason why the intensity in case of the deflection on the opposite side to the slit was not zero, but it may not be a problem if the double quadrupole focusing lens are used.

As the next step, the maximum transverse deflected angle was investigated when the input power for the tank circuit is 30 W and 40 W to determine the voltage between the electrodes, Q-factor and inductance of the tank circuit. The following values are substituted for parameters of Eqs. (1) and (2) :

$$
m = 4.14\times10^{-8}\,\mathrm{eV\cdot s^2/m^2},\quad v_L = 2.64\times10^{7}\,\mathrm{m/s},\quad q = 2e\ [\mathrm{C}],
$$

$$
L = 0.200\,\mathrm{m},\quad d = 0.020\,\mathrm{m},\quad f = 24.783\times10^{6}\,\mathrm{Hz},
$$

$$
2\pi f t_0 = \frac{\pi}{2} - \frac{\pi f L}{v_L} = 0.312\pi ,
$$

and we can obtain equations to express the relation between RF high voltage and deflection as

$$v_T = 17.3\ V_0\ [\mathrm{m/s}]\,, \qquad y = 6.54\times10^{-8}\ V_0\ [\mathrm{m}]\ .$$

Now D of Eq. (3) is 0.57 m in this experiment, so that the high voltage supplied between the electrodes is calculated from the transverse position Y measured experimentally with the following equation :

$$V_0 = 2.28\times10^{6}\ Y\ [\mathrm{V}]\,.$$

Since Y was measured as 6 mm for an input power of 30 W to the tank circuit and 9 mm for 40 W, the voltage is determined as 14 $\mathrm{kV_{p\text{-}p}}$ for 30 W and 21 $\mathrm{kV_{p\text{-}p}}$ for 40 W. So the Q-factor of the tank circuit is supposed to be around 140-150.

Conclusion

Through these measurements and calculations it was made sure that this RF separator is good enough for a practical use. Particularly, the RF high voltage of 10-20 kV enough to separate secondary-beam ^{13}N from inelastically scattered ^{13}C could be generated.

References

1) A. P. Banford B. Sc., The Transport of Charged Particle Beams, E.& F. N. Spon Ltd. (1966).
2) Matsuyama S. et al., Nucl. Instr. and Meth. **A348** (1994) 34.
3) J. H. Dave et al., Nucl. Instr. and Meth. **200** (1982) 285.
4) Hasegawa K. et al., Proc. of 11th Int. Conf. on Cyclotrons and Their Applications, Tokyo, Japan, (1986) 642.
5) Yamaya T. et al., Nucl. Instr. and Meth. **B70** (1992) 374.

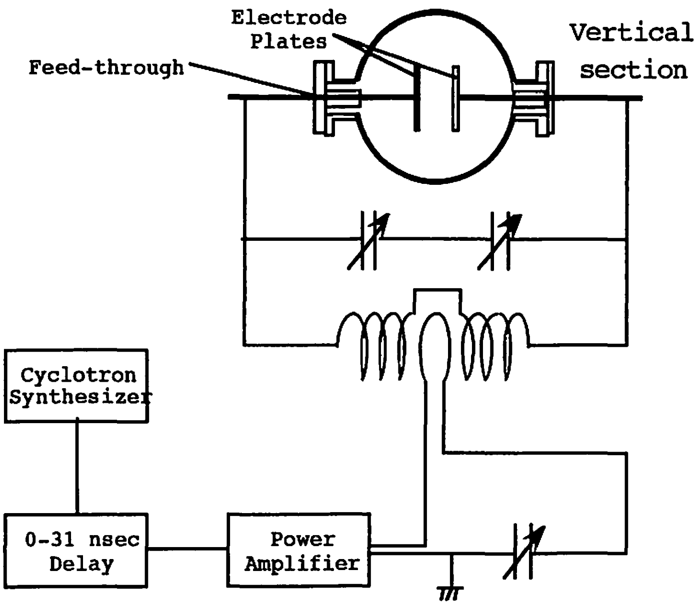

Fig. 1. Block diagram of the RF separator.

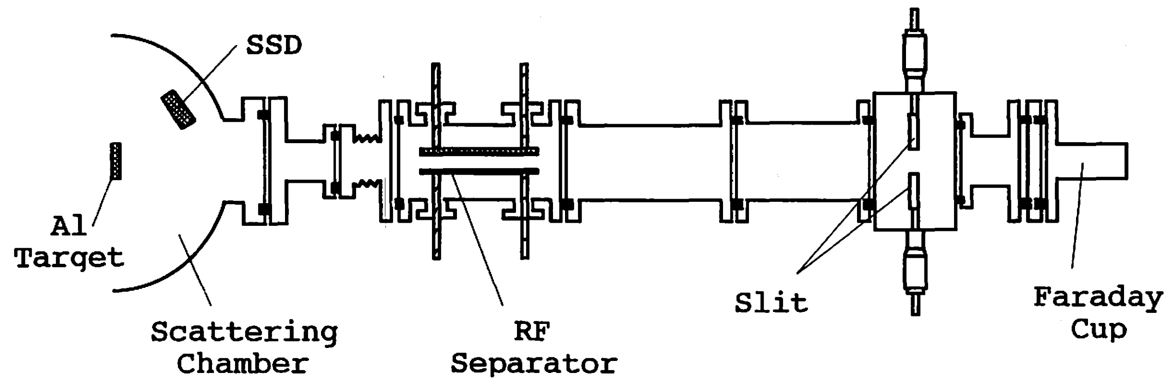

Fig. 2. Experimental arrangement for the measurements of the deflected angle of α-beam from CYRIC AVF cyclotron.

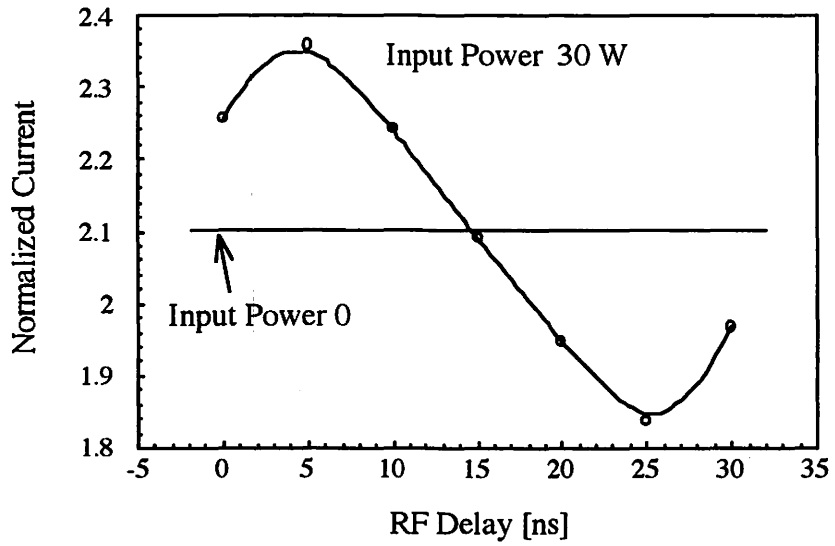

Fig. 3. Dependence of the intencity of α-beam deflected in half the side on the delay time of the RF high voltage from the cyclotron RF timing.

I. 21. Alignment of atomic inner-shells by proton impact

Futatsugawa S., Ishii K., Sera K.**, and Orihara H.****

Nishina Memorial Cyclotron Center, Japan Radioisotope Association, Tomegamori, 020-01 Takizawa
*Department of Quantum Science and Energy Engineering, Tohoku University**
*Cyclotron Research Center, Iwate Medical University, Tomegamori, 020-01 Takizawa***
*Cyclotron and Radioisotope Center, Tohoku University****

Introduction

By bombardments of electrons or heavy charged particles, inner-shell electrons of target atoms are ionized and the inner-shells are aligned to the direction of incident beam[1]. There are two methods to investigate this alignment effect on the inner-shell ionization: measurement of angular distribution of x-ray intensity and measurement of polarization of x-rays. Here, results on the measurement of the polarization of characteristic x-rays induced by proton bombardments are reported.

Experiment

Targets of Si, Mo, and Zr were bombarded by 3MeV proton beams from the AVF cyclotron at CYRIC, Tohoku University and characteristic x-rays emitted to the direction of 90° with respect to the incident beam were analysed with a crystal spectrometer, which was designed to be rotated from 0° to 90° in a plane perpendicular to the direction of x-ray beam for the measurement of x-ray polarization. This crystal spectrometer consists of a solar slit, an EDDT crystal, a goniometer, and a position sensitive proportional counter (PSPC). The direction of grid of the solar slit is parallel to the x-ray diffraction plane. This solar slit prevents scattered x-rays from entering the position sensitive proportional counter. The x-ray energy-range, which can be measured with the EDDT crystal, is from 1.74 keV to 2.45keV.

The target of Si was prepared by vacuum evaporation onto a thin aluminium backing foil. By measuring K_α-x-rays of Si, uniformity of the detection efficiency for the rotation of spectrometer was tested and as shown in Fig.1, the detection efficiency is uniform within ± 2%.

The self supporting targets of Mo and Zr were obtained by using a rolling mill. L_α- and L_β- x-rays of these elements were observed with our crystal spectrometer and their yields were normalized by the beam currents. The angular distributions of these x-rays are shown in Figs. 2 and 3.

Results and discussion

As seen in Figs.2 and 3, we can recognize the anisotoropy of angular distributions in L_α- and L_β- x-rays of Mo and Zr. Especially, it is remarkable in the case of L_α- x-rays. The L_α-x-rays are produced by radiative transition to the subshell of 2p3/2. Therefore, this anisotropy means the alignment of 2p3/2 subshell. Theoretical treatment for the polarization effect on the x-rays produced by heavy charged particle bombardments is now in progress.

Reference

1) Kamiya M., Kinefuchi Y., Endo H., Kuwako A., Ishii K., and Morita S., Phys.Rev. **A20** (1979) 1820.

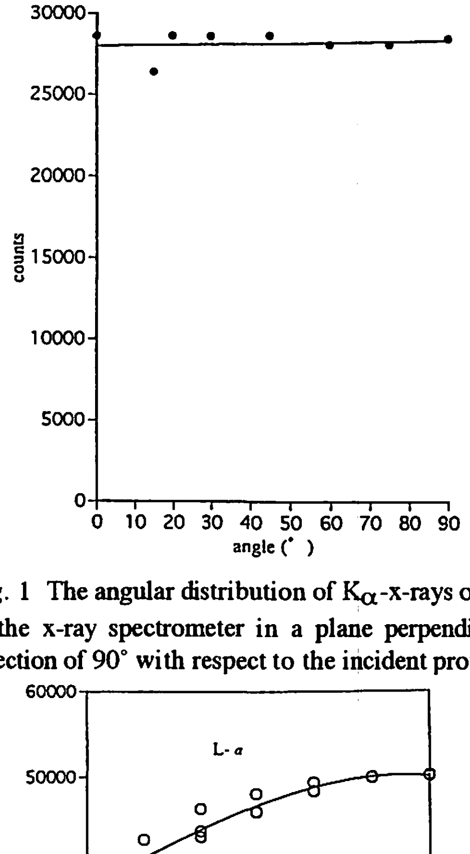

Fig. 1 The angular distribution of K_α-x-rays of Si for 3MeV proton impact. The angles are rotation angles of the x-ray spectrometer in a plane perpendicular to the direction of x-ray beam which is taken in the direction of 90° with respect to the incident proton beam.

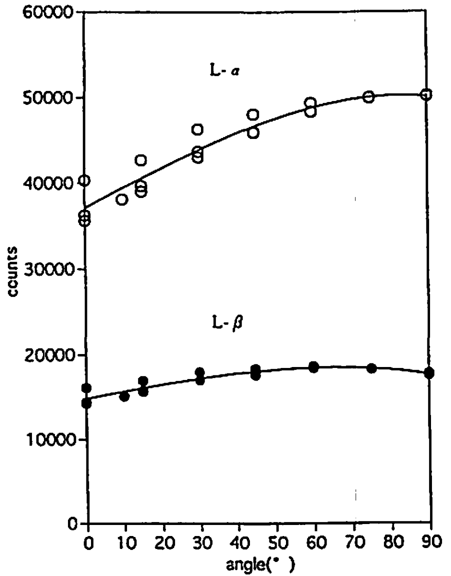

Fig. 2 The angular distributions of L $_\alpha$- and L_β-x-rays of Mo for 3MeV proton impact.

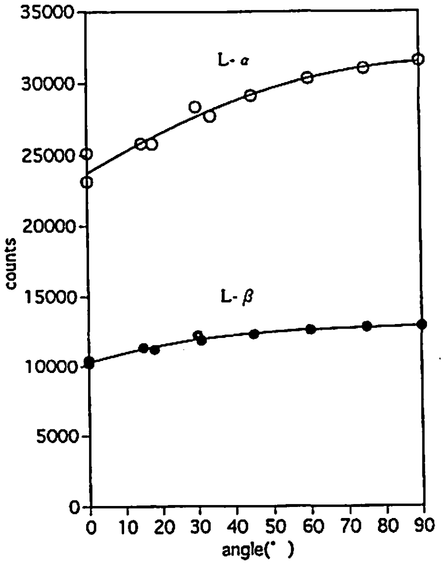

Fig. 3 Same as Fig.3 except for Zr.

II. CHEMISTRY

II. 1. Separation of ^{95m}Tc Produced in Proton Irradiated Molybdenum by Sublimation Method

Sekine T., Mine T., and Kudo H.

Department of Chemistry, Graduate School of Science, Tohoku University

Migration behavior of long-lived fission products in the environment has attracted increasing interest from a view point of nuclear waste management$^{1)}$. Among a number of fission products, ^{99}Tc (2.111×10^5 y) is one of the most important nuclides produced with comparatively high yield (6%). Although technetium is a well known element that migrates easily in an aquifer system, little is known on the chemical species of technetium including colloids or pseudo colloids under reductive condition and on the complexation with naturally occurred organic materials such as a humic acid. To study chemical reactions of technetium in a trace amount, we intended to prepare ^{95m}Tc, which was a gamma emitter with a suitable half-life of 61 d, by the proton bombardment of molybdenum. A sublimation method was applied to separate ^{95m}Tc from macroscopic molybdenum, based on the volatility difference between technetium oxide (Tc_2O_7 or $HTcO_4$) and molybdenum oxide (MoO_3). The former is much volatile than the latter, and the resulting deposition sites are different under an appropriate temperature gradient.

Molybdenum(natural) metal foils (12mm×12mm, 0.1 mm thick) were irradiated with proton (E_p = 24 MeV, 10 μA) for 3 hours at the Cyclotron Radioisotope Center, Tohoku University, and the irradiated target was stored for about a month for decay out of nuclides with shorter half-lives. After cooling, technetium was separated by sublimation using an electric furnace (Fig. 1) which had temperature gradient shown in Fig. 2. The molybdenum foil was placed in a quartz tube (5 or 6 mm i.d., about 1200 mm long) at the highest temperature site and heated at 760°C under oxygen gas flow (50 ml/min). Fig. 3 shows a change of gamma-ray dose rate outside the electric furnace at the sample position as a function of the heating time, measured with a NaI(Tl) scintillation detector. The decrease of the gamma-ray dose with time was due to the sublimation of ^{95m}Tc. It took about 2 hours for complete sublimation of ^{95m}Tc irrespective of high volatility of technetium oxide. The phenomenon was caused by lower volatility of molybdenum oxide which was successively formed and sublimed from the surface of molybdenum metal by heating under oxygen gas flow.

Fig. 4 shows the distribution of radioactivity deposited inside the quartz tube, measured with a Ge detector equipped with a 4 k multi-channel analyzer. ^{95m}Tc was deposited around the end of the electric furnace where the temperature steeply decreased from 200 to 100°C. The macroamount of molybdenum oxide was deposited in the region of 650 to 400°C and was completely separated from the technetium oxide as expected. Rösch *et al.* studied the sublimation condition on the separation of ^{94m}Tc ($T_{1/2}$ = 52 min) from the proton bombarded molybdenum oxide or metal for nuclear medical application[2). They pointed out the formation of TcO_x depositing at the band around 400°C which overlapped with the MoO_3 band. In our separation, however, the technetium species were not deposited at such a high temperature site (400°C). The result may be attributed to the difference of flowing gas component ; they used mainly air or air with moisture but we used oxygen for complete oxidation of technetium.

The ^{95m}Tc deposited onto the inner surface of the quartz tube could be quantitatively removed with a minimum amount of dil. NaOH solution, and the stock solution of ^{95m}Tc (some MBq / ml) was successfully prepared for the tracer use thereafter.

Another reaction for the production of ^{95m}Tc recommended is by the alpha particle irradiation of niobium that consists of only ^{93}Nb as a stable isotope. An advantage for this reaction is that contamination with other long-lived technetium isotopes, such as ^{97}Tc, ^{98}Tc or ^{99}Tc, is excluded in the ^{95m}Tc fraction separated, while such contamination occurs by the proton bombardment of natural molybdenum that has a number of stable isotopes.
Furthermore, the separation of technetium from niobium by sublimation is well established as shown in Fig. 4, in which ^{91m}Nb and ^{92m}Nb produced by the (p,α) reactions of molybdenum deposited near the heating site in contrast to the ^{95m}Tc deposition at much lower temperature site. The high purity of ^{95m}Tc tracer has been demanded to examine the yield of chemical procedures especially for the analysis of ^{99}Tc in environmental samples by ICP-MS[3), the contamination from long-lived isotopes of technetium being avoided.

References

1) Desmet G., Myttenaere C., "Technetium in the Environment", Elsevier Applied Science, New York, 1986.
2) Rösch F., Novgorodiv A. F., and Qaim, S. M. Radiochim. Acta **64** (1994) 113 and references here in.
3) Tagami K., private communication.

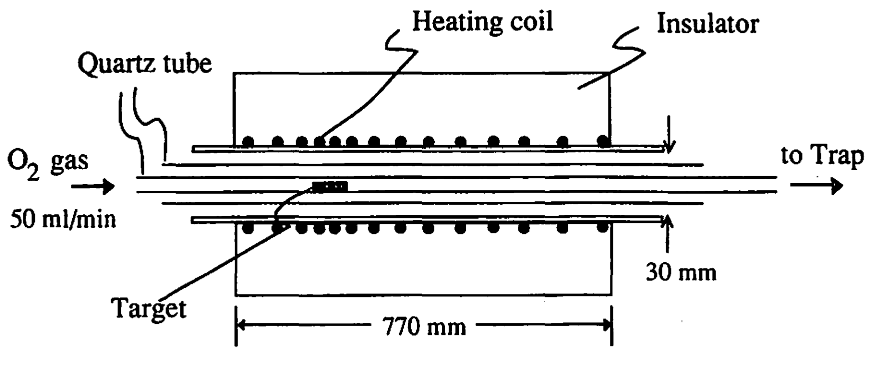

Fig. 1. A schematic figure of the electric furnace used in this study.

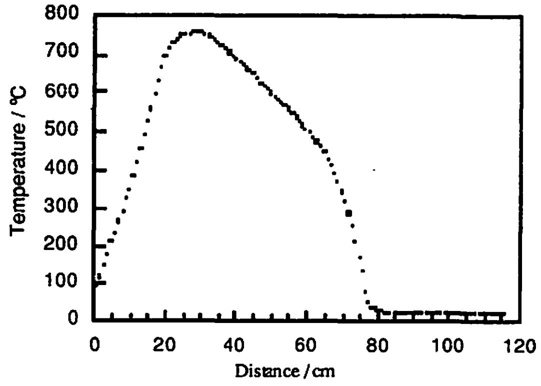

Fig. 2. The temperature gradient along the electric furnace.

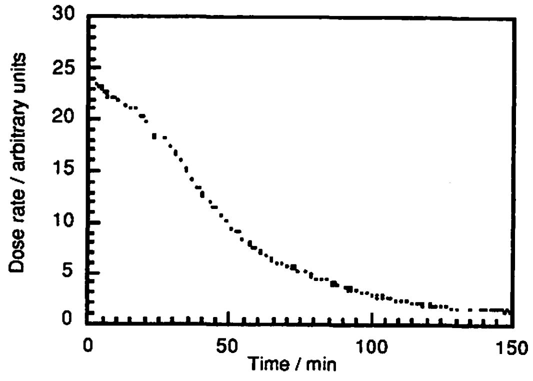

Fig.3. The gamma dose rate change outside the electric furnace at the sample position as a function of the heating time.

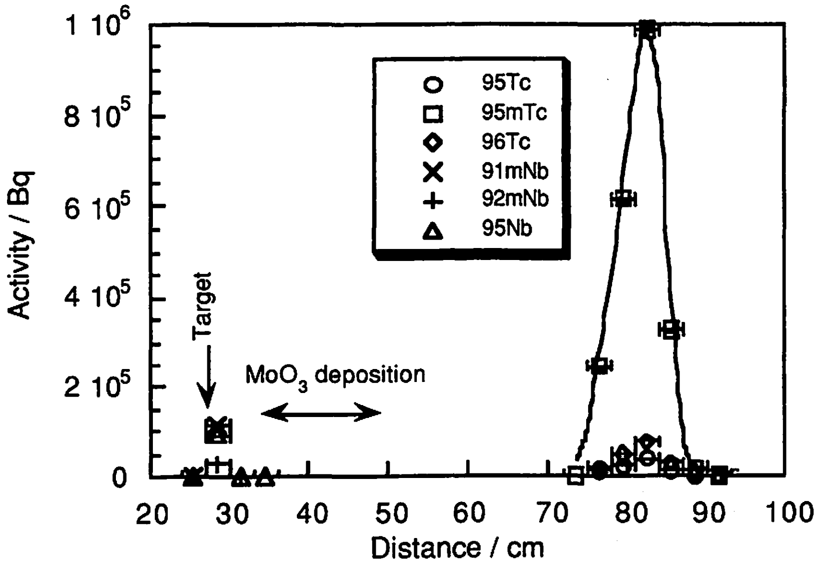

Fig. 4. The distribution of radionuclides along the quartz tube after sublimation. The deposition zone of macroscopic MoO_3 is also indicated.

II. 2. Highly Sensitive Determination of Oxygen in Copper by Charged Particle Activation Analysis

Sakurai H., Sayama Y., Masumoto K., and Ohtsuki T.**

Central Research Institute, Mitsubishi Materials Corporation
*Laboratory of Nuclear Science, Faculty of Science, Tohoku University**

The electrical and mechanical properties (e.g. electrical conductivity) of copper are strongly influenced by the presence of oxygen[1]. As growing use of highly purified copper in various industrial fields, it has been needed to develope an accurate analytical method of oxygen contained at the order of $\mu g \cdot g^{-1}$ in copper. Among various analytical methods, the activation method which uses the $^{16}O(^{3}He, p)^{18}F$ reaction gives high sensitivity and selectivity for the analysis of oxygen. In order to prevent the interference from the intense radioactivity induced in copper by the $^{65}Cu(^{3}He, 2n)^{66}Ga$ reaction, the chemical separation of ^{18}F is indespensable. As this matrix activity can not be perfectly removed by the direct precipitation as an insoluble fluoride, the steam distillation method has been widely adopted for the separation of ^{18}F. Although this method is time-consuming and the recovery and reproducibility of this method is not so good. In this work, the combination of pyrohydrolysis and LaF_3 precipitation method[2] has been tried to the oxygen analysis by charged-particle activation for the first time. The etching condition has been also investigated to remove the surface contamination of oxygen from the atmosphere.

All copper samples were obtained in disk (diameter:10 mm, thickness:2 mm). The BCR CRM 054R "low oxygen copper" which contains 0.47 $\mu g \cdot g^{-1}$ of oxygen and a pure quartz glass were used as comparative standards. Samples and standards were wrapped with pure aluminium foil of 10 μm in thickness. Irradiation was done at the No.1 irradiation channel for radioisotope production of Cycrotron Radioisotope Center, Tohoku University. Each sample was irradiated by 20 MeV ^{3}He for 50 min at the average current of 1 μA. In order to monitor the beam intensity of ^{3}He, a copper foil of 10μm in thickness was placed before the sample. The surface of sample was cooled by blowing He-gas and the reverse side of sample was cooled with water indirectly.

Fluorine was separated as follows, using the apparatus shown in Figure 1. The irradiated sample was etched with $3M\text{-}HNO_3$ for 10 min. The etching depth was checked by measuring the weight loss of samples after etching. Then it was set into an alumina crucible containing 0.1 g of CaF_2 as the F carrier, and covered with 2 g of $Na_2W_2O_7$[3] as the auxiliary reagent. The crucible was inserted in an electric furnace which was heated at 1100°C. Then the moist oxygen was passed into a furnace at the rate of 500 $cm^3 \cdot min^{-1}$. The fine solid particles from the furnace were retained by a quartz-wool. The liberated fluorine was finally trapped in 40 ml of 0.025 M - NaOH solution.

The solution was heated up to 90°C and 1ml of conc. HNO_3 and 5 ml of 1M-$La(NO_3)_3$ solution were added to precipitate as LaF_3. Then 25 mg of $Al(SO_4)_3 \cdot Na_2SO_4 \cdot 24H_2O$ was added as the flocculating agent. After 5 minutes, the precipitate was collected on a membrane filter (poresize; 0.45mm, diameter; 47 mm) Finally the filter was put into a polyethylene bag to measure the radioactivity under the same counting condition. The 511 keV annihilation γ-ray from ^{18}F was measured with a high purity Ge detector and a pair of BGO-scintillation detector. At least, each sample was measured for three times at one half-life intervals.

Figure 2 shows the depth profile of fluorine activity expressed as the count rates of 511 keV γ-ray per μm thickness of a copper sample. It was found that the surface contamination reached at 4 μm depth. Therefore, the etching depth was fixed at about 10 μm to remove the contamination completely. The surface of the sample was still smooth after etching.

The concentration of oxygen in four copper samples have been determined as shown in Table 1. The certified reference material BCR CRM No.054R was used as a comparative standard. In the case of Cu-D sample, the oxygen concentration was also determined using a high purity quartz as a standard. The result was in good agreement with that obtained by the BCR standard. The analytical results of the samples (Cu-C, Cu-D) containing more than 1 $\mu g \cdot g^{-1}$ of oxygen were in good agreement with the results of the other method. But in the case of the sample (Cu-A, Cu-B) containing less than 1 $\mu g \cdot g^{-1}$ of oxygen, the results did not agreed with the results of the other method and the relative standard deviation was over 50 % (Cu-A). It is not certain that this result means the unhomogeneity of oxygen in these samples. Therefore, the improvement of sensitivity is still nesessary to make clear the behavior of oxygen under 1 $\mu g \cdot g^{-1}$.

Acknowledgement

The authors thank the crew of the Cycrotron and Radioisotope Center for their kind operation of cyclotron irradiation.

References

1) Kraft G., Eurisotop Office Information Booklet 59, Eurisotop, Brussels, 1972.
2) Sakurai H., Hayashibe Y., Fukuda M., Sayama Y., Masumoto K. and Ohtsuki T., to be published.
3) Berns E. G., and Van der Zwaan P. W., Anal. Chim. Acta, 59 (1972) 293.

Table 1. Results for oxygen in copper samples (concentrations in $\mu g \cdot g^{-1}$)

Sample	Found	Av. ± S. D.	Other Method*
Cu-A	0.053, 0.013, 0.027, 0.032, 0.018	0.029 ± 0.016	0.2
Cu-B	0.35, 0.25	0.30	0.5
Cu-C	1.4, 1.3, 1.3, 1.4	1.3 ± 0.1	1.3
Cu-D	2.6, 3.1, 3.2, 2.8	2.9 ± 0.3	3.0
Cu-D**	3.1, 3.0	3.1	3.0

*Inert gas fusion method, ** a high purity quartz was used as a standard.

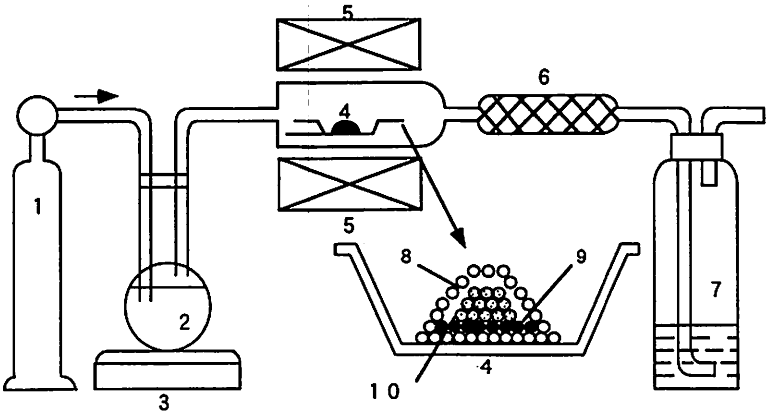

Fig. 1. Apparatus for fluorine separation by the pyrohydrolysis;
1- oxygen, 2- H_2O, 3- heater, 4- alumina boat, 5- electric furnace,
6- quartz- wool, 7- absorption bulb, 8- $Na_2W_2O_7$, 9- carrier, 10- sample

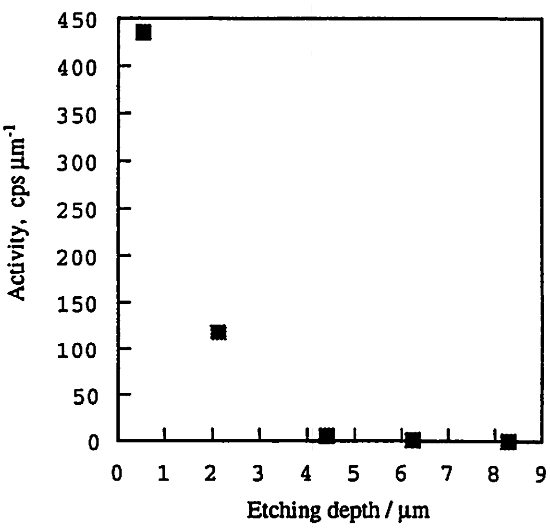

Fig. 2. Depth profile of ^{18}F activity in a copper disk

III. BIOLOGY AND MEDICINE (Basic)

III. 1. Effects of Haloperidol and Cocaine on Pharmacokinetics of [^{11}C]Methamphetamine in Methamphetamine Sensitized Dog

Mizugaki M., Nakamura H., Hishinuma T., Tomioka Y., Ishiwata S.,
Ido T., Iwata R.*, Funaki Y.*, Itoh M.*, Fujiwara T.**
*Sato M.**, Numachi Y.** and Yoshida S.***

Department of Pharmaceutical Sciences, Tohoku University Hospital
*Cyclotron and Radioisotope Center, Tohoku University**
*Department of Psychiatry, Tohoku University School of Medicine***

Introduction

The subchronic administration of methamphetamine (MAP) or amphetamine (AMP) to experimental animals produces progressive and enduring augmentation of hyper locomotion and stereotyped behavior[1,2]. The precise neurochemical mechanism underlying this phenomenon, referred to as behavioral sensitization or reverse tolerance, is not completely understood. Although various mechanisms have been proposed to explain the expression of MAP or AMP-induced behavioral sensitization, little attention has been paid to the pharmacokinetic change. We have previously studied the pharmacokinetic change of MAP in the brain following repeated MAP administration and reported the significant increase in [^{11}C]MAP uptake in the MAP-sensitized mouse brain[3] and [^{14}C]MAP uptake in the MAP-sensitized rat brain[4]. In addition, we reported that the maximum accumulation level of [^{11}C]MAP in the MAP-sensitized dog brain was 1.4 times higher than that in the control[5]. These observations raise the possibility that increased brain MAP levels mediate the development of MAP-induced behavioral sensitization.

In the present study, to investigate the relation between the MAP-induced behavioral sensitization and the pharmacokinetics of MAP, we examined the pretreatment effects of haloperidol and cocaine on brain distribution of [^{11}C]MAP in MAP sensitized dog.

Materials and Methods

SYNTHESIS OF [^{11}C]MAP

The synthesis of [^{11}C]MAP was carried out by modifying the on-line [^{11}C]methylation method[6] as previously report[5]. The mass spectra, HPLC and TLC of this material were identical to authentic material. The specific activity was about 48.1 GBq/μmol at the time of supply. The radiochemical purity of [^{11}C]MAP was determined to be more than 99 %.

POSITRON EMISSION TOMOGRAPHY (PET) STUDY IN A DOG

The MAP-sensitized dog, used in our previous study$^{5)}$, was initially anesthetized with ketamine (10 mg/kg, s.c.) and maintained under pentobarbital (25 mg/kg, i.v.) anesthesia. Catheters were inserted into the arterial vein for arterial blood sampling and into the venous vein of the foreleg for administration of [^{11}C]MAP. Vital signs (blood pressure, pulse rate, blood pH, pO2, pCO2 and body temperature), monitored and recorded throughout the PET study, were kept within a physiological range. In the haloperidol pretreatment study, haloperidol (1 mg/kg) was intramuscularly administrated at 60 min before injection of [^{11}C]MAP. In the cocaine pretreatment study, cocaine hydrochloride (5 mg/kg) was intravenously administrated three times at 15 min before and 15 and 45 min after injection of [^{11}C]MAP. After an intravenous injection of [^{11}C]MAP (248-418 MBq) into the animal, dynamic scan was carried out parallel to the orbitomeatal (OM) line using PET scanner (PT931, CIT Inc, Noxvile USA at the Cyclotron and Radioisotope Center, Tohoku University, Sendai, Japan) for 90 min. The following regions of interest were selected according to our previous report$^{7)}$: parietal cortex, occipital cortex, temporal cortex, frontal cortex and cerebellum. Tissue concentration of [^{11}C]MAP was measured using a ROI program.

DOG PLASMA METABOLITE ANALYSIS

Arterial blood samples were collected in heparinized tubes at 5, 10, 20, 40 and 50 min after the injection of [^{11}C]MAP and centrifuged (3000 rpm x 3 min). Plasma samples (0.5 ml) were added to 1 ml of methanol, and the mixture was sonicated and centrifuged (15,000 rpm x 45 sec). The supernatant with the addition of unlabeled MAP was injected into the analytical HPLC system. The [^{11}C]MAP fraction were collected and counted by an automated NaI counter. The percentage of [^{11}C]MAP activity in plasma activity was calculated.

QUANTITATION OF HALOPERIDOL AND COCAINE IN DOG PLASMA

Plasma concentration of haloperidol was determined using a MARKIT-M® Haloperidol Kit (Dainippon Pharmaceutical Co. Ltd, Osaka, Japan).

Plasma concentration of cocaine was determined by modifying the solid-phase extraction and the GC/MS quantitation method previously described by Abuseda *et al.*$^{8)}$.

Results

PET STUDY IN A DOG

Fig. 1 shows the effects of haloperidol and cocaine pretreatment on the time course of regional distribution of [^{11}C]MAP in a sensitized dog. [^{11}C]MAP showed a widespread distribution throughout the brain. Under the sensitized condition, the maximal level of accumulation of [^{11}C]MAP was 1.4 times higher than that in the control (Fig. 1A). This phenomenon is prevented by pretreatment of haloperidol (Fig. 1B) and cocaine (Fig. 1C). We found very little difference of the regional distribution of [^{11}C]MAP between the three PET studies, but [^{11}C]MAP clearance from the brain in the two pretreatment studies was a little slower than that in the non-pretreatment study.

DOG PLASMA METABOLITE ANALYSIS

The results of metabolite analysis in the three PET studies are depicted in Fig. 2. At 50 min after the injection, only 20% of MAP was in the unmetabolic form. In the comparison of each PET study, slight but not significant differences were found in metabolism of MAP.

PLASMA CONCENTRATION OF HALOPERIDOL AND COCAINE

The haloperidol plasma level profile during the haloperidol pretreatment PET study is shown in Fig 3A. Blood clearance of haloperidol was linear during the PET study, ranging from 60 to 150 min after the intramuscular administration, and the biological half-life was approximately 180 min. The haloperidol plasma concentration during PET study ranged from 37 to 50 ng/ml.

The cocaine plasma level profile during the cocaine pretreatment PET study is shown in Fig. 3B. Although the blood clearance of cocaine was rapid, the minimal cocaine plasma level remained at 400 ng/ml.

Discussion

In order to investigate the pharmacokinetic change of [^{11}C]MAP in MAP sensitized animals using PET, we created a MAP sensitized dog by repeated MAP administration$^{5)}$. In the present PET study using this sensitized dog model, we performed a challenge test applying MAP 7 days before each PET study. The challenge injection of MAP (1 mg/kg) after a 90 days withdrawal period reproduced the hyperlocomotion and stereotyped behavior. This result suggests that the MAP induced behavioral sensitization may last for a long period of abstinence after subchronic MAP administration.

We measured plasma concentration of haloperidol and cocaine to evaluate their pretreatment effects during the PET study. As reviewed by Dahl$^{9)}$, therapeutic plasma haloperidol concentrations in the range of 5-20 ng/ml have been reported by some investigators, but others have found no such relationship. A generally valid therapeutic plasma concentration range for haloperidol has not yet been defined. However, we considered that the haloperidol plasma level in this study was sufficient for antidopaminergic activity in the brain. In a pharmacokinetic study of cocaine in humans$^{10)}$, the terminal plasma half-life after intravenous administration of cocaine was relatively short ranging from 31 to 63 min. Since we also found that the clearance of cocaine from the brain was rapid$^{11)}$, cocaine was injected three times at 30 min intervals. In this PET study, cocaine plasma concentrations declined exponentially after intravenous injection, but the minimal cocaine plasma level was 400 ng/ml, which was also sufficient to induce a pharmacological effect.

One factor that changes the pharmacokinetics of MAP is the alteration in the metabolism of MAP. Metabolite analysis revealed that the pretreatment of haloperidol and cocaine do not influence the rate of MAP metabolism. This result leads to the conclusion that the pharmacokinetic changes were not due to the changes in the rate of MAP metabolism.

In behavioral studies, dopamine antagonists prevent the development of behavioral sensitization induced by repeated MAP administration12). This evidence indicates that stimulation of dopamine receptor by MAP-released dopamine may be necessary for the induction of behavioral sensitization. The present study demonstrated that pretreatment of haloperidol prevents the elevation of brain MAP levels following repeated MAP administration. This observation raises the possibility that dopamine antagonists also influence the pharmacokinetics of MAP and prevent the development of behavioral sensitization.

MAP increases synaptic dopamine primarily by stimulating presynaptic release rather than by blocking the dopamine reuptake, as is the case with cocaine. The molecular mechanism of dopamine efflux of MAP has been attributed to an exchange-diffusion process via the dopamine transporter13). Since cocaine binds to dopamine transporter and inhibits the uptake processes for MAP, the result of cocaine pretreatment study apparently suggests that repeated MAP administration causes an increased MAP uptake into the dopaminergic nerve terminal via dopamine transporter. However, cocaine prevented the enhancement of the MAP level in the whole brain, indicating the mechanism of this phenomenon occurs the blood and brain compartments. Although we can not explain this mechanism, it is interesting that cocaine produced a cross-behavioral sensitization with MAP and affected the pharmacokinetics of MAP in MAP-sensitized animal.

While it is unlikely that the elevation of MAP level at the dopamine nerve terminal alone can account for behavioral sensitization, it is possible that the enhanced MAP level may affect its development or expression. Further studies on the pharmacokinetic change of MAP in MAP sensitized animals are presently in progress using rhesus monkeys.

Acknowledgment

We are grateful to the PET staffs of the Cyclotron and Radioisotope Center, Tohoku University, for their cooperation. A part of this research was supported by a scientific research fund from the Ministry of welfare of the Japanese Government.

References

1) Seagal D. S. and Mandell A. J., Pharmacol. Biochem. Behav. **2** (1974) 249.
2) Nishikawa T. et al., Eur. J. Pharmacol. **88** (1983) 190.
3) Mizugaki M. et al., Nucl. Med. Biol. **20** (1993) 487.
4) Numachi Y. et al., Ann. N. Y. Acad. Sci. **654** (1992) 153.
5) Mizugaki M. et al., Nucl. Med. Biol. **22** (1995) 803.
6) Iwata R. et al., Appl. Radiat. Isot. **43** (1992) 1083.
7) Hatazawa J. et al., J. Nucl. Med. **32** (1991) 713.
8) Abusada G. M. et al., J. Anal. Toxicol. **17** (1993) 353.
9) Dahl S. D., Clin. Pharmacokinet. **11** (1986) 36.
10) Chow M. J. et al., Clin. Pharmacol. Ther. **38** (1985) 318.
11) Mizugaki M. et al., Nucl. Med. Biol. **21** (1994) 793.
12) Ujike H. et al., Psychopharmacology **98** (1989) 89.
13) Fischer J. F. and Cho A. K., J. Pharmacol. Exp. Ther. **208** (1979) 203.

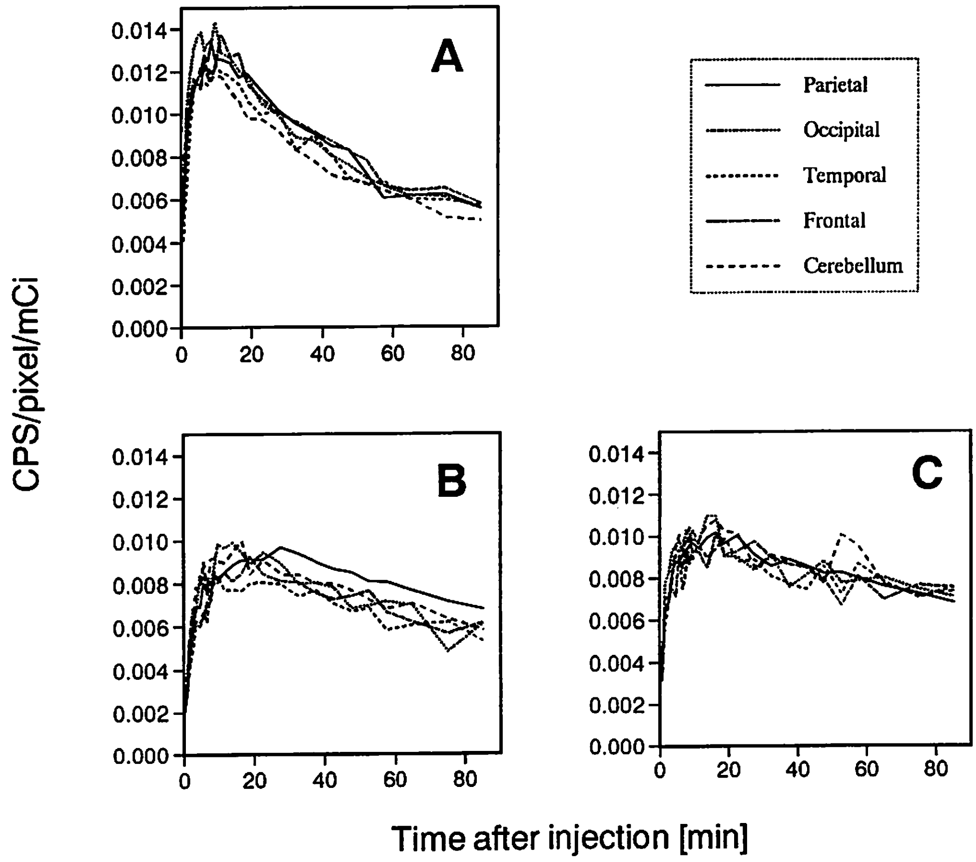

Fig. 1 Time courses of regional distribution of [^{11}C]methamphetamine in a sensitized dog brain. (A) non pretreatment (B) haloperidol pretreatment (C) cocaine pretreatment.

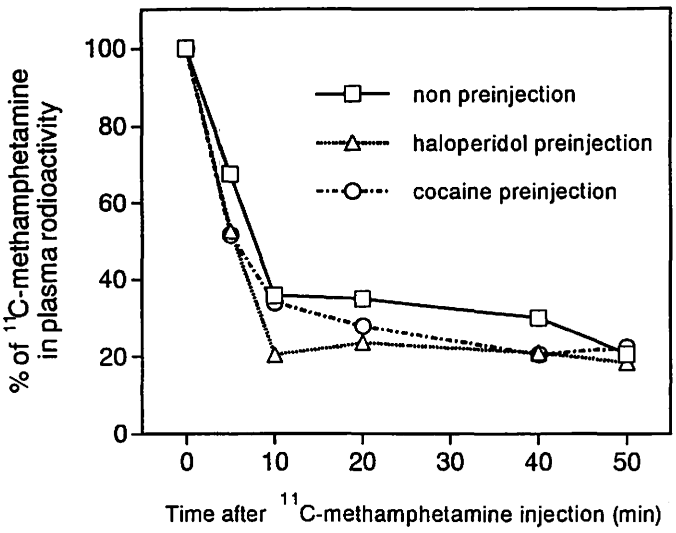

Fig. 2 HPLC analysis of ^{11}C activity in MAP-sensitized dog plasma. The percent of [^{11}C]MAP activity in plasma activity is indicated.

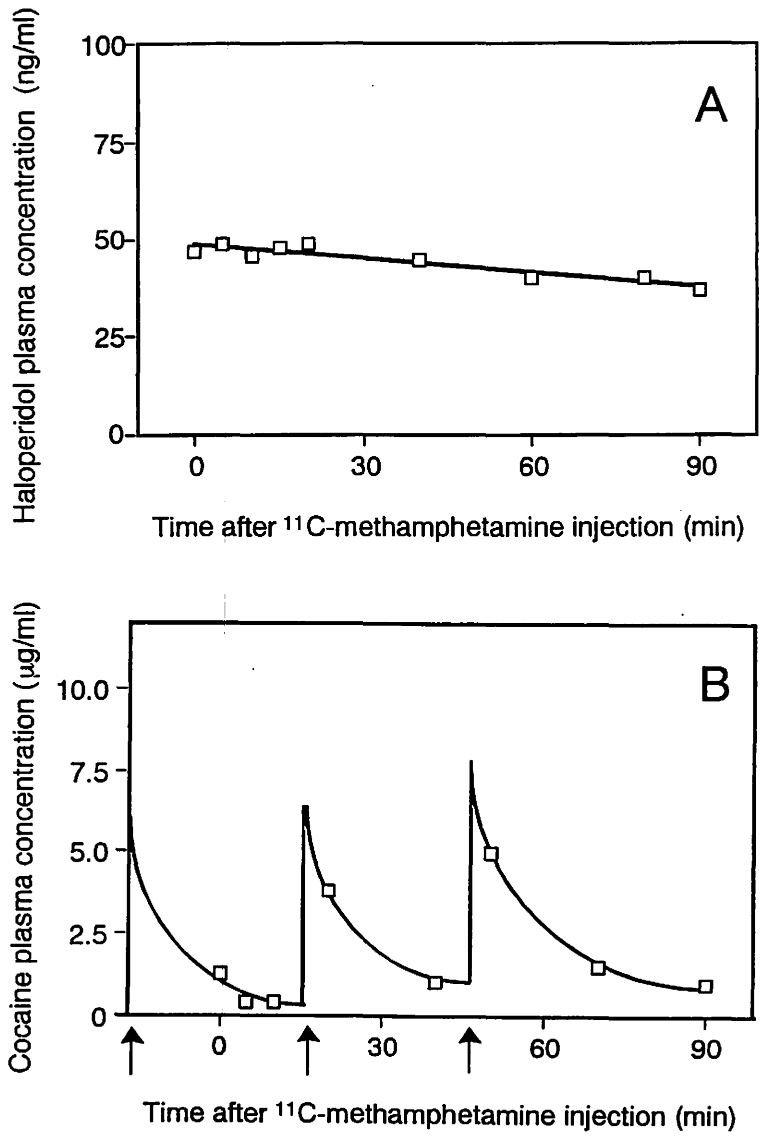

Fig. 3 Plasma concentration of haloperidol (A) and cocaine (B) in MAP-sensitized dog.

III. 2. Present Status of the [^{18}F]FDG Production at CYRIC

Iwata R., Ishikawa Y., Funaki Y., Naitoh Y. and Ido T.

CYRIC Tohoku University

At CYRIC 2-deoxy-2-[^{18}F]fluoro-D-glucose ([^{18}F]FDG) was prepared for clinical PET studies for the first time in 1983 after a fully automated synthesis system based on the original method$^{1)}$ had been developed$^{2)}$. Approximately 120 preparations were made for 3 years with the average yield of 16 mCi and then the synthesis system was replaced with a new automated synthesis system based on the improved method utilizing [^{18}F]acetyl hypofluorite$^{3)}$ in 1985. This second automated system was used until quite recently at CYRIC although a novel excellent synthesis method by the nucleophilic fluorination with no-carrier-added [^{18}F]fluoride was developed in 1986$^{4)}$. In total, nearly 330 preparations were made with the average shipped yield of 33 mCi for 9 years.

We developed a new automated system for the preparation of no-carrier-added [^{18}F]FDG$^{5)}$. The third synthesis system was, however, used only to supply the labeled compound for basic animal studies, while we modified the system to simplify the procedure for future routine use. A new 3D PET (Shimadzu SET 2400W) was installed at CYRIC in 1994 and began to be available for clinical use early in 1995. The demand for [^{18}F]FDG was thus increased and this situation led us to decide to introduce the third system for routine production of [^{18}F]FDG.

The present report describes the development of the automated system for the preparation of no-carrier-added [^{18}F]FDG together with the improvement made on the target system for the [^{18}F]fluoride production with ^{18}O-enriched water.

[^{18}F]Fluoride production

A static target was substituted for the circulating target used for a long time at CYRIC$^{6)}$ to reduce the volume of expensive ^{18}O-enriched water (50 atom%) to a minimum and to increase the specific activity of [^{18}F]fluoride. As shown in Fig. 1, 1.5 mL of the target water was remotely loaded into the irradiation chamber (the body: Ag, the beam window: 30 mm Ti, the net volume: *ca.* 1.2 mL) via two pneumatic 6-way valves (Valco) using an HPLC pump and an overflow was recovered in a reservoir. The irradiation was carried out using a 18 MeV proton beam at a beam current of 10 mA for 90 min. The target pressure was always monitored with a small pressure sensor and displayed on a computer CRT (see Fig. 2). After the irradiation the target water was transferred to the automated system with a H_2 flow at 30 mL/min. The chamber and the transfer line (i.d 0.8 mm and 20 m long polyethylene tube) was washed with another 1 mL of the enriched water. The combined water was passed through an anion exchange membrane filter (Bio-Rad) to conveniently recover the target water[7) and the [^{18}F]fluoride retained by the membrane was then eluted with a carbonate solution for subsequent use in the [^{18}F]FDG synthesis.

A new window cooling system with a circulating cold He flow was introduced to efficiently cool the beam window during the beam irradiation, in addition to a water cooling at the back side of the target. Figure 2 illustrates two typical pressure profiles during the irradiation at 10 mA. A sudden drop in the target pressure indicates that the increase in the pressure is mainly due to vaporization of the water and a remaining pressure can be ascribed to gaseous products radiolytically produced. When the Ti window was replaced with a 25 mm Havar foil to enhance the window strength, a gradual increase in the pressure was observed and it stayed at the same level when the irradiation was interrupted. This attempt was abandoned. The pressure increase changed day by day and it seemed to be affected by surface conditions of the beam window apart from cooling conditions.

The average production yield of [^{18}F]fluoride was 350 mCi/10 mAhr and the specific activity of the [^{18}F]fluoride was determined to be about 4 Ci/mmol by ion chromatography with a Dionex QIC Analyzer quipped with an Ion Pac A S4A-SC 4 mm column.

Automated [^{18}F]FDG synthesis

The prototype automated system of NKK Corp., based on our third automated system, was installed[8) and modified. As illustrated in Fig. 3, the system has a specially designed flask, attached to a small rotary evaporator and working as both reaction vessel and evaporation flask. Tetrabutylammonium bicarbonate (TBAHCO$_3$) instead of commonly used Kryptofix 222 was adopted as phase transfer catalyst for a simple one-pot synthesis[9). The whole synthetic procedure is as follows:

1. One mL of water containing 50 mmol TBAHCO$_3$ was passed through the membrane to elute the [^{18}F]fluoride into the flask.
2. One mL of acetonitrile (MeCN) was added to the flask and the mixture was dried by azeotropic evaporation under reduced pressure. This step was repeated for complete dryness.
3. Twenty five mg of 1,3,4,6-Tetra-*O*-acetyl-2-*O*-triluoromethanesulfonyl-b-D-mannopyranose (Aldrich) dissolved in 1 mL anhydrous MeCN was added to the residue and the mixture was heated at 80∞∞C for 5 min.
4. The solvent was evaporated and 1 mL of 1.2 M HCl was added. The hydrolysis was carried out at 100∞∞C for 10 min.

5. The hydrolysis mixture was passed through a short cation exchange resin column (Alltech), an AG11A8 ion retarding resin column (Bio-Rad), a Sep-Pak C18 cartridge (Waters) and a Sep-Pak alumina N cartridge (Waters) and then collected in a large evaporating flask. The reaction flask and columns were washed with 5 mL of water and the washing was combined to the first eluate.
6. The aqueous solution containing purified [^{18}F]FDG was evaporated to dryness and 8 mL of saline was added to dissolve the residue and then passed through a 0.22 mm membrane filter into a sterile vial.

The above procedure, including the target irradiation and recovery, was totally automated with a personal computer (NEC 9801). The use of TBAHCO$_3$ allowed us to simplify the automated synthesis procedure to a great extent, compared with the previous method using Kryptofix 222.

The preparation of [^{18}F]FDG was thus completed within 90 min after the irradiation. The average yield of [^{18}F]FDG starting from the [^{18}F]fluoride (*ca.* 500 mCi at EOB) was 200 mCi at EOS. The radiochemical purity of [^{18}F]FDG determined by radio-HPLC on Carbohydrate (Waters) was always over 99% and TBAHCO$_3$ was not detected in the final solution by the extraction-spectrophotometric method$^{10)}$ (detection limit: 0.02 mmol). The low reproducibility of the [^{18}F]FDG yield in the previous preparations, probably due to the low specific activity of the [^{18}F]fluoride produced with the circulating target, was overcome in the present method as the specific activity was greatly improved up to over 4 Ci/mmol at EOB$^{11)}$.

Recently much attention has been paid to basic hydrolysis owing to its short, high-yield procedure at room temperature in contrast to acid hydrolysis$^{12)}$. Another advantage of this basic hydrolysis is that the formation of 2-deoxy-2-chloro-D-glucose is avoided$^{13)}$. From this viewpoint, hydrolysis with cation exchange resin is also an attractive alternative$^{14)}$. This hydrolysis method has the possibility of exploiting a new method for a total on-column preparation of [^{18}F]FDG$^{15)}$. All these things will be achieved in our next system in near future.

References

1) Ido T., Wan C.-N., Casella V., Fowler J. S. and Wolf A. P.. J. Labeld. Compd. Radiopharm. **14** (1978) 175.
2) Iwata R., Ido T., Takahashi T. and Monma M., Int. J. Appl. Radiat. Isot. **35** (1984) 445.
3) Shiue C.-Y., Salvadori P. A., Wolf A. P., Fowler J. S. and MacGregor R. R., J. Nucl. Med. **23** (1982) 899.
4) Hamacher K., Coenen H. H. and Stöcklin G., J. Nucl. Med. **27** (1986) 235.
5) Yamazaki S., Iwata R. and Ido T., CYRIC Annual Reports (1989) 158.
6) Iwata R., Ido T., Brady F., Takahashi T. and Ujiie A., Appl. Radiat. Isot. **37** (1987) 979.
7) Iwata R. and Ido T., CYRIC Annual Report (1992) 111.

8) Iwata R., Takahashi T., Yanai K., Ishikawa Y., Naitoh Y. and Ido T., CYRIC Annual Report (1992) 98.
9) Culbert P. A., Adam M. J., Hurtado E. T., Huser M .A., Jivan S., Lu. J., Ruth T. J. and Zeisler S. K., Appl. Radiat. Isot. **46** (1995) 887.
10) Inoue S. and Sasaki M., Memoirs of Kitami Instit. Tech. **12** (1981) 221.
11) Chirakal R., McCarry B., Lonergan M., Firnau G. and Garnett S., Appl. Radiat. Isot. **46** (1995) 149.
12) Füchtner F., Steinbach J., Mäding P. and Johannsen B., Appl. Radiat. Isot. **47** (1996) 61.
13) Alexoff D. L., Casati R., Fowler J. S., Wolf A. P., Shea C., Schlyer D. J. and Shiue C.-Y., Appl. Radiat. Isot. **43** (1992) 1313.
14) Mulholland G.K., Nucl. Med. Biol. **22** (1995) 19.
15) Toorongian S. A., Mulholland G. K., Jewett D. M., Bachelor M. A. and Kilbourn M. R., Nucl. Med. Biol. **17** (1990) 273.

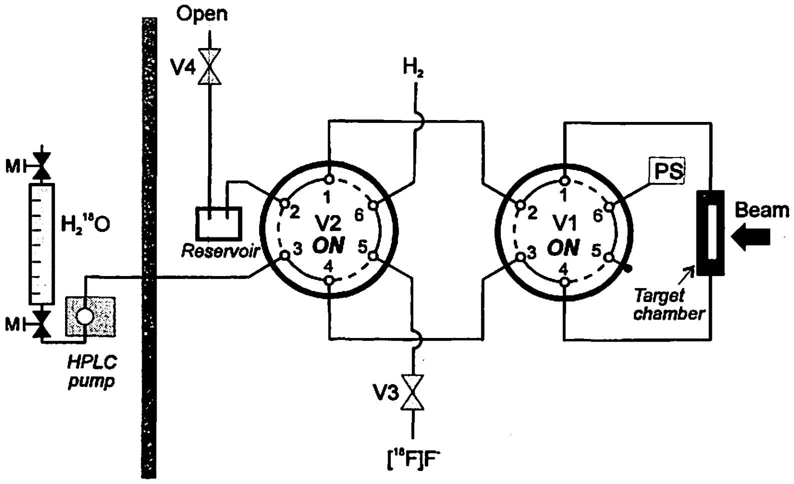

Fig. 1. The static target system for the [^{18}F]fluoride production.

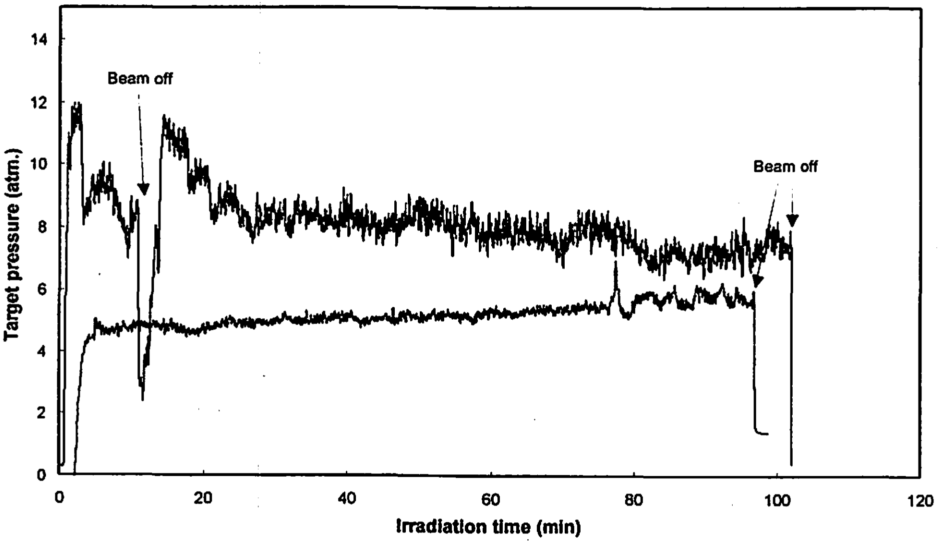

Fig. 2. Target pressure profile.

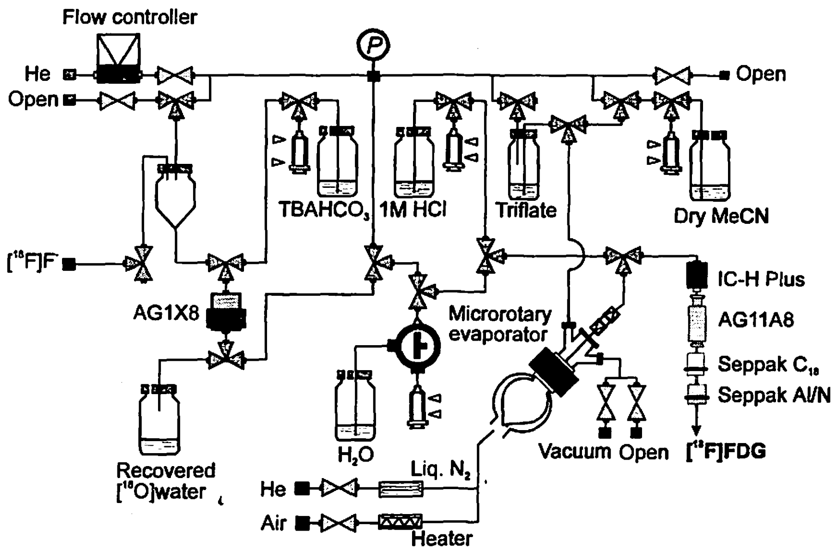

Fig. 3. The automated [^{18}F]FDG synthesis system.

III. 3. [^{18}F]Labeling of Pyruvic Acid

*Takahashi T. *, Ido T. and Iwata R.*

Cyclotron and Radioisotope Center, Tohoku University
*Radioisotope Center, Niigata University **

Introduction

In previous papers[1-4], Bjurling *et al.* showed the usefulness of [^{11}C]labeled pyruvic acid as a synthon for the synthesis of [^{11}C]labeled amino acids such as L-tryptophan, 5-hydroxy-L-tryptophan, L-tyrosine and L-DOPA using a multi-enzymatic reaction. However, for a longer and closer measurement study by PET, the radiopharmaceuticals labeled with a longer half-life positron emitter such as ^{18}F ($t_{1/2}$ = 109.8 min) seem to be more suitable. We have proposed the [^{18}F]labeling of those amino acids by a similar enzymatic synthesis to that Bjurling demonstrated. For this proposal, an efficient synthesis of [^{18}F]fluoropyruvic acid is needed. In this paper, we report an easy and convenient synthesis of 3-[^{18}F]fluoropyruvic acid.

Materials and Methods

GENERAL

^{1}H-NMR spectra were recorded on a JNM-FX 100 spectrometer with TMS as the internal standard and i.r. spectra on a Jasco A-202 i.r. spectrometer.

CHROMATOGRAPHY

Column chromatography was carried out on silica-gel (Wakogel C-200 (Wako Pure Chem. Ind. Ltd.)) using the solvent indicated below. Analytical HPLC was performed using an ion exchange column (Radialpak SCX (Watman), 10 μ m, 8 mm i.d. × 10 cm long) with potassium citrate buffer (potassium dihydrogen citrate (6.91 g) and citric acid (14.71 g) dissolved in water (final volume 500 mℓ)) as the solvent (flow rate : 1 mℓ / min).

SYNTHESIS OF STARTING MATERIALS

3-Bromopyruvic acid and thionyl chloride were purchased from Wako Pure Chem. Ind. Ltd.

Methyl 3-bromopyruvate : Methyl 3-bromopyruvate was prepared by a method similar to that described in the literature[5]. To a solution of 3-bromopyruvic acid (1.0 g, 6 mmol) dissolved in abs. MeOH (70 mL), thionyl chloride (10 mL) was added dropwise at 0°C. The mixture was stirred at 0°C for 15 min and then refluxed for 1hr. After removal of the solvent, the residue was purified by column chromatography (CH_2Cl_2) to give methyl 3-bromopyruvate (791 mg). Yield : 73% (from 3-bromopyruvic acid). pale yellow oil. i. r. ($CHCl_3$) : 1730 cm^{-1} (CO-OMe). ^1H-NMR ($CDCl_3$) :δ 3.83 (3H, s, -COOCH$_3$), 3.90 (2H, s, Br-CH$_2$-CO-).

^{18}F-LABELING

Kryptofix 2,2,2 was purchased from Merck, dehydrated acetonitrile (for nucleic acid synthesis) used for [^{18}F]labeling was from Dojin Chem. Lab. Ltd. and 3-fluoropyruvic acid sodium salt was from Aldrich Chem. Co. Inc.,

Production of [^{18}F]fluoride : [^{18}F]Fluoride was produced *via* the $^{18}O(p,n)$ ^{18}F reaction by proton bombardment (18 MeV, 10 μ A) of a circulating 50% enriched [^{18}O]water target using the CGR-MeV model 680 Cyclotron located at Tohoku University$^{6)}$.

Synthesis of 3-[^{18}F]fluoropyruvic acid : The labeling procedure is shown in Fig. 1. The substitution reaction was carried out according to a literature procedure$^{7)}$. To the [^{18}F]water (150 μL), 0.15 M K_2CO_3 aq. sol. (50 μL) and a solution of Kryptofix 2,2,2 (K 2,2,2) (6.3 mg, 17 μmol) dissolved in acetonitrile (250 μL) were added. While purging with flowing N_2, the solvent was completely evaporated to dryness at 100°C. To the residue, a solution of methyl 3-bromopyruvate (2 mg, 11 μmol) dissolved in acetonitrile (1 mL) was added and then the mixture was refluxed for 5 min at 100°C. Subsequently 0.5 N methanolic KOH (1 mL) was added and the solution was refluxed again for a further 10 min at the same temperature. 2N HCl (1 mL) was added and the solvent was evaporated *in vacuo.*

Quality control : The radiochemical purities of the final products were determined by analytical HPLC and the chemical purities on UV detector (220 nm). The retention time of 3-fluoropyruvic acid sodium salt was 4.2 min.

Results and Discussion

Methyl 3-bromopyruvate was used as a starting material for this [^{18}F]fluorination according to the synthesis of ω -[^{18}F]fluorofatty acids$^{5)}$. This starting material is somewhat less stable and seems to decompose slowly on standing at room temperature.

The decay-corrected radiochemical yields of 3-[^{18}F]fluoropyruvic acid were 38-56% and the time required for the synthesis was 55-65 min from the start of reactive [^{18}F]F$^-$ ([K 2,2,2]$^+$ ^{18}F$^-$) production. The radiochromatogram of the final product is shown in Fig. 2. The radiochemical purities were > 97% and the obtained 3-[^{18}F]fluoropyruvic acid will be used for the following enzymatic synthesis without further purification.

Now, we have studied the next enzymatic synthesis step using 3-fluoropyruvic acid sodium salt in cold runs and the further synthesis of chemically pure 3-[^{18}F]fluoropyruvic acid from methyl 3-O-tosylpyruvate (synthesis : see ref. 8) for preventing enzyme inactivation with residual bromopyruvic acid in [^{18}F]fluorination.

References

1) Bjurling P., Watanabe Y. and Långström B., Appl. Radiat. Isot., **39** (1988) 627.
2) Bjurling P., Watanabe Y., Tokushige M. et al., J. Chem. Soc. Perkin Trans. 1., (1989) 1331.
3) Bjurling P., Antoni G., Watanabe Y. et al., Acta chem. Scand., **44** (1990) 178.
4) Bjurling P., Watanabe Y., Oka S. et al., Acta chem. Scand., **44** (1990) 183.
5) Takahashi T., Ido T. and Iwata R., Appl. Radiat. Isot., **42** (1991) 801.
6) Iwata R., Ido T., Brady F. et al., Appl. Radiat. Isot., **38** (1987) 979.
7) Coenen H. H., Klatte B., Knöchel A. et al., J. Labelled Compd. Radiopharm., **23** (1986) 455.
8) Takahashi T., Ido T., Mukoyoshi M. et al., CYRIC Annual Report (1994) 115.

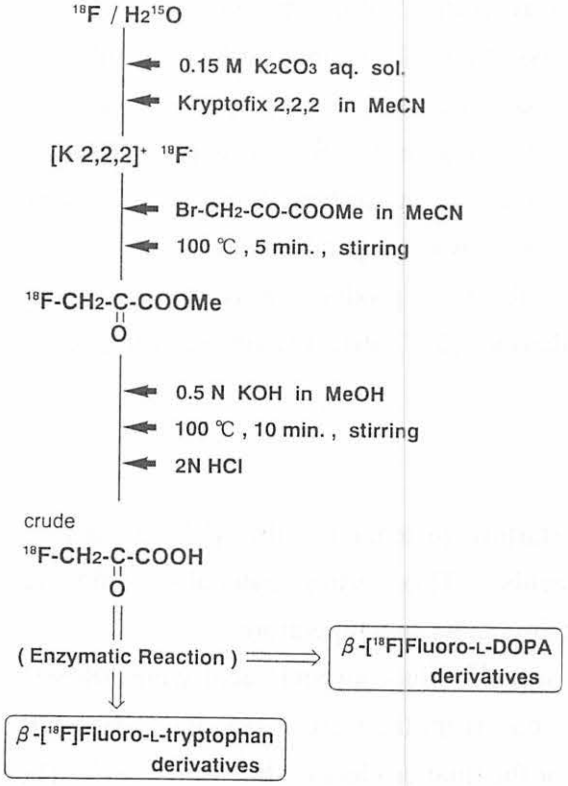

Fig. 1. Labeling Procedure.

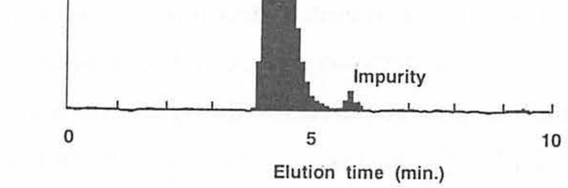

Fig. 2. HPLC Radiochromatogram of 3-[^{18}F]Fluoropyruvic Acid.

III. 4. In Vivo Distribution of ^{18}F-fluoromisonidazole

Kubota K., Tada M., Susumu Y., Iwata R.**, Sato K.,*
*Fukuda H., and Ido T **.*

Department of Nuclear Medicine and Radiology,
Institute of Development Aging and Cancer, Tohoku University.
*Department of Pharmacological Chemistry, Institute of Development Aging and Cancer, Tohoku University**
*Radioisotope laboratory, Cyclotron Radioisotope Center, Tohoku University***

Introduction

Misonidazole and its congeners are metabolically trapped in cells that are alive but at low oxygen tension, and are known as radiosensitizers of cancer radiotherapy, also known as markers of ischemic cells[1]. Fluorine-18-labeled fluoromisonidazole ([^{18}F]FMISO) has been developed and studied for in vivo imaging of hypoxic tissue of tumor that is important as radiotherapy-resistant component, and for imaging of ischemic myocardium using positron emission tomography (PET)[2,3]. Preliminary PET imaging study has visualized various types of tumors[2], however definition of hypoxic tissue nor possible role of [^{18}F]FMISO in oncology diagnosis have not yet been evaluated in detail. We have started a project for re-evaluation of [^{18}F]FMISO using in vivo tumor model and here we report the initial result of tissue distribution study of [^{18}F]FMISO.

Materials and Methods

A new one-pot synthesis of [^{18}F]FMISO using v-vial will be reported separately[4]. Radiochemical yield was 20%, with radiochemical purity over 98% and total synthesis time was about 80 min. Seven-week old male Donryu rats were transplanted with 0.1 mℓ suspension of 10^7 AH109A hepatoma cells injected subcutaneously in the thigh region. Tracer experiments were performed 8 days after tumor transplantation following 8hr of fasting. Thirty rats bearing AH109A tumor were injected intravenously into the lateral tail vein with a 1.85MBq (50 m Ci) of [^{18}F]FMISO and killed 5 (n=3), 30 (n=3), 60 (n=6), 120 (n=6), 180 (n=6), 240 (n=6) min later. Tissue samples were excised and weighed, and ^{18}F radioactivity was measured using an automated gamma-scintillation counter. Tissue radioactivity was expressed as the differential uptake ratio.

$$\mathrm{DUR} = \frac{\text{Tissue radioactivity / Tissue weight}}{\text{Injected radioactivity / Animal weight}}$$

Result and Discussion

Time course tissue distribution of [^{18}F]FMISO in rats showed the highest uptake by liver followed by kidney. Blood, lung, heart, muscle, and brain are the third group of uptake level. All normal tissues showed slow exponential clearance patterns after initial accumulation with the $T_{1/2}$ about 2hr. Tumor uptake was the second and reached a plateau at 30 min, remained constant up to 2hr, and decreased. Tumors to blood or muscle uptake ratios were about 2 and stable from 2 to 4 hr after injection. It suggested that positive tumor imaging is feasible in various parts of the body except in liver and kidney. The uptake patterns suggested some metabolic interaction of [^{18}F]FMISO with tumor but not with any normal tissue. Our data is consistent with previous report of the metabolic stability of [^{18}F]FMISO in vivo. AH109A tumor is a radiosensitive tumor$^{5)}$, and the tumor size at the experiment is about 1cm in diameter. It seems to be consisted of mostly viable cancer cells with few necrotic portions. In another word, tumor may not be hypoxic. Tumor trapping mechanism and its correlation of hypoxia seems to be not so simple and further evaluation will be performed.

References

1) Rasey. J. S. et al., Rad. Res. **111** (1987) 292.
2) Koh. W. J. et al., Int. J. Rad. Oncol. Bio. Phys. **22** (1991) 199.
3) Martin. G. V. et al., J. Nucl. Med. **33** (1992) 2202.
4) Tada M. et al., J. Labelled Compds. Radiopharm. **36** (1996) in press.
5) Kubota K. et al., J. Nucl. Med. **30** (1989) 2012.

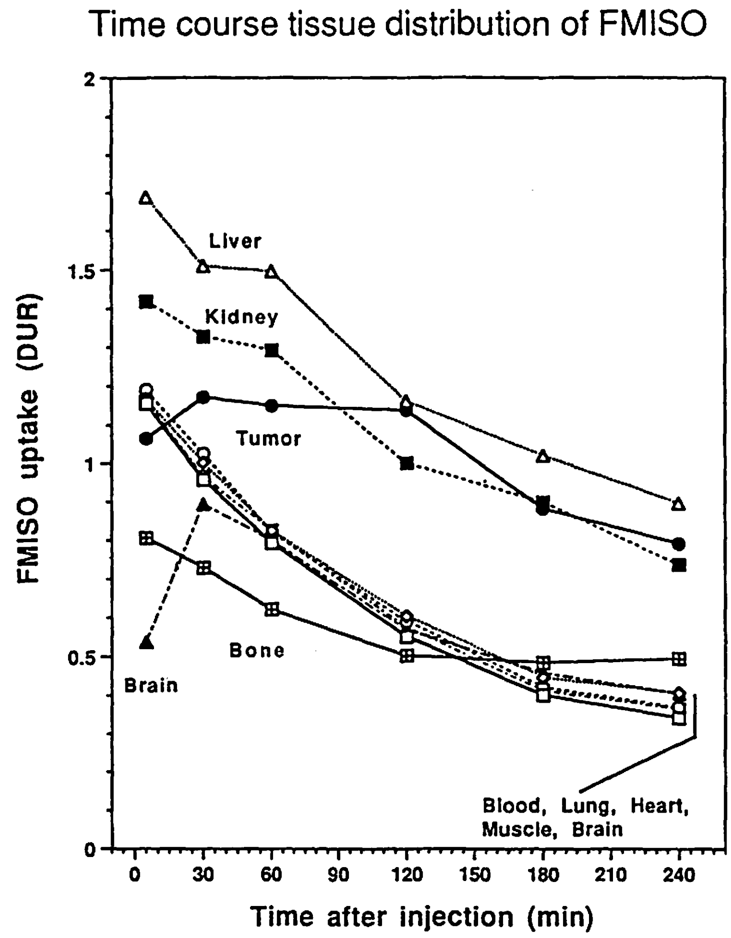

Fig. 1. Results of time course tissue distribution study of [^{18}F]FMISO in rats with AH109A tumor. All normal tissues showed slow exponential excretion patterns after initial distribution. Only tumor showed significant retention of the tracer.

III. 5. Effect of Granulocyte-Colony Stimulating Factor on ^{18}F-FDG Uptake in Experimental Inflammatory Tissue

Yamada S., Kubota K., Kubota R., Tamahashi N., and Ido T.***

Department of Nuclear Medicine and Radiology,
Institute of Development, Aging and Cancer, Tohoku University
*Clustercore Institute of Biology**
*Cyclotron and Radioisotope Center, Tohoku University***

Introduction

In previous report, we demonstrated that ^{18}F-FDG in inflammatory tissue increased progressively to a peak on day 4 after inoculation of turpentine oil and then decreased[1-2)]. Macro- and micro-autoradiography showed a high density of silver grains in the abscess wall consisting of an inflammatory cell layer and granulation tissue[2)]. In this study, we examined the effect of granulocyte colony stimulating factor (G-CSF) on ^{18}F-FDG uptake in inflammatory tissue by tissue distribution study.

Materials and Methods

Male Donryu rats weighing about 100 g were used. To induce inflammation, animals were inoculated with 0.2 ml of turpentine oil subcutaneously in the left groin. Six rats were subcutaneously injected with 5 μg/0.2 ml of G-CSF and other 6 rats as control group with 0.2 ml of saline every 12 hours from day 1 to day 3 after inoculation of turpentine oil, respectively. On day 4, each rat was injected with 740 kBq (20 μCi) of ^{18}F-FDG through the tail vein. They were analyzed 1 hour later. The inflammatory tissue sample, including inoculated turpentine-oil, was excised and trimmed off the neighboring subcutaneous tissue. The heart, liver, spleen, muscle and bone tissues were excised and the blood collected from the heart as samples. Each sample was weighed and the ^{18}F radioactivity was counted with a well-type NAI(TI) autogamma counter and corrected for decay. Data were expressed as the differential uptake ratio (DUR). Simultaneously, blood cell counts in blood samples were measured.

Results and Discussion

Table 1 summarizes results of ^{18}F-FDDG uptakes in various tissues of rats in two groups (G-CSF and Control). Mean differential uptake ratios (DUR's) in spleen, bone and inflammation in G-CSF group were significantly higher than those in Control group. There were no significant changes in DUR's of blood, heart, liver and muscle. Table 2 shows the blood cell count. White blood cell counts including lymphocyte and neutrophil in G-CSF group were significantly higher than those in Control group. There were no significant differences in red blood cell and platelet.

G-CSF is a cytokine which acts directly on neutrophil-restricted progenitor cells, stimulating their proliferation3), enhances neutrophil activation4) and is relevant to wound healing5). In G-CSF group of this study, white blood cell count in blood, ^{18}F-FDG uptakes in spleen, bone and inflammatory tissue were significantly increased, respectively. Those results are consist with G-CSF's ability and function.

References

1) Yamada S. et al., CYRIC Annual Report (1992).
2) Yamada S. et al., J. Nucl. Med. **36** (1995) 1301.
3) Souza L. M. et al., Science **232** (1986) 61.
4) Roilides E. et al., J. Pediatr. **117** (1990) 531.
5) Wang J. M. et al., Immunology **60** (1987) 439.

Table 1. ^{18}F-FDG uptake in rats 4 days after inoculation of turpentine oil.

	Blood	**Heart**	**Liver**	**Spleen**	**Muscle**	**Bone**	**Inflammation**
G-CSF	0.23±0.02	5.23±2.00	0.31±0.03	1.69±0.15	0.82±0.27	1.66±0.30	2.26±0.25
Control	0.22±0.06 (NS)	6.01±1.96 (NS)	0.28±0.06 (NS)	1.34±0.14 ($p<0.005$)	0.66±0.23 (NS)	1.19±0.36 ($p<0.05$)	1.86±0.36 ($p<0.05$)

Values are Mean±SD (Differential Uptake Ratio) using 6 rats.
(NS): not significant. ( ): p value between G-CSF and Control groups.

Table 2. Blood cell count in rats 4 days after inoculation of turpentine oil.

	White Blood Cell x10^3/mm^3	**Lymphocyte** x10^3/mm^3	**Neutrophil** x10^3/mm^3	**Red Blood Cell** x10^6/mm^3	**Platelet** x10^3/mm^3
G-CSF	11.4±3.9	5.7±1.8	5.7±2.1	6.13±0.29	1045±98
Control	3.4±1.3 ($p<0.005$)	2.4±0.5 ($p<0.005$)	1.0±0.8 ($p<0.005$)	6.38±0.20 (NS)	1138±67 (NS)

Values are Mean±SD using 6 rats. (NS): not significant. ( ): p value between G-CSF and Control groups.

III. 6. Double-Tracer Tissue Distribution Study of ^{3}H-Thymidine and ^{18}F-FDG in Experimental Inflammatory Tissue

Yamada S., Kubota K., Kubota R., Tamahashi N., and Ido T.***

Department of Nuclear Medicine and Radiology,
Institute of Development, Aging and Cancer, Tohoku University
*Clustercore Institute of Biology**
*Cyclotron and Radioisotope Center, Tohoku University***

Introduction

We have reported that high accumulation of ^{18}F-FDG was observed in the inner side of abscess wall consisting of inflammatory cells of neutrophils and macrophages, endothelial cells of young vessels and young fibroblasts$^{1)}$. It is thought that ^{18}F-FDG is utilized as energy source for the chemotaxis and phagocytosis of inflammatory cells and the proliferation of endothelial cells and fibroblasts. On the other hand, ^{3}H-thymidine is an indicator of proliferation. In this study, we examined the distribution of ^{3}H-thymidine (^{3}H-Thd) in the inflammatory tissue comparing with ^{18}F-FDG by double-tracer tissue distribution study.

Materials and Methods

Male Donryu rats weighing about 100 g were used. To produce experimental inflammatory tissue, the rats were subcutaneously inoculated with 0.2 ml of turpentine oil in the left groin. Each rat was injected with a mixture of 740 kBq (20 μCi) of ^{18}F-FDG and 37 kBq (1 μCi) of ^{3}H-Thd through the tail vein at 1, 2, 4, 7, and 14 days postinoculation (n=5, each). Another five rats without inoculation were used as controls. Animals were analyzed 1 hour after injection of ^{18}F-FDG and tissue samples were excised and weighed. The ^{18}F radioactivity of the sample was counted immediately with a well-type NaI(Tl) autogamma counter, and the ^{3}H radioactivity with liquid-scintillation counter a week later. Data were expressed as differential uptake ratio (DUR).

Results and Discussion

Table 1 summarizes the time-course of ^{18}F-FDG and ^{3}H-Thd uptakes in various tissue of rats in double-tracer tissue distribution. In blood, heart, liver and muscle, there were no significant changes in ^{18}F-FDG and ^{3}H-Thd uptakes during this experimental period. In inflammatory tissue, however, significant changes were observed in both uptakes. ^{18}F-FDG uptake increased progressively to a peak on day 4 after inoculation and then decreased. ^{3}H-Thd uptake increased after inoculation. The uptakes after inoculation during day 1 to day 14 were almost constant and about twice times greater than that in control.

Inflammatory tissue produced by turpentine oil shows "abscess" formation$^{2)}$. In this abscess wall, many inflammatory cells accumulate, and young endothelial cells of vessels and fibroblasts are observed. The result that higher uptake of ^{3}H-Thd after inoculation may reflect the proliferation of endothelial cells and fibroblasts for tissue repair.

References

1) Yamada S. et al., CYRIC Annual Report 1992, (1992) 2.
2) Yamada S. et al., J. Nucl. Med. **36** (1995) 1301.

Table 1. Time-course of ^{18}F-FDG and ^{3}H-Thd uptakes in double-tracer tissue distribution.

		Control	**Day 1**	**Day 2**	**Day 4**	**Day 7**	**Day 14**
Blood	**^{18}F-FDG**	0.24±0.05	0.25±0.03	0.22±0.06	0.24±0.04	0.26±0.06	0.17±0.03
	^{3}H-Thd	0.57±0.08	0.55±0.05	0.54±0.11	0.54±0.07	0.52±0.11	0.53±0.06
Heart	**^{18}F-FDG**	5.09±0.48	4.70±0.86	5.31±1.22	5.43±1.43	6.68±1.12	4.81±0.68
	^{3}H-Thd	0.81±0.08	0.76±0.06	0.78±0.12	0.72±0.21	0.82±0.16	0.67±0.17
Liver	**^{18}F-FDG**	0.25±0.06	0.28±0.03	0.25±0.05	0.28±0.04	0.31±0.05	0.21±0.03
	^{3}H-Thd	3.56±0.63	3.61±1.10	3.44±1.15	3.65±0.16	3.52±1.48	2.91±0.10
Muscle	**^{18}F-FDG**	0.59±0.15	0.53±0.17	0.52±0.16	0.57±0.18	0.55±0.13	0.60±0.10
	^{3}H-Thd	0.64±0.06	0.52±0.22	0.57±0.20	0.67±0.16	0.63±0.21	0.66±0.10
Inflammation	**^{18}F-FDG**	0.41±0.06	1.13±0.26	1.26±0.29	1.78±0.32	1.18±0.18	0.57±0.19
	^{3}H-Thd	0.47±0.01	0.72±0.22	0.89±0.10	0.84±0.03	0.74±0.26	0.81±0.39

Values are Mean ± SD (Differential Uptake Ratio) using 5 rats.

III. 7. Mastoparan Induces Phosphatidylcholine Hydrolysis by Phospholipase D Activation in Human Astrocytoma Cells

Mizuno K., Nakahata N., and Ohizumi Y

Department of Pharmaceutical Molecular Biology,
Faculty of Pharmaceutical Sciences, Tohoku University

Introduction

Mastoparan is a versatile tetradecapeptide purified from wasp venom[1)] which stimulates phospholipase A_2[2)] , phosphoinositide-specific phospholipase C[3,4)]. Mastoparan also acts as a strong secretagogue in many cell lines and tissues including mast cells[1,3)] and platelets[5)]. In some of these cell lines[3)] and in other cell lines[6)], mastoparan induces phosphatidylinositol turnover and increases an intracellular free calcium ion concentration. It is well known that mastoparan mimics hormone receptor activity and stimulates the guanine nucleotide exchange reaction of the α-subunit of heterotrimeric G protein G_i/G_o family[7-9)].

Phosphatidylcholine (PC) is the principal phospholipid in mammalian tissue. Besides its role as a structural component of cellular membranes, the metabolism of PC generates second messengers for signal transduction in response to extracellular stimuli[10)]. Hydrolysis of PC by phosphatidylcholine-specific-phospholipase C (PC-PLC) produces diacylglycerol (DG) and phosphocholine, while hydrolysis of PC by phospholipase D (PLD) produces phosphatidic acid (PA) and choline. DG is known as an activator of PKC[11)] and PA potentially serves as a mediator for a number of cellular functions[12)]. The observed fusiogenic ability of PA is consistent with the suggestion that PLD is involved in secretory responses[10)]. The products of PC hydrolysis by either PC-PLC or PLD can be interconverted through the actions of DG kinase and phosphatidate phosphohydrolase. Thus, PA also can be a precursor for production of DG.

Activation of PLD by hormones and other extracellular stimuli has been shown in a variety of intact cells. It has been reported that calcium ions[13)], PKC[14)], G proteins[15)] and tyrosine phosphorylation[16)] regulate PC hydrolysis by PLD. However, the mechanisms for regulation of PLD activity remain unknown.

In the present study, we examined the effect of mastoparan on PC hydrolysis in 1321N1 human astrocytoma cells. The results obtained suggest that mastoparan is an activator of PLD.

Materials and Methods

METARIALS

Mastoparan was obtained from Peptide Institute Inc. (Osaka, Japan). Pertussis toxin (PT), DG and PA were from Funakoshi Inc. (Tokyo, Japan). [^{3}H]Palmitic acid was from Amersham Japan (Tokyo, Japan). Fetal bovine serum was from Bioserum (Victoria, Australia). C3 ADP-ribosyltransferase was a gift from Prof. S. Narumiya, Department of Pharmacology, Kyoto University Faculty of Medicine, Japan. Phosphatidylbutanol (PBut) was produced from soybean PC using crude cabbage PLD by the method of Yang et al[17)].

CELL CALTURE

1321N1 human astrocytoma cells were grown in Dulbecco's modified Eagle's medium with 5% fetal bovine serum, 50 U ml^{-1} of penicillin and 50 μg ml^{-1} streptomycin at 37°C in an atmosphere of 5% CO_2 in air. For experiments, the cells were seeded at a density of 10^5 cells/well in a 12-well culture plate and were used after culturing for 3-4 days.

MEASUREMENTS OF PLD ACTIVITY IN INTACT CELLS

To determine the PLD activity in intact cells, the cellular phospholipid pool was labeled by incubating cells in growth medium containing 10 μCi ml^{-1} [^{3}H]palmitic acid at 37°C for 18-22 h in an atmosphere of 5% CO_2 in air. To examine the effects of ADP-ribosylation catalyzed by PT or C3 ADP-ribosyltransferase, 200 ng ml^{-1} of PT or 1 μg ml^{-1} C3 ADP-ribosyltransferase were included in the medium during the labeling. After washed three times with Eagle's minimal essential medium containing 10 mM HEPES (pH 7.35), the prelabeled cells were preincubated at 37°C for 10 min in Eagle's Minimal Essential medium containing 10 mM HEPES (pH 7.35) in the presence or absence of 2% n-butanol. Then, the reagents were added to the medium, and the reactions were terminated by addition of 1ml of methanol/1N HCl=10/1. Lipids were extracted by the method of Bligh and Dyer[18)]. Authentic PBut, PA and DG as standards were added to each sample. The extracted lipids were separated on LK5D silica gel (Whatman Inc.) with the organic layer of ethyl acetate/iso-octane/water/acetic acid=11/5/10/2 and then detected with iodine vapor. DG was separated with hexane/ether/ethyl acetate=25/75/1. Spots corresponding to PBut, PA and DG were scraped off and their radioactivities were quantified by liquid scintillation counting.

Resuls

To determine whether mastoparan hydrolyzes PC by activation of PC-PLC or PLD, the effect of mastoparan on PC hydrolysis was examined in the presence of 2% n-butanol. In [^{3}H]palmitic acid prelabeled cells, mastoparan stimulated transphosphatidylation reaction and induced [^{3}H]PBut accumulation. The accumulation of [^{3}H]PBut induced by mastoparan was concentration- and time-dependent fashion (Figure 1). [^{3}H]PBut accumulation was detectable at 5 μM mastoparan and reached a maximum at 30 μM mastoparan. [^{3}H]PBut accumulation induced by 30μM mastoparan was reached plateau within 15min (Figure 1). From these results, mastoparan activates PLD resulting in PC hydrolysis.

Furthermore, the effect of the phosphatidiate phosphohydrolase inhibitor, propranolol, on accumulation of [^{3}H]DG and [^{3}H]PA induced by mastoparan was examined. Propranolol concentration-dependently reduced mastoparan-induced [^{3}H]DG accumulation and increased the [^{3}H]PA level (Figure 2). These results also suggest that mastoparan activates PLD.

Because of the ability of mastoparan to activate G proteins, we examined the mastoparan-induced PLD activation in the cells pretreated with PT or C3 ADP-ribosyltransferase. As shown in Table 1, mastoparan-induced PLD activation was not inhibited by the cells pretreated with PT or C3 ADP-ribosyltransferase. From these results, it seems that mastoparan activates PLD neither via the heterotrimeric G protein Gi/Go family nor by the small molecular weight G protein rho/rac family.

Discussion

This is the first report to demonstrate that mastoparan is a strong activator of PLD resulting in PC hydrolysis. It has been reported that the vesicle fusion requires an activation of PLD, which generates PA from PC. The action of PLD can potentially alter the surface milieu of membranes by producting negatively charged phospholipids from neutral PC. It is very interesting that mastoparan, which is a strong secretagogue, can activate PLD. Although it has been thought that mastoparan induces histamine release from mast cells by activating of phosphoinositide-specific phospholipase C mediated via PT sensitive G protein, resulting in an accumulation of inositol 1,4,5-trisphosphate and intracellular calcium mobilization, mastoparan stimulates exocytosis in a calcium independent manner in some cases. Mastoparan induced serotonin release from intact human platelets without an elevation of intracellular free calcium ion concentration[3)]. It has been substantiated that the stimulatory effects of mastoparan show to be mediated via G protein activation because of the inhibitiory action of PT on mastoparan-induced cellular functions. However, it is reported that mastoparan-stimulated exocytosis is not inhibited by pretreatment of the cells with PT in some cell lines including the RINm5F β-cell line[19)]. It is a possible that mastoparan stimulates cell function by activating of PLD in some of these cases.

It has been reported that mastoparan increases GTPase activity and [^{35}S] GTPγS binding of Gi/Go in phospholipid vesicles[7,8)]. It has been also reported that mastoparan inhibits the ADP-ribosylation of 20kDa human platelet membrane proteins catalyzed by C3 ADP-ribosyltransferase[20)]. This result suggests that mastoparan interacts not only with the heterotrimeric G protein Gi/Go family but also with the small molecular weight G protein rho/rac family. On the other hand, there is much evidence that PLD activity is regulated by G proteins[15], and that ADP-ribosylation catalyzed by PT inhibits agonist-induced PLD activation in neutrophils[21]. It has been also reported that PLD is activated by a membrane-associated rho family small molecular weight G protein because of inhibition of GTPγS-stimulated PLD activity by rho GDP dissociation inhibitor and stimulation of GTPγS-stimulated PLD activity by small molecular weight G protein GDP dissociation stimulator in neutrophils[22]. However, in 1321N1 human astrocytoma cells pretreated with PT or C3 ADP-ribosyltransferase mastoparan retained the ability to stimulate PLD activity. These results suggest that mastoparan stimulates PLD by a mechanism not mediated via G protein activation, such as Gi and Rho.

Acknowledgments

We thank Prof. S. Narumiya and Dr. N. Morii, Department of Pharmacology, Kyoto University Faculty of Medicine, Japan, for providing C3 ADP-ribosyltransferase. We are also grateful to Cyclotron Radioisotope Center, Tohoku University for co-operation in radiochemical analysis. This work was supported by grant-in-aids for Scientific Research from Ministry of Education, Science and Culture of Japan.

References

1) Hirai Y., Yasuhara T., Yoshida H., Nakajima T., Fujino M. and Kitada C., Chem. Pharm. Bull., **27** (1979) 1942.
2) Argriolas A. and Pisano J. J., J. Biol. Chem. **258** (1983) 13697.
3) Okano Y., Takagi H., Tohmatsu T., Nakashima S., Kuroda Y., Saito, K. and Nozawa, Y., FEBS Lett. **188** (1985) 363.
4) Gusovsky F., Soergel D. G. and Daly J. W., Eur. J. Pharmacol. **206** (1991) 309.
5) Ozaki Y., Matsumoto Y., Yatomi Y., Higashihara M., Kariya,T. and Kume, S., Biochem. Biopys. Res. Commun. **170** (1990) 779.
6) Perianin A. and Snyderman R., J. Immunol. **143** (1989) 1669.
7) Hiigashijima T., Burnier J. and Ross E. M., J. Biol. Chem. **265** (1990) 14176.
8) Higashijima T. and Ross E. M., J. Biol. Chem. **266** (1991) 12655.
9) Higashijima T.,Uzu S., Nakajima T., and Ross E. M., J. Biol. Chem. **263** (1988) 6491.
10) Exton J. H., Biochim. Biophys. Acta **1212** (1994) 26.
11) Nishizuka Y., Science **258** (199 607.
12) Yu C. L., Tsai M. H. and Stacey D. W., Cell **52** (1988) 63.
13) Halenda S. P. and Rhem A. G., Biochem. J. **267** (1990) 479.
14) Liscovitch M. and Amsterdam A., J. Biol. Chem. **264** (1989) 11762.
15) Kusner D. J., Schomisch S. J. and Dubyak, G. R., J. Biol. Chem. **268** (1993) 19973.
16) Bourgoin S. and Grinstein S., J. Biol. Chem. **267** (199 11908.
17) Yang S. F., Freeer S. and Benson A. A., J. Biol. Chem. **242** (1967) 477.
18) Bligh E. G. and Dyer W. J., Can. J. Biochem. Physiol. **37** (1959) 911.
19) Komatsu M., McDermott A. M., Gillson S. L. and Sharp G. W. G., J. Biol. Chem., **268** (1993) 23297.
20) Koch G., Habermsann B., Mohr C., JUST I. and Aktories K., FEBS Lett. **291** (1991) 336.
21) Kanaho Y., Kanaho H. and Nozawa Y., FEBS Lett. **279** (1991) 249.
22) Bowman E. P., Uhliger D. J. and Lambeth J. D., J. Biol. Chem. **268** (1993) 21509.

Table 1. The Relation of G Protein to Mastoparan-induced PLD Activation.

	Phosphatidylbutanol (dpm/well)	
	PT-treatment	
	−	+
control	12769.89 ± 607.25	12646.54 ± 939.39
Mastoparan	31232.48 ±1282.67	39767.89 ±1107.09
	C3-treatment	
	−	+
control	2257.68 ± 218.27	2274.15 ± 508.03
Mastoparan	10793.35 ± 851.28	10953.63 ± 292.46

For ADP-ribosylation experiments, 1321N1 human astrocytoma cells were treated with or without 200 ng ml^{-1} PT or 1 μg ml^{-1} C3 during prelabeling with $[^3H]$palmitic acid, then incubated with 2% butanol and 30 μM mastoparan at 37°C for 10 min. After the reaction was terminated, $[^3H]$PBut was determined. Data represent the mean ± s.e.mean of three independent experiments.

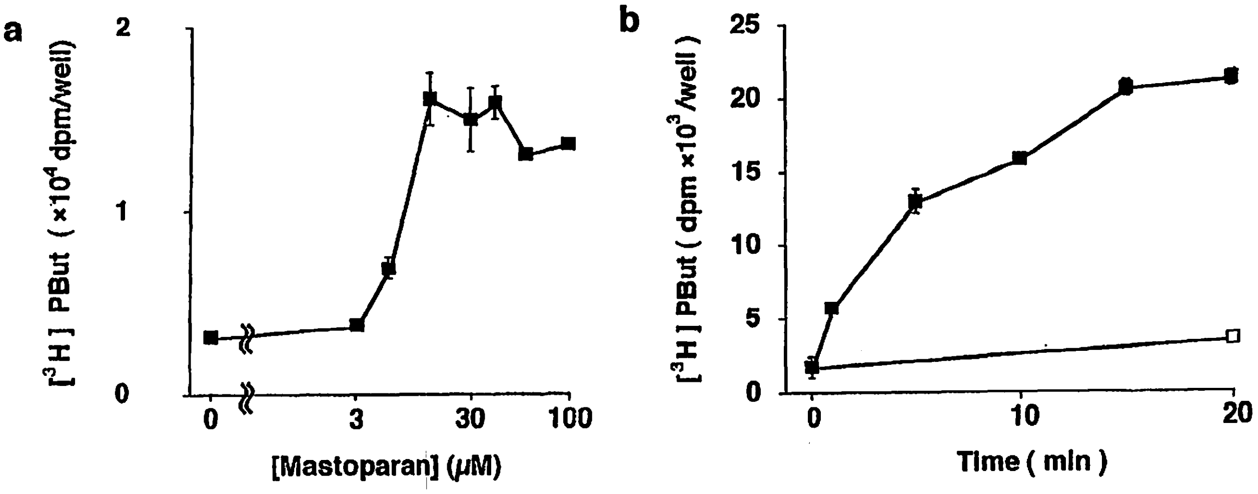

1321N1 human astrocytoma cells prelabeled with $[^3H]$palmitic acids were incubated with 2% butanol and the indicated concentrations of mastoparan at 37°C for 10 min (a) or incubated with 2% butanol and 30 μM mastoparan (■) or vehicle (□) at 37°C for the indicated time (b). After the reaction was terminated, determined, $[^3H]$Pbut was determined Data represent the mean ± s.e.mean of three independent experiments.

Fig. 1. Effect of mastoparan on $[^3H]$PBut accumulation in 1321N1 human astrocytoma cells.

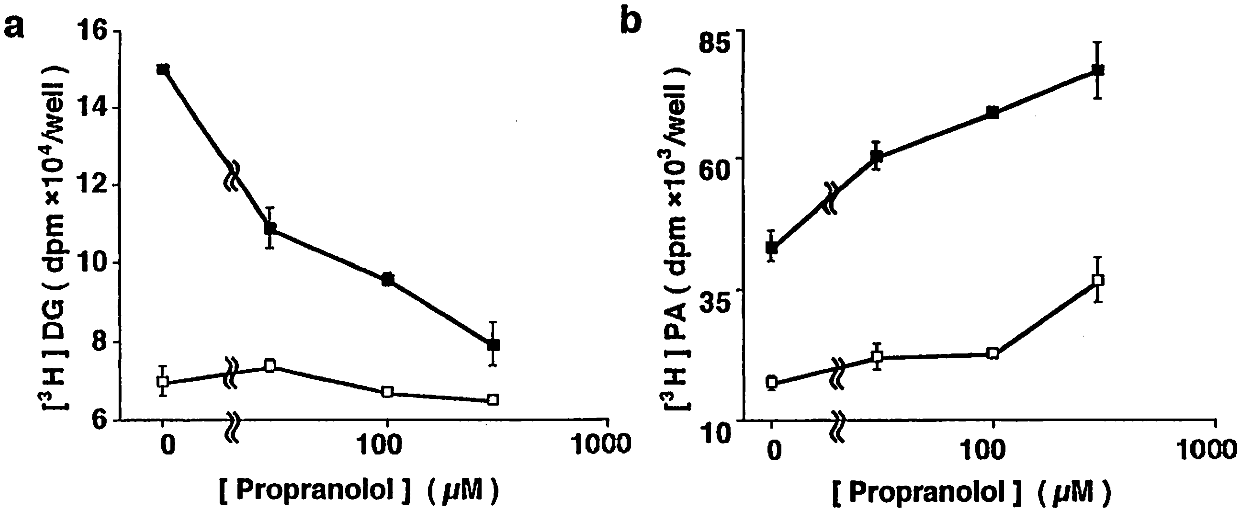

1321N1 human astrocytoma cells prelabeled with [^{3}H]palmitic acids were incubated with the indicated concentrations of propranolol at 37°C for 10 min, supplemented with (■) or without (□) μM mastoparan. After the reaction was terminated, [^{3}H]DG (a) and [^{3}H]PA (b) were determined. Data represent the mean ± s.e.mean of three independent experiments.

Fig. 2. Effect of propranolol on accumulation of [^{3}H]DG and [^{3}H]PA induced by mastoparan in 1321N1 human astrocytoma cells.

III. 8. 4,6-Dibromo-3-Hydroxycarbazole (an Analogue of Caffeine-like Ca^{2+} Releaser), a Novel Type of Inhibitor of Ca^{2+}-Induced Ca^{2+} Release in Skeletal Muscle Sarcoplasmic Reticulum.

Takahashi Y., Furukawa K.-I., Kozutsumi D., Ishibashi M.*, Kobayashi J.**
and Ohizumi Y.

Department of Pharmaceutical Molecular Biology, Faculty of Pharmaceutical Sciences, Tohoku University
*Department of Pharmacognosy, Faculty of Pharmaceutical Science, Hokkaido University**

Introduction

Ca^{2+} release from the sarcoplasmic reticulum (SR) plays a key role in excitation-contraction coupling (EC-coupling) in skeletal muscle1,2). It is well known that ryanodine, a plant alkaloid, promotes Ca^{2+} release from skeletal and cardiac SR and interferes with the inactivation of Ca^{2+}-induced Ca^{2+} release (CICR) from SR3). The alkaloid binds with high affinity to a receptor localized in the heavy fraction of SR (HSR)4). The purified ryanodine receptor5,6) is identical in morphology with the "feet" structures to span the transverse tubule-SR junction and form caffeine-sensitive Ca^{2+} channels. It has been reported that ryanodine locks the Ca^{2+} release channels of SR in an open state and that its high affinity binding site is localized in terminal cisternae of SR4). These studies revealed that the ryanodine receptor is identical with CICR channels of SR7). One of the useful approaches to achieve a better understanding of the molecular mechanism of Ca^{2+} release is the application of specific drugs that affect the releasing mechanisms.

It has been reported that caffeine increases the Ca^{2+} sensitivity of CICR channels and the open probability of the channels at saturating Ca^{2+} concentrations. Numerous studies using skinned skeletal muscle fibres and isolated SR membrane preparations have revealed the presence of a caffeine-sensitive Ca^{2+} release pathway through CICR channels. However, the characterization of the caffeine receptor site in Ca^{2+} release channels has not been possible because of its low affinity and the detailed molecular mechanism of Ca^{2+} release from SR remains unresolved.

We have reported that bromoeudistomin D (BED), a derivative of eudistomin D isolated from the Caribbean tunicate Eudistoma olivaceum, induces Ca^{2+} release from HSR. Our pharmacological studies indicate that BED is approximately 500 times more potent than caffeine in Ca^{2+} releasing activity. For the purpose of finding the inhibitor in order to investigate the function of CICR channels, numerous analogues of BED were synthesized.

Materials and Methods

HSR was prepared from skeletal muscle of male rabbits as reported previously8). In order to estimate the Ca^{2+} releasing activity, the concentration of extravesicular Ca^{2+} in the HSR suspension was measured at 30°C with a Ca^{2+} electrode as described previously9). $^{45}Ca^{2+}$ release from HSR passively preloaded with $^{45}Ca^{2+}$ was measured at 0°C according to the method of Nakamura et al10). [^{3}H]MBED and [^{3}H]ryanodine binding experiments were performed by the method of Seino et al9).

Results and Discussion

In the course of our survey of inhibitors of Ca^{2+}-induced Ca^{2+} release (CICR) in natural products and their derivatives, we have been succeeded in finding 4,6-Dibromo-3-hydroxycarbazole (DBHC) as a CICR inhibitors. The pharmacological properties of DBHC were examined. In Ca^{2+} electrode experiments, DBHC (10^{-4} M) markedly inhibited Ca^{2+} release from the heavy fraction of sarcoplasmic reticulum (HSR) induced by caffeine (1 mM) and BED (10^{-5} M). DBHC (10^{-4} M) abolished $^{45}Ca^{2+}$ release induced by caffeine (1 mM) and BED (10^{-5} M) in HSR. These results indicate DBHC to be a CICR inhibitors. As shown in Fig. 1b-1d, inhibitory effects of CICR blockers such as procaine, ruthenium red and Mg^{2+} on $^{45}Ca^{2+}$ release were clearly observed at Ca^{2+} concentrations from pCa 7 to pCa 5.5, and were decreased at Ca^{2+} concentrations higher than pCa 5.5 or lower than pCa 7. However, DBHC decreased $^{45}Ca^{2+}$ release induced by Ca^{2+} over the wide range of extravesicular Ca^{2+} concentrations (Fig. 1a). These results indicate that the inhibitory effects of procaine, ruthenium red and Mg^{2+} but not DBHC are suppressed at high Ca^{2+} concentrations and that DBHC is a novel type of CICR inhibitors having unique pharmacological properties. [^{3}H]Ryanodine binding to HSR was suppressed by ruthenium red, Mg^{2+} and procaine, but was not affected by DBHC up to 10^{-4} M. [^{3}H]Ryanodine binding to HSR was enhanced by caffeine and BED. DBHC antagonized the enhancement in a concentration-dependent manner. 9-[^{3}H]Methyl-7-bromo-eudistomin D, a [^{3}H]-labeled analogue of BED, specifically bound to HSR. Both DBHC and caffeine increased the Kd value without affecting the Bmax value, indicating a competitive mode of inhibition (Fig. 2). These results suggest that DBHC binds to the caffeine binding site to block Ca^{2+} release from HSR. This drug is a novel type of inhibitor for the CICR channels in SR and may provide a useful tool for clarifying the Ca^{2+} releasing mechanisms in SR.

Acknowledgments

The authors greatly appreciate the cooperation of the stuff members of the Cyclotron and Radioisotope Center.

References

1) Ebashi S., Annu. Rev. Physiol. **53** (1991) 1
2) Endo M., Curr. Top. Membr. Transp. **25** (1985) 181.
3) Meissner G., J. Biol. Chem. **261** (1986) 8643.
4) Fleischer S. et al., Proc. Nat. Acad. Sci. USA (1985) 7256.
5) Imagawa T. et al., J. Biol. Chem. **262** (1987) 16636.
6) Inui M. et al., J. Biol. Chem. **262** (1987) 1740.
7) McPherson P. S. et al., J. Biol. Chem. **268** (1993) 13765.
8) Takahashi Y. et al., Eur. J. Pharmacol. **288** (1995) 285.
9) Seino A. et al., J. Pharmacol. Exp. Ther. **256** (1991) 861.
10) Nakamura Y. et al. J. Biol. Chem. **261** (1986) 4139.

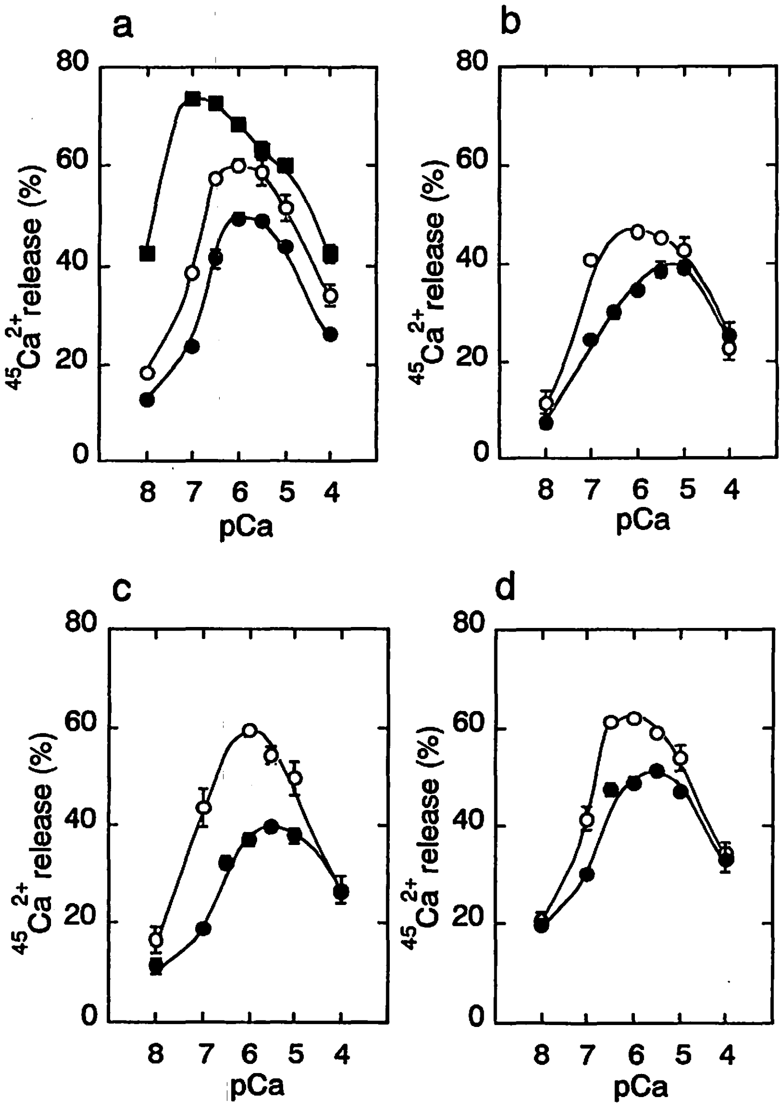

Fig. 1. Inhibitory effects of CICR inhibitors on $^{45}Ca^{2+}$ release at various Ca^{2+} concentrations. $^{45}Ca^{2+}$ release at various concentrations of free Ca^{2+} was measured during 1 min after dilution. Each value was normalized against the amount of $^{45}Ca^{2+}$ in HSR at zero time. (a) Control (○), 10^{-4} M DBHC (●), 10^{-5}M BED (■). (b) Control (○), 3 mM procaine (●). (c) Control (○), 30 nM ruthenium red (●). (d) Control (○), 3 × 10^{-5} M Mg^{2+} (●). Data are mean ± s.e.mean (n = 4).

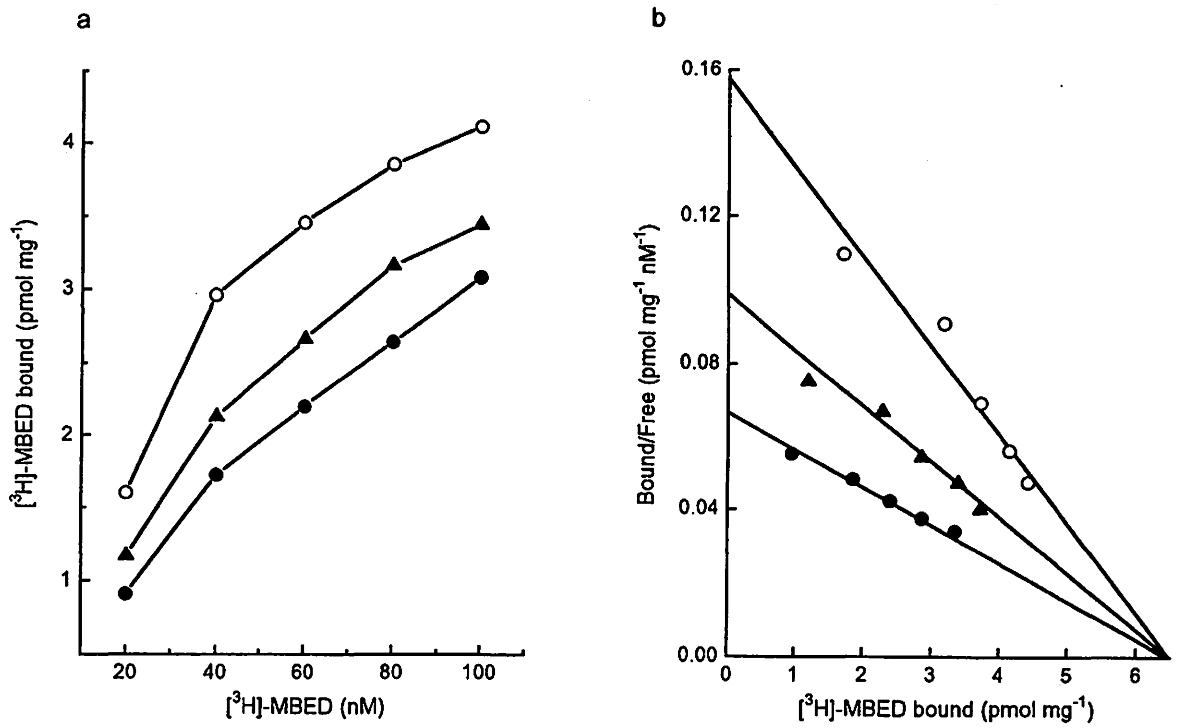

Fig. 2. Effects of DBHC and caffeine on [^{3}H]MBED binding. HSR (0.3 mg ml^{-1}) was incubated with increasing concentration of [^{3}H]-MBED from 20 to 100 nM for 45 min at 0°C. (a) [^{3}H]-MBED binding was measured in the presence or absence (○) of 0.05 mM DBHC (●) or 0.5 mM caffeine (▲) and is plotted. (b) [^{3}H]-MBED binding in (a) is presented as a Scatchard plot.

III. 9. Structure-Activity Relationship of Bromoeudistomin D, a Powerful Ca^{2+} Releaser in Skeletal Muscle Sarcoplasmic Reticulum

Takahashi Y., Furukawa K.-I., Ishibashi M., Kozutsumi K.*, Ishiyama H.*, Kobayashi J.*, and Ohizumi Y.*

Department of Pharmaceutical Molecular Biology, Faculty of Pharmaceutical Sciences, Tohoku University
*Department of Pharmacognosy, Faculty of Pharmaceutical Science, Hokkaido University**

Introduction

Mobilization of intracellular Ca^{2+} has been shown to be involved in such diverse cellular processes as surface receptor activation and fertilization. In skeletal muscle Ca^{2+} release from sarcoplasmic reticulum (SR) plays a important role in excitation-contraction coupling[1]. Although caffeine has been used extensively as a inducer of Ca^{2+} release from SR, the direct binding studies for the identification or characterization of the caffeine receptor site have not been possible because of its low affinity. Furthermore, caffeine has multiple other effects such as inhibition of phosphodiesterase activity and activation of adenosine receptors. These problems make the use of caffeine problematical. We have reported that bromoeudistomin D (BED), a derivative of eudistomin D isolated from the Caribbean tunicate Eudistoma Olivaceum, induces Ca^{2+} release from heavy fraction of SR (HSR). From the results of computer graphics, it was found that there were structural similarities between BED, 9-metyl-7-bromoeudistomin D (MBED) and caffeine. Our pharmacological studies indicate that BED and MBED are approximately 500 and 1000 times more potent than caffeine in the Ca^{2+}-releasing activity without other pharmacological action. We also reported that ^3H-labeled MBED shares the same binding site on Ca^{2+} release channels with caffeine. The present report deals with the opening mechanism of the ryanodine receptor/Ca^{2+} release channels investigated using the eudistomin analogues. Our results suggest that these compounds modify the function of Ca^{2+}-induced Ca^{2+} release channels.

Materials and Methods

Bromoeudistomin D (BED), 9-methyl-7-bromoeudistomin D (MBED) and its analogues (Fig. 1) were synthesized as reported previously[2]. The heavy fraction of sarcoplasmic reticulum (HSR) was prepared from skeletal muscle of male rabbits according to the method of Kim et al[3]. The $^{45}Ca^{2+}$ release from passively preloaded-HSR was measured at 0-4°C according to the method of Nakamura et al[4]. [^3H]Ryanodine binding to HSR was measured according to the method of Seino, et al5). All other chemicals were of reagent grade.

Results and Discussion

Bromoeudistomin D or 9-methyl-7-bromoeudistomin D which have a β-carboline skeleton are powerful Ca^{2+} releasers from skeletal muscle sarcoplasmic reticulum exhibiting caffeine-like properties. We examined the effects of bromoeudistomin D analogues (Fig. 1) on Ca^{2+}-induced Ca^{2+} release from skeletal muscle sarcoplasmic reticulum. Table 1 shows the effects of BED and its analogues (A[1]-A[19]) on $^{45}Ca^{2+}$ release. Among bromoeudistomin D analogues, the Ca^{2+}-releasing activities of carboline derivatives (A[5]-A[9] and A[12]-A[19]) were higher than those of carbazole derivatives (A[1]-A[4], A[10] and A[11]), suggesting that carboline skeleton is significantly important for the exhibiting the Ca^{2+}-releasing activity and Ca^{2+} sensitivity of Ca^{2+}-induced Ca^{2+} release. On the contrary, the analogues having carbazole skeleton and bromine at C-6 (A[4] and A[10]) inhibit both Ca^{2+}- and caffeine-induced Ca^{2+} release. 9-Methyl-substitution of the analogue (A[11]) elevated its Ca^{2+}-releasing activity. The binding of [^{3}H]ryanodine to the Ca^{2+}-releasing channels is enhanced by compunds which activate the channels and inhibited by other agents which reduce channels activity. Therefore, [^{3}H]ryanodine can be used as a probe for studying the functional state of the Ca^{2+} release channels. [^{3}H]Ryanodine biding was markedly potentiated by BED and A[5] which are powerful Ca^{2+} releasers, and left almost unchanged by analogues which effect Ca^{2+} release only slightly. Therefore, there are close correlation between the enhancement of [^{3}H]ryanodine binding to sarcoplasmic reticulum by the analogues and the activation of Ca^{2+} release by them. Bromoeudistomin D analogues may provide valuable information about the structure-function relationship of the ryanodine receptor/Ca^{2+} release channels in skeletal muscle sarcoplasmic reticulum.

Acknowledgments

The authors greatly appreciate the cooperation of the stuff members of the Cyclotron and Radioisotope Center.

References

1) Ebashi S., Annu. Rev. Physiol. **53** (1991) 1.
2) Takahashi Y. et al., Eur. J. Pharmacol. **288** (1995) 285.
3) Kim D. H. et al., J. Biol. Chem. 258, 9662.
4) Nakamura Y. et al., J. Biol. Chem. **261** (1986), 4139.
5) Seino A. et al., J. Pharmacol. Exp. Ther. **256** (1991), 861.

Table 1. Effects of bromoeudistomin D analogues on $^{45}Ca^{2+}$ releasing activity. The amount of released $^{45}Ca^{2+}$ was calculated from the decrease in $^{45}Ca^{2+}$ content in the heavy fraction of sarcoplasmic reticulum vesicles in a period of 1 min after dilution. Each value was obtained by subtracting the amount of released $^{45}Ca^{2+}$ in the absence of test compound from that in its presence. The activities are presented as values relative to the control value.

compounds	concentration	Change in $^{45}Ca^{2+}$-releasing activity (%)[a] pCa 7	pCa 6
	μM		
bromoeudistomin D	10	+150 ±10	+20 ± 6
A[1]	100	+65 ± 3	+9 ± 2
A[2]	100	+60 ± 4	+9 ± 3
A[3]	100	+30 ± 1	+4 ± 2
A[4]	100	-30 ± 5	-88 ± 5
A[5]	100	+138 ± 6	+9 ± 3
A[6]	100	+62 ± 7	+0 ± 5
A[7]	100	+66 ± 3	+0 ± 3
A[8]	100	+30 ± 3	+4 ± 7
A[9]	100	+120 ± 7	+5 ± 4
A[10]	100	-35 ± 4	-68 ± 3
A[11]	100	+27 ± 5	+40 ± 2
A[12]	100	+96 ± 2	+34 ± 1
A[13]	100	+69 ±11	+30 ± 1
A[14]	100	+5 ± 9	-40 ± 4
A[15]	100	+27 ± 3	+21 ± 2
A[18]	100	+64 ± 6	+32 ± 0
A[19]	100	+27 ± 3	+25 ± 2

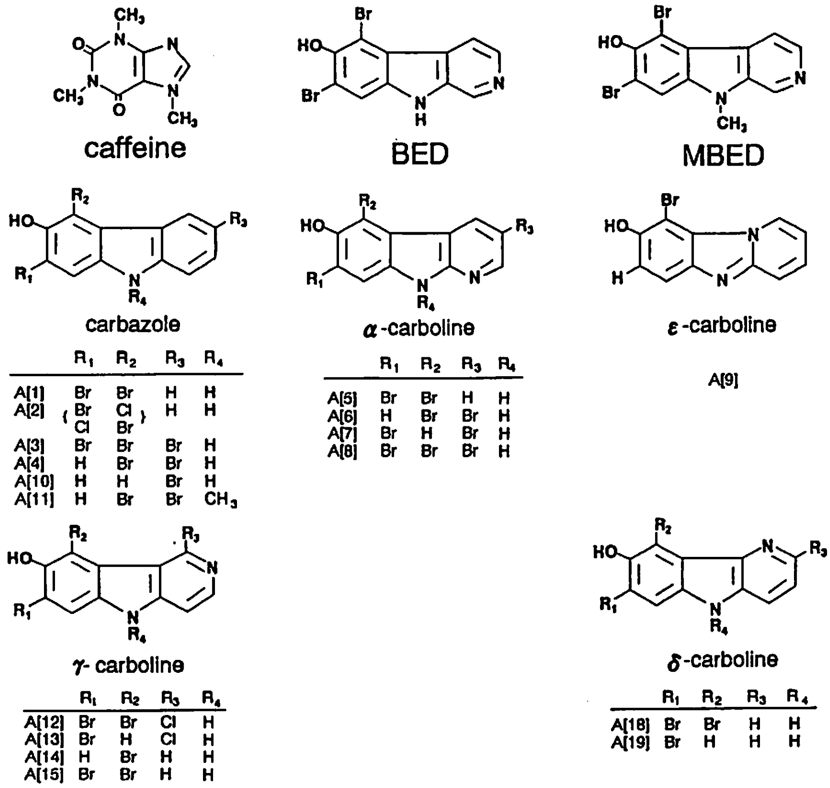

Fig. 1. Chemical structure of caffeine, bromoeudistomin D (BED), 9-methyl-7-bromoeudistomin D (MBED) and the analogues.

III. 10. The Properties of Specific Binding Site of ^{125}I-Radioiodinated Myotoxin *a*, a Novel Ca^{++} Releasing, agent in Skeletal Muscle Sarcoplasmic Reticulum

Ohkura M., Furukawa K.-I., Oikawa K. and Ohizumi Y.

Department of Pharmaceutical Molecular Biology, Faculty of Pharmaceutical Sciences, Tohoku University

Introduction

Myotoxin *a* (MYTX) isolated from prairie rattlesnakes (*Crotalus viridis viridis*) is a muscle-damaging polypeptide that is composed of 42 amino-acid residues including 3 disulfide bonds1). The electron-microscopic study has revealed that MYTX causes muscle degeneration and disturbance of the sarcoplasmic reticulum (SR) functions and muscle filaments2). Recently, we found that MYTX strongly induced Ca^{++} release from skeletal muscle SR with the EC$_{50}$ value of 0.5 μM. The properties of MYTX-induced Ca^{++} release were different from those induced by the other Ca^{++}-releasing agents such as caffeine, MBED, a powerful caffeine-like Ca^{++} releaser, and adenosine 5'-(β,γ-methylene)triphosphate (AMP-PCP)3).

In order to characterize the molecular mechanism of action of MYTX, we prepared ^{125}I-labeled MYTX (^{125}I-MYTX), and studied its binding to the heavy fraction of fragmented SR (HSR), in which the ryanodine receptor is enriched abundantly. Our results indicated that MYTX induced Ca^{++} release by binding to a specific site which is distinct from the ryanodine receptor. MYTX may be useful as a biochemical probe not only for clarifying the regulatory mechanism of physiological Ca^{++} release but also for purifying a novel type of Ca^{++} release channels or their regulatory proteins.

Materials and Methods

MATERIALS

HSR was prepared from rabbit skeletal muscle by the method of Kim et al.4). The ryanodine receptor was purified from skeletal muscle by the method of Shoshan-Barmatz and Zarka5). MBED was synthesized by the method described previously6,7). Chemicals used were obtained from following sources; crude venom of prairie rattlesnakes (*Crotalus viridis viridis*) from Sigma; ryanodine from S.B. Penick Company; ^{45}CaCl$_2$ (25.9 Bq/pmol), ^{3}H-ryanodine (2.22 kBq/pmol) and $Na^{125}I$ (95.3 kBq/pmol) from Du-Pont New England Nuclear; All other chemicals were of reagent grade.

METHODS

MYTX (Fig. 1) was purified as described previously$^{2)}$. ^{125}I-Labeling of MYTX was performed by the chloramine T method. ^{125}I-MYTX binding was measured by the method of Penefsky$^{8)}$ with a slight modification. ^{3}H-Ryanodine binding was measured as described previously$^{7)}$. The extravesicular Ca^{++} concentration was monitored with a Ca^{++} electrode prepared by the method of Nakamura et al.$^{9)}$. $^{45}Ca^{++}$ release from HSR passively preloaded with 45Ca++ was measured at 0°C as described previously$^{9)}$ with a slight modification.

Results and Discussion

It was found that MYTX is a powerful Ca^{++} releaser in the HSR. ^{125}I-MYTX with high Ca^{++}-releasing ability was successfully prepared. It specifically bound to a single class of binding sites in HSR with a K_D of 0.4 μM and B_{max} of 6 nmol/mg protein (Fig.1). ^{125}I-MYTX binding was markedly inhibited by Na^+ and K^+, whereas that was little affected by Ca^{++} and Mg^{++}. The binding activity was markedly decreased by spermine, a blocker of Ca^{++} release channels, and was not affected by the other modulators of Ca^{++} release such as caffeine, procaine or ruthenium red (Table 1). Spermine decreased the binding in a concentration-dependent manner with the IC_{50} value of 20 μM. Scatchard analysis of ^{125}I-MYTX binding indicated that the Bmax value was decreased by spermine, while the K_D value was not changed, indicating a noncompetitive mode of inhibition. ^{125}I-MYTX did not bind to the purified ryanodine receptor. Ca^{++} electrode experiments indicated that MYTX induced Ca^{++} release from HSR at 0.1 μM or more, which was abolished by spermine. The maximal response to MYTX (10 μM) was further increased by caffeine (10 μM) in $^{45}Ca^{++}$ release, probably indicating that the effects of MYTX and caffeine are synergistic in Ca^{++}-releasing action (Fig. 2). These results suggest that MYTX binds to an important regulatory protein of Ca^{++} release which is not the ryanodine receptor.

References

1) Fox J. W. et al., Biochemistry **18** (1979) 678.
2) Cameron D. L. and Tu A. T., Biochemistry **224** (1977) 89.
3) Funayama K. et al., Jpn. J. Pharmacol. **58** (1992) suppl. I, 208P.
4) Kim D. H. et al., J. Biol. Chem. **258** (1983) 9662.
5) Shoshan-Barmatz V. and Zarka A., Biochem. J. **285** (1992) 61.
6) Kobayashi J. et al., J. Pharm. Pharmacol. **40** (1988) 62.
7) Seino A. et al., J. Pharmacol. Exp. Ther. **256** (1991) 861.
8) Penefsky H. S., Methods Enzymol. **56** (1979) 527.
9) Nakamura Y. et al., J. Biol. Chem. **261** (1986) 4139.

Table 1. Effects of various modulators of Ca^{++} release on ^{125}I-MYTX binding to HSR. HSR vesicles (50 μg/ml) were incubated with ^{125}I-MYTX (0.3 μM) at 0° C for 60 min in the presence or absence (control) of various modulators. Values, expressed as percents of control, are means ± S.E.M. (n = 3). Significantly different from control: ** ($p < .01$).

Modulators	^{125}I-MYTX Bound
	% of Control
Control	100.0 ± 2.63
Caffeine (2 mM)	93.5 ± 10.10
MBED (10 μM)	106.5 ± 1.36
AMP-PCP (100 μM)	100.1 ± 6.22
Inositol (1,4,5)trisphosphate (10 μM)	104.1 ± 2.80
Procaine (10 mM)	113.4 ± 5.93
Ruthenium red (1 μM)	96.2 ± 2.66
Spermine (100 μM)	31.0 ± 3.78*
Dantrolene (10 μM)	98.8 ± 3.22

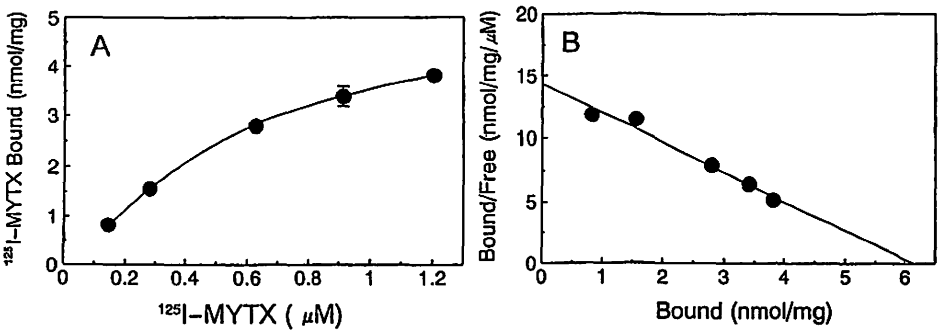

Fig. 1. Saturation (A) and Scatchard (B) plots of ^{125}I-MYTX binding to HSR. HSR (50 μg/ml) was incubated with ^{125}I-MYTX at various concentrations at 0°C for 60 min. Values are means with S.E.M. (n=3).

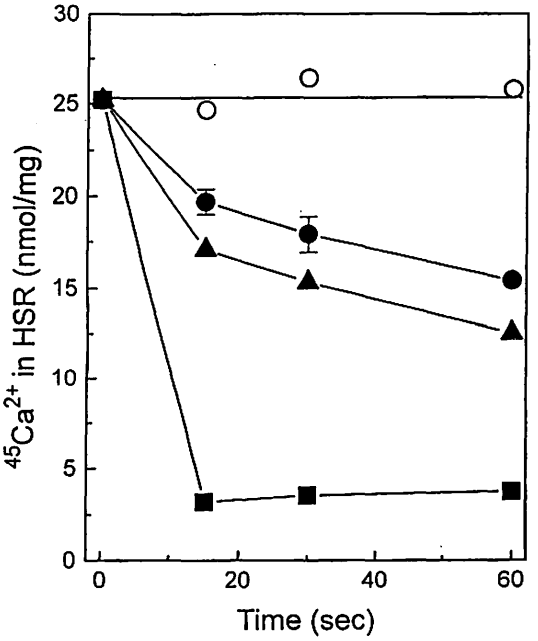

Fig. 2. Interrelations between the Ca^{++}-releasing activities of MYTX and caffeine in ^{45}Ca^{++} release experiments on HSR. The ^{45}Ca^{++} content of HSR was measured at 0° C by the filtration method. Values are means with S.E.M. (n = 3). Control (○); MYTX (10 μM) (●) ; caffeine (10 mM) (▲); MYTX (10 μM) plus caffeine (10 mM) (■).

III. 11. Effect of Aging in Bindings of Second Messengers in the Rat Brain

Araki T., Kato H., Nagasawa H.,Fujiwara T. and Yasuto Itoyama.*

Department of Neurology, Tohoku University School of Medicine
*Division of Cyclotron Nuclear Medicine, Cyclotron and Radioisotope Center, Tohoku University**

It is generally accepted that neurotransmitters play an important role in neuronal function and neurotransmission in the central nervous system (CNS). The process of aging can be characterized by a great number of physiological and biochemical modifications such as neuronal degeneration and alterations in neurotransmitter receptors. Several lines of evidence demonstrate that the age-related decline in cognitive functions such as memory and learning is closely linked to dysfunction of various neurotransmitter systems1-5). Therefore, the effect of aging on neurotransmitter systems is of great interest in regards to the specificity of age-related neuronal dysfunction and decline in cognitive function.

Many receptors for neurotransmitters in the CNS are well known to be coupled to the intracellular second messenger systems, the adenylate cyclase and phosphoinositide cycle systems. The two second messenger systems play a crucial role in mediating the actions of various neurotransmitters in the brain6-8). Recent studies suggested that a decrease in protein kinase C (PKC) activity in the phosphoinositide cycle system was found in the cortex and hippocampus of aged rats9,10) and was closely associated with the impairment of spatial learning in the hippocampus9). On the other hand, Worley et al11). demonstrated that a reduction in adenylate cyclase activity was seen in the striatum and substantia nigra of aged rats. These observations are great interest in regard to any age-related decline in cognitive function. However, the role of second messenger alterations in aging processes is not fully understood. In the present study, therefore, we focused on major second messengers and analyzed the regional age-related changes of these bindings in the rat brain, using in vitro receptor autoradiography. For this purpose, [^{3}H]PDBu and [^{3}H]forskolin were used to label to protein kinase C (PKC) and adenylate cyclase, respectively.

Materials and Methods

Experimental animals: Male Fischer 344 rats, 3 weeks and 6, 12, 18 and 24 months of age, were used throughout the experiments. Animals were killed by decapitation: then brains were removed quickly, frozen in powdered dry ice, and stored at -80°C until assay.

Sagittal sections 12 mm in thickness were cut on a cryostat and thaw-mounted onto gelatin-coated cover slides. Adjacent sections stained with Cresyl violet were examined with a light microscope.

Receptor autoradiography

[^{3}H]PDBu binding

Autoradiographic localization of PDBu binding in the brain was performed as described previously[12,13]. Brain sections were incubated with 2.5 nM [^{3}H]PDBu (New England Nuclear, spec. act. 20.7 Ci/mmol) in 50 mM Tris-HCl buffer (pH 7.7) containing 100 mM NaCl and 1 mM NaCl for 60 min at 25°C. Following incubation, the sections were washed twice at 4°C for 2 min in the buffer and briefly rinsed in distilled water at 4°C. Non-specific binding was determined using 1 μM PDBu (Sigma).

[^{3}H]Forskolin binding

Autoradiographic distribution of forskolin binding was performed as described previously[14,15]. Brain sections were incubated with 10 nM [^{3}H]forskolin (New England Nuclear, spec. act. 33.0 Ci/mmol) in 50 mM Tris-HCl buffer containing 100 mM NaCl and 5 mM $MgCl_2$ for 10 min at 25°C. Following incubation, the sections were washed twice for 2 min at 4°C in the buffer. Non-specific binding was determined using 10 μM forskolin (Sigma).

All procedures were performed under subdued lighting. The sections were dried under a cold air stream and apposed to Hyperfilm-^{3}H (Amersham) for 7 days (PDBu binding) and 4 weeks (forskolin binding) in X-ray cassettes with a set of tritium standards. The optical density of the brain regions was measured by a computer-assisted image analyzer as described previously[14,15]. The relationship between optical density and radioactivity was obtained with reference to ^{3}H-microscales co-exposed with the tissue sections using a third-order polynomial function. Anatomical structures were verified by examination of Cresyl violet-stained sections. Binding assays were performed in duplicate. Values were expressed as mean± S.E. Statistical comparisons were determined using the ANOVA following by Dunnett's multiple comparison test. Each group contained five to seven animals.

Results

Regional age-related alterations of [^{3}H]PDBu and [^{3}H]forskolin bindings are summarized in Tables 1 and 2.

[^{3}H]PDBu binding

Regional distribution of [^{3}H]PDBu binding throughout the brain was relatively heterogeneous. In adult rats (6-month-old), the highest density of [^{3}H]PDBu binding was noted in the molecular layer of cerebellum, hippocampus and neocortex. The striatum, nucleus accumbens, substantia nigra and thalamus also exhibited relatively high [^{3}H]PDBu binding. Other regions such as hypothalamus, midbrain and brain stem had a low grain density of [^{3}H]PDBu binding. In immature rats (3-week-old), the cerebellum showed a significant decrease in [^{3}H]PDBu binding as compared to that in adult animals. However, other regions exhibited no significant change in [^{3}H]PDBu binding. In contrast, no significant changes of [^{3}H]PDBu binding was observed in all brain areas in 12-, 18- and 24-months-old rats, as compared with 6-month-old rats.

[^{3}H]Forskolin binding

Autoradiographic localization of [^{3}H]forskolin binding in the rat brain was strikingly heterogeneous. In adult animals, the highest binding was noted in the striatum and nucleus accumbens followed by the hilus of the dentate gyrus, the molecular layer of the cerebellum, the hippocampal CA3 pyramidal layer and substantia nigra. Other regions showed relatively low [^{3}H]forskolin binding. In immature rats, a significant increase in [^{3}H]forskolin binding was observed in the neocortex, nucleus accumbens, thalamus and substantia nigra. Other regions revealed no significant changes in [^{3}H]forskolin binding. On the other hand, [^{3}H]forskolin binding was not significantly changed in the rat brain of 12-month-old rats. However, [^{3}H]forskolin binding in various brain regions showed a significant decline in 18-month-old rats. The age-related reduction was noted in the neocortex, hippocampal CA3 pyramidal cell layer, dentate gyrus, thalamus and molecular layer of the cerebellum. In 24-month-old rats, [^{3}H]forskolin binding showed significant decreases in various brain regions, as compared with 6-month-old animals.

Discussion

The present study provides evidence that adenylate cyclase system in the rat brain was more susceptible to aging processes than phosphoinositide cycle system. Furthermore, our autoradiographic results suggest that the change in the adenylate cyclase system is more pronounced than that in the phosphoinositide cycle system in immature rat brain. These findings suggest that the adenylate cyclase system is primarily affected in aging processes and this may lead to neurological deficits.

Aging in mammals is associated with striking changes in neurotransmission which may underlie the age-related deficits in psychomotor performance and cognitive function1,16). Numerous previous studies suggest that the binding sites of various neurotransmitters, such as acetylcholine, glutamate, dopamine, serotonin and noradrenaline, are altered in various brain regions during aging processes17-22). Furthermore, a selective loss of glutamate receptors and cholinergic neurons has been reported in the brain of Alzheimer's disease23-26).

Thus, alterations in neurotransmitter receptors may play a key role not only in aging processes, but also in age-related neurodegenerative process such as Alzheimer' s disease.

Intracellular second messenger systems are well known to be crucial to various aspects of cellular functions. In particular, much evidence has emerged over the past decade to suggest that PKC in phosphoinositide cycle system is a widespread family of kinases responsible for neurotransmitter release, neuronal activity, synaptic plasticity, long-term potentiation (LTP), growth and differentiation27-29). Therefore, this enzyme is thought to play a major role in neuronal function. Previous investigations suggested an impaired PKC function in T lymphocytes of aged mice and a reduced phosphorylation of protein F_1, a specific endogenous PKC substrate in aged rat brain30,31). Friedman and Wang10) also demonstrated the reduced PKC activity in aged rat brain. On the other hand, several neurotransmitters are known to stimulate the formation of cyclic-AMP by activation of adenylate cyclase32). Cyclic-AMP plays a role in expression or activation of ion channels and acetylcholine receptors33,34). Further, the cyclic-AMP cascade including adenylate cyclase is involved in learning, short-term memory and synaptic plasticity35,36). Nomura et al8). also suggest that basal activity of brain adenylate cyclase was significantly reduced in aged rats. Therefore, the adenylate cyclase system is rather likely implicated in aging processes as well as cognitive function.

In the present study, a significant decrease in [^{3}H]PDBu binding was observed only in the cerebellum of 3-week-old rats as compared with 6-month-old animals. In contrast, a significant increase in [^{3}H]forskolin binding was found in various brain regions, such as cerebral cortex, nucleus accumbens, thalamus and substantia nigra of 3 week-old animals. Interestingly, ontogenetic studies of PKC in the rat brain have demonstrated that this enzyme increases rapidly after birth and reaches the maximal level at about 4 weeks of postnatal age37,38). Therefore, no significant changes in [^{3}H]PDBu binding in most brain areas of 3-week-old rats observed in our study may reflect that the binding rapidly reaches near the adult level in the brain after birth. Although the detailed reason for this phenomenon is presently unclear, our finding may suggest the conspicuous differences in the developmental pattern between [^{3}H]PDBu and [^{3}H]forskolin binding in the brain after birth.

On the other hand, the present study also showed that age-related change in [^{3}H]forskolin binding was noted in various brain regions, whereas no significant alterations in [^{3}H]PDBu binding were observed in the brain of aged rats. In particular, the age-related reduction in [^{3}H]forskolin binding was observed in the cerebral cortex, striatum, nucleus accumbens, hippocampus such as CA3 pyramidal cell layer and dentate gyrus, thalamus and molecular layer of cerebellum. This finding seems to relate the finding that basal activity of adenylate cyclase is significantly decreased in aged rat brain. From these observations, we suggest that adenylate cyclase system in most brain regions may be susceptible to aging processes as compared with phosphoinositide cycle system. However, several subtypes of

PKC have been identified by protein purification and by cloning of cDNAs[39-42]. Therefore, it is necessary to investigate the regional pattern of each subtype of PKC for the further understanding of age-related changes in the brain using receptor autoradiographic and immunohistochemical techniques.

There is abundant evidence that several neurotransmitters, their marker enzymes and any neurotransmitter receptors are significantly reduced in brain tissue from Alzheimer's disease[23-26,43-47]. The dysfunction of intracellular second messenger systems is also known to occur in such age-related neurodegenerative disorders as Alzheimer's disease. Several studies have shown a marked reduction of PKC levels and the number of 1,4,5-trisphosphate(1P3) bindion in the neocortex and hippocampus of Alzheimer's disease patients[48,49]. Dewer et al[50]. also reported that [^{3}H]forskolin binding was significantly reduced in the cerebral cortex of Alzheimer's disease. These observations seem to suggest that the dysfunction of second messenger systems may reflect the impairment of cognitive function occurring not only in aged animals, but also in age-related neurodegenerative disorders such as Alzheimer's disease. Therefore, our finding may help to further elucidate the relationship between aging processes and cognitive function. However, the present study could not determine whether the observed changes in [^{3}H]PDBu and [^{3}H]forskolin bindings are due to changes in the affinity constant (Kd) or the number of binding sites (Bmax). Therefore, further studies are needed to investigate the precise biochemical mechanisms for our findings.

Conclusion

The present study demonstrates that adenylate cyclase system in the rat brain is more susceptible to aging processes than phosphoinositide cycle system. Furthermore, our results suggest that the changes in the adenylate cyclase system are more pronounced than that in the phosphoinositide cycle system in immature rat brain. These findings suggest that intracellular signal transduction is affected in aging processes and this may provide a new approach to age-related neurological deficits.

References

1) Bartus R. T., Dean R. L., Beer B. et al., Scinece **217** (1982) 408.
2) Beninger R. T., Brain Res. Rev. **6** (1983) 173.
3) Dunbar G. L., Rylett R. J., Schmidt B. M. et al., Brain Res. **604** (1993) 266.
4) Ikegami S., Behav. Brain Res. **65** (1994) 103.
5) Morris P. G.M., J. Neurosci. **9** (1989) 3040.
6) Nichols R., Haycock J. W., Wang J. K. T. et al., J. Neurochem. **48** (1987) 615.
7) Nishizuka Y., Nature **334** (1988) 661.
8) Momura Y., Makihata J. and Segawa T., Eur. J. Pharmacol. **106** (1984) 437.
9) Fordyce D. E. and Wehner J. M., Neurobiol. Aging **14** (1993) 309.
10) Friedmann, E. and Wang, H.-Y., J. Neurochem. **52** (1989) 187.
11) Worley P. F., Baraban J. M. and Snyder S. H., Ann. Neurol. **21** (1987) 217.
12) Araki T., Kato H. and Kogure K., Brain Res. Bull. **28** (1992) 843.
13) Araki T., Kato H., Hara H. et al., Neuroscinece **46** (1992) 973.
14) Araki T., Kato K., Kanai Y. et al., J. Neural Transm. **97** (1994) 135.
15) Araki T., Kato H., Kanai Y. et al., Neurochem. Int. **23** (1993) 541.
16) Joseph J. A., Bartus R. T., Clody D. et al., Neurobiol. Aging **4** (1983) 313.
17) Gozlan H., Daval G., Verge D. et al., Neurobiol. Aging **11** (1990) 437.
18) Morelli M., Mennini T., Cagnotto A. et al., Neuroscinece **36** (1990) 403.
19) Najlerahim A., Francis P. T. and Bowen D. M., Neurobiol. Aging **11** (1990)155.
20) Scarpace P/J. and Abrass I. B., Neurobiol. Aging **9** (1988) 53.
21) Wagster M. V., Whitehouse P. J., Walker L. C. et al, J. Neurosci. **10** (1990) 2879.
22) Wenk G. L., Walker L. C., Price D. L. et al., Neurobiol. Aging **12** (1990) 93.
23) Coyle J. T., Price D. L. and Delong M. R., Science **219** (1983) 1184.
24) Greenamyre J. T., Penney J. B., D'Amato C. J. et al., Science, **227** (1985) 1496.
25) Greenamyre J. T., Penney J. B., D'Amato C. J. et al., J. Neurochem. **48** (1987) 543.
26) Simpson M. D. C., Royston M. C., Deakin J. F. W. et al., Brain Res. **462** (1988) 76.
27) Alkers R. F., Lovinger D. M., Colley P. A. et al., Science **231** (1986) 587.
28) Nishizuka Y., Nature **308** (1984) 639.
29) Nishizuka, Y., Science **233** (1986) 305.
30) Barnes C. A., Mizumori S. J. Y., Lovinger D. M. et al., Neurobiol. Aging **9** (1988) 393.
31) Miller R. A., J. Immunol. **137** (1986) 805.
32) Phillis J. W., Can. J. Neurol. Sci. **2** (1977) 153.
33) Artalejo C. R., Ariano M. J., Perlman R. L. et al., Nature **348** (1990) 239.
34) Ifune C. K. and Steinbach J. H., Brain Res. **506** (1990) 243.
35) Buxbaum J. D. and Dudai Y., J. Biol. Chem. **264** (1989) 9344.
36) Zhong Y., Budnik V. and Wu C. F., J. Neurosci. **12** (1992) 644.
37) Turner R. S., Raynor R. L., Mazzei G. J. et al., Proc. Natl. Acad. Sci. USA **81** (1984) 3143.
38) Wise B. C., Anderrson R. G. G., Mackerlova L. et al., Biochem. Biophys. Res. Commun. **99** (1981) 407.
39) Housey G. M., O Brien C. A., Johanson M. D. et al., Proc. Natl. Acad. Sci. USA **84** (1987) 1065.
40) Huang K. P. and Huang F. L., J. Biol. Chem. **261** (1986) 14781.
41) Knopf J. L., Lee M. H., Sultzman L. A. et al., Cell **46** (1986) 491.
42) Ono Y., Kikkawa U., Ogita K. et al., Science **236** (1987)1116.
43) Cross A. J., Crow T. J., Ferrier I. N. et al., J. Neurochem. **43** (1984) 1574.
44) Cross A. J., Crow T. J., Perry E. K. et al., Br. Med. J. **282** (1981) 93.
45) Flynn D. D., Ferrari-DiLeo G., Mash D. C. et al., J. Neurochem. **64** (1995) 1888.
46) Mash D. C., Flynn D. D. and Potter L. T. et al., Science **228** (1985) 1115.
47) Palmer A. M. and Burns M. A., J. Neurochem. **62** (1994) 187.
48) Cole G., Dobkins K. R., Hansen L. A. et al., Brain Res. **452** (1988) 165.
49) Young L. T., Kish S. J., Li P. P. et al., Neurosci. Lett. **94** (1988) 198.
50) Dewer D., Horsburgh K., Graham D. I. et al., Brain Res. **511** (1990) 241.

Table 1. Regional age-associated changes in [^{3}H]PDBu binding in the rat brain.

Region	Age				
	3 weeks	6 months	12 months	18 months	24 months
Frontal cortex	852 ± 176	762 ± 71	801 ± 110	821 ± 91	732 ± 68
Parietal cortex	808 ± 204	895 ± 249	772 ± 103	794 ± 91	700 ± 74
Striatum	743 ± 134	622 ± 49	654 ± 42	741 ± 175	634 ± 55
Nucleus accumbens	785 ± 162	701 ± 112	725 ± 79	854 ± 313	776 ± 55
Hippocampus					
CA1 sector	960 ± 252	1091 ± 226	998 ± 125	1018 ± 66	891 ± 71
CA3 sector	896 ± 212	894 ± 80	885 ± 143	910 ± 159	875 ± 62
Dentate gyrus	888 ± 181	896 ± 56	906 ± 120	900 ± 95	901 ± 95
Thalamus	614 ± 140	501 ± 26	499 ± 85	529 ± 98	510 ± 43
Substantia nigra	727 ± 193	662 ± 112	602 ± 192	615 ± 137	668 ± 81
Cerebellum					
Molecular layer	1042 ± 120 *	1259 ± 90	1358 ± 133	1234 ± 123	1213 ± 94
Granule cell layer	410 ± 42 **	483 ± 58	465 ± 51	541 ± 70	477 ± 18

Optical density was coverted to fmol/mg tissue using [^{3}H]microscales. Values are expressed as means±S.E. *$p<0.05$, **$p<0.01$ vs 6 months old group (Dunnett's multiple range test). n=5-7

Table 2. Regional age-associated changes in [^{3}H]forskolin binding in the rat brain.

Region	Age				
	3 weeks	6 months	12 months	18 months	24 months
Frontal cortex	75 ± 7 **	56 ± 6	53 ± 5	46 ± 4 *	45 ± 9 *
Parietal cortex	78 ± 7 *	62 ± 11	63 ± 8	52 ± 11	54 ± 9
Striatum	269 ± 34	255 ± 17	236 ± 46	215 ± 13	201 ± 40 *
Nucleus accumbens	263 ± 23 *	222 ± 19	214 ± 25	205 ± 19	174 ± 32 **
Hippocampus					
CA1 sector	40 ± 9	33 ± 7	33 ± 7	30 ± 5	32 ± 8
CA3 sector	79 ± 8	73 ± 13	75 ± 10	59 ± 9	60 ± 16
CA3 pyramidal-cell layer	127 ± 14	134 ± 15	125 ± 15	105 ± 15 **	106 ± 19 **
Dentate gyrus	88 ± 11	80 ± 7	77 ± 5	71 ± 7	69 ± 8 *
Hilus	194 ± 19	183 ± 31	193 ± 20	178 ± 19	160 ± 22
Thalamus	101 ± 7 **	47 ± 7	47 ± 4	34 ± 8 *	35 ± 11 *
Substantia nigra	193 ± 41 **	118 ± 19	102 ± 15	99 ± 17	87 ± 14
Cerebellum					
Molecular layer	169 ± 20	161 ± 16	149 ± 8	142 ± 8 *	132 ± 8 *
Granule cell layer	50 ± 9	52 ± 12	53 ± 8	47 ± 9	45 ± 7

Optical density was coverted to fmol/mg tissue using [^{3}H]microscales. Values are expressed as means±S.E. *$p<0.05$, **$p<0.01$ vs 6 months old group (Dunnett's multiple range test). n=5-7.

III. 12. Effect of Sewage on Plasma Cortisol and Element Concentrations in Goldfish, *Carassius auratus*

Kakuta I. and Ishii K.[*]

Department of Biotechnology, Senshu University of Ishinomaki
*Department of Nuclear Engineering, Tohoku University**

Raw sewage contains high levels of BOD, ammonia, nutritive salts and other pollutants. Ammonia, in particular, is a serious toxicant to aquatic animals[1-3). High BOD also causes the decrease in dissolved oxygen (DO), while low DO lowers the lethal concentrations for various toxicants[4-6). Raw sewage thus give harmful effects on the health of fish in and around the inflow area.

It is well known that plasma cortisol increases under stress conditions[7,8). Elemental contents of plasma may provide a good indication of the physiological conditions of fish, as it has been known in mammals that the contents are related closely to the host's health[9,10). In the present study, the effect of exposure to raw sewage on plasma cortisol and element levels of goldfish were investigated.

Materials and Methods

Goldfish, *Carassius auratus*, weighing about 8g were used in the experiment. Fish were adapted to 20°C for 2 weeks in an indoor tank with 60ℓ of dechlorinated water. During the rearing period, they were fed with a commercial diet. They were examined after being fasted for 24 hours. The experiment was performed at a constant temperature of 20°C. Throughout the experimental period, fish were fasted.

Raw sewage collected at the influx of a sewage plant in Miyagi Prefecture. For the test group, this sewage was diluted to 10% and 50% with temperature adjusted dechlorinated water. Experimental fish were exposed to undiluted and diluted raw sewages for 3 days. Throughout the experimental period, control fish were kept in dechlorinated water. Each tank had twenty fish. Half of the rearing water was exchanged softly every day. The dissolved oxygen levels (DO) were not less than 6mg/l during the experiment. Water quality of experimental tank was measured by the methods[11) described previously.

Blood was collected from the heart of alive fish in the experimental groups using a heparin-treated syringe. After measurement of haemoglobin (Hb) concentration, the levels of eight elements in plasma were measured by PIXI11). Plasma cortisol was also measured by the method using Gammacoat [^{125}I] cortisol12).

Results

Water quality in tanks at the beginning of this experiment is shown in Table 1. Parameters of raw sewage in the initial period were several hundreds times for BOD and ammonia-N, hundred times for total-N, several ten times for total-P, K and Mg, ten times for Na, Ca, Cl and Fe and two to three times for Cu and Zn in comparison with those of the control.

Goldfish exposed to undiluted raw sewage exhibited occasionally laboured respiratory movement in subsequent several hours. No fish exposed to 10% and 50% raw sewages exhibited significant changes in behavior. No fish died during this experiment. In goldfish exposed to undiluted raw sewage, a slight hemolysis was observed.

Changes in Hb, plasma cortisol and elements of goldfish exposed to sewages are shown in Table 2. When fish were exposed to undiluted raw sewage, decreases in Hb and plasma Zn and increases in plasma P, Br and cortisol were found after 3 days. In goldfish exposed to 50% raw sewage for 3 days, significantly higher values for plasma P, Br and cortisol and lower values for Fe and Zn than those of the control were found. Elevated plasma cortisol was closely related to increase in the concentration of sewage. No statistically significant changes in these blood parameters were found in fish exposed to 10% sewage for 3 days, however, a slight increase in plasma cortisol was observed.

Discussion

Chemicals such as ammonia and copper exert genaral stress effects, that is, increase cotrisol and catecholamines in plasma. Raw sewage contained much higher level of ammonia-N compared to that of the control. Significant increase in plasma cortisol in goldfish exposed to 50% and undiluted sewages was found. In fish exposed to 10% sewage, a slight increase in cortisol was also observed. It is thus considered that goldfish exposed to sewages incurred considerable stress and might have physiological abnormalities even in 10% sewage even with sufficient DO in water.

In this study, plasma Zn decreased 3 days after the exposure to 50% and undiluted sewages. Catecholamines stimulate the urine excretion of K, Mg and Zn13,14). Adrenocorticosteroid decreases Zn in plasma15). These could account for the decreased Zn. It has been suggested that elevated cortisol16) and lowered Zn9,10) levels in plasma reduces powers of biodefence. It may thus be possible that goldfish exposed to sewages are subjected to suppression of the immune response. Elevated glucocorticoids in plasma also facilitate P release from the bones17,18). The reason why plasma Br increased and Fe decreased is not clear. Changes in plasma P, Br and Fe in the test group may have resulted from transfer to these elements between plasma and various tissues and/or are inversion of these elements from environmental water during the exposure.

It follows from the present data that goldfish exposed to sewages incur physiological abnormalities, even to 10% sewage for 3 days. Immediate construction and improvement projects of municipal and regional sewage treatment plants with high treatment capacity are thus required.

References

1) Danecker E., Osterreichs Fischerei **3/4** (1964) 55.
2) Smart G. R., J. Fish Biol. **8** (1978) 471.
3) Thurston R. V., et al., Trans. Am. Fish. Soc. **107** (1978) 361.
4) Downing K. M. and Merkens J. C., Ann. Appl. Biol. **43** (1955) 243.
5) Merkens J. C. and Downing K. M., Ann. Appl. Biol. **45** (1957) 521.
6) McKee J. E. and Wolf H. W., Water Quality Criteria (1963) 548.
7) Hirano T. and Utida S., Endocrinol. Japan. **18** (1971) 47.
8) Demael A. and Garin D., Cahiers du Laboratoire de Montereau **7** (1978) 15.
9) Hayashi O., Bunseki **6** (1989) 427.
10) Hemphill D. D., Biomed. Res. Trace Elements **3** (1992) 1.
11) Kakuta I., et al., Comp. Biochem. Physiol. **107C** (1994) 289.
12) Jibiki K., et al., Horumon to Rinsho **128** (1980) 1127.
13) Saito N. and Konishi Y., Biomed. Res. Trace Elements **2** (1991) 31.
14) Tanaka S., et al., Biomed. Res Trace Elements **2** (1991) 33.
15) Wada O., "Kinzoku to Hito" Asakura, Tokyo (1985) 82.
16) Ikeda Y., "Discharge from municipal sewarage and marine environment" (Sekine T., et al., eds), Koseisya-koseikaku, Tokyo (1987) 56.
17) Rasmussen H., et al., Am. J. Med. **56** (1974) 751.
18) Fucik R. E., et al., J. Clin. Endocr. **40** (1975) 152.

Table 1. Water quality in tank at the beginning of this experiment.

		Control	Raw sewage
pH		6.9	7.1
BOD	(mg/l)	0.2	140
Total-N	(mg/l)	0.2	23.2
Ammonia-N	(mg/l)	0.04	16.1
Total-P	(mg/l)	0.1	7.2
Na	(mg/l)	18	127
K	(mg/l)	1.4	36
Ca	(mg/l)	3.5	37
Mg	(mg/l)	0.9	28
Cl	(mg/l)	10	90
Fe	(mg/l)	0.02	0.24
Cu	(mg/l)	0.01	0.02
Zn	(mg/l)	0.01	0.03

Table 2. Changes in haemoglobin (Hb), plasma cortisol and elements of goldfish exposed to sewages for 3 days.

		Control	Raw sewage		
			10%	50%	100%(undiluted)
Hb	(g/100ml)	7.3±0.4	6.9±0.8	6.4±0.9	6.2±0.7*
P	(mg/l)	174±34	195±46	242±38*	229±34*
Cl	(mg/l)	3530±345	3625±420	3360±320	3375±315
Ca	(mg/l)	123±27	141±41	140±36	127±28
K	(mg/l)	118±29	132±36	107±39	126±28
Fe	(mg/l)	0.3±0.1	0.4±0.2	0.2±0.1*	0.3±0.1
Cu	(mg/l)	0.1±0.1	0.1±0.1	0.2±0.2	0.1±0.1
Zn	(mg/l)	2.4±0.5	1.9±0.8	1.5±0.6*	1.6±0.5*
Br	(mg/l)	1.2±0.4	1.5±0.7	2.1±0.6*	1.8±0.5*
Cortisol	(ng/ml)	69±23	82±36	126±43*	162±65*

Data are given as mean ±S. D., N=8.

* Significant difference from those of the control ($p<0.05$).

IV. BIOLOGY AND MEDICINE (Clinical)

IV. 1. 3D PET system with supercomputer

Fujiwara T., Watanuki S., Itoh M., Ishii K., Orihara H., Yamamoto S., and Takahashi S.**

Cyclotron and Radioisotope Center, Tohoku University
*Shimadzu Corporation, Kyoto**

The main advantage of 3D data acquisition in PET using enlarged field of view scanners with retracted septa is the better sensitivity to 2D imaging with septa. The SET-2400W is a newly designed whole body tomograph with 20 cm axial filed of view. Since full 3D acquisition and reconstruction required large data files and extended computational time for a built-in workstation, we developed 3D reconstruction system with a supercomputer.

Materials and Methods

The tomograph consists of four rings of 112 BGO detector units (22.8 mm in-plane × 50 mm axial × 30 mm depth). Each detector unit has 6 (in-plane) × 8 (axial) matrix of BGO crystals coupled to two dual photo multiplier tubes. Crystal size is 3.8 mm (in-plane), 6.25 mm (axial) and 30 mm (depth). The detectors are arranged in 32 rings with 672 crystals each. Axial field of view is 200 mm. Sixty-three sinograms are stored in a large scale of acquisition memory (1 GBytes) in 2D mode. All sinograms have corrections for normalization and attenuation that are obtained from blank, transmission, and calibration scans. A ^{68}Ge-^{68}Ga external rod source (10 mCi) can be orbited at 640 mm radius to measure blank scan and 2D transmission scan data. Total sensitivity in 2D mode was 220 kcps/μCi/ml with coincidence path acceptance of neighboring rings. Total sensitivity in 3D mode was 3600kcps/μCi/ml before scatter subtraction. In-plane resolution in 2D mode was 3.9 mm FWHM at the center and 4.4 mm FWHM tangentially, 5.4 mm FWHM radially at 100 mm from the center. Average axial resolution in 2D mode was 4.5 mm FWHM at the center and 5.8 mm FWHM at 100 mm from the center. In-plane resolution in 3D mode was 5.7 mm FWHM at the center and 6.0 mm FWHM tangentially, 6.5 mm FWHM radially at 100 mm from the center. Average axial resolution in 3D mode was 7.9 mm FWHM at the center. Average scatter fraction in 2D mode among all slices for septa in was 8%. For septa out, average scatter fraction was increased up to 40%. Maximum count rate for all slices was 210 kcps (3.0μCi/ml) in 2D mode and 340 kcps (0.3μCi/ml) in 3D mode.

The 2D data were processed using the standard SET-2400W reconstruction software. In 3D mode, all possible coincidence pairs of 1024 sinograms are stored in the same memory.

Corrections for dead time and decay of radioisotopes can be performed in real-time in the memory. All data are transferred to TITAN-2 (Kubota, Tokyo) workstation connected via VME-bus. The workstation provides control for the system and a 2D and 3D image reconstruction unit. A 2D set of 63 sinograms requires 5.7 Mbytes. A full 3D sinogram requires 124 Mbytes. In order to reconstruct the 3D images, all data were transferred to a supercomputer (SX-3/44R, NEC, Tokyo) via FDDI network. This computer has 25.6 Gflops of maximum operating speed. The reconstruction processes were summarized in figure 1. For the reduction of the scattered photons in the final images, the 3D reconstructed images are digitally post processed using a low pass filter and these images are weighted and subtracted from the original 3D images to remove the scattered photons1).

Results

All data were transferred from storage disks in the workstation to the working area of SX-44/R with the speed of 3 MBytes per second. It took 4 min for the full reconstruction of a 3D image with SX-44/R, where same data sets took more than 4 hours with TITAN-2. The brain images of the normal volunteer administered with 2.4 mCi of ^{18}F-FDOPA are shown in figure 2. Clear visualization of striatum in 3D mode is noticeable. Whole body multiposition FDG scans of 3D data acquisition and reconstruction are shown in figure 3. Only 9 positions were necessary to obtain an overview of the FDG uptake in all the organs of interest including the brain, heart, and bladder, corresponding to 540 image planes. For this case, the 3D emission scan time was 45 min.

Discussion

The main advantage of 3D PET is the detection of lower tracer activities. The 3D PET has obvious advantage of better signal to noise ratio compared with 2D imaging and may preferable to 2D PET where tracer accumulation in well defined regions is expected. This is especially important for the studies of the distributions of ligands for neuroreceptors such as ^{18}F-FDOPA, ^{11}C-Benztropine, and ^{11}C-Doxepin since these ligands show low accumulation in brain. Reduction of scanning time is also useful for patients who are not permitting extended scanning periods. The scanner with enlarged field of view enables whole body scanning with short examination time and may be useful for cancer detection. Since fully 3D image reconstruction requires considerable amount of computational time compared with 2D reconstruction, several limited 3D reconstruction algorithms were proposed for reduction of time2). The algorithms are useful to the object in the center of the field of view such as brain. However, these approaches are not applicable for whole body 3D reconstruction. Although the substantial progress in computer hardware has been occurring in the past years, reconstruction time with a single workstation is not enough at present. The use of a high-speed processor such as supercomputer will be one approach of the reduction of reconstruction time.

References

1) Sashin D. et al., IEEE Conference on Nuclear Science and Medical Imaging (1993) 1332.
2) Townsend D. W., Quantification of Brain Function (1993) 3.

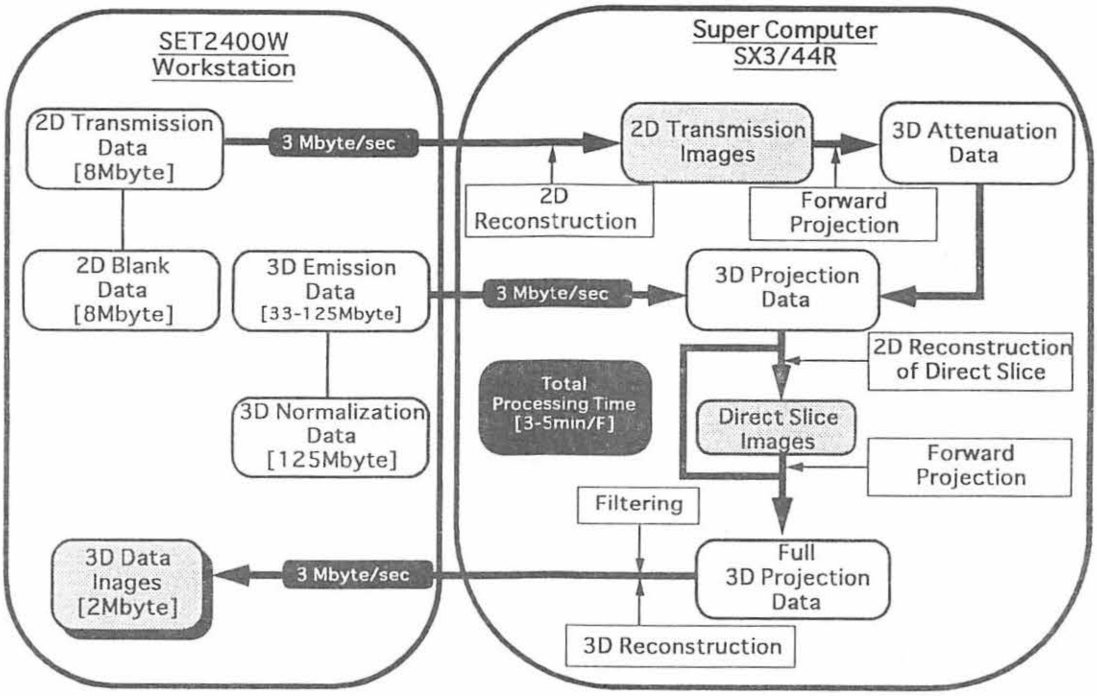

Fig. 1. Flow chart of 3D data processing.

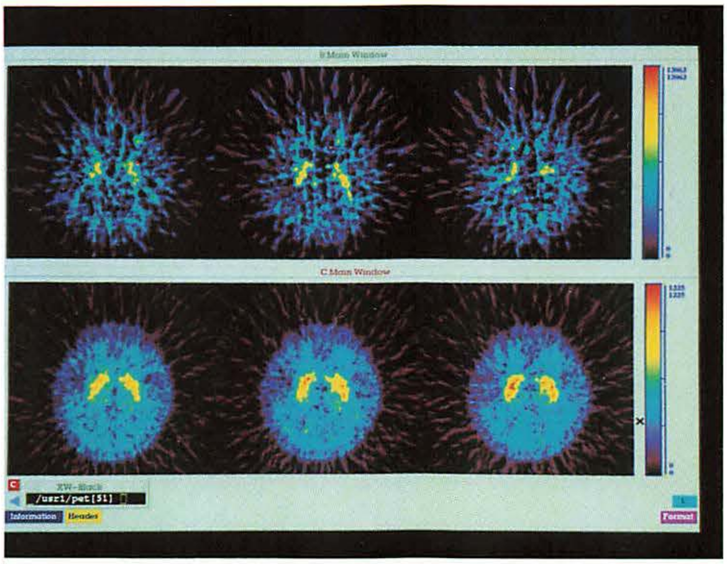

Fig. 2. Representative brain sections of normal volunteer imaged with ^{18}F-FDOPA with 5 min 2D scan (top) and 5 min 3D scan (bottom).

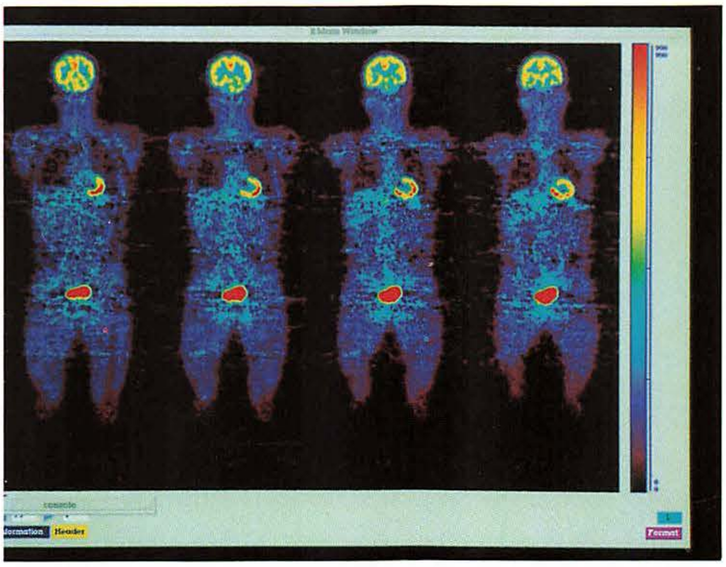

Fig. 3. Whole-body 3D PET images shows normal distribution of accumulation of ^{18}F -FDG (1 mCi) in contiguous coronal sections.

IV. 2. Functional Anatomical Studies of Encoding and Retrieval in Verbal Recognition Tasks

Fujii T., Kawashima R., Okuda J., Yamadori A., Fukatsu R.**,*
*Suzuki, K., Ito M.***, Goto R.*, and Fukuda H.**

Department of Neuropsychology, Tohoku University Graduate School of Medicine
*Institute of Development Aging & Cancer (IDAC), Tohoku University**
*Department of Neurology, Miyagi National Hospital***
*Cyclotron and Radioisotope Center, Tohoku University****

Introduction

Several neuropsychological and neuroimaging studies have suggested that the human hippocampal regions play an important role in memory processing[1,2]. However, a number of studies relevant to memory function have failed to show activations of the medial brain structures, damage to which causes amnesia, and little is known about the functional difference of each hippocampal region. In the present study, the different role of each hippocampal region in the verbal memory was investigated further using PET.

Methods

SUBJECTS

Nine healthy young male volunteers participated. All subjects were right handed. A written informed consent was obtained from each subjects.

TASK DESIGN

In each task, subjects listened to 30 words presented by a tape recorder through earphones. Except for the experiment 2, the list of 30 words was comprised of 15 different words, each of them appearing twice. Different lists were presented in each task. Average scores of imagery were equal in each list[3]. Control task: subjects were asked to repeat every other word heard. Experiment 1: subjects were instructed to repeat the words when heard for the first time and not to repeat the words when heard for the second time in this experiment. Then, before the experiment 2, subjects memorized the 15 words used in experiment 1. The list of 15 words was presented three times, and at this time subjects did not undergo the PET scan. Distraction task: subject's task was the same as the control task. Experiment 2: subjects were required to repeat the words memorized about 20 minutes before and not to repeat non-memorized words. This list consisted of 15 memorized and 15 non-memorized words.

SCANNING METHODS AND REGIONAL ANALUSIS

Regional cerebral blood flow (rCBF) was measured using PET (SET2400W, Shimadzu) and ^{15}O labeled water (approximately 35 mCi for each injection). All rCBF images were transformed into the standard anatomical format using Human Brain Atlas system4) and each subject's MRI. After the anatomical standardization procedure, subtractions of control from each task were calculated for each subject on a voxel by voxel basis. Then, descriptive t-images of each task minus control were calculated to find significant changes.

Results

Subjects were quite accurate in their behavioural performances in these two experimental tasks.

When compared with the control task, both the experiment 1 and experiment 2 tasks activated fields in the left cuneus, orbital cortex and caudate nucleus, in the right middle temporal, occipital association, premotor, insula, globus pallidus, anterior and posterior cingulate, and in the bilateral superior and middle prefrontal, inferior parietal association, precuneus and cerebellum. The regions activated during the experiment 1 task but not during experiment 2 task were listed in Table 1. Note that a number of activated regions are present in the left hemisphere; the left parahippocampal gyrus(see, Fig.1), the left basal forebrain, the left hypothalamus, the left putamen, the left inferior frontal gyrus, the left inferior occipital gyrus and the left superior temporal gyrus. On the other hand, the regions activated during experiment 2 task but not during experiment 1 task were listed in Table 2. Many regions in the both hemisphere were activated including the caudal part of the right parahippocampal gyrus(see, Fig.2), the right inferior frontal gyrus, the left amygdala, the left insula and the left precentral gyrus., although several posterior regions also revealed increased blood flow.

Discussion

Our experiment is, as far as we are aware, the first demonstration that the activity in each hippocampal region is related to the different verbal recognition task.

Common processes in the two experimental conditions and control condition are auditory analysis of the heard words and oral pronunciation of half of the heard words. These three conditions concurrently involve retrieval of information from semantic memory and encoding of information into episodic memory5). However, it can be surmised that the level of encoding processing differs considerably among these three tasks. Experiment 1 require deeper processing than does the experiment 2 because of the novelty of the stimuli5). It is probable that experiment 1 requires deeper encoding processing than does the control noun repetition task6). Therefore experiment 1 minus control task represents relatively deep episodic encoding and short-term episodic recognition. As compared with the control task, experiment 2 may require deeper encoding processing because this task is important for the subjects. So we assume that experiment 2 minus control noun repetition task represents shallower episodic encoding and long-term episodic recognition. The major differences between two experimental conditions were the depth of encoding processing and the retention interval.

According to the reasoning above outlined, deeper encoding and short-term episodic recognition(experiment 1) are associated with blood flow increase in the left hippocampal region. Shallower episodic encoding and long-term episodic recognition(experiment 2) are associated with blood flow increase in the right hippocampal region.

It is becoming increasingly clear that episodic encoding task involves activity in the left prefrontal regions and episodic retrieval task involves activity in the right prefrontal regions[5,7]. Because there are major connections between the dorsolateral prefrontal region and the hippocampus[8], it is not surprising that we found the left hippocampal activity together with the left prefrontal activity in the deeper encoding task and the right hippocampal activity together with the right prefrontal activity in the long-term recognition task. In the former task, we also found blood flow increase in the left inferior frontal region, on the contrary, in the latter task blood flow increase in the right inferior frontal region. We speculate that each hippocampal region have a strong functional relationship to ipsilateral inferior frontal region. In both experiments, we found blood flow increases in both superior and middle prefrontal regions. The right superior and middle prefrontal activity in the experiment 1 may reflect recognition processes despite of the retention interval. Longer retention interval may be necessary to activate the right hippocampal region. The left superior and middle prefrontal activity in the experiment 2 may be ascribable to encoding processes though the encoding processing was shallower as compared with the experiment 1. Deeper encoding processing may be required to activate the left hippocampal region.

Taking into account many regions activated in both tasks, specific neuronal networks including each hippocampal region may be involved in different aspects of the verbal memory processing.

Acknowledgement

This work was supported by a Grant-in Aid (05267103) for scientic research from the Ministry of Education, Science and Culture, Japan.

References

1) Buckner R. L., Petersen S. E., Ojemann, J. G. et al., J Neurosci. **15** (1995) 12.
2) Squire L. R. and Zola-Morgan S., Science. **253** (1991) 1380. 8) Goldman-Rakic, P. S., Selemon L. D. and Schwarts M. S., Neuroscience. **12** (1984) 719.
3) Ogawa T. and Inamura Y., Shinrigaku Kenkyu. **44** (1974) 317.
4) Roland PE., Graufelds C J., Wahlin J. et al., Human Brain Mapping. **1** (1994) 173.

5) Tulving E., Kapur S., Craik F. I. M. et al., Proc. Natl. Acad. Sci. USA. **91** (1994) 2016.
6) Slamecka N. J. and Graf P., J. Exp. Psychol. Hum. Learn. Mem. **4** (1978) 592.
7) Shallice T., Fletcher P., Frith C. D. et al., Nature. **368** (1994) 633.

Table 1. Activation foci associated with only experiment 1. Stereotaxic coordinates refer to the maximal activation indicated by the highest Z score in a particular cerebral structure. Distances refer to the stereotactic space defined by Talairach and Tournoux. Numbers in parenthesis refer to Brodmann areas.

	Anatomical Structure	x (mm)	y (mm)	z (mm)	t value
Left	Superior Temporal Gyrus(22)	50	-47	20	8.789
	Inferior Occipital Gyrus (17)	15	-96	0	6.113
	Inferior Frontal Gyrus (46)	41	35	10	10.26
	(45)	38	13	18	5.596
	Parahippocampal Gyrus (36)	18	-34	-13	11
	Subcallosal Gyrus	20	2	-8	5.447
	Hypothalamus	8	-1	-4	7.912
		6	-17	0	6.217
	Putamen	23	2	7	9.186
Right	Superior Occipital Gyrus (19)	-34	-80	31	5.313
	Orbital Gyrus (11)	-8	14	-19	5.16

Table 2. Activation foci associated with only experiment 2. Stereotaxic coordinates refer to the maximal activation indicated by the highest Z score in a particular cerebral structure. Distances refer to the stereotactic space defined by Talairach and Tournoux. Numbers in parenthesis refer to Brodmann areas.

	Anatomical Structure	x (mm)	y (mm)	z (mm)	t value
Left	Middle Temporal Gyrus (39)	42	-66	20	10.18
	Middle Occipital Gyrus (19)	45	-67	-4	5.816
	(19)	39	-74	5	14.45
	Superior Occipital Gyrus (19)	32	-88	24	9.698
	Precentral Gyrus (6)	41	-2	44	7.998
	(6)	16	-14	58	6.468
	Posterior Insula	38	-13	-8	5.762
	Anterior Insula	31	16	-1	5.802
		36	5	19	8.463
	Uncus (34)	12	-4	-20	8.089
Right	Lingual Gyrus (17)	-3	-88	-12	6.733
	(18)	-19	-80	-15	12.32
	Inferior Occipital Gyrus (18)	-30	-84	-9	5.081
	Cuneus (17)	-1	-85	9	7.347
	Intra Parietal Sulcus	-16	-62	34	7.612
	Inferior Frontal Gyrus (45)	-41	34	2	6.676
	Parahippocampal Gyrus (36)	-36	-28	-15	9.789
		-16	-48	-10	12.87

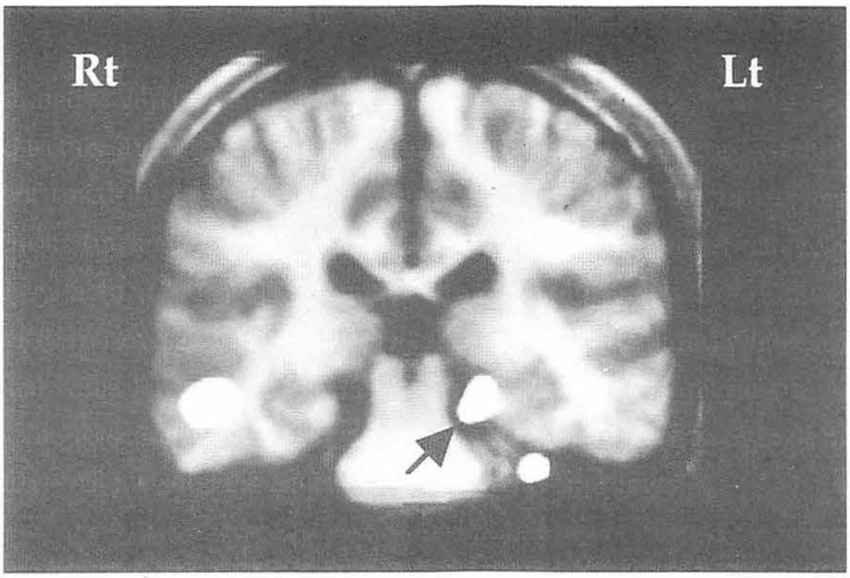

Figure 1. Parahippocampal regions significantly activated while performing experiment 1 compared to the control task. Areas of significant activation (p<0.001) have been superimposed on mean reformatted MRI of nine subjects. Black arrow indicates the activated left hippocampal region (18, -34, -13, t=11) during experiment 1.

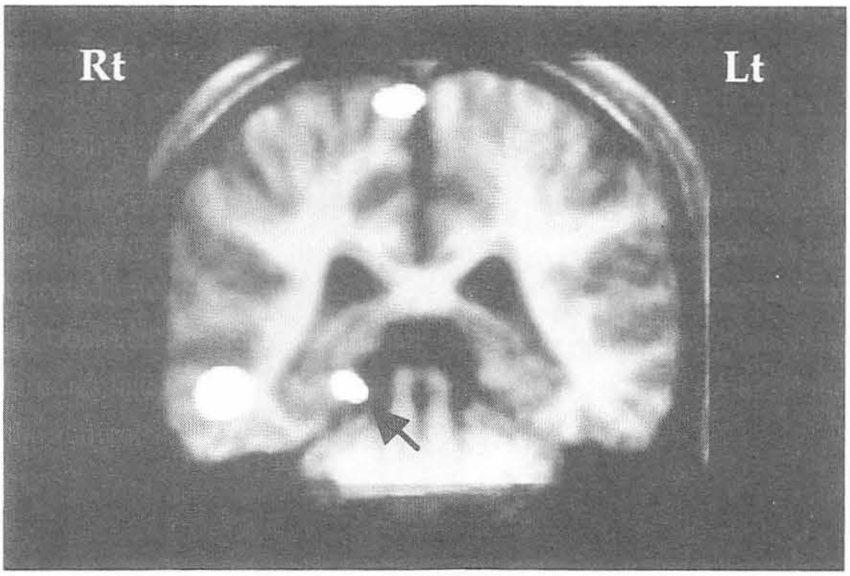

Figure 2. Parahippocampal regions significantly activated while performing experiment 2 compared to the control task. Areas of significant activation (p<0.001) have been superimposed on mean reformatted MRI of nine subjects. Black arrow indicates the activated focus of the caudal part of the right hippocampal region (-36, -28, -15, t = 9.789) during experiment 2.

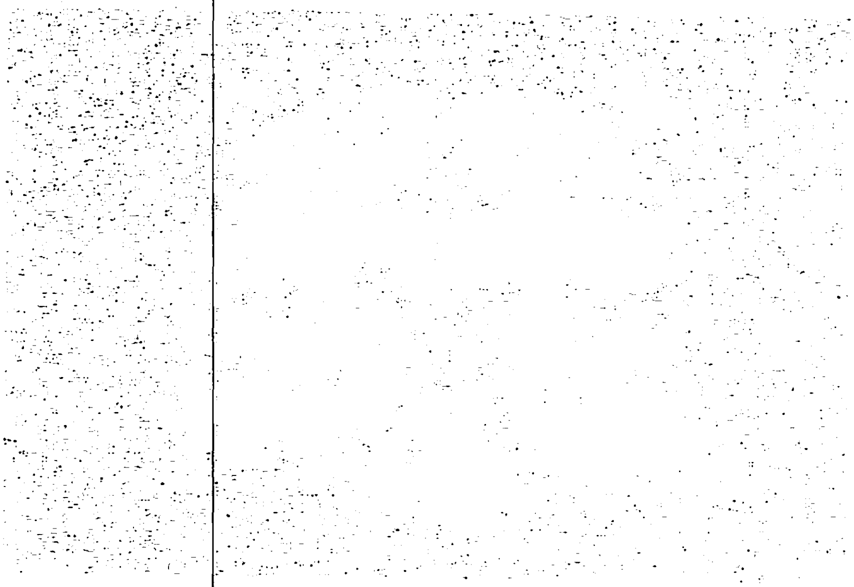

[illegible]

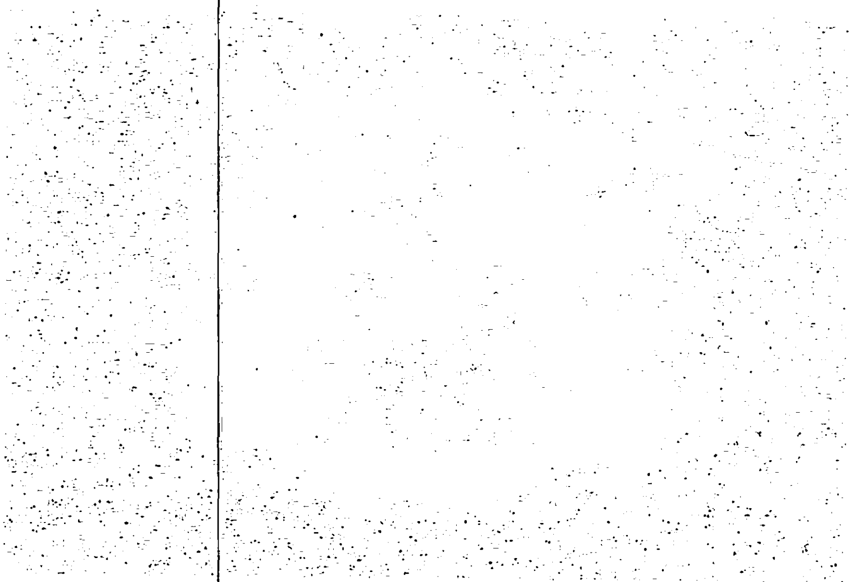

[illegible]

IV. 3. Neuroanatomical Correlates of Semantic Processing: A Positron Emission Tomographic Study

Imamura T., Nagasawa H., Masatoshi I., and Itoyama Y.*

Department of Neurology, Tohoku University School of Medicine,
*Division of Nuclear Medicine, Cyclotron and Radioisotope Center, Tohoku University**

Introduction

A recent theoretical framework of cognitive neuropsychology (Figure. 1) assumes that information about words is stored in a functional architecture, which consists of one central semantic system and modality-specific input and output lexicons1). Semantic system is a central structure of human language system, but its anatomical distribution has remained poorly understood. Several neuroscientists assessed this issue by cognitive activation study using positron emission tomography (PET), and obtained controversial results2-4). We here accessed this issue by an activation paradigm, that is, word finding. Subject are instructed to retrieve words in one minute with a given category (categorical word finding), or with a given initial letter (phonological word finding). These two types of the task are thought to use different component processes of cognitive structures5,6) and the schematic processes of the tasks are shown in Fig. 2. In categorical word finding (Fig. 2-A), a category is presented as an auditory word and accepted by semantic system. Then, semantic system prepares the representations of an adequate categorical word list. They activate phonological output representations one by one, and words are finally pronounced. In phonological word finding (Fig. 2-B), a presented letter is transferred, via a process of auditory analyses, to a certain problem solving system for strategic word search. Because there are no phonological representations of words in semantic system, the problem solving system directly controls phonological output lexicon and prepares the representations of an adequate word list. Then, the words are pronounced in the final process. Internal re-hearing (Fig. 2-B; broken arrows) may activate semantic system in phonological word finding. This process, however, is not essential for phonological word finding, and the activation would be in less degree than categorical word finding. In summary, categorical word finding activates semantic system and phonological output lexicon, while, phonological word finding activates problem solving system and phonological output lexicon. Thus, the across-task comparison is expected to detect relative activation of semantic system and problem solving system for strategic word search.

Subjects and Methods

SUBJECTS

Seven right-handed, native Japanese, normal volunteers (5 men and 2 women, age 27-65 years) were recruited to this study. We examined the subjects' ability for word finding before PET study, and confirmed no significant difference between their categorical and phonological word productions (mean ± SD words/min is 11.0 ± 5.2 with animal category and 9.1 ± 2.2 with initial syllable [a]; $t = 1.59$, n.s.). In phonological word finding, Japanese subjects are asked to retrieve as many words beginning with a certain syllable as possible because every initial Kana letter of words represents a syllable, not a phoneme, in Japanese writing system. The Research Ethics Committee of Tohoku University School of Medicine approved this study. All the subjects gave written informed consents.

POSITRON EMISSION TOMOGRAPHY

The PET study was performed with a scanner (PT931, CTI Inc., USA) at the Cyclotron and Radioisotope Center, Tohoku University, Sendai, Japan. A 15-minute transmission scan was performed using a retractable ^{68}Ge / ^{68}Ga ring source to correct tissue attenuation before the study. The subjects underwent two studies of regional cerebral blood flow (rCBF) by $C^{15}O_2$ steady state inhalation method with arterial blood samplings[7]. Subjects were blindfolded during the studies. After an instruction and a practice of each task, prepared cassette tape and earphone provided a series of 8 categories (fruit, bird, vehicle, stationery, flower, vegetable, fish, kitchen ware) or 8 syllables ([ta], [ko], [ma], [hi], [ka], [to], [ha], [ya]) at a rate of one per minute. Vocalization was prohibited during task performance and subjects' silence was confirmed by a microphone attached to the mask. In each study, the scanner collected emission data for 7 minutes after the first category or syllable was provided, and obtained 14 plains with an 8 mm of axial and transaxial resolution. The two rCBF studies had a 10 minutes of washout interval, and the order of the two tasks was balanced in the subjects.

DATA ANALYSIS

We reconstructed the calculated rCBF images to 36 interpolated plains parallel to the intercommissure line, and 3-dimensionally normalized to the coordinate reference space from the atlas of Talairach and Tournoux[8]. The voxel size was 1.3 × 1.3 × 2.6 mm. We performed across task comparisons of rCBF (categorical-phonological task, and phonological-categorical task) with voxel by voxel analysis of variance, and plotted the voxels with rCBF increase exceeding a threshold of probability of 0.05. A region was considered to be significantly activated if a spatially contiguous set of voxels were all independently significant at a level of $P < 0.05$ and if it had more than 20 mm of major axis. We believe these criteria for significant activation guard against excessive false positives in multiple comparison, and did not conduct a statistical correction for multiple comparison because of the explorative nature of this study.

Results

Figure 3 presents significantly activated regions in categorical or phonological word finding comparing to each other task. These regions are summarized in Table 1, with 3-dimensional coordinates of the midst voxel in Talairach's atlas8), Brodomann's area number, anatomical location, and inter-task difference of mean rCBF of midst nine voxels. In categorical word finding, two activated foci were observed in left temporal lobe. One of them was in the posterior part of superior temporal gyrus, and adjacent to postcentral gyrus (area 42). This region corresponds to anterior part of Wernicke's area. The other region was in the posterior part of middle temporal gyrus (area 21, 37). We found 4 more activated foci in bilateral parahippocampal gyri (area 35, 36) and bilateral cerebellar hemispheres. Three regions had significant increase of rCBF in phonological word finding. Two of them were located in right middle frontal gyrus (area 6, 8), and one in the midline structure corresponding to posterior cingulate gyrus (area 23, 31).

Discussion

Our tasks would minimally activate primary motor system for speech production because the subjects were required no verbal output. Thus, the inter-task differences in this study would be originated from the central cognitive processes mentioned above. Several activated foci were observed in categorical word finding (Fig. 3 and Table 1). They located in left posterior temporal, bilateral medial temporal, and bilateral cerebellar regions. Among them, we consider the left posterior temporal regions are involved in semantic processing.

An activation study of Petersen et al.2,3) compared a semantic task to a repetition task. The semantic task required to say a verb related to each presented noun, and the repetition task needs only to repeat the noun. They assumed simple word repetition needs no semantic processing, and semantic system is activated only in the verb generation task. The results showed the significant increase of rCBF in the inferior prefrontal cortex of left hemisphere (Broca's area) during the semantic task, and the authors associated semantic system with the region of the left frontal cortex. However, their presumption is disputed. Wise et al.9) reported no significant activations in the tasks with semantic judgment of word pairs comparing to the task of simple listening to nonwords with word-like phonological structure. This means the presented words or nonwords may automatically activate semantic system even in a simple listening or repetition task which dose not explicitly demand comprehension. Recent studies4,10,11) showed the activation of Broca's area during subvocal pronunciation and rehearsal of words or non-words. In the study of Petersen et al.2,3), the verb generation task may require both the subvocal pronunciation of the stimulus word and the vocalization of the output word, while repetition task needs only to vocalize the stimulus word. This may be why the former task relatively activates Broca's area.

On the other hand, Démonet et al.$^{4)}$ reported the increase of rCBF in left temporo-parietal regions during a semantic judgment task comparing with a phonological judgment task. The two tasks required to respond according to whether the presented noun has a given semantic attribute, or whether it includes particular phonemes. They associated the semantic processing with the left temporo-parietal area. The results of our study further specified the left posterior temporal area as a probable anatomical structure for semantic processing. Wernicke's area is established to be important for language comprehension. A recent study$^{12)}$ showed the left temporal lesions disrupt semantic processing of words. We must, however, note that our statistical methods elucidate the anatomical foci, rather than the circumscribed structures, of cognitive processing. The neural system for semantic processing surely includes, and may be distributed beyond, the left posterior temporal area.

We observed two more activated areas in categorical word finding, that is, parahippocampal gyri and cerebellar hemispheres (Fig. 3 and Table 1). Medial temporal structures are thought to contribute episode memory system, and several studies$^{13\text{-}15}$ reported the parahippocampal activation in various memory tasks. Why did categorical word finding in our study activate this region? One possible explanation is that the subjects may employ a strategy referring to episode memory to perform the task. For example, a housewife may retrieve the vision of her kitchen to produce as many names of kitchen ware as possible. Another possibility is, as Kapur et al.$^{15)}$ discussed, the medial temporal structures have a role in both episode memory system and semantic processing. The activation of cerebellum in categorical word finding is also difficult to interpret, but several activation studies$^{3,14,16)}$ suggested probable contributions of cerebellum in various cognitive functions.

Activated foci were found in right dorsolateral prefrontal and posterior cingulate areas during phonological word finding (Fig. 3 and Table 1). We consider the right dorsolateral prefrontal regions may be associated to the strategic word search for this task. Damages to this area cause deficits in problem solving tasks including word finding$^{17)}$. Grasby et al.$^{14)}$ observed the bilateral prefrontal activation in supraspan memory task comparing to subspan memory task, and discussed to relate the area to the strategic organization and retrieval of supraspan information. Our study underlined their assumption, but detected only unilateral activation of prefrontal area. In our study, subvocal pronunciation of generated words would activate left prefrontal region, including Broca's area, during both categorical and phonological tasks. Thus, the inter-task comparison may cancel the increased rCBF of the left dorsolateral prefrontal area during the strategic word search of phonological task. Several studies$^{4,11,14)}$ reported the activation of posterior cingulate area, but the interpretation of the findings remain controversial. Our study also suggests the relation between this structure and some cognitive processes, but we need further studies to understand its role in higher brain functions.

References

1) Miceli G. Giustolisi L. and Caramazza A. *Cortex* **27**, 57-80 (1991).
2) Petersen S. E., Fox P. T., Posner M. I., et al. *Nature* **331**, 585-589 (1988).
3) Petersen S. E., Fox P. T., Posner M. I., et al. *J Cognitive Neurosci* **1**, 153-170 (1989).
4) Démonet J. F., Chollet F., Ramsay S., et al. *Brain* **115**, 1753-1768 (1992).
5) Martin A., Wiggs C.L., Lalonde F., et al. *Neuropsychologia* **32**, 1487-1494 (1994).
6) Rosser A. and Hodges J. R. *J Neurol Neurosurg Psychiatry* **57**, 1389-1394 (1994).
7) Frackowiak R. J. S., Lanzi G.L., Jones T., et al. *J. Comput Assist Tomogr* **4**, 727-736 (1980).
8) Talairach J. and Tournoux P.,*Co-planar Stereotactic Atlas of the Human Brain.* Stuttgart: Thieme 1988.
9) Wise R., Chollet F., Hadar U., et al. *Brain* **114**, 1803-1817 (1991).
10) Paulesu E., Frith CD and Frackowiak R. S. J., *Nature* **362**, 342-345 (1993).
11) Démonet J. F., Price C., Wise R., et al. *Brain* **117**, 671-682 (1994).
12) Hart J. and Gordon B., *Ann Neurol* **27**, 226-231 (1990).
13) Squire L. R., Ojemann J. G., Miezin FM, et al. *Proc Natl Acad Sci USA* **89**, 1837-1841 (1992).
14) Grasby P. M., Frith C. D., Friston K. J., et al. *Brain* **116**, 1-20 (1993).
15) Kapur N., Friston K. J., Young A., et al. *Cortex* **31**, 99-108 (1995).
16) Petrides M., Alivisatos B., Meyer E., et al. *Proc Natl Acad Sci USA* **90**, 878-882 (1993).
17) Cummings J. L,. *Arch Neurol* **50**, 873-880 (1993).

Table 1. Significantly activated regions.

Coordinates (mm) X	Y	Z	Brodomann's area	Anatomical location	Mean difference of rCBF (ml/100g/min)
Categorical word finding					
-55	-27	16	Area 42	Left superior temporal gyrus (posterior part)	14
-55	-56	8	Area 21, 37	Left middle temporal gyrus (posterior part)	9
-36	-22	-16	Area 35, 36	Left parahippocampal gyrus	11
22	-23	-16	Area 35, 36	Right parahippocampal gyrus	13
-46	-59	-21		Left cerebellar hemisphere	14
35	-64	-23		Right cerebellar hemisphere	12
Phonological word finding					
27	24	39	Area 8	Right middle frontal gyrus	13
35	0	39	Area 9	Right middle frontal gyrus	10
0	-33	29	Area 23	Posterior cingulate gyrus (midline)	13

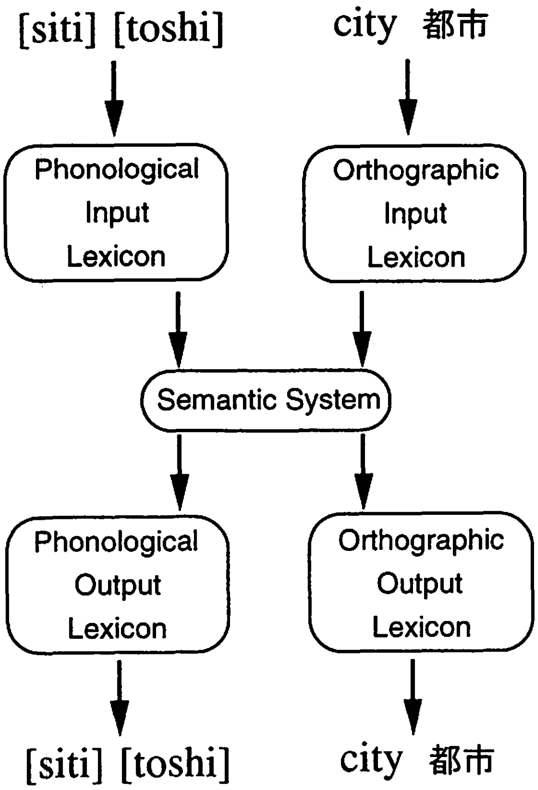

Fig. 1. A cognitive neuropsychological model of the lexical-semantic system for word comprehension and production.

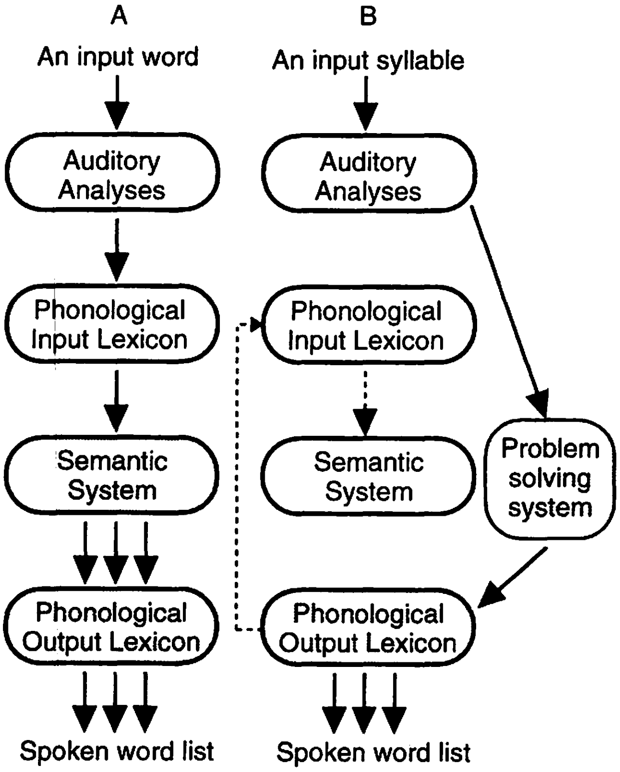

Fig. 2. The schematic processes of categorical word finding (A) and phonological word finding (B). Tripled arrows represent the transmission of the information for the adequate word list. Broken arrows indicate the process of internal re-hearing. Shadows show the expected activation in the processes of each task.

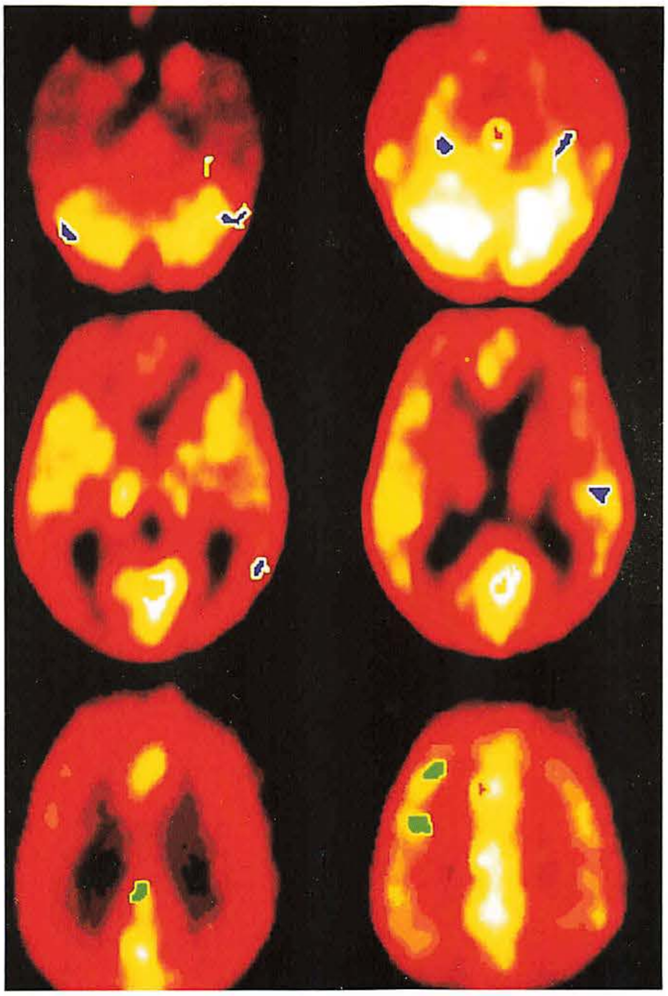

Fig. 3. The activated foci in categorical word finding (blue) and phonological word finding (green) are displayed on the standardized mean rCBF images of all studies.

IV. 4. Assessment of a Non-Anastomotic Bypass Surgery in Childhood Moyamoya Disease:Characteristics of Cerebral Blood Flow and Oxygen Metabolism

Shirane R., Takahashi T., Kusaka Y., and Yoshimoto T.

Department of Neurosurgery, Tohoku University School of Medicine

Introduction

Therapeutic methods for Moyamoya disease are divided into direct or indirect anastomotic bypass surgery. The problems in direct anastomosis is thought to be difficult in reconstruction of blood flow in the frontal area or the territories of the anterior cerebral artery. It has been reported that even when TIA disappeared in the early stage after direct bypass surgery, mental retardation and psychomotor disturbance may develop as far as chronic circulation failure remains in the frontal area[1,2]. Therefore, treatment of childhood Moyamoya disease will not be completed by obtaining disappearance of existing symptoms in a short period of time. Patients who underwent surgery in childhood and had remission may be require to undergo surgical treatment again because the disease progressed in angiographical stage until adolescence[3,4]. Since therapeutic plan mainly consisting STA-MCA anastomosis for the second surgery. STA can be used effectively in the future if non-anastomotic bypass surgery preserving STA is performed first as the present method. In addition, this method consists of combination of various types of non-anastomotic bypass surgeries using temporal muscle, galea and dura, operation can be expanded to the brain surface wider than the range of the operation field, and ischemia in the frontal lobe can be treated easily by changing the site of craniotomy, and blood flow in the skin flap can be maintained[5]. Besides emphasizing the advantages of the surgical procedure of this method, we assess long-term clinical outcome and discuss the characteristics of cerebral blood flow and oxygen metabolism using PET in this report.

Materials and Methods

PATIENT POPULATION

The subjects were 19 patients with childhood Moyamoya disease, 15 girls and 4 boys, admitted to our institution in 7 years from 1988 through 1995. This type of surgery was performed for a total of 39 hemispheres (Table 1), and the patients have been followed up 1 to 7 years (mean 49.3 months) after operation.

The initial and subsequent symptoms due to cerebral ischemia were observed in all patients. Among them, 8 cases showed obvious cerebral infarction on CT scan. Angiographic studies were performed in all patients, and the abnormal findings were shown in Table 1. Preoperative evaluation of cerebral blood flow using PET with O^{15} (CO_2, O_2, CO) was performed in 9 cases (case$^{6-14}$) for evaluating cerebral oxygen metabolism and blood flow. Six cases were studied with PET, postoperatively.

PET PROCEDURE

We used a PT-931 (CTI, Knoxville, Tennessee) in accordance with the policies of the committee for clinical PET study in Tohoku University. The spatial resolution of the image was 8 mm full width at half maximum (FWHM), and the slice thickness was 7 mm. Seven slices were obtained simultaneously. All subjects were scanned in the axial tomographic plane from the cerebellum to the cerebrum. Measurement of the regional cerebral blood flow (rCBF), the regional cerebral metabolic rate of oxygen (rCMRO2), and the regional oxygen extraction fraction (rOEF) was performed with steady state inhalation of O15 labeled CO_2,O_2, CO, respectively$^{6,13)}$. The region of interest (ROI) was between the axial slices through the cerebellum and the central semivowel. The frontal association cortex (FC), sensorimotor cortex (SM), parietal cortex (PC), visual cortex (VC), and thalamus (TH) were estimated. Oval ROIs located in each structure were verified by MRI. The rCBF, rOEF, and rCMRO2 were determined from these ROIs.

OPERATIVE METHOD

For decision of the operation field, ischemic site was identified based on overall evaluation of findings in preoperative cerebral angiography, cerebral blood flow and metabolism, then, the area of priority for operation was determined. The operation field was determined based on the ischemic site. In order to perform anastomosis of STA and middle cerebral arteries (STA-MCA) when ischemic changes develop newly in the future, STA was kept intact at the time of skin incision. A skin flap was prepared by peeling the temporal muscle with galea from the cranium and rolling back. Burr holes were made on the cranium avoiding the running dural artery as much as possible based on the cerebral angiographic observation, and a bone flap was formed.

The dura was incised and rolled back by avoiding cutting the main branches of middle menigeal artery and keeping blood flow without disturbing anastomosis of dural and brain surface vessels. Thickened arachnoid membrane of the brain surface was cut along sulci, and blood vessels of the brain surface were exposed. On the other hand, the dura rolled back was cut into strips with pedicle preserving the dural artery and inserted in the brain surface around the bone window toward the ischemic region, and the external surface of dura was attached to the brain surface. The temporal muscle with galea of the skin flap was peeled to make a thin monolayer flap, and the layer was tightly attached to the brain surface and connected to the cut-end of the dura by suturing. After removing minimal part of the bone flap for preventing insufficient blood flow caused by oppression of the inserted temporal muscle, the bone flap together with skin flap were returned and the temporal muscle, fascia and skin remaining in the skin flap side were arranged to the normal order and the incision was closed.

Results

The subjects were 19 patients with childhood Moyamoya disease who underwent surgery in our department between 1989 and 1995. Their age was 1 to 12 years old. The clinical results were summarized in Table 2. Surgery was performed bilaterally at different time in each of 14 patients, unilaterally in one patient. Additional surgeries were carried out in 3 cases due to newly ischemic changes during the follow-up period, for a total of 39 times. Bilateral surgery was performed on both side by two stages with an interval of two months or more until the ischemic symptoms of the operated side disappeared. The postoperative observation period was from one to five years. In all of the cases, preoperative symptoms were ameliorated or disappeared. On angiography performed two months to one year after operation, good development of collateral circulation from the external artery into the cranium in the operation area was observed in every patient. All cases involving the fronto-temporal area showed an excellent collateral circulation in both anterior and middle cerebral arterial territories. Obvious improvement was also found in the examination of cerebral blood flow and metabolism after operation in all patients. Regarding the operation site, since the superficial portion of the temporal muscle attached to the skin flap was left, the skin flap at the operation site did not depress, and the site was satisfactory from the point of beauty also. Owing to the preservation of the STA, no necrosis of the skin at the operation site, or no infection or alopecia at the operation site developed.

Results of PET Study

Values of rCBF, rOEF, and rCMRO2 in childhood Moyamoya patients were compared to normal children under the same protocol[14]. In normal children, rCBF values showed gradual increase from neonatum in all cerebral regions, having a peak value around aged 7 (150% of the adults' value). During adolescence rCBF usually decreased to the adult level. However, from the present study, we found rCBF in the frontal and parietal cortex showed the same value as in adult, while the value of rCMRO2 was lower than normal individuals'. Increasing of rOEF was observed in occasional cases in the frontal cortex, but the difference was not significant. Comparison with the above values of age matched control and postoperative data were summarized in Table 2 and 3.

Compared to age matched control values, we found a significantly decreasing of rCBF in the frontal, sensorimotor, and parietal cortex (-30.5%, -40%, and -43%) preoperatively. After surgery, the values of rCBF increased +25.5%,+11.4%, and +11.3%, respectively.

However, there was no significant difference in the thalamus and occipital cortex. The values of rOEF in childhood Moyamoya patients were slight higher than the control group, particularly in the frontal (+14.9%), sensorimotor (+11.1%), and parietal cortex (+12.2%). Although variations were found among them, postoperative data showed decreasing rOEFs in the frontal (-7.5%) and sensorimotor (-7.8%). Decreasing of rCMRO2 was observed in the frontal, sensorimotor, and parietal cortex (-14.7%, -34.8%, and -28.5%) when compared with the control values, preoperatively. After operation, rCMRO2 was increasing in the frontal, sensorimotor, and parietal cortex +19.5%, +14.5%, and +17.7%, respectively.

Discussion

In Tohoku University, we experienced over one hundred cases of childhood Moyamoya disease, and we have been studing about hemodynamics[10,15)], angiographical findings[11,13)], and electroencephalography[8)] in order to clarify the pathophysiology of this disease. Although many therapeutic methods for Moyamoya disease have been reported, the optimal treatment is still controversial[16,12)]. Various problems in bypass surgery for children have been described: these are technical difficulty in operation due to small diameters of both STA and MCA, disadvantage of possible sacrifice of internal and external anastomosis due to temporary occlusion of blood flow or cut of STA during operation of branches of MCA of the brain surface, difficulty in maintaining anesthsia for a long operation period, and moreover, thining or obstruction of ansatomosed blood vessels along with the recipient artery[7,14,17,18)]. On the otherhand, question whether an effective increase in cerebral blood flow in non-bypass surgery have also been noted, such as revascularization is limited at the temporal region after EMS surgery, collateral channels are restricted within the territory of STA after EDAS surgery. Inrecent literature, though EMS surgery with EDAS an both anteruir and posteruir branches of STA has been reported, it is still thought to be difficult to make enough collateral sirculation in the territory of ACA[9,19)]. Therefore, in order to secure collateral circulation in a wide range in childhood Moyamoya disease particular in the frontal region, it is necessary to contact cortical branches of blood vessels of the brain surface in a range as wide as possible. According to the present method that consists of combination of various types of non-anastomotic bypass suegeries using temporal muscle, galea and dura, operation can be expanded to the brain surface wider than the range of the operation field, and ischemia in the frontal lobe can be treated easily by changing the site of craniotomy. In the present study, although PET and acetazolamide SPECT revieled significantly low metabolism and cerebral blood flow in most cases in the territory of ACA, infarcted foci oof the frontal lobe were observed in only 2 out of 38 hemispheres on CT and MRI. Furthermore, there is no definite method to recognized the preceeding frontal signs from routine neurological examinations. These mean that findings on cerebral angiography, CT, MRI and clinical manifestations are not enough to predict the intellectual xhanges in childhood Moyamoya disease which is known to be progress, through investigations including detection of cerebral blood flow and oxygen metabolism seem indispensible before and after an optimal operation. From the present data, the PET study showed that the rOEF was not always increased in each case and every region of the brain compared with the control value, and patterns or degrees varied individually. Furthermore, low values of rCBF and rCMRO2 with a relatively high value of rOEF in the frontal region were found in all of the cases. These findings indicated that immediate blood supply is not always necessary to all of the hemispheres affected by Moyamoya disease, and slow circulation improving effect of the present method using indirect anastomotic surgery may be superior to the direct anastomotic surgery since revascularization developed when the cerebral cortex was under misery perfusion.

References

1) Ikezaki K, matsushima T, Kuwabara Y et al:Cerebral circulation and oxygen metabolism in childhood moyamoya disease: a perioperative positron emission tomography. J neurosurg 81:843-850, 1994
2) Ishii R, Takeuchi S, Ibayashi K, et al: Intelligence in children with moyamoya disease: Evaluation after surical treatments with special reference to changes in cerebral blood flow. Stroke 15 : 873-7, 1984.
3) Ezura M, Yoshimoto T, Fujiwara S, et al : Clinical and angiopraphic follow-up of childhood-onset
moyamoya disease. Child's Nerv Syst 11:591-594, 1995.
4) Miyamoto S, Kikuchi H, Karasawa J, et al: Pitfalls in the surgical treatment of moyamoya disease. Operative techniques for refractory cases. J Neurosurg 68 : 537-43, 1988
5) Hara Y, Shirane R, Yoshimoto T, et al : Reconstructive operation for childhood moyamoya disease: Dural pedicle insertion over the brain surfice combined with EGMS. nerv Syst Child (Tokyo) 19;271-276, 1994.
6) Frackowiak RSJ, Lenzi GL, Jones T, et al : Quantitative measurement of regional cerebral blood flow and oxygen metabolism in man using 15O2 and positron emission tomography : Theory, procedure and normal values. J Comput Assist Tomogr 4 : 727-736, 1980.
7) Karasawa J, Kikuchi H, Furuse S, et al : A surgical treatment of "moyamoya" disease. "Encephalomyosynangiosis." Neurol Med Chir 1977;17 : 29-37.
8) Kodama N, Aoki Y, Hiraga H, et al: Electroencephalographic findings in children with moyamoya disease. Arch Neurol 36 : 16-9, 1979.
9) Matsushima T, Fukui M, Kitamura K et al: Encephalo-duro-arterio-synangiosis in children with moyamoya disease. Acta neurochir 104: 96-102, 1990
10) Ogawa A, Nakamura N, Yoshimoto T, et al : Cerebral blood flow in Moyamoya disease, part II: autoregulation and CO2 response. Acta Neurochir (Wien) 105: 107-111, 1990.
11) Suzuki J, Takaku A :Cerebrovascular "Moyamoya" disease. Disease showing abnormal net-like vessels in base of brain. Arch Neurol 20: 288-299, 1969.
12) Suzuki J, Takaku A, Kodama N, et al: An attempt to treat cerebrovascular Moyamoya disease in children. Childs Brain 1 : 193-206, 1975.
13) Takahashi A, Fujiwara S, Suzuki J: Long term follow-up angiography of moyamoya disease - Cases followed-up from childhood to adolescence. Neurol Surg 14:23-29 (Jpn).
14) Takahashi T, Shirane R, Hara Y et al: Developmental changes of cerebral blood flow and oxygen metabolism in children. J Cereb Blood Flow Metabol 15 suppl 559, 1995.
15) Kameyama M, Shirane R, Tsurumi Y, et al: Evaluation of cerebral blood flow and metabolism in childhood Moyamoya disease. An investigation into "re-build-up" on EEG by positron CT. Child's Nerv Syst 2: 130-133, 1986.
16) Olds MV, Griebel RW, Hoffman HJ, et al: The surgical treatment of childhood moyamoya disease. J Neurosurg 66 : 675-80, 1987.

17) Cahan LD: Failure of encephalo-duro-arterio-synangiosis procedure in moyamoya disease. Pediatr Neurosci 12 : 58-62. 1985.

18) Karasawa J, Kikuchi H, Furuse S, : Treatment of moyamoya disease with STA-MCA anastomosis. J Neurosurg 1978;49 : 679-88.

19) Abe H, Takahashi A, Houkin K, et al: Surgical treatment of the spontaneous occlusion of the circle of Willis. Comparison between the results of indirect procedures and bypass combined with indirect procedures.] The Research Committee on Spontaneous Occlusion of the Circle of Willis (Moyamoya Disease) of the Ministry of Health and Welfare, Japan, 1992 : 83-89 (Jpn).

Table 1.

CASE	Symptons	age	onset	stage		infraction	PET	Operation	Result
			sex	right	left		date	site	
1	convulsion	1	0.8 m	III	I	none		R FTP	
								L FT	conv.(-)
2	Linf, TIA	3	1 f	III	III	RF		R FTP	
	R TIA							L FTP	TIA(-)
3	R TIA, L inf	3	1.2 m	IV	II	RP		R FTP	
				IV	III			L FTP	TIA(-)
4	L TIA	4	4 m	III	III	none		R FTP	
	R TIA			III	III		94/7/15	L FT	
	Legs, R TIA						94/2/23	L PTO	TIA(-)
5	Blt TIA	5	2 f	III	III	LPO		L FTP	
								R FTP	TIA(-)
6	L RIND	5	4 f	VI	III	RP		R FTP	
								L FTP	TIA(-)
7	R TIA	6	3 m	IV	III	none		L FTP	
	L TIA			IV	III			R FTP	TIA(-)
8	Blt TIA	7	6 f	III	I	none		R FTP	
		8		IV	II			L FTP	TIA(-)
9	Blt TIA	7	4 f	II	III	none	94/7/6	R FTP	
							96/7/10	L FTP	TIA(-)
10	R Vis Blt TIA	8	5 f	III	III	Blt P, LO		L FTP	
							94/3/4	R FTP	TIA(-)
11	convulsion	8	2 f	III	III	R FT	94/11/4	R FTP	conv.(-)
	Blt TIA							L FTP	TIA(-)
12	L TIA Motor	8	5 f	II	I	none		R FT	
	L TIA Sens	11		III	II		94/11/11	R PTO	
	R TIA	11		III	II		95/6/23	L FTP	TIA(-)
13	L TIA	9	5 f	III	III	R P		R FTP	
	R TIA	9		III	III			L PTO	TIA(-)
	L frontalgia	11		IV	III			L FT	headache(-)
14	Blt TIA	9	8 f	IV	III	none	94/7/13	R FTP	
							95/3/28	L FTP	TIA(-)
15	R TIA	9	9 f	I	III	none		L FTP	TIA(-)
16	Blt TIA	9	8 f	III	III	none		L FPT	
							94/12/8	R FTP	TIA(-)
17	R invol move	12	10 f	I	III	none	89/11/2	L FT	invol m(-)
							93/12/3		
18	L Vis	12	f	IV	III	RPO	94/2/25	R FTP	
							95/6/14	L FTP	TIA(-)
19	Blt TIA	12	8 f	III	IV	none	93/12/15	L FT	
							95/6/7	R FTP	TIA(-)

Table 2.

	Moyamoya patients		Normal Children		
	mean	S.D.	mean	S.D.	
Age	9.9	1.9	10	3.4	

	Moyamoya patients		Normal Children		
	mean	S.D.	mean	S.D.	
rCBF					
frontal	40.1	10.4	57.7	13.4	p<0.01
sensorimotor	42.9	12.2	71.4	7.6	p<0.001
parietal	42.2	14.3	74.1	8.6	p<0.001
visual	63.6	20.9	55.5	9.5	n.s.
thalamus	56.4	11.8	73.7	9.9	p<0.01

(ml/min/100g)

	Moyamoya patients		Normal Children		
	mean	S.D.	mean	S.D.	
rCMRO2					
frontal	3.71	1.01	4.35	0.84	n.s.
sensorimotor	3.32	0.99	5.09	0.99	p<0.01
parietal	3.58	1.27	5.01	0.37	p<0.01
visual	4.94	1.61	4.51	1.28	n.s.
thalamus	4.39	1.22	4.49	0.83	n.s.

(ml/min/100g)

	Moyamoya patients		Normal Children		
	mean	S.D.	mean	S.D.	
rOEF					
frontal	0.54	0.05	0.47	0.13	n.s.
sensorimotor	0.49	0.05	0.44	0.08	n.s.
parietal	0.46	0.04	0.41	0.07	p<0.05
visual	0.43	0.06	0.43	0.08	n.s.
thalamus	0.43	0.05	0.45	0.08	n.s.

Table 3.

	preoperation		postoperation		
	mean	S.D.	mean	S.D.	
Age	10.3	2.1	10.7	2.1	
rCBF					
frontal	39.2	7.9	49.1	11.1	
sensorimotor	44.5	13.1	50.9	11.9	
parietal	44.3	16.8	50.1	8.9	
visual	67.1	19	62.8	11.3	
thalamus	60.1	12.6	59.9	11.8	
			(ml/min/100g)		
rCMRO2					
frontal	3.94	1.01	4.71	0.74	
sensorimotor	3.46	1.04	3.96	0.99	
parietal	3.89	1.36	4.58	1.04	
visual	5.24	1.21	5.33	1.55	
thalamus	5.37	1.39	5.37	1.39	
			(ml/min/100g)		
rOEF					
frontal	0.53	0.03	0.49	0.02	p<0.01
sensorimotor	0.51	0.04	0.47	0.03	p<0.05
parietal	0.47	0.03	0.48	0.05	
visual	0.48	0.04	0.51	0.06	
thalamus	0.47	0.04	0.51	0.05	

IV. 5. Normal Distribution of the Muscarinic Cholinergic Receptors in the Human Brain Studied with ^{11}C-Benztropine and the Human Brain Atlas System

Ono S., Kawashima R., Ito H., Koyama M., Goteau R., Inoue K., Sato K.
Fujiwara T., Meguro K.**, Yanai K.***, Sasaki S.****, Ido T.*,*
Ito M., and Fukuda H.*

Department of Nuclear Medicine and Radiology, Institute of Development, Aging, and Cancer, Tohoku University
*Cyclotron and Radioisotope Center, Tohoku University**
*Section of Neuropsychology, Graduate School of Medicine, Tohoku University***
*Department of Pharmacology I, School of Medicine, Tohoku University****
*Department of geriatric medicine, School of Medicine, Tohoku University*****

Introduction.

We investigated regional distribution of the muscarinic cholinergic receptor in the normal human brain with ^{11}C-benztropine (BZT)1) and positron emission tomography (PET) using Patlak plot2) slope calculation images and an anatomical standardization technique3).

Subjects and Methods.

Seven normal male volunteers who gave an informed consent were involved in this study, which was approved by the Research Ethic Committee of Tohoku University. Their age ranged from 18 to 51 (mean 28.0 SD 12.0) years old.

The subject was injected with ^{11}C-BZT intravenously in extended bolus fashion. Injected dose was 362.6-740.0MBq (9.8- 20.0 mCi), mean 680.8 SD140.6MBq (mean 18.4 SD 3.8mCi). Immediately after injection, we started dynamic PET scanning. The PET scanner used was the PT931/04 (CTI). The dynamic scan protocol was; 1 min. 2 scans, 2 min. 4 scans, 5 min. 10 scans, 10 min. 1 scan, total 70 min. or; 1 min. 2 scans, 2 min. 4 scans, 5 min. 16 scans, total 90 min. After those dynamic scans, 2 static scans of 10 min. duration were added. And serial frequent arterial blood sampling was also started simultaneously with 15 seconds interval at the beginning and gradually longer intervals later on the study. Analyses of plasma metabolites were also performed at selected time points (5, 10, 30, and 60 minutes) using the HPLC technique1). And plasma time activity curves (TAC) of unmetabolized ligand were obtained. From these PET and TAC data, we obtained Patlak plot slope calculation images. In this analyses, we employed the Patlak plot data from 5 to 60 minutes of the study.

Using the HBA (human brain atlas) system[3], the Patlak plot slope calculation image of each subject was transformed into the shape of the standard brain. Mean and standard deviation (SD) calculation images were generated from those anatomically standardized images. On these mean and SD images, we placed regions of interest which were previously outlined on a MR image of the standard brain.

Results and Discussion.

From those data, we found the highest receptor distribution in the striatum and occipital cortex, as well as high distribution in the frontal, parietal, and temporal cortices (Table 1), which were consistent with previous reports[4,5].

We also found considerable affinity in the cerebellar hemispheres. This fact may reflect the characteristics of the BZT, which has affinity both to the M1 and M2 muscarinc cholinergic receptors[1]. The M1 type receptors are rich in the cerebral cortices, hippocampus, and basal ggl., while M2 receptors are rich in the cerebellum and the brain stem[6]. This may explain, at least partially, the affinity in the cerebellum.

From these results, we concluded that anatomical standardization of PET receptor images with ^{11}C-BZT will be useful for delineating the physiological or pathological alterations of the muscarinic cholinergic receptor in the human brain.

References

1) Dewey S. L, et al., Synapse **5** (1990) 213.
2) Patlak C. S., and Blasberg R. G., J. Cereb. Blood Flow Metab. **5** (1985) 584.
3) Roland P. E., et al., Human Brain Mapping **1** (1994) 173.
4) Suhara T., et al., Psychopharmacol. **113** (1994) 311.
5) Frey K. A., et al., J. Cereb. Blood Flow Metab. **12** (1992) 147.
6) Wang J. X., et al., Life Sci. **41** (1987) 1751.

Table 1. Regional incorporation of ^{11}C-BZT

	Regions	Mean	SD
Brain stem	pons	0.0861	0.0513
Cerebellum	rt cerebellum	0.0879	0.0493
	lt	0.0907	0.0463
Central gray	rt putamen	0.1052	0.0590
	lt	0.1080	0.0712
	rt caudate head	0.1030	0.0574
	lt	0.1010	0.0576
Frontal lobe	rt inf. frontal	0.0771	0.0543
	lt	0.0779	0.0527
	rt mid. frontal	0.0986	0.0536
	lt	0.1020	0.0458
	rt sup. frontal	0.0950	0.0545
	lt	0.0888	0.0627
	rt cingulate	0.0847	0.0454
	lt	0.0865	0.0796
Temporal lobe	rt inf. temporal	0.1028	0.0435
	lt	0.0945	0.0606
	rt mid. temporal	0.1001	0.0559
	lt	0.0926	0.0447
	rt sup. temporal	0.0943	0.0587
	lt	0.0842	0.0554
	rt hippocampus	0.1065	0.0576
	lt	0.0993	0.0619
Occipital lobe	rt post occipital	0.0983	0.0568
	lt	0.1022	0.0586
	rt lat occipital	0.1001	0.0531
	lt	0.0909	0.0569

ml/g/min

IV. 6. Brain 6-[^{18}F]fluorodopa Uptake in Early and Late Onset Parkinson's Disease Assessed by Positron Emission Tomography: Clinical and Neurochemical Correlations

Nagasawa H.,**, *Tanji H.***, *Saito H.****, *Kimura I.*****, *Itoyama Y.***,
*Fujiwara T.******, *Itoh M.******, *Iwata R.****** *and Ido T.******

*Department of Neurology, Miyagi National Hospital**
*Tohoku University School of Medicine***,
*Nisitaga National Hospital****
*Yamagata National Hospital*****
*Cyclotron and Radioisotope Center, Tohoku University******

Introduction

Onset of idiopathic Parkinson's disease is unusual in patients below the age 40. Quinn et al. studied 60 cases of parkinsonism with onset under the age of 40 and they proposed that cases of idiopathic Parkinson's disease beginning between 21-40 years should be called "young onset Parkinson's disease", which differentiated from cases of parkinsonism beginning before age 20 years defined as juvenile parkinsonism because of clinical features with familial cases1). There were several studies indicating some clinical features observed in young onset Parkinson's disease such as more prominent dystonia, earlier manifestation of levodopa-related dyskinesia and higher frequency of levodopa-dose-related motor fluctuations than seen in idiopathic Parkinson's disease of late onset2).

Positron emission tomography (PET) using 6-[^{18}F]fluorodopa (FDOPA) is an efficient method of studying the nigrostriatal dopaminergic system in living subjects3). Intravenously injected FDOPA that crosses the blood-brain-barrier, is decarboxylated to fluorodopamine by L-aromatic amino acid decarboxylase, and remains in the nerve terminals during the scanning. Recent PET studies revealed striatal uptake of FDOPA was reduced in parkinsonism caused by loss of nigrostriatal neurons4).

In the present study, we measured FDOPA metabolism in patients with early and late onset Parkinson's disease using PET and analyzed the correlations between presynaptic dopaminergic function in the caudate nucleus and the putamen, and individual clinical symptoms of the patients.

Subjects and methods

SUBJECTS

We divided patients with parkinsonism into two groups focusing on onset age of Parkinson's disease (PD), such as early onset PD (EOPD) and late onset PD (LOPD) groups. EOPD group consisted of 10 patients, 4 men and 6 women, who were diagnosed PD by a neurologist before 40 years. The age of onset of their initial Parkinson's symptoms was ranged from 24 to 39 years (mean±SD, 30.6±6.0). The mean duration of the disease was 7.5 years. Nine patients were treated with levodopa, of which 2 patients also received a D_2 agonist (bromocriptine) and an anticholinergic agent (trihexyphenidyl); 5 patients received trihexyphenidyl; 1 patient received bromocriptine. One patient was treated with trihexyphenidyl. LOPD group consisted of 10 patients, 7 men and 3 women, who were diagnosed PD by a neurologist after 40 years. The age of onset of their initial symptoms was ranged from 46 to 60 years (52.9±4.5). The mean duration of the disease was 7.8 years. Eight patients were treated with levodopa, of which 3 patients also received a D_2 agonist (bromocriptine) and an anticholinergic agent (trihexyphenidyl); 3 patients received trihexyphenidyl; 1 patient received bromocriptine. One patient was treated with bromocriptine and trihexyphenidyl. One patient was treated with trihexyphenidyl.

Magnetic resonance imaging (MRI) and/or computed tomography (CT) scans of the brain, obtained in all patients were normal. No dementia was detected on formal neuropsychological testing. All patients were rated on overall disease severity rated from grade I to IV according to Hoehn and Yahr[5]. The degree of main symptoms in clinical rating for bradykinesia, limb rigidity and tremor was scored from 0 to 3 (0, absent; 1, mild; 2, moderate; 3, severe). Clinical assessment did not reveal any pyramidal, cerebellar or oculomotor disturbances in all patients. The clinical profiles of the studied patients of EOPD and LOPD groups are summarized in Table 1. The drug treatment was stopped at least 24 h before the PET study.

Two control groups consisted of 10 normal healthy volunteers with an age range of 29-40 years (32.4±7.0), and other 10 volunteers with an age of 46-77 years (60.0±10.6), without a history of medical illness, neurological diseases, developmental disorders or substance abuse. Control subjects underwent a complete neurological examination and a neuropsychological evaluation before PET study. MRI and/or CT scans of the brain, obtained in the control groups, were normal. The project was approved by the Research Ethics Committee of the Tohoku University, School of Medicine. All subjects gave their written informed consent after a full explanation of the procedure.

POSITRON EMISSION TOMOGRAPHY

FDOPA scans were performed on a scanner, PT-931 (CTI Inc., USA), at the Cyclotron and Radioisotope Center, Tohoku University, Sendai, Japan. Patients and subjects were positioned in the scanner, with the orbitomeatal (OM) line parallel to the detector rings according to the brain slices by MRI. A cross of light was projected onto marks on the subjects' heads from three dimensions and the heads were positioned at 40 mm above and parallel to the OM line. All studies were conducted in a quiet, semi-darkened room with minimal background noise. The subjects' eyes were open and their ears were unplugged.

A 15-min transmission scan was collected using a ^{68}Ge-^{68}Ga external ring source. FDOPA was synthesized by the method described by Adam et al. with a radiochemical purity of more than 99%[6). After an intravenous bolus injection of FDOPA (2.5 - 8.3 mCi or 14.9 - 49.5 nmol) into the subjects, positron emission scan was carried out using PT-931 with an 8 mm axial and transaxial resolution. A series of 5 min emission scans was performed over 60 min and emission data were simultaneously collected from seven contiguous axial sections, each about 6 mm in thickness from OM + 66 to OM + 22 mm

DATA ANALYSIS

After data collection, the latter six contiguous images of the same brain slice scanned between 30 and 60 min after administration of FDOPA were added and composite images were obtained in order to improve the contrast between dopaminergic and non-dopaminergic brain regions to aid the definition of anatomical regions of interest (ROIs). In each case, two different pairs of images, the PET images and the images obtained by MR, were registered and matched with each other using image scaling to bring the disparate pairs of image data into congruence at the same brain slices according to the previous study[7). To ascertain the anatomical position of each brain structure, the position of ROIs were manually defined using the overlapped images, e.i., PET images and MR images of the same brain slices. Influx constants (Ki min^{-1} value) were calculated for the caudate nucleus and the putamen separately using a multiple graphical analysis method with cerebellar tissue input function[8,9). The Ki value is a rate constant that reflects uptake and decarboxylation of FDOPA into [^{18}F]dopamine and its metabolites by the nigrostriatal nerve terminals.

The average values of influx rate constants within each structure were presented as means±SD. The Mann-Whitney U-test was used to compare the Ki values in each structure of the brain between patients and controls with $p<0.01$ considered to be statistically significant.

Results

Representative images of FDOPA influx rate obtained by graphical analysis at the level of the caudate nucleus and the putamen from age matched control group and from the patients with EOPD and LOPD are shown in Fig. 1. FDOPA and its labeled metabolites were highly concentrated in the caudate nucleus and the putamen of both hemispheres of the normal control. On the contrary, in the patients with EOPD and LOPD, FDOPA uptake was markedly reduced both in the caudate nucleus and the putamen. The mean influx rate constant values(Ki) were significantly reduced in the caudate nucleus and the putamen of the patients with EOPD and LOPD compared with age matched control groups ($p<0.01$), respectively, as shown in Table 2 and Fig 2. There were significant negative correlations between Ki values in the caudate nucleus ($r=-0.67$, $p=0.0024$) and the putamen ($r=-0.67$, $p=0.0014$), and duration of disease in LOPD group compared with EOPD group (Fig. 3B). Similar negative relationships between Ki values and clinical stages by Hoehn and Yahr and degrees of main clinical symptoms (bradykinesia, tremor and rigidity) were more markedly seen in LOPD group than in EOPD group (Figs. 3A and 4).

Discussion

We divided the patients with PD into two groups, EOPD and LOPD, from the viewpoint of onset age of parkinsonism in order to compare the relationships between presynaptic dopaminergic function and their clinical features in the groups. Selective degeneration of dopaminergic neurons within the pars compacta of the substantia nigra with a resultant reduction in striatal dopamine content is the critical pathological process in PD[10,11,12)]. We studied presynaptic dopaminergic function in the striatum by measuring FDOPA uptakes with PET. The uptake rate constant of FDOPA is determined by the transfer of FDOPA across the blood-brain-barrier, its decarboxylation to fluorodopamine, and the retention of fluorodopamine in nerve terminals of the striatum[13,14)]. Therefore, the Ki value relates to the rate of exogenous dopa metabolism but not reflects the rate of endogenous dopamine synthesis because of tyrosine hydroxylase is regulated as a rate-limiting enzyme[8,9)]. PET study using FDOPA is dependent on the structural as well as the biochemical integrity of the nigrostriatal pathway.

In the present study, reduction of Ki value was more closely related to pathogenesis of LOPD group than EOPD group. Negative relationships between Ki values and clinical stages by Hohn and Yahr and degrees of main clinical symptoms (bradykinesia, tremor and rigidity) were more markedly seen in LOPD group than in EOPD group. The clinical severity was dependent on reduced FDOPA uptake rate in the striatum and presynaptic dopaminergic dysfunction reflected the clinical features in LOPD. On the other hand, in EOPD group, there was dissociation between Ki values and clinical features of parkinsonism. Similar negative relationship between Ki values and degree of tremor was revealed and no significant relationships between Ki values and other clinical symptoms were seen. In some cases (cases 1 and 7) of EOPD group, Ki values were markedly reduced, though their clinical symptoms were quite mild with minimum drug treatment. FDOPA influx rate in the presynaptic sites of the striatum might not always well reflected individual clinical measures in such cases. In other cases (cases 3 and 4) of EOPD group, much smaller doses were needed for treatment compared with similar stage of the patient (case 11) of LOPD.

Moreover, recent PET studies revealed postsynaptic dopamine receptors function was also involved in PD[15) and striatal D_2-receptor binding was increased in untreated patients with PD[16). However, there were not significant differences in D_1-receptor binding between untreated parkinsonian patients and controls[17). Rinne et al. reported that dopamine D_2-receptor supersensitivity was observed in the striatum of untreated patients with EOPD[18). Postsynaptic denervation supersensitivity occurred with dopamine D_2-receptors, although this was less evident with D_1-receptors[19,20,21). We speculate that a series of compensatory mechanisms within dopaminergic system may facilitate to maintain clinical function in EOPD compared with LOPD in the presence of persisted dopamine loss and up-regulation of dopamine receptor binding may modify the degree of main clinical features and disease severity of EOPD. Although some elements of the compensatory mechanism of dopaminergic treatment may appear in patients with EOPD, which may be related to the dopamine receptor supersensitivity[21). On the other hand, motor fluctuations may appear in chronically treated patients with PD due to progressive loss of dopaminergic neurons, which may cause reduced compensatory capacity in the dopaminergic system[22,23).

In conclusion, the present study indicates that the absence of the correlations between striatal FDOPA uptake and clinical disease severity in the EOPD group is due to more efficient regulatory mechanisms with compensating postsynaptic receptor function in the younger patients. We speculate thus compensatory functional deficits due to the dopamine loss in the striatum may be modified disease severity and the degrees of main clinical symptoms of EOPD group.

References

1) Quinn N., Critchley P. and Marsden C. D., Mov. Disord. **2** (1987) 73.
2) Globe L. I., Neurology **41** (1991) 168.
3) Garnett E. S., Firnau G. and Nahmias C., Nature **305** (1983) 137.
4) Nahmias C., et al., J. Neurol. Sci. **69** (1985) 223.
5) Hoehn M. M. and Yahr M. D., Neurology **12** (1967) 427.
6) Adam M. J., et al., J. Nucl. Med. **26** (1985) 125.
7) Nagasawa H., et al., J. Neurol. Sci. **115** (1993) 136.
8) Patlak C. S., et al., J. Cereb. Blood Flow Metab. **3** (1983) 1.
9) Patlak C. S. and Blasberg R.G., J. Cereb. Blood Flow Metab. **5** (1985) 584.
10) Bernheimer H., et al., J. Neurol. Sci. **20** (1973) 415.
11) Hornykiewicz O. Neurochemistry of parkinsonism. A. Lajtha ed. Handbook of Neurochemistry Vol. 7 (1972) 465.
12) Hornykiewicz O. Brain neurotransmitter changes in Parkinson's disease. C. D. Marsden and S. Fahn ed. Movement Disorders, (1982)
13) Firnau G., et al., J. Neurochem. **48** (1987) 1077.
14) Melaga W. P., et al., J. Cereb. Blood Flow Metab. **11** (1991) 890.
15) Brooks D. J., et al., Ann. Neurol. **31** (1992) 184.
16) Antonini A., et al., Neurology **44** (1994) 1325.
17) Guttman M. Neurol. Clin. **10** (1992) 377.
18) Rinne U. K., et al., Mov. Disord. **5** (1990) 55.
19) Rinne J. O., et al., J. Neurosci. Res. **27** (1990) 494.
20) Rinne J. O., et al., Mov. Disord. **8** (1993) 134.

21) Donnan G. A., et al., Mol. Neurobiol. **5** (1991) 421.
22) Fabbrini G., et al., Ann. Neurol. **24** (1988) 366.
23) Mouradian M. M. et al., Ann. Neurol., **24** (1988) 372.

Table 1. Summary of patients with early and late onset of Parkinson's disease.

Patient No.	Age at Scan(yr)	Sex	Age of Onset(yr)	Duration (yr)	Stage (H&Y)	Symtoms BR	T	R	Drugs
Early onset of Parkinson's disease									
1	29	F	25	4	I	1	1	1	1, 3
2	37	F	39	11	III	3	2	2	1, 2
3	46	M	39	7	II	1	2	1	1, 2, 3
4	46	M	39	7	II	2	1	1	1, 3
5	44	M	38	6	III	3	1	3	1, 3
6	36	F	30	6	III	1	0	2	1, 3
7	28	M	26	3	I	1	1	1	3
8	33	F	24	9	III	3	1	1	1, 3
9	36	F	26	11	III	2	1	1	1, 3
10	42	F	32	10	III	2	0	2	1, 2, 3
Late onset of Parkinson's disease									
11	59	M	54	6	II	1	0	1	1, 2
12	51	M	46	6	I	1	9	1	2, 3
13	57	M	50	8	IV	3	2	3	1, 2, 3
14	61	F	57	5	III	2	1	2	1
15	60	M	50	10	III	2	3	2	3
16	63	M	54	9	II	2	0	1	1, 3
17	64	M	60	4	I	1	2	1	1, 3
18	56	M	48	9	II	1	2	2	1, 3
19	69	F	58	11	III	3	1	1	1, 2, 3
20	62	F	52	10	IV	3	2	3	1, 2, 3

H&Y, Hoehn and Yahr; BK, Bradykinesia; T, Tremor; R, Rigidity.
Clinical scores: 0, absent; 1, mild; 2, moderate; 3, severe.
Medications are signified numerically; 1, levodopa; 2, D_2 agonist (bromocriptine); 3, anticholinergic drugs (trihexyphenidyl)

Table 2. [^{18}F]Dopa uptake as measured by positron emission tomography in normal control and patients with early and late onset of Parkinson's disease

		Caudate Nucleus (Ki)	Putamen (Ki)
Young control	(N=10)	0.0176 ± 0.0039	0.0164 ± 0.0044
Aged control	(N=10)	0.0197 ± 0.0034	0.0194 ± 0.0038
Early onset of PD	(N=10)	0.0132 ± 0.0031**	0.0093 ± 0.0024**
Late onset of PD	(N=10)	0.0110 ± 0.0040**	0.0095 ± 0.0026**

Values are given in mean ± SD. Ki= [^{18}F]Dopa influx constant (min^{-1}).
N: number of subjects. **:$p<0.01$ significant compared with age-matched controls using the Mann-Whitney U-test.

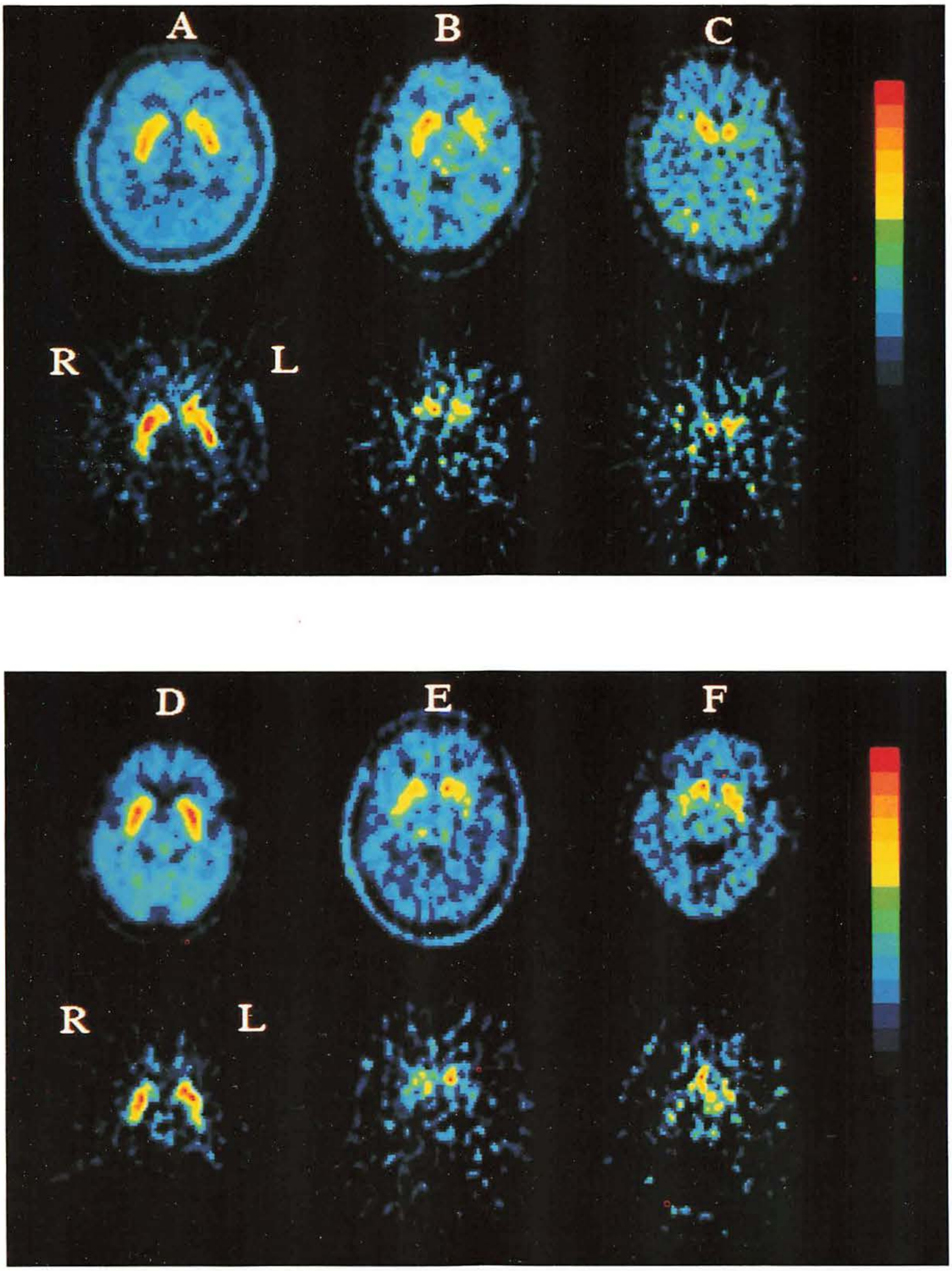

Fig. 1. Representative appearances of brain images of FDOPA uptake (upper) and FDOPA influx rate (lower) at the level of the striatum. FDOPA uptake images were added from 30 to 60 min after FDOPA injection. FDOPA influx rate was calculated using graphical analysis by Patlak et al. A: young normal control; B, C: early onset Parkinson's disease (B: case 3, C: case 7); D: aged normal control; E, F: late onset Parkinson's disease (E: case 11, F: case 18).

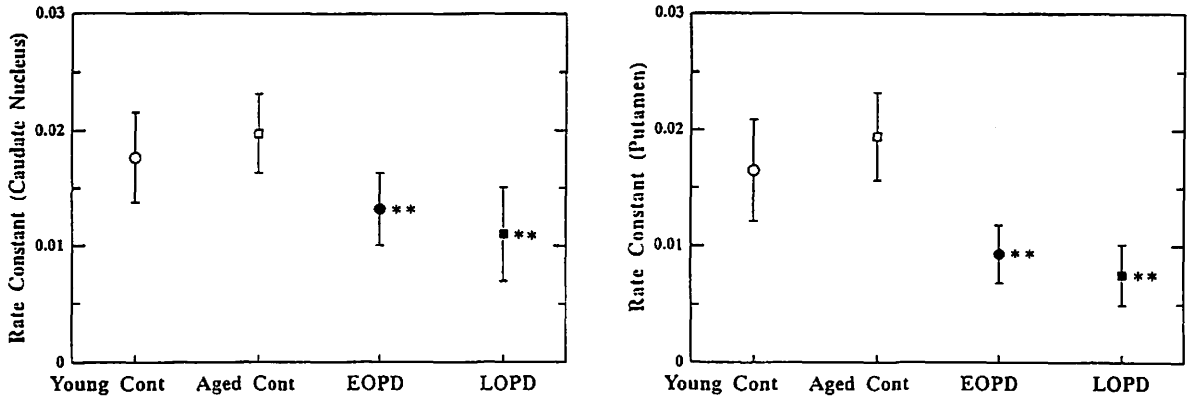

Fig. 2. FDOPA influx rate in the caudate nucleus and the putamen from young (○) and aged (□) normal controls, early (●) and late (■) onset Parkinson's disease. **: $p<0.01$; statistic significance compared with normal control groups using the Mann-Whitney U-test.

Figure 3 A

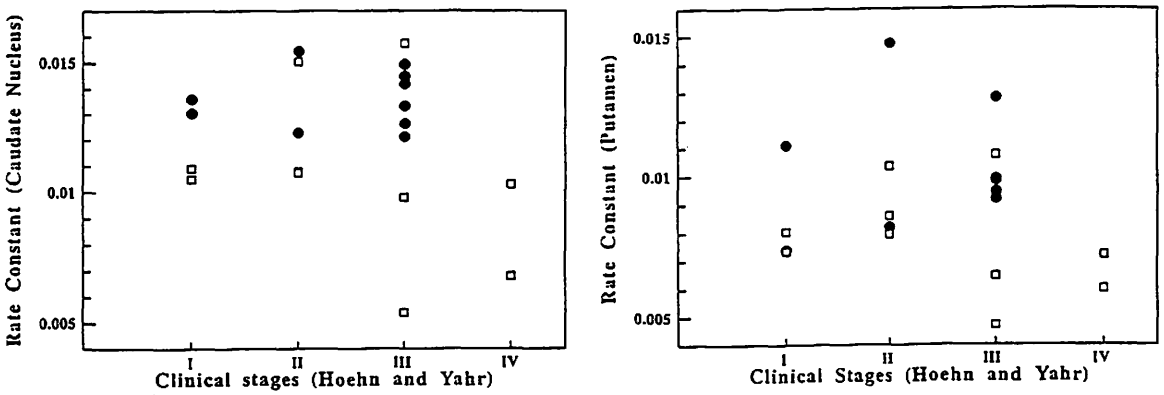

Figure 3 B

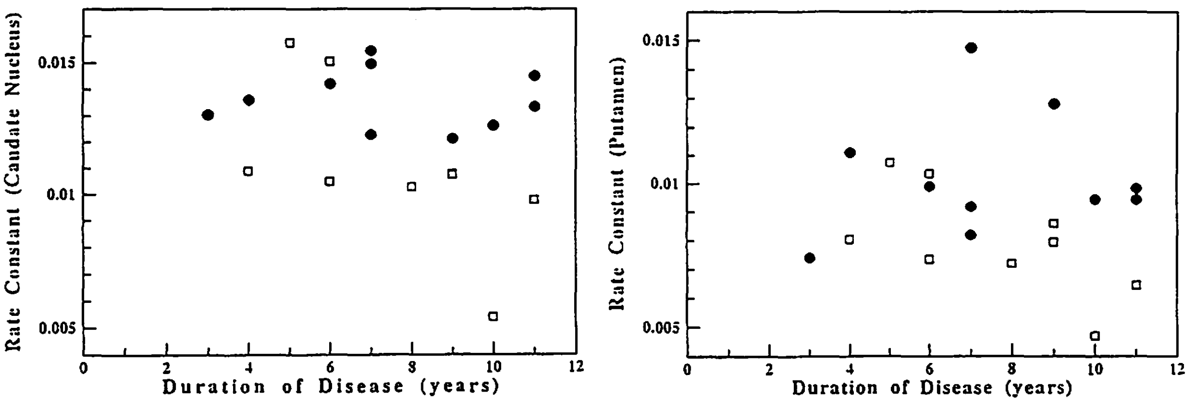

Fig. 3. Correlations between FDOPA influx rates and clinical stages (A) and the duration of disease (B) in early (●) and late (□) onset Parkinson's disease.

Figure 4 A

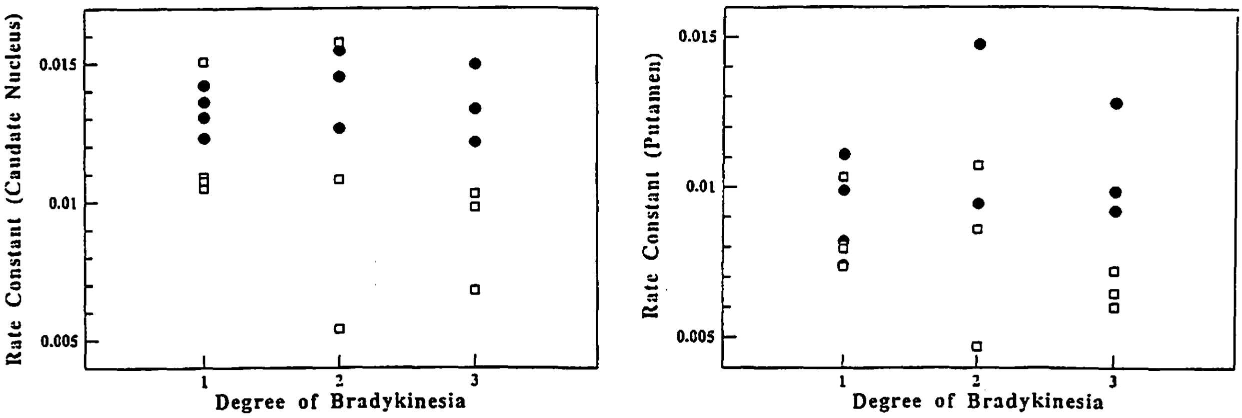

Figure 4 B

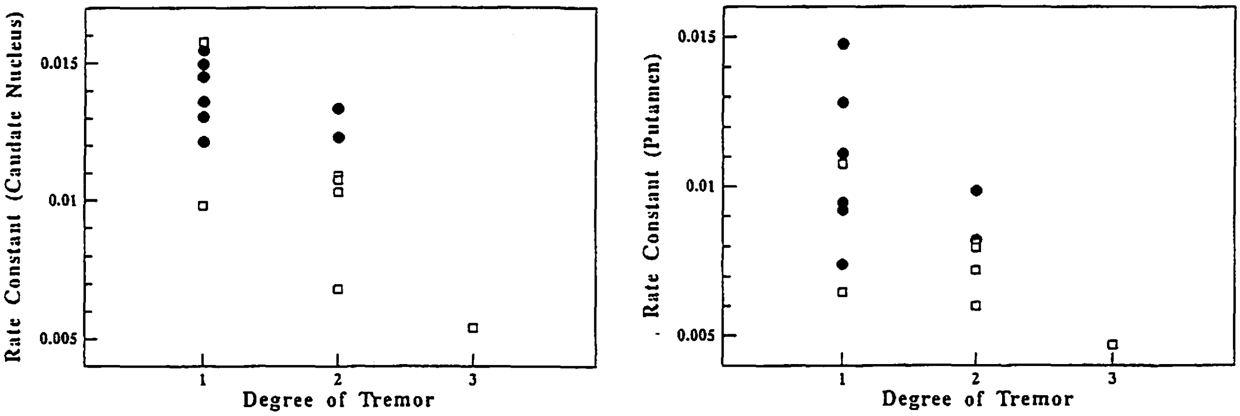

Figure 4 C

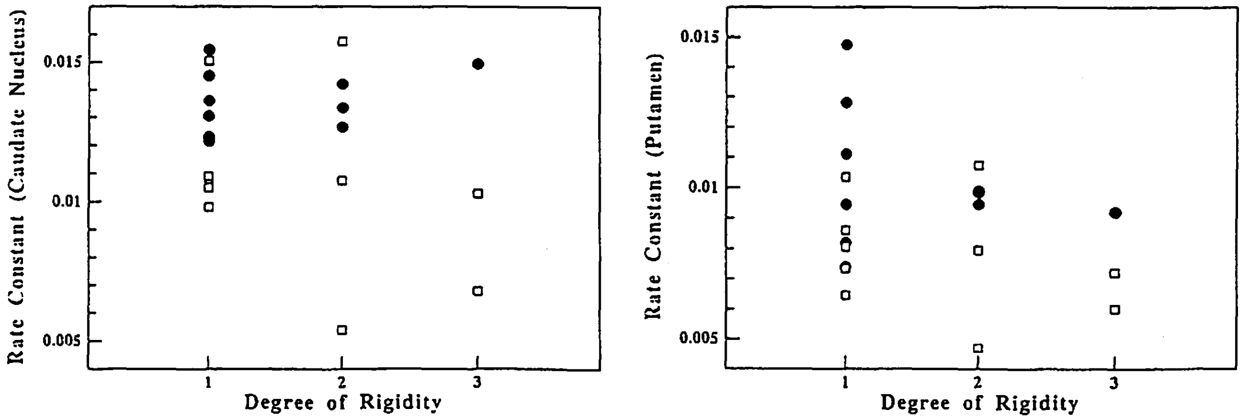

Fig. 4. Correlations between FDOPA influx rates and individual clinical symptoms (A: bradykinesia; B: tremor; C: rigidity) in early (●) and late (□) onset of Parkinson's disease.

IV. 7. PET Study of Striatal Fluorodopa Uptake and Dopamine D2 Receptor Binding in a Patient with Juvenile Parkinsonism

Tanji H., Nagasawa H., Onodera J., Takase S.**, Funaki Y.***, Iwata R.***, Itoh M.***, Ido T.***, and Itoyama Y.*

Department of Neurology, Tohoku University School of Medicine
*Department of Neurology, Miyagi National Hospital**
*Department of Neurology, Kohnan Hospital***
*Cyclotron and Radioisotope Center, Tohoku University****

Introduction

Juvenile parkinsonism (JP), dopa-responsive dystonia (DRD) and hereditary progressive dystonia with marked diurnal fluctuation (HPD) are all major syndromes which are characterized both by parkinsonism and dystonia in the early decades of life and by good response to L-dopa treatment. Although the clinical entity and pathomechanism of the disorder and their relationship have been discussed in the past at great length, it still difficult to differentiate clinically JP from DRD or HPD. Positron emission tomographic (PET) study using [^{18}F]6-fluorodopa (^{18}FDOPA) has been able to provide efficient information on the pre-synaptic function of nigrostriatal dopaminergic neurons in patients with parkinsonism or dystonia[1-10]. Furthermore, it is known that the PET study of the post-synaptic D2 receptor function using ^{11}C-YM-09151-2 (^{11}C-YM), N-[(2RS, 3RS)-1-benzyl-2-methyl-3-pyrrolidinyl]-5-chloro-2-methoxy-4-methylaminobenzamide, a highly selective antagonist to the brain dopamine D2 receptor, can be very informative [11-14], as regards the pathomechanism of these L-dopa responsive disorders. Of particular importance is information on striatal fluorodopa uptake and dopamine D2 receptor binding. We report here on the neuroimaging data of these, and on the cerebral glucose metabolism, in a patient with JP.

Patient and Methods

PATIENT

A 17-year-old girl had an uneventful birth and normal growth until 7 years of age. There was no significant family history except consanguinity on her mother's side. At age 8, she noted abnormal gait; she always walked on tiptoe except when stationary. Her gait became gradually worse, and she developed a tendency to fall over backwards. At age 9, she received treatment with L-dopa and muscle relaxants. After medication, her general condition improved appreciably, and she became able to walk more comfortably. Unfortunately, her gait became gradually worse again, particularly when she walked long distance. At age 12, she complained of clumsiness in upper limbs, and these symptoms started to fluctuate. At age 15, she had to take greater dose of L-dopa, and involuntary movement began to appear in her legs.

On admission, she was a well-developed and well-nourished girl, 152 cm in height and 45 kg in weight. She was alert and well-oriented. Neurological examination revealed marked akinesia and rigidity in all four limbs, especially the upper ones. There was mild postural tremor in the upper limbs and prominent dystonia in the lower. These findings almost improved by L-dopa treatment. Although diurnal fluctuation of the symptoms was uncertain, marked improvement was seen after sleep. Although wearing-off and on-off phenomena were also uncertain, involuntary movement suspected dopa-induced dyskinesia was seen in her legs. Based on these clinical features, she was diagnosed as JP with dystonia.

Routine blood tests and cerebrospinal fluid examination were normal, as were serum ceruloplasmin and copper levels. Magnetic resonance imaging (MRI) was normal in the cerebral hemispheres, basal ganglia, cerebellum and brainstem.

PET STUDIES AND DATA ANALYSIS

PET studies of fluorodopa uptake and glucose metabolism were performed with a model PT-931 scanner (CTI Inc., USA), and the study of dopamine D2 receptor was performed with a model SET-2400W scanner (Shimazu, Japan), at the Cyclotron and Radioisotope Center, Tohoku University, Sendai, Japan. These studies were approved by the Research Ethics Committee of Tohoku University School of Medicine. Informed consent was obtained from the patient and her parents. The patient's head was positioned in the scanner with her eyes closed, and the whole procedure was performed in a semi-darkened room with minimal background noise. Before the emission scan, a 15-min ^{68}Ge-^{68}Ga transmission scan was performed.

In the study of fluorodopa uptake, ^{18}FDOPA was synthesized as descrived by Adam et al(15) with a radiochemical purity of more than 99%. After an intravenous bolus injection of ^{18}FDOPA (7.7 mCi) into the patient, a series of 5 min emission scans was performed over 60 min, and emission data were simultaneously collected from seven contiguous axial sections, each about 6 mm in thickness from orbitomeatal (OM) line + 66 to OM + 22 mm. After data collection, the latter six continuous images of the same brain slices, scanned between 30 and 60 min after administration of ^{18}FDOPA, were added and composite images were obtained in order to improve the contrast between dopaminergic and nondopaminergic brain regions, in order to aid the definition of anatomical regions of interest according to the method of Nagasawa et al(4). Moreover, the ^{18}FDOPA uptake rate constant was calculated pixel-by-pixel utilizing the Patlak graphical analysis method(16,17) to generate the parametric image for the image plane that had the highest contrast between the striatum and background. In this analysis, the input function was the dynamic image pixel values of the cerebellum as a reference tissue region which was devoid of dopaminergic terminals.

In the study of dopamine D2 receptor, ^{11}C-YM was synthesized according to the method of Hatano et al[13]. After an intravenous bolus injection of ^{11}C-YM (3.06 mCi), twenty emission scans were performed in series over 90 min using a SET-2400W. After data collection, the latter five continuous images of the same brain slices scanned between 60 and 90 min after administration of ^{11}C-YM were added and composite images were obtained in order to improve the contrast between dopaminergic and nondopaminergic brain regions.

In the study of glucose metabolism, ^{18}FDG was synthesized according to the method of Ido et al[18]. ^{18}FDG (5.3 mCi) was injected as an intravenous bolus. 30 to 60 min after the injection, a series of three emission scans, each of 10 min duration, was performed at standard points 16, 63 and 110 mm above and parallel to the OM line. Each emission data was simultaneously collected from seven contiguous axial sections. A total of 21 slices parallel to the OM line with a slice thickness of 6 mm were analyzed. Twenty blood samples were collected from the brachial artery during the study, and they were immediately centrifuged, and the arterial plasma radioactivities of ^{18}FDG were measured with a cross-calibrated well- counter. The cerebral metabolic rate for glucose (CMRGlc) was calculated using the operational equation derived by Phelps et al[19] and Huang et al[20] from that of Sokoloff et al[21].

Results

PET images of three contiguous axial sections added between 30 and 60 min after administration of ^{18}FDOPA and images of ^{18}FDOPA uptake rate constant, of a young normal subject (33-year-old male) are shown in Fig 1 A and B. High concentration of ^{18}FDOPA and its labeled metabolites and high value of ^{18}FDOPA uptake rate constant in the bilateral striata are clearly visible. On the other hand, for this patient diagnosed as JP, ^{18}FDOPA accumulation and its uptake rate constant were markedly decreased in the putamen on both hemispheres. ^{18}FDOPA uptake was preserved only in the bilateral lower parts of the caudate nucleus. (Fig 2 A and B).

There was a high accumulation of ^{11}C-YM in the caudate nucleus and the putamen on both hemispheres (Fig 3), which indicated no decrease of dopamine D2 receptor binding in the striatum of this patient.

The CMRGlc was almost normal in the whole brain including both basal ganglia without asymmetry in this patient (Fig 4).

Discussion

The clinical entities or nosological concepts of JP, DRD and HPD and the relationship of these disorders have been controversial[7-10,22-28]. Yokochi[27] suggests that"dopa-responsive syndrome" may be divided into two groups; one is "dopa-responsive disease characterized by dystonia" and the other is "dopa-responsive disease characterized by parkinsonism". The former included DRD and HPD and the latter included JP and Parkinson's disease. However, there are some difficulties in clinically differentiating JP from DRD or HPD.

In comparison with Parkinson's disease, JP is clinically characterized as follows: there is a much higher familial incidence; disease progression is much slower; more cases lack tremor, which, if it exists, occurs mostly in posture or in action, but not at rest; dystonic movements are observed more often, especially in cases of onset at an early age; more effective responses to L -dopa are observed; adverse effects such as wearing-off phenomenon and dopa-induced dyskinesia sometimes appear in the extremities[27)]

The present case has no family history of parkinsonism. Initially she noted gait disturbance due to dystonia of the legs at 8 years of age, and its symptoms were slowly progressive and developed parkinsonism with postural tremor. The clinical effect of L-dopa was remarkable. Wearing-off or on-off phenomenon was not obviously observed. However, dopa-induced dyskinesia was seen in the legs. Diurnal fluctuation was uncertain, but her symptoms improved after sleep. Based on these clinical features, JP is probably the most appropriate as diagnosis. However, it remains difficult to differentiate her condition clearly from DRD or HPD.

There have been several reports on PET studies using ^{18}FDOPA in patients with DRD [6-8,10)]. Nygaard et al[7)], Takahashi et al[8)] and Snow et al[10)] reported normal striatal ^{18}FDOPA uptake in DRD patients. Sawle et al[6)] described that modest reduction of ^{18}FDOPA uptake was observed in the striatum of 6 patients with typical DRD, but such a finding was not as evident as that observed in Parkinson's disease. Okada et al[9)] reported a Japanese patient with HPD, so-called "Segawa's disease", studied by PET using ^{18}FDOPA. They observed no significant difference in ^{18}FDOPA uptake into the striatum of the patient compared with age matched controls. On the other hand, Snow et al[10)] reported marked decrease of ^{18}FDOPA uptake into the striatum in three patients with JP who were under 20 years of age.

The PET study using ^{18}FDOPA in the present case shows marked decrease of ^{18}FDOPA uptake into both putamen and caudate nucleus compared with the control case. This finding is different from those in patients with dystonia syndromes such as DRD and HPD, and it is rather similar to Parkinson's disease. Therefore, we diagnosed this patient as JP with conviction on the basis of her clinical features and the result of ^{18}FDOPA PET study.

Fluorodopa is metabolised to fluorodopamine by L-aromatic amino acid decarboxylase, and this enzyme is located primarily within the nigrostriatal nerve endings in the striatum. We consider that the accumulation of ^{18}FDOPA in striatum provides an index of the pre-synaptic function of the dopaminergic pathway. The decrease of the striatal ^{18}FDOPA uptake in this patient may indicate a defect in the decarboxylation, disturbance of vesicular uptake and decreased capasity for storage of ^{18}FDOPA. It may also indicate neuronal loss in the substantia nigra, findings which may be similar to pathogenesis observed in Parkinson's disease.

On the other hand, there have been few reports about dopamine D2 receptor in JP. In Parkinson's disease, it has been described that striatal dopamine D2 receptor binding was raised in untreated patients at an early stage, but reduced in chronically treated patients with fluctuating response to L-dopa at an advanced stage, by PET studies[29-34) or post-mortem studies[35,36). In this patient with JP, ^{11}C-YM was highly accumulated in the striatum, which indicates no decrease of dopamine D2 receptor binding. It suggests that the post-synaptic D2 receptor function in the striatum is almost normal in this patient with JP.

Also there have been few reports about cerebral glucose metabolism in JP. However, in Parkinson's disease, some PET studies[37,38) have demonstrated the diffuse and mild decrease of cerebral glucose metabolism, whereas others[39) have described these as normal in the patient without dementia. Especially in Parkinson's disease with dementia, severe hypometabolism in the temporoparietal cortex, which is similar to that seen in Alzheimer's disease, has also been described[37,38). In this patient with JP, the CMRGlc did not decrease in the whole cerebrum. This suggests that there is no marked morphological changes with loss of synapses due to decreased numbers of cortical neurons or degeneration of axons.

A PET study measuring striatal fluorodopa uptake is essential for the diagnosis of JP, as well as for distinguishing from DRD and HPD. This is the first report to have performed three types of PET study, involving fluorodopa uptake, dopamine D2 receptor binding and glucose metabolism, in a JP patient. Such studies can provide efficient information about the pathomechanism of JP.

Acknowledgement

We are grateful to Mr. Shinya Seo and Mr. Shoichi Watanuki for expert technical assistance.

References

1) Nahmias C., et al., J. Neurol. Sci. **69** (1985) 223.
2) Leenders K. L., et al., J. Neurol. Neurosurg. Psychiatry. **49** (1986) 853.
3) Otuka M., et al., J. Neurol. Neurosurg. Psychiatry. **54** (1991) 898.
4) Nagasawa H., et al., J. Neurol. Sci. **115** (1993) 136.
5) Martin W. R. W., et al., Adv. Neurol. **50** (1988) 223.
6) Sawle G. V., et al., Ann. Neurol. **30** (1991) 24.
7) Nygaard T. G., et al., Ann. Neurol. **32** (1992) 603.
8) Takahashi H., et al., Adv. Neurol. **60** (1993) 586.
9) Okada A., et al., Adv. Neurol. **60** (1993) 591.
10) Snow B. J., et al., Ann. Neurol. **34** (1993) 733.
11) Terai M., et al., Jpn. J. Pharmacol. **33** (1983) 749.
12) Nikzik H. B., et al., Arch. Pharmacol. **329** (1985) 333.
13) Hatano K., et al., J. Nucl. Med. **30** (1989) 515.
14) Hatazawa J., et al., J. Nucl. Med. **32** (1991) 713.
15) Adam M. J., et al., J. Nucl. Med. **26** (1985) 125.
16) Patlak C. S., Blasberg R. G. and Fenstermacher J. D., J. Cereb. Blood Flow Metab. **3** (1983) 1.
17) Patlak C. S. and Blasberg R. G., J. Cereb. Blood Flow Metab. **5** (1985) 584.

18) Ido T., et al., J. Org. Chem. **42** (1977) 2341.
19) Phelps M. E., et al., Ann. Neurol. **6** (1979) 371.
20) Huang S. C., et al., Am. J. Physiol. **238** (1980) E69.
21) Sokoloff L., et al., J. Neurochem. **28** (1977) 897.
22) Yokochi M., et al., Adv. Neurol. **40** (1984) 407.
23) Quinn N., Critchley P. and Marsden C. D., Mov. Disord. **2** (1987) 73.
24) Nygaard T. G., Marsden C. D. and Duvoisin R. C., Adv. Neurol. **50** (1988) 377.
25) Ujike H., et al., Clin. Neurol. **29** (1989) 890.
26) Lamberti P., et al., Acta Neurol. Napoli **14** (1992) 451.
27) Yokochi M., Adv. Neurol. **60** (1993) 548.
28) Yamamura Y., et al., Clin. Neurol. **33** (1993) 491.
29) Hagglund J., et al., Acta Neurol. Scand. **75** (1987) 87.
30) Rinne U. K., et al., Mov. Disord. **5** (1990) 55.
31) Rinne J. O., et al., J. Neurosci. Res. **27** (1990) 494.
32) Brooks D. J., et al., Ann. Neurol. **31** (1992) 184.
33) Snow B. J., Can. J. Neurol. Sci. **19** (1992) 138.
34) Rinne J. O., et al., Mov. Disord. **8** (1993) 134.
35) Guttman M. and Seeman P., Adv. Neurol. **45** (1986) 51.
36) Rinne J. O., et al., Brain Res. **556** (1991) 117.
37) Kuhl D. E., Metter E. J. and Riege W. H., Ann. Neurol. **15** (1984) 419.
38) Peppard R. F., et al., Arch. Neurol. **49** (1992) 1262.
39) Sasaki M., et al., Ann. Nucl. Med. **6** (1992) 214.

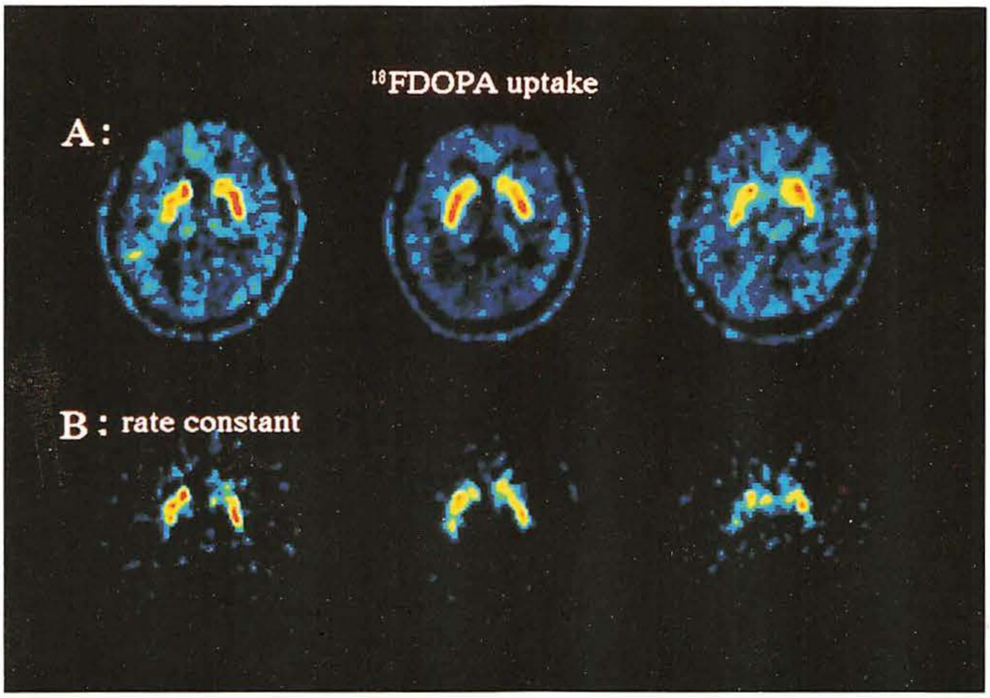

Figure 1. PET images of three contiguous axial sections added between 30 and 60 min after administration of ^{18}FDOPA (A), and parametric images (Patlak Image) of the ^{18}FDOPA uptake rate constant (B), of a young normal subject. High concentration of ^{18}FDOPA and its labeled metabolites and high value of ^{18}FDOPA uptake rate constant in the bilateral striata were clearly visible.

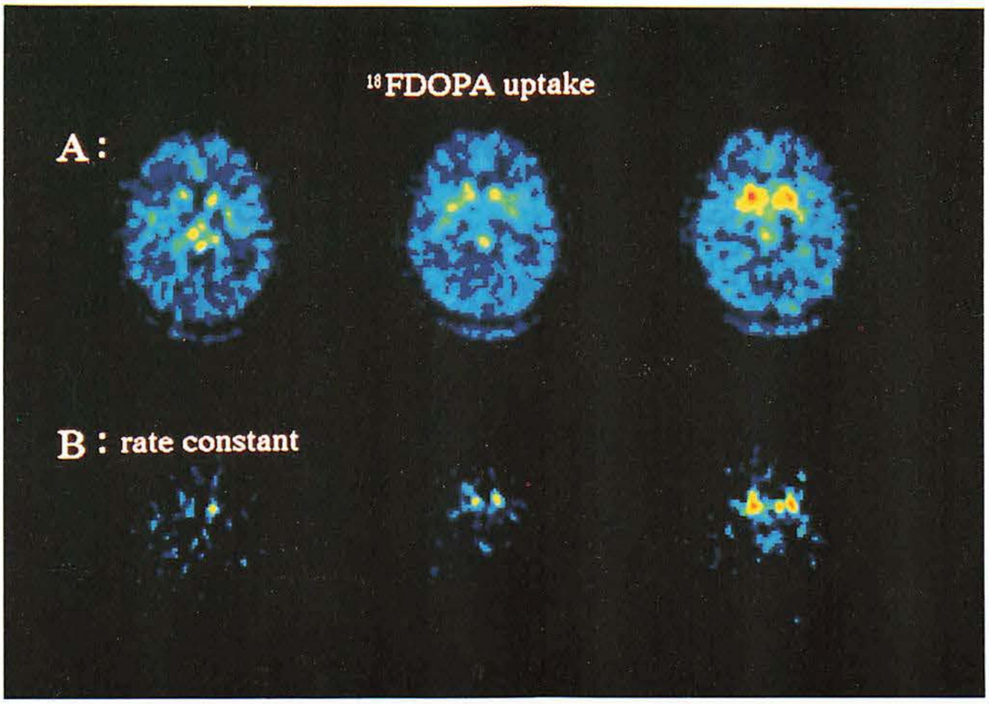

Figure 2. PET images of three contiguous axial sections added between 30 and 60 min after administration of ^{18}FDOPA (A), and parametric images (Patlak Image) of the ^{18}FDOPA uptake rate constant (B), of this patient with JP. ^{18}FDOPA accumulation and its uptake rate constant were markedly decreased in the putamen on both hemispheres. ^{18}FDOPA uptake was preserved only in the bilateral lower parts of the caudate nucleus.

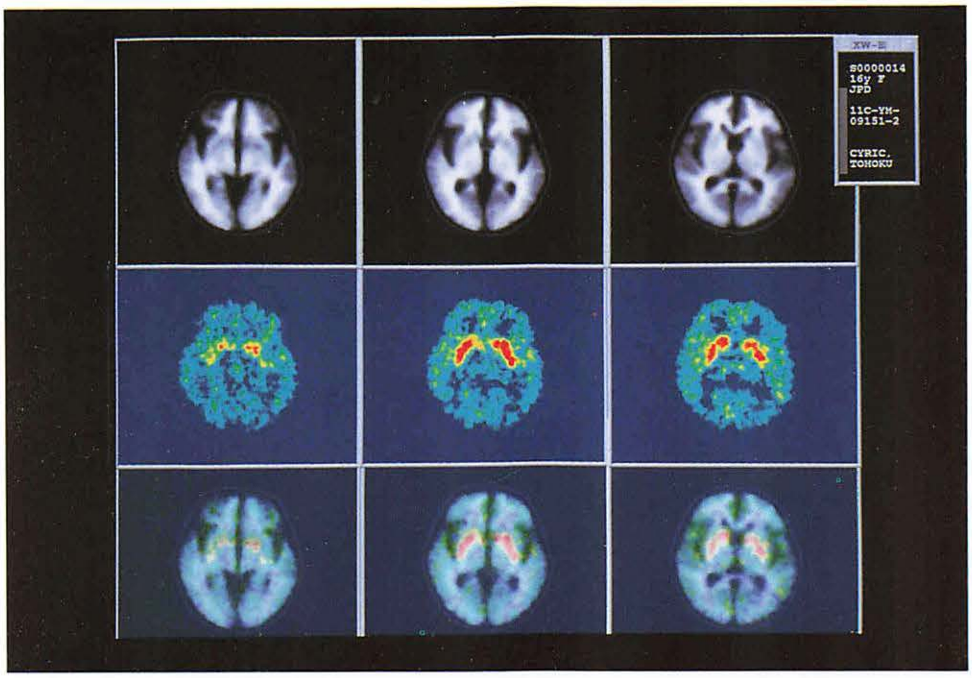

Figure 3. Aligned MR images, PET images added between 60 and 90 min after administration of ^{11}C-YM and the overlapped images at the same brain slices, of this patient with JP. ^{11}C-YM was highly accumulated in the caudate nucleus and the putamen on both hemispheres, which indicated no decrease of dopamine D2 receptor binding in the striatum.

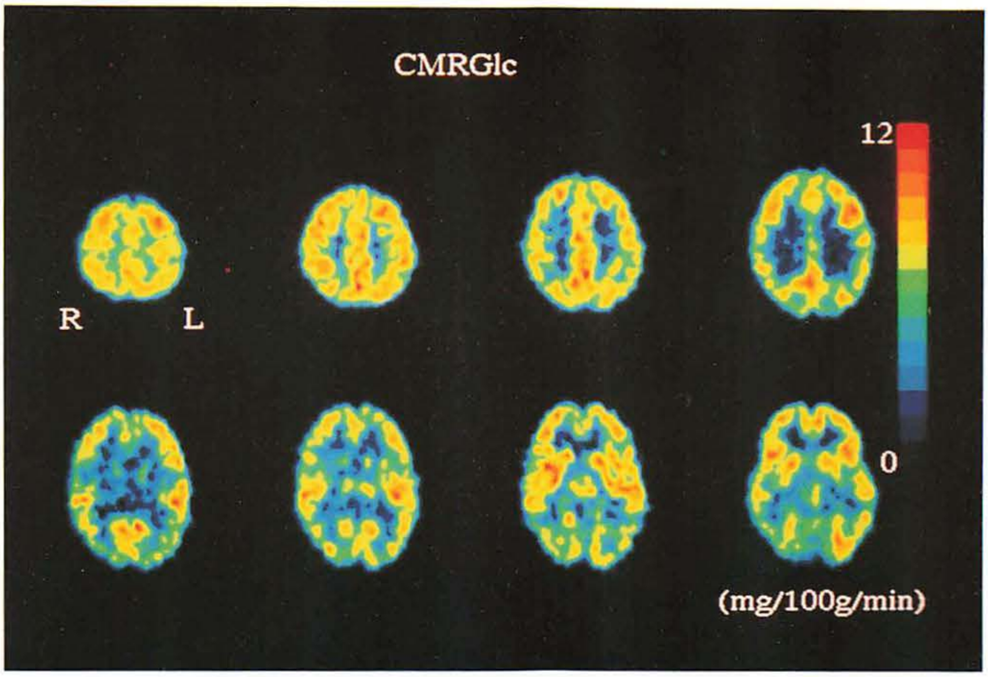

Figure 4. PET images of cerebral metabolic rate for glucose (CMRGlc) of this patient with JP. The CMRGlc was almost normal in the whole cerebrum including both basal ganglia without difference between right and left.

IV. 8. Regional Glucose Metabolism and Dopamine Uptake in the Brain of Patients with Corticobasal Degeneration Studied with Positron Emission Tomography

Nagasawa H.[*,**], *Tanji H.*[**], *Nomura H.*[***], *Saito H.*[****], *Kimura I.*[*****], *Itoyama Y.*[**], *Tsuji S.*[******], *Fujiwara T.*[*******], *Iwata R.*[*******], *Itoh M.*[*******] *and Ido T.*[*******]

Department of Neurology, Miyagi National Hospital[*]
Tohoku University School of Medicine[**]
Konan Hospital[***]
Nisitaga National Hospital[****]
Yamagata National Hospital[*****]
Brain Research Institute, Niigata University[******]
Cyclotron and Radioisotope Center, Tohoku University[*******]

Introduction

Rebeiz et al. described the clinical and pathological findings in three patients who presented in late middle age with variable combinations of an asymmetric akinetic-rigid syndrome, apraxia, supranuclear palsy and frontal lobe sign, and they called "corticodentatonigral degeneration with neuronal achromasia" as a novel degenerative disease[1]. Thereafter, Gibb et al. reported three patients and reviewed the clinical and pathological features of corticobasal degeneration[2]. The diagnosis of corticobasal degeneration can be predicted during life on the basis of clinical features referable to both cerebral cortical and basal ganglionic dysfunctions, but a definitive diagnosis requires confirmation by autopsy[3]. However, recent studies using positron emission tomography (PET) indicated that distinctive supportive findings for the diagnosis could be obtained with this technique[4-7]. In the present study, we measured regional glucose utilization and striatal $[^{18}F]$dopa uptake in clinically diagnosed cases of corticobasal degeneration and we indicated that this unique combination of PET studies could provide efficient information to differentiate them from other degenerative diseases with cognitive and movement disorders.

Subjects and methods

SUBJECTS

We studied 6 patients, 2 men and 4 women, who were clinically diagnosed corticobasal degeneration by neurologists. The age of onset of their initial symptoms was ranged from 57 to 68 years (mean ± SD, 60.8 ± 2.5). The main clinical pictures of the patients are composed of distinctive symptoms of akinetic-rigid symdrome, apraxia and other cerebral dysfunction, those which are compared with previous reports[1-6]. There were no effective response to levodopa therapy against parkinsonism in all patients. The clinical profiles of the studied patients are summarized in Table 1.

POSITRON EMISSION TOMOGRAPHY

PET study was performed with a model PT-931 scanner (CTI Inc., USA) at the Cyclotron and Radioisotope Center, Tohoku University, Sendai, Japan. The project was approved by the Research Ethics Committee of the Tohoku University, School of Medicine. The control group consisted of healthy normal volunteers with an age range 49-74 years (mean±SD, 63.5±9.0), without a history of recent medical illness, neurological diseases, developmental disorders or substance abuse. Control subjects underwent a complete neurological examination and neuropsychological evaluation before PET and their magnetic resonance imaging (MRI) findings of the brain were normal. All subjects gave their written informed consent.

Cerebral metabolic rate for glucose (CMRGlc) was measured in all six patients and six normal control subjects. Before the study, a short 21-gauge cannula was placed in a brachial or a radial artery under local anesthesia for arterial blood sampling. Each subject was then positioned in the scanner, with the orbitomeatal (OM) line parallel to the detector rings according to the brain slices by MRI. A cross of light was projected onto marks on the subject's head from three dimensions, and heads were set at the standard points of 16, 63 and 110 mm above and parallel to the OM line. All studies were conducted in a quiet, semi-darkened room with minimal background noise. The subjects' eyes were open and their ears were unplugged.

Before the emission scanning, a 20-min transmission scan using a ^{68}Ge-^{68}Ga external ring source was performed to correct for tissue attenuation. Three to 5 mCi of 2-[^{18}F]fluoro-2-deoxy-D-glucose (^{18}FDG) was injected as an intravenous bolus. Thirty to 60 min after the injection, a series of three emission scans was performed by using a PT-931 with an 8 mm axial and transaxial resolution at the center of each standard point. Each emission datum was simultaneously collected from seven contiguous axial sections. A total of 21 slices parallel to the OM line with a slice thickness of 6 mm, encompassing virtually the whole brain, were analyzed. Twenty blood samples were collected from the arterial cannula according to the following protocol: from injection to 2 min, one sample every 20 seconds, then samples at 2.5, 3, 4, 5, 7.5, 10, 15, 20, 25, 40, 45, 50 and 60 min after the intravenous administration of ^{18}FDG. The blood samples were immediately centrifuged, and arterial plasma radioactivities of ^{18}FDG were measured with a cross-calibrated well counter. The arterial plasma glucose concentrations were measured every 10 min during the study.

On a separate occasion, in the 4 patients and 10 normal control subjects, dopamine metabolism was measured using [^{18}F]-6-fluorodopa (FDOPA) in order to assess the presynaptic functional integrity of the nigrostriatal system. FDOPA was synthesized by method by Adam et al. with a radiochemical purity of more than 99%[8]. After a 15-min transmission scan, FDOPA (2.5-8.3 mCi or 14.9-49.5 nmol) was intravenously injected into the subjects and dynamic emission scans, each of 5 min duration, were performed over 60 min. Emission data were simultaneously collected from seven contiguous axial sections, each of about 6 mm in thickness from OM + 66 to OM + 22 mm.

DATA ANALYSIS

After data collection, the latter six contiguous images of the same brain slice scanned between 30 and 60 min after administration of FDOPA were added and composite images were obtained in order to improve the contrast between dopaminergic and non-dopaminergic brain regions to aid the definition of anatomical regions of interest (ROIs)[9]. In each case, two different pairs of images, the PET images and the images obtained by MR, were registered and matched with each other using image scaling to bring the disparate pairs of image data into congruence at the same brain slices according to the previous study[9]. To ascertain the anatomical position of each brain structure, the position of ROIs were manually defined using the overlapped images, e.i., PET images and MR images of the same brain slices. Influx constants (Ki min^{-1} value) were calculated for the caudate nucleus and the putamen separately using a multiple graphical analysis method with cerebellar tissue input function[10,11]. The Ki value is a rate constant that reflects uptake and decarboxylation of FDOPA into [^{18}F]dopamine and its metabolites by the nigrostriatal nerve terminals.

To obtain values of regional CMRGlc, a total of 22 ROIs in each hemisphere were placed on these overlapped images by reference to neuroanatomical atlases[12,13] as reported previously[14]. CMRGlc was calculated using the operational equation derived by Phelps et al.[15] and Huang et al.[16] from that of Sokoloff et al[17]. Values of the rate constants and lumped constant were those proposed by Phelps et al[15]. The average values of CMRGlc within each structure are presented as means ± SD. The Mann-Whitney U-test was used to compare the values of CMRGlc in each structure of the brain between patients and controls with $p<0.05$ and $p<0.01$ considered to be statistically significant.

Results

Representative images obtained by ^{18}FDG PET and magnetic resonance at the levels of corresponding brain slices from the patients are shown in Fig. 1. Values of regional CMRGlc in each brain structure of six normal controls and six patients with corticobasal degeneration are summarized in Table 2. The most prominent changes of CMRGlc in the patients were demonstrated with an asymmetry in the parietal cortex, the thalamus, the caudate nucleus and the putamen contralateral to the dominantly affected symptoms. The reduction of CMRGlc in these regions was significant compared with normal control values in the corresponding regions. In the cerebral cortex, regional CMRGlc was variably decreased in frontal, parietal and temporal cortices relating to the clinical symptoms in the individual patient with relative sparing bilateral occipital cortex including primary and associative visual areas. In the parietal cortex of the dominantly affected hemisphere, regional CMRGlc decreased in the primary motor and sensory cortex and the lateral parietal cortex with variable involvement of the adjacent centrum semiovale, and these lesions could be responsible for the referable clinical symptoms, such as motor apraxia. There were no significant abnormalities of CMRGlc in the brainstem and the cerebellum of the patients.

The images obtained by MR and FDOPA PET at the level of the caudate nucleus and the putamen, and the overlapped image from a normal subject and the patients are shown in Fig. 2. The values of rate constant of FDOPA uptake in the caudate nucleus and the putamen are given in Table 3. In the normal control subjects, the accumulation of [^{18}F] activity was uniformly concentrated in the caudate nucleus and the putamen on both hemispheres. However, in patients 1, 3 and 4, FDOPA uptake was severely impaired in the caudate nucleus and the putamen contralateral to the clinically most severely affected side, while in patient 2, FDOPA uptake was decreased with selective impairment of the left putamen, compared with normal control group.

Discussion

The main clinical pictures of the patients are composed of distinctive symptoms of akinetic-rigid syndrome, apraxia and other cerebral dysfunction, those which are compared with previous reports[1-6)]. The patients 2 and 5 were less affected with akinesia, but more affected with rigidity and mild tremor of their limbs. By the time of their PET studies, all patients had developed signs of akinetic-rigid syndrome and all had apraxia of one or more limbs. Some patients had more severely affected with cerebral symptoms, mild dementia in the patient 4 and moderate degree of aphasia in the patient 6, than other cortical dysfunction. However, their MRI revealed no responsible ischemic lesions in the cerebral cortices except for mild cortical atrophy.

The most prominent abnormalities of PET findings in the studied patients were a significant reduction of CMRGlc with an asymmetry in the thalamus, the striatum and the parietal cortex contralateral to the more affected side, those which compared with normal control values in each corresponding region. In the present study, such findings were in agreement with asymmetric clinical symptoms manifested in the individual case. A distinct asymmetrical decrease of CMRGlc detected in cortical and subcortical regions may be characteristic in all patients with the disease and such finding is consistent with the previous study[18)].

A significant reduction of CMRGlc in the primary motor and sensory regions of parietal cortex observed in the patients is distinct and we consider that hypometabolism of this region can be responsible for motor apraxia which is one of the main symptoms of patients with corticobasal degeneration. Such finding is also important to differentiate them from Alzheimer's disease. The impairment of metabolism in fact affects all cortical regions in Alzheimer's disease, but is much less pronounced in the primary motor and sensory regions as well as the visual cortex[19-21]. Furthermore, reduction of CMRGlc in the thalamus was also asymmetrically observed in the ipsilateral to the parietal cortical regions. Therefore, it is not easy to explain that the hypometabolism observed in the thalamus might be caused by primary neuronal damage itself or secondary neuronal degeneration[14,22]. A further detailed study for more cases is required to clarify the mechanism of glucose hypometabolism due to neuronal network disturbances observed in the thalamus of patients with corticobasal degeneration.

PET study using FDOPA can provide further supportive evidence for clinical diagnosis of corticobasal degeneration. FDOPA accumulation was markedly reduced with an asymmetry in the caudate nucleus and the putamen contralateral to the dominantly manifested symptoms in the individual case. In the patient 2, the rate constant (Ki) of FDOPA was not severely reduced and an asymmetry of FDOPA accumulation was not so remarkable as compared with the other cases. We consider the reason why such finding might be related to basal ganglionic dysfunctions and his clinical signs, which were characterized that he was less affected with akinesia, but he was only suffered from mild rigidity and tremor during his clinical history. The Ki value reflects uptake and decarboxylation of [^{18}F]dopa into [^{18}F]dopamine and its metabolites by the nigrostriatal nerve terminals. It therefore relates to the rate of exogenous dopa metabolism but not reflect the rate of endogenous dopamine synthesis because of tyrosine hydroxylase is regulated as a rate-limiting enzyme[10,11]. Reduced uptake rate of FDOPA is considered to represent a reduction in the number of functional nigrostriatal dopaminergic neurons at the presynaptic sites of the affected striatum[23].

In the present study, PET images can reveal dysfunction not only in fluorodopa metabolism, but also in glucose utilization of the affected striatum of the patients. We consider that reduction of CMRGlc is distinct and important to differentiate them from other degenerative disorders with basal ganglionic dysfunction, since the caudate nucleus and the putamen are frequently and relatively spared in degenerative disease, such as Parkinson's disease[24-27]. These findings indicate that damage of the striatum might be more severely involved not only in the presynaptic sites but also in the postsynaptic sites of the nigrostriatal system, and that other neurotransmitter receptor systems might be involved in the striatum during the progressive course of the disease. A new brain imaging study using other radioactive ligands will be performed in order to clarify such problems in the future.

Sawle et al. reported that the combination PET study using FDOPA and cerebral oxygen metabolism was useful for diagnosis of corticobasal degeneration[6]. We indicated that measurement of glucose metabolism could provide more efficient information for diagnosis than that of cerebral blood flow and oxygen metabolism. In conclusion, we consider the unique combination study measuring both cerebral glucose utilization and dopamine metabolism with PET can provide further supportive evidences for the clinical diagnosis of corticobasal degeneration. Moreover, we also realize that further detailed investigation is needed to confirm these clinical observations obtained by PET study will correlate to the biochemical deficits with individual neuropathological findings in order to define the diagnostic criteria for the disorder.

References

1) Rebeiz J. J., Kolodny E. H. and Richardson E. P., Arch. Neurol. **18** (1986) 20.
2) Gibb W. R. G., Luthert P. J. and Marsden C.D., Brain **112** (1989) 1171.
3) Riley D. E., et al., Neurology **40** (1990) 1203.
4) Watts R. L., et al., Neurol. **35** (Suppl.) (1985) 178.
5) Eidelberg D., et al., Neurology **164** (Suppl.) (1989) 164.
6) Sawle G. V., et al., Brain **114** (1991) 541.
7) Nagasawa H., et al., Behavioral Neurol. **6** (1993) 59.
8) Adam M. J., et al., J. Nucl. Med., **26** (1985) 125.
9) Nagasawa H., et al., J. Neurol. Sci. **115** (1993) 136.
10) Patlak C. S., et al., J. Cereb. Blood Flow Metab. **3** (1983) 1.
11) Patlak C. S. and Blasberg R. G. J. Cereb. Blood Flow Metab. **5** (1985) 584.
12) Salamon G. and Huang Y. P. Computed Tomography of the Brain. Springer Verlag, Berlin, Heidelberg, New York.
13) Talairach J. and Tournoux P. Co-planar stereotaxic atlas of the human brain. 3-dimensional proportional system: an approach to cerebral imaging. George Thiem Verlag, Stuttgart.
14) Nagasawa H., et al., J. Neurol. Sci. **123** (1994) 147.
15) Phelps M. E. et al., Ann. Neurol. **6** (1979) 371.
16) Huang S. C., et al., Am. J. Physiol. **238** (1980) E69.
17) Sokoloff L., et al., J. Neurochem. **28** (1977) 897.
18) Blin J., et al., Mov. Disord. **7** (1991) 348.
19) Ferris S. H., et al., Neurobiol. Aging **1** (1981) 127.
20) Frackowiak R .S. J., et al., 104 Brain 753.
21) Friedland R. P., et al., J. Comput. Assist. Tomogr. **7** (1983) 590.
22) Nagasawa H., et al., Neuroreport **5** (1994) 961.
23) Leenders K. L., et al., J. Neurol. Neurosurg. Psychiat., **49** (1986) 853.
24) Kuhl D. E., et al., Ann. Neurol. 15 (Suppl.) (1984) S119.
25) Kuhl D. E., Metter E. J. and Riege W. H., Ann. Neurol. **15** (1984) 419.
26) Martin W. R. W., et al., Can. J. Neurol. Sci. **11** (1984) 169.
27) Rougemont D., et al., J. Neurol. Neurosurg. Psychiat., **47** (1984) 824.

Table 1 Clinical summary of study patients with corticobasal degeneration.

Patients	1	2	3	4	5	6
Age at onset (years)	68	60	61	58	61	57
Sex	M	M	F	F	F	F
FDG study	+	+	+	+	+	+
FDOPA study	+	+	+	+	-	-
MRI	+	+	+	+	+	+
Main Clinical Symptoms						
Limb kinetic apraxia	+	++	+	+	++	+
Constructural apraxia	++	++	+	+	++	+
Hyperreflexia	++	+	+	-	-	++
Forced grasp reflex	+	-	-	-	+	+
Alien limb	+	-	-	-	+	+
Dementia	-	-	-	+	-	-
Aphasia	-	-	-	-	-	++
Akinesia	++	-	+	+	-	+
Postural disturbance	++	-	+	-	-	+
Frozen gait	+	-	+	+	-	-
Dystonia	+	-	-	-	-	-
Tremor	-	+	-	-	+	-
Rigidity	+	+	+	+	+	+

Main clinical symptoms are scored: -, absent; +, mild; ++, moderate.
MRI: magnetic resonance imaging. M: male; F: female.

Table 2 Cerebral metabolic rate for glucose in each brain structure of normal control and patients with corticobasal degeneration.

Structure	Controls	Patient (N = 6)	
	(N = 6)	Dominantly affected side	Contralateral side
Frontal cortex			
Superior frontal cortex	8.67±0.66	6.81±1.06	7.89±1.03
Medial frontal cortex	8.67±0.97	6.76±1.06	7.67±1.05
Medial mesial frontal cortex	8.53±1.10	7.40±1.19	7.99±1.16
Inferior frontal cortex	8.72±1.31	7.79±1.23	7.29±0.90
Lateral frontal cortex	8.16±1.30	6.68±1.81	7.78±0.63
Lateral posterior frontal cortex	8.23±0.92	6.19±1.57	7.23±0.61
Parietal cortex			
Primary motor and sensory cortex	9.17±0.77	6.58±0.71**	7.83±0.72
posterior parietal cortex	8.64±0.51	7.16±1.62	
Lateral parietal cortex	8.66±1.20	6.47±1.12*	7.49±0.98
Temporal cortex			
Superior temporal cortex	8.70±0.88	7.16±1.49	8.36±1.23
Medial temporal cortex	8.64±0.51	6.54±1.70	7.63±1.60
Inferior temporal cortex	7.70±0.80	6.70±1.53	7.54±0.71
Temporal pole	7.25±0.99	6.57±1.06	7.25±0.91
Occipital cortex	8.35±0.84	7.91±1.10	8.35±1.02
Primary visual area	9.45±0.88	8.61±0.71	8.91±1.02
Associative visual area	9.45±1.11	8.20±1.84	8.90±2.06
Centrum semiovale	7.34±0.68	5.85±1.04**	6.55±0.82
Thalamus	8.79±0.95	7.03±0.36**	8.22±0.94
Caudate nucleus	9.13±0.88	7.21±0.71*	8.05±0.57
Putamen	8.67±0.88	7.22±0.64*	8.57±0.85
Brainstem	7.06±0.46	6.46±0.54	6.30±0.34
Cerebellum	7.70±1.23	8.03±0.38	7.73±0.57

Values of cerebral metabolic rate for glucose represent in mean ± SD mg/100g/min. N: number of subjects.
$^{*}p<0.05$; $^{**}p<0.01$, compared with normal control value using the Mann-Whitney U-test.

Table 3 [^{18}F]Dopa uptake as measured by positron emission tomography in 4 patients with corticobasal degeneration.

	Caudate nucleus (Ki)		Putamen (Ki)	
	Affected side	Contralateral side	Affected side	Contralateral side
Controls(N=10)	0.0197±0.0054		0.0194±0.0038	
patient				
1	0.0055	0.0137	0.0061	0.0104
2	0.0105	0.0147	0.0102	0.0172
3	0.0056	0.0149	0.0067	0.0143
4	0.0049	0.0112	0.0056	0.0102

Values for controls are mean ± SD. Ki=[^{18}F]dopa influx constant (min^{-1}). N: number of subjects.

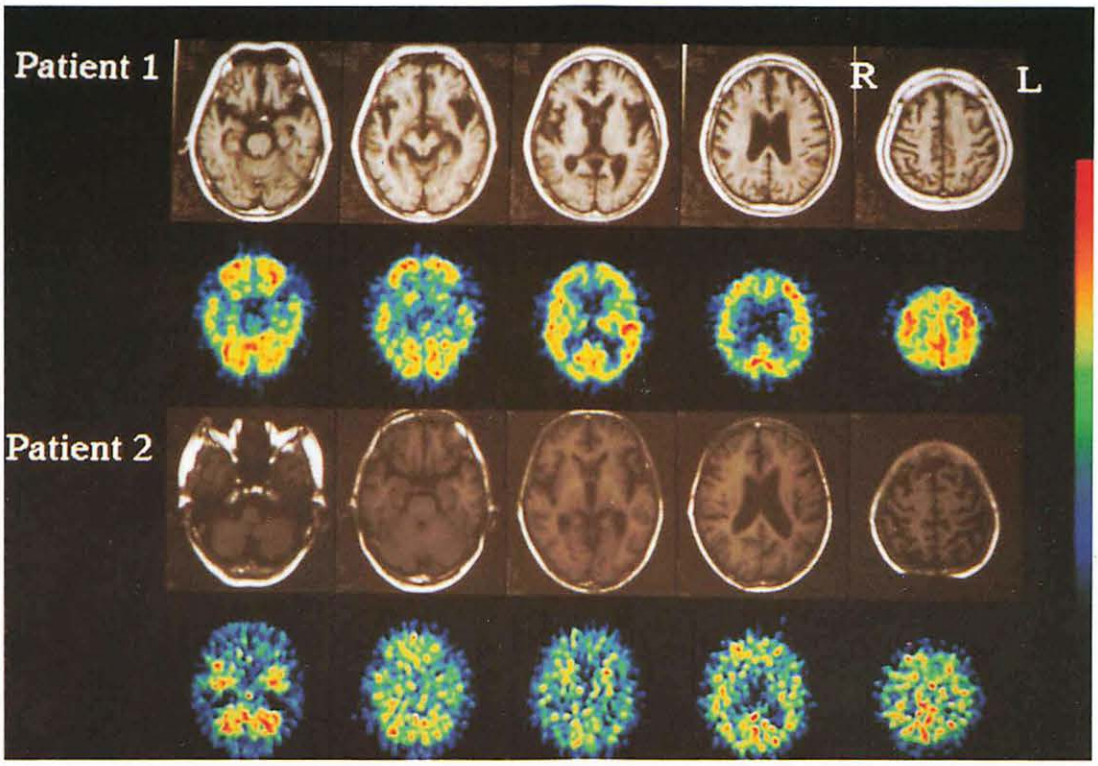

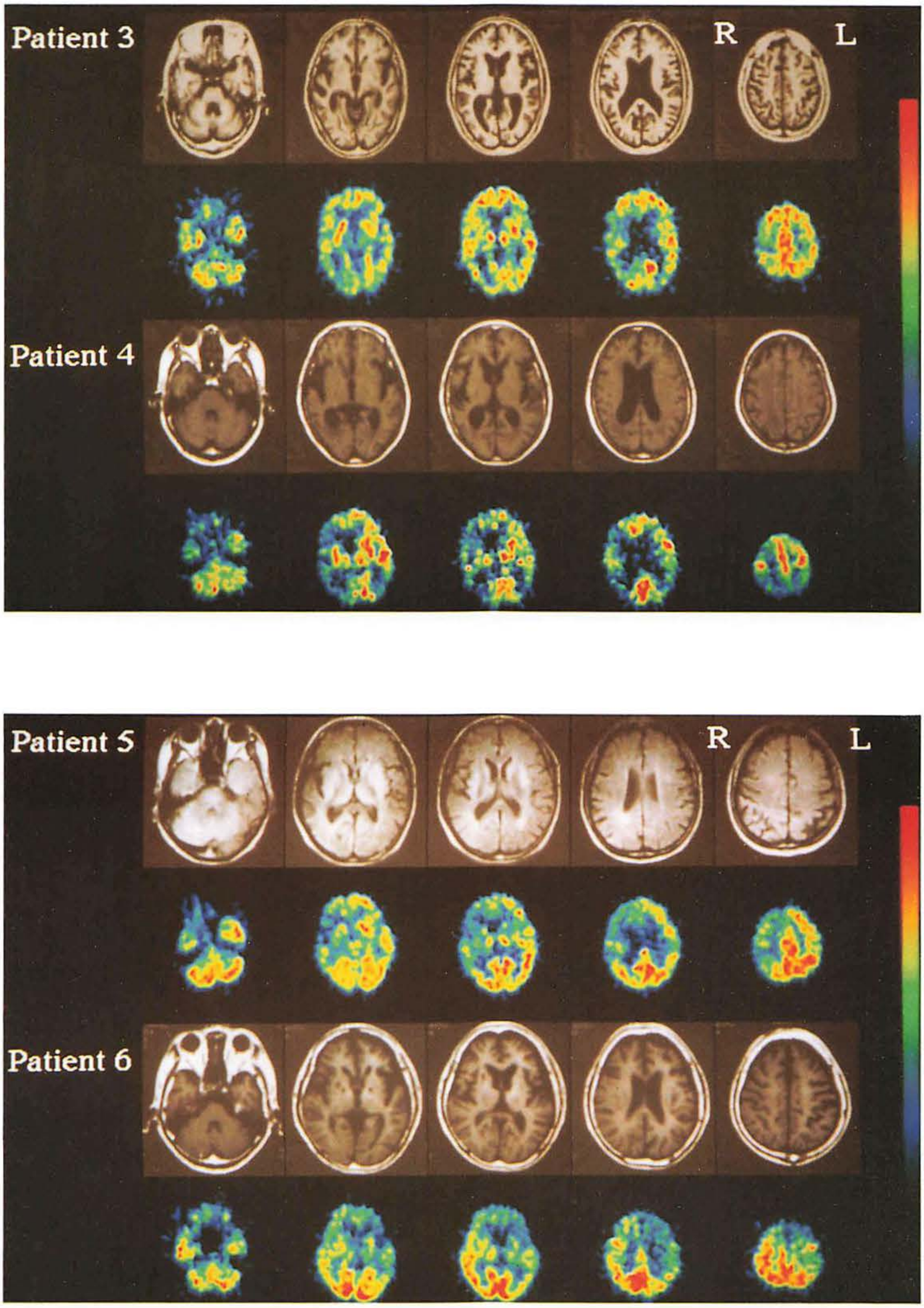

Fig. 1 Representative images obtained by ^{18}FDG positron emission tomography and magnetic resonance at the levels of corresponding brain slices from the six patients with corticobasal degeneration. The color scale is ranged from 0 to 10 mg/100g/min.

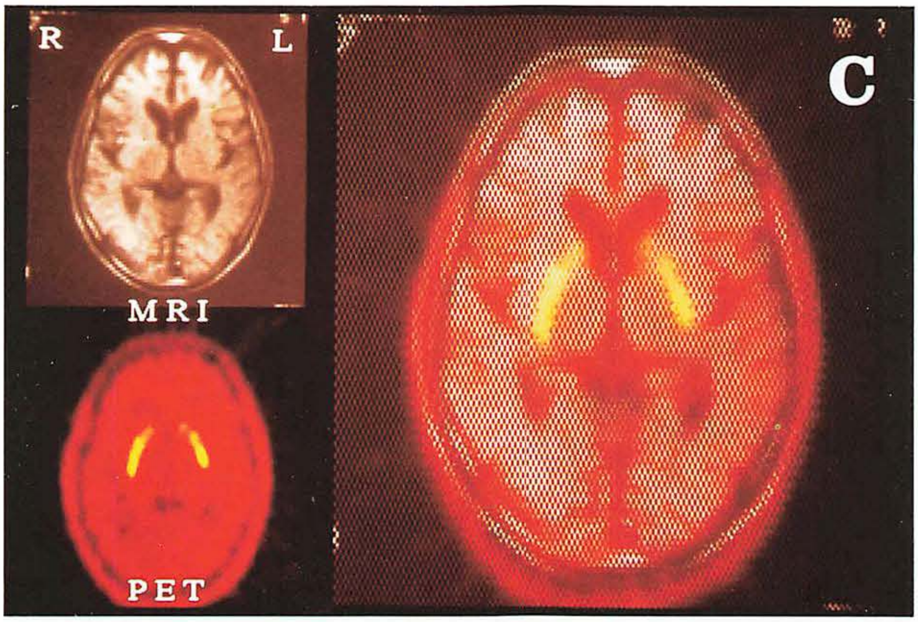
R
L
C
MRI
PET

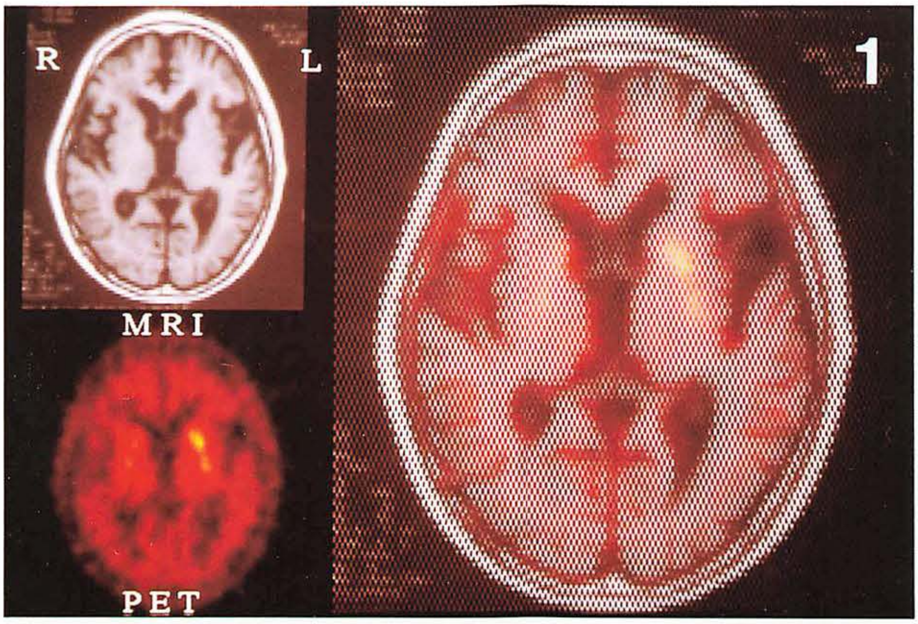
R
L
1
MRI
PET

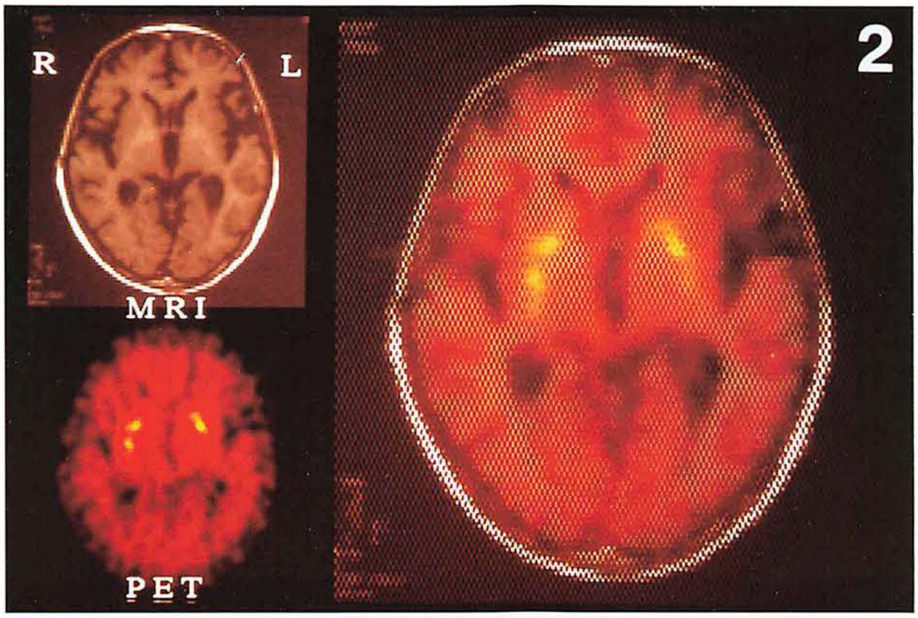
R
L
2
MRI
PET

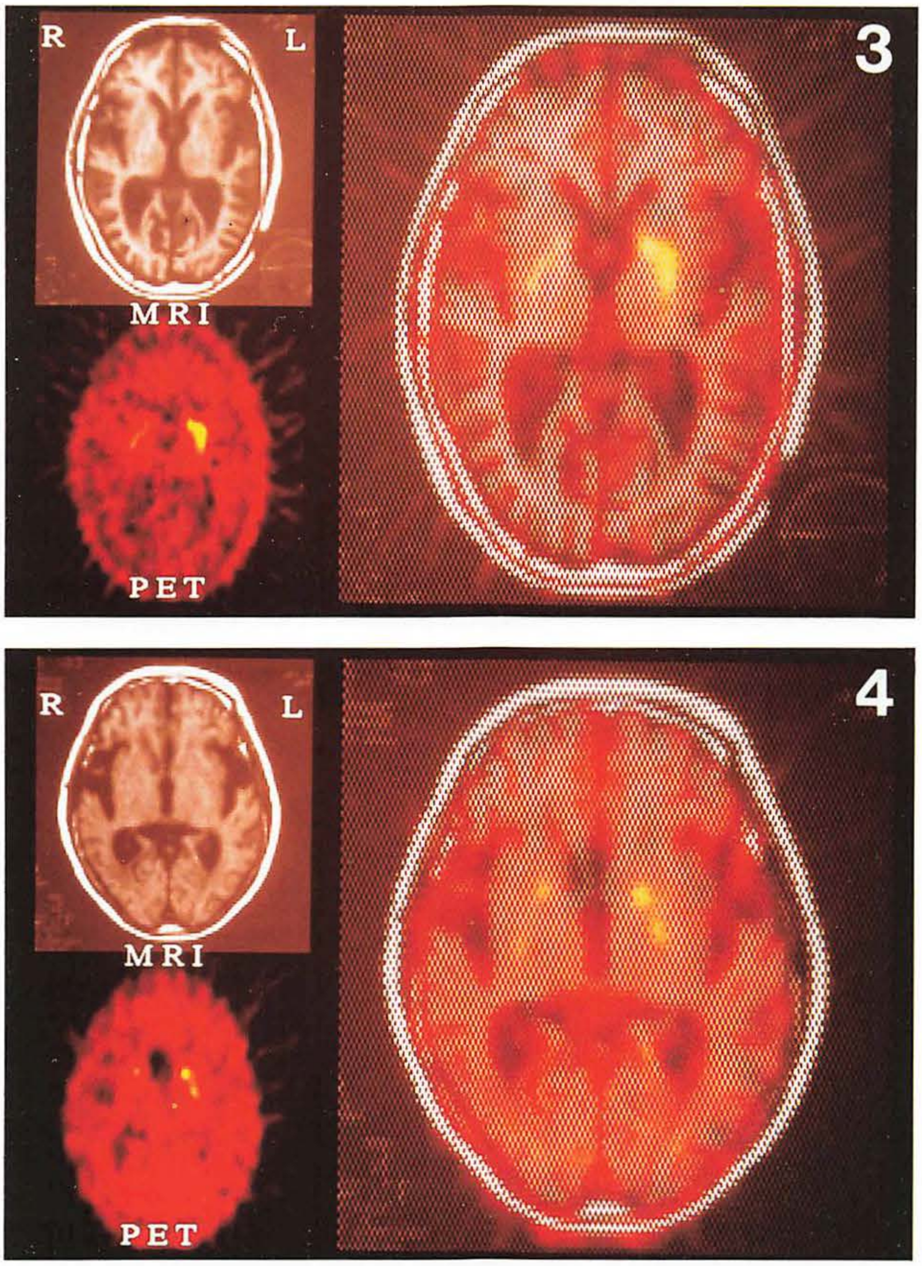

Fig. 2 Two different images obtained by [^{18}F]fluorodopa (FDOPA) positron emission tomography and magnetic resonance were overlapped at the levels of the caudate nucleus and the putamen from a normal control subject (C) and four patients (1-4) with corticobasal degeneration. FDOPA activity was symmetrically accumulated in the caudate nucleus and the putamen on both hemispheres of the normal control (C). In the patients, however, FDOPA accumulation was decreased in an asymmetric pattern with more severe impairment in the dominantly affected caudate nucleus and the putamen.

V. RADIATION PROTECTION AND TRAINING OF SAFE HANDLING

V. 1. Visualization of Radiation Distribution with High Sensitive CCD Camera

Miyake M., Hoshi K., Deloar H. M., Yamadera A., and Nakamura T.

Cyclotron and Radioisotope Center, Tohoku University

Introduction

For tumor localization at early stage, we have developed an endoscopic probe using a small BGO scintillator coupled with an optical fiber which can detect gamma rays from tumor-seeking radiopharmaceuticals[1,2]. We are also proceeding to develop a beta-ray endoscopic probe using a plastic scintillator coupled with an optical image fiber. An invisibly small tumor can be localized by counting of gamma-ray and beta-ray pulses through a MCS (multi-channel scalar) during the subject's body scanning.

For routine use in clinical diagnostics, it is strongly needed to identify tumors instantly as visual images. The CCD (charge coupled device) camera is widely used to get a visual image for visible lights, but has too low sensitivity to get a visual image for scintillation lights from the radiation detector. We therefore introduced a high sensitive cooled CCD camera equipping two MCPs (multi-channel plates) and tested its performance.

Methods

The CCD camera is a cooled CCD camera with I. I. (Image Intensifier) implementing two MCPs (multi-channel plates), the HAMAMATSU C4880-92, fabricated by the Hamamatsu Photonix Co. Ltd. The MCP which is coated for UV fluorescence has 15% of quantum efficiency for light of the wave length between 200nm and 400nm. The CCD is a 12.2mm square size, full frame transfer type. In order to reduce the dark current, the CCD is cooled down -50°C lower than the room temperature by a peltier device. The resolution of the A/D converter is from 12bit to 14bit, and the minimum exposure time is 5ns. A C-mount lens for the TV camera, CANON VF12.5 1.4 (f=12.5mm, F=1:1.4) was attached to this camera and close rings were used if necessary. The digital output data from the A/D converter of CCD are transferred to a personal computer for constructing various two dimensional images.

In this study, we first investigated the performance of this CCD, such as linearity, stability, uniformity and sensitivity, then measured the direct visual images of scintillation lights from NE102A plastic and liquid scintillation detectors irradiated by beta and gamma rays.

We also visualized the scintillation light images transported through an optical image fiber coupled with the NE102A scintillator.

Results and Discussions

Dark counts

First, we measured dark counts of the CCD covered with lens cap by varying the acquiring time, the CCD temperature and the MCP gain.

Dark counts come from the resetting noise and readout noise, and are approximately proportional to the acquiring time, and the square of the CCD absolute temperature and the MCP gain.

From this data, we determined the optimum values of these parameters.

Point source images whit plastic scintillator

Point source images were observed with the CCD camera by measuring the scintillation lights from the 3mm thick NE102A plastic scintillator which was placed closely to point sources. Figure 1. shows the images of 9 gamma-ray point sources, ^{22}Na, ^{57}Co, ^{60}Co, ^{152}Eu, ^{88}Y, ^{54}Mn, ^{133}Ba, ^{137}Cs, ^{241}Am from the top left to the bottom right. The left images are the visual images under the visible fluorescence light, the right images are the images of scintillation lights corresponding to the gamma-ray intensities under the dark root, and the middle images are the superposition of these two images.

The bright gamma-ray images from ^{152}Eu and ^{137}Cs sources and a faint gamma-ray image from ^{60}Co source can only be seen in Fig.1, because these sources have about 5 times stronger intensities of 2.5μCi than other sources of <0.5μCi.

Collimated gamma-ray images with plastic scintillator

We measured scintillation images of the 3mm thick NE102A with the CCD camera by using collimated gamma rays of 100mCi ^{137}Cs source. The collimator is made of 20cm long Pb blocks and have a slit of 0.5mm width, which makes a vertical fan gamma-ray beam. The scintillator was placed 3cm apart from the lens. A distance from the source to Pb blocks is 150mm, and from Pb blocks to NE102A is 100mm.(Fig.2-a).

The I. I. and MCP have some sensitivity for gamma rays. We got images by scintillation of NE102A(FWHM=1.22mm) and by direct irradiation to I. I. (FWHM = 1.62mm) as seen in Fig. 3. Because of the size of I. I. (12.2mm) which is smaller than that of NE102A (27.2mm, same size as CCD's view), the image of I. I. seems to be wider than scintillation image.

Imaging of V-shaped line gamma-ray source with liquid organic scintillator

We measured the scintillation images with a liquid organic scintillator by using a gamma ray line source. The line source was made of 11.1μCi ^{85}Sr in a capillary which has 0.5mm outer diameter. The line source has a shape of a letter "V". The liquid scintillator was sealed into a pair of 5mm thick glass plates with O-ring, which has 5mm thickness and 145mm diameter. The line source was set in contact with the glass.

The image shown in the lower photograph of Fig.4 represents a V-shaped line source, but spreads much wider than the original line source as seen in the upper photograph of Fig. 4. The FWHM of this image is 17.8mm as shown in the bottom graph of Fig. 4. This image spreading comes from a distance of source and detector, a reflection of scintillation on the surfaces of glass plates, and scattering of gamma rays and scintillation.

Scintillation image transported through optical image fiber

The scintillation light image was transported with an optical image fiber made by Olympus Optical Co. Ltd. The image fiber has 3.5mm effective diameter and 1m length, and is connected to 1mm thick NE102A scintillator with an optical silicon oil. The scintillator was irradiated with a collimated gamma-rays with 0.5mm width. As seen in Fig.2-b, a distance from a ^{137}Cs source to Pb blocks of 50mm length is 80mm, and that from Pb blocks to NE102A is 0mm. Another side of the image fiber was placed 3cm apart from the lens.

Figure 5 shows the collimated gamma-ray image due to the scintillation light transported through the image fiber. The 3.5mm diameter of image fiber is very small compared with the CCD's view of 27.2mm. The image transported with the image fiber has 1.33mm FWHM spatial resolution of the image which is only 10% wider than the 1.22mm FWHM of the image (Fig. 3) observed without the image fiber. This reveals that 1m long image fiber well transports the original image without spreading lights.

Conclusion

These observations clarified that the high sensitivity CCD camera can detect weak scintillation light of NE102A plastic scintillator as visual images and the image fiber can transport the scintillation light of NE102A as an image without spreading it.

We are now planning to apply this CCD camera system for a clinical radiation endoscope and a handy gamma-ray camera.

Refernces

1) Watabe H. et al., IEEE Trans. Nucl. Sci., **40** (1993) 88.
2) Deloar H. M, et al., submitted to J nucl. Med.

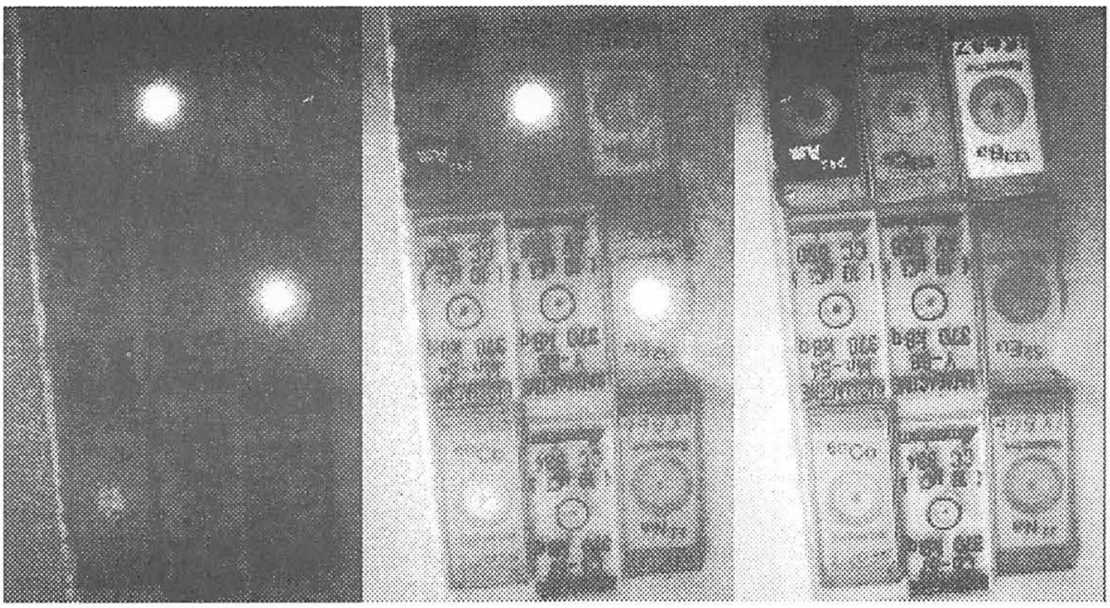

Fig. 1. An images with point sources. From top left they are ^{22}Na, ^{57}Co, ^{60}Co, from middle left are ^{152}Eu, ^{88}Y, ^{54}Mn from bottom left are ^{133}Ba, ^{137}Cs, ^{241}Am. The left images are the visual images under the visible fluorescence light, the right images are the images of scintillation lights corresponding to the gamma-ray intensities under the dark room, and the middle images are the superposition of these two images. The another measuring condition were not recorded.

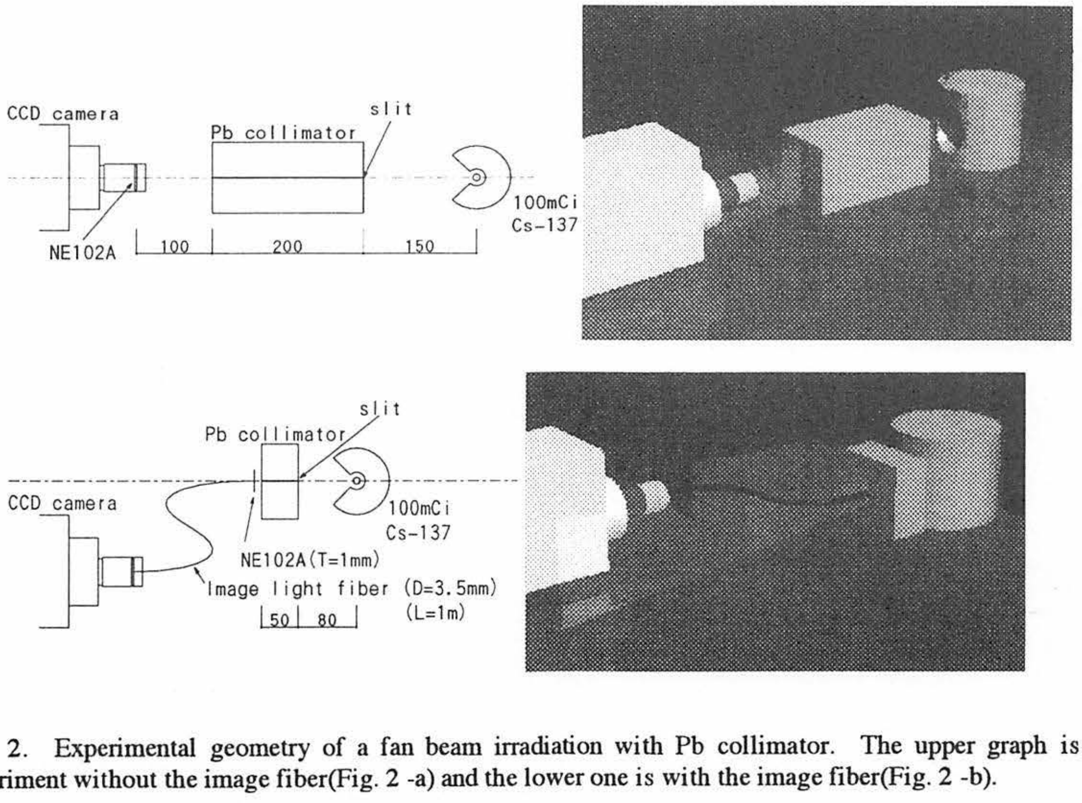

Fig. 2. Experimental geometry of a fan beam irradiation with Pb collimator. The upper graph is the experiment without the image fiber(Fig. 2 -a) and the lower one is with the image fiber(Fig. 2 -b).

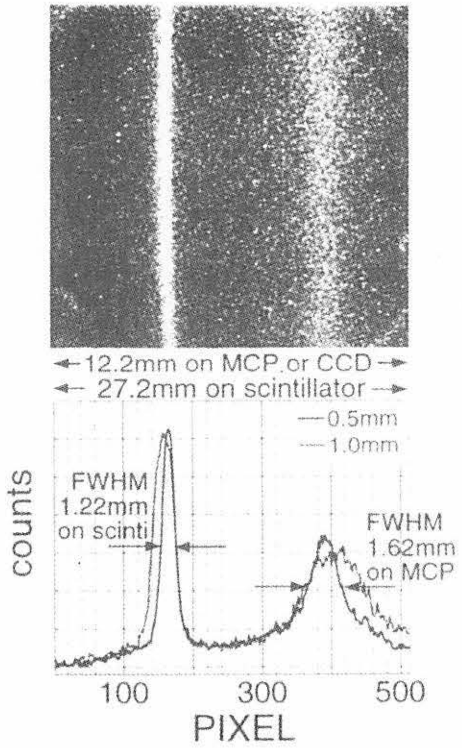

Fig. 3. An image with a fan beam gamma ray. A MCPgain is 13. An irradiation time is the 10min.

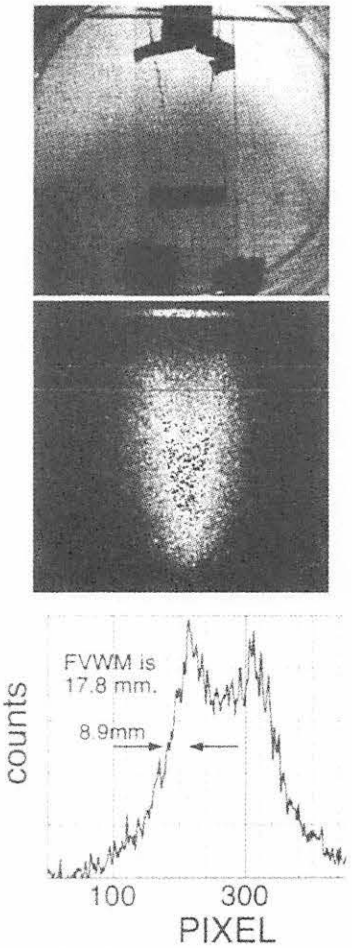

Fig. 4. An image with a liquid organic scintillator by using a V-shaped gamma-ray line source. The upper image is thevisual image under the visible fluoresense light, the middle image is the image of scintillation lights under the dark room, the bottom graph is a profile of scintillation intensity between two horisonal lines of the middle image. A MCPgain is 13.
This images of 100sec irradiations are added 10 times.

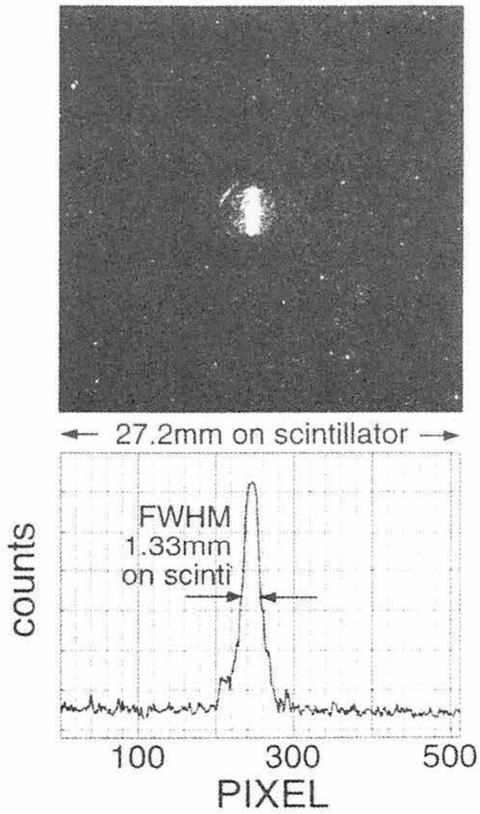

Fig. 5. An image through a image fiber with a fan beam gamma ray. A MCPgain is 13. An irradiation time is 10min.

V. 2. Internal Dose Estimation for Continuous Inhalation of $C^{15}O_2$, $^{15}O_2$ and $C^{15}O$, using TLD method

Deloar H. M., Watabe H., Nakamura T., Narita Y., Yamadera A., Fujiwara T., and Itoh M.*

Cyclotron and Radioisotope Center, Tohoku University
*Department of Investigative Radiology, National Cardiovascular Center**

Introduction

Internal radiation absorbed doses in target organs due to continuous inhalation of $C^{15}O_2$, $^{15}O_2$ and $C^{15}O$ into the body were estimated [1,2] where the lung for all the three gases[1] and spleen for $C^{15}O$[2] were considered to be the critical organ at highest risk. The nasal cavity and major airway were, however, not considered in the dose calculation procedure but these two organs might get substantial amount of dose during inhalation of those gases due to short half life of ^{15}O. Powell et al[3]. and Meyer et al[4]. measured the dose in the airways, which includes pharynx, larynx and trachea for continuous inhalation of $C^{15}O_2$ by direct PET measurements and a highest dose at the airways were observed. In their procedure MIRD method was not applied. Due to highest dose accumulation those organs must be considered as the target organs as well as the source organs. In this study we then calculated the absorbed doses of all target organs, including the nasal cavity and major airway with the MIRD method[5].

To calculate the dose with the MIRD method, S values (absorbed dose per unit cumulated activity) for all source organs to target organs are required. It is also necessary to know the cumulated activities of all source organs. We first calculated the S values of all source organs to target organs, including nasal cavity and major airway[6] and then applied the TLD method[7] to estimate the bio-distribution of radioactivities in the source organs from continuous inhalation of gases.

Finally, the absorbed doses in 23 target organs were estimated according to the MIRD method for continuous inhalation of three gases of $C^{15}O_2$, $^{15}O_2$ and $C^{15}O$.

Materials and Methods

During clinical PET studies at the Cyclotron and Radioisotope Center (CYRIC), Tohoku University, body surface doses were estimated by TLD during successive continuous inhalation of O-15 labeled gases ($C^{15}O_2$, $^{15}O_2$ and $C^{15}O_2$), on 5 adult subjects. The ages of the subjects were 20 to 30 yrs. The flow rates of $C^{15}O_2$ and $^{15}O_2$ were 370

MBq/min to 740 MBq/min and that of $C^{15}O$ was 259 MBq/min to 481 MBq/min. The subjects inhaled the gases sequentially (first $C^{15}O_2$, 2nd $^{15}O_2$ and 3rd $C^{15}O_2$) under their own control. The inhalation periods for $C^{15}O_2$ and $^{15}O_2$ were 10 to 15 minutes and for $C^{15}O$ was 2 to 5 minutes.

Basic Theory

In the MIRD method[5], the internal absorbed dose from source to target organs are given as follows:

$$D_i = \sum_j S_{i,j}\,\tilde{A}_j \ , \tag{1}$$

where D_i is the absorbed dose in the i-th target organ, $S_{i,j}$ the absorbed dose in the i-th target organ per unit cumulated activity of the j-th source organ and $\tilde{A}_j$ the cumulated activity of the j-th source organ.

In our TLD method a number of TLDs are placed on the body surface near the source organs and the body surface doses are measured by TLDs[7]. The body surface dose at the i-th TLD position can be expressed as:

$$T_i = \sum_j R_{i,j}\,X_j \ , \tag{2}$$

where $R_{i,j}$ is the absorbed dose at the i-th TLD position per unit cumulated activity of the j-th source organ[6] and X_j is the cumulated activity of the j-th source organ integrated during the TLD attachment, which can be calculated from an inverse transformation method by utilizing a slightly modified SAND-II unfolding code[8], based on the successive iteration method. In the inverse transformation method the total uptake of the radioactive gases is used as a constraint condition which can be expressed by:

$$\tilde{A} = f\left(\int_0^t \frac{A_o}{\lambda}(1 - e^{-\lambda\tau})\,d\tau + \int_t^\infty \frac{A_o}{\lambda}(1 - e^{-\lambda t})\,e^{-\lambda(\tau-t)}\,d\tau\right) = f\,\frac{A_o}{\lambda}\,t \ , \tag{3}$$

where A_o is the flow rate of the gas in MBq min^{-1}, λ is the decay constant of ^{15}O, t is the inhalation period in min. and f is the uptake percentage of the individual gas[7]. The first term of Eq. (3) is the cumulated activity during the inhalation period and the second term is the cumulated activity after inhalation stops, considering only physical decay of the activity.

Results and Discussion

Using the body surface dose measured by TLDs and the unfolding technique from Eq. (2), the mean cumulated activities of 11 source organs due to uptake of O_2, CO_2 and CO were estimated and a comparision was done with the present study and other results[1,2]. Our result show in general good agreement with other results.

In the comparative study by Bigler et al.[1] for O_2 and CO_2 shown in Fig. 1, the cumulated activities of brain, liver and heart for O_2 inhalation and for lung and heart for CO_2 inhalation in this study are however around 2 to 3 times higher than those by Bigler et al[1].

For CO gas, our data are compared with the results of Bigler et al.[1] and Kearfott et al.[2] in Fig. 1. Our data for the cumulated activity of kidney is in between the values of reported by Bigler et al.[1] and Kearfott et al[2]. A big difference is found for brain between the results of Bigler et al.[1] and Kearfott et al.[2]), which are 5.48 and 0.29 kBq-hr MBq^{-1}, respectively, our result of 2.9 kBq-hr MBq^{-1}, gives an average value of them. Results for liver is 3 times higher than the result of Bigler et al. but pretty close to the reported value of Kearfott et al.

The absorbed dose estimates in the 23 target organs due to uptake of O-15 labeled gases, O_2, CO_2 and CO were calculated with the MIRD method[5] by using Eq. (1), and are shown in Fig. 2. Our results are compared with the values reported by ICRP Publ. 53[9].

Among the target organs, the nasal cavity and major airway give highest absorbed doses and these doses are higher for CO_2, CO and O_2 in this descending order. For all gases, the critical organs are the nasal cavity and major airway which includes the pharynx, larynx and trachea. The radiation dose in the upper airways from the 1 hour inhalation of O-15 labeled CO_2 with 1 mCi/l of air has been calculated for adult subjects by several authors[3,4]. In our study the doses in the nasal cavity and major airway due to inhalation of CO_2 are 1.47E-02 mGy MBq^{-1} and 1.10E-02 mGy MBq^{-1}, and the total value is 2.57E-02 mGy Mbq^{-1}. This value is very close to 2.85E-02 mGy MBq^{-1} reported by Meyer et al.[3] but higher than the results of 2.47E-03 mGy Mbq^{-1} given by Powel et al[4].

For all gases, next highest absorbed dose is the lung. The ICRP doses of lung for O_2 and CO are close to our estimated dose but for CO_2, our results become about 4 times higher than the ICRP dose. The doses of the brain is higher for CO, CO_2 and O_2, in this descending order, reflecting the higher accumulation of brain.

The doses of the other target (non source) organs are relatively lower than those of the 10 source organs and agree with the ICRP reported values around a factor of 2. Generally speaking, our results show rather good a greement with the ICRP results.

Conclusion

For continuous inhalation of O-15 labeled gases, we calculated the cumulated activities of 11 source organs based on the TLD method[7] and then estimated the internal absorbed doses in 23 target organs by the MIRD method. Our results show generally a good agreement with the values reported by ICRP[9], which are based on the biological analysis[1,2].

Among the target organs the airway is the critical organ and the absorbed dose is 2.57E-02 mGy Mbq^{-1} which is very close to 2.85E-02 mGy MBq^{-1} reported by Meyer et al[4].

References

1) Bigler R. E., and Sgouros G., J. Nucl. Med. **24** (1983) 431.
2) Kearfott K. J., J. Nucl. Med **23** (1982) 1031.
3) Powell G. F., Schuchard R. A., Reff C. S., et al., Ann. Neurl. 1984;(Suppl Vol. 15):S107-S109.
4) Meyer E., et al., J. Nucl. Med. **28** (1987) 234.
5) Loevinger R., Buidinger T. F., and Watson E. E., The Society of Nuclear Medicine, Inc., New York. 1988.
6) Deloar H. M., et al., (Submitted to the J. Nucl. Med.)
7) Matsumoto M., J. Med. & Biol. Eng. Comput. **31** (1993) 151.
8) McElroy W. N., Berg S. et al., 1967; AFWL-TR-67-41, Air Force Weapons Laboratory.
9) Annals of the ICRP, ICRP publication 53., Vol. 18 No. 1-4; 1987.

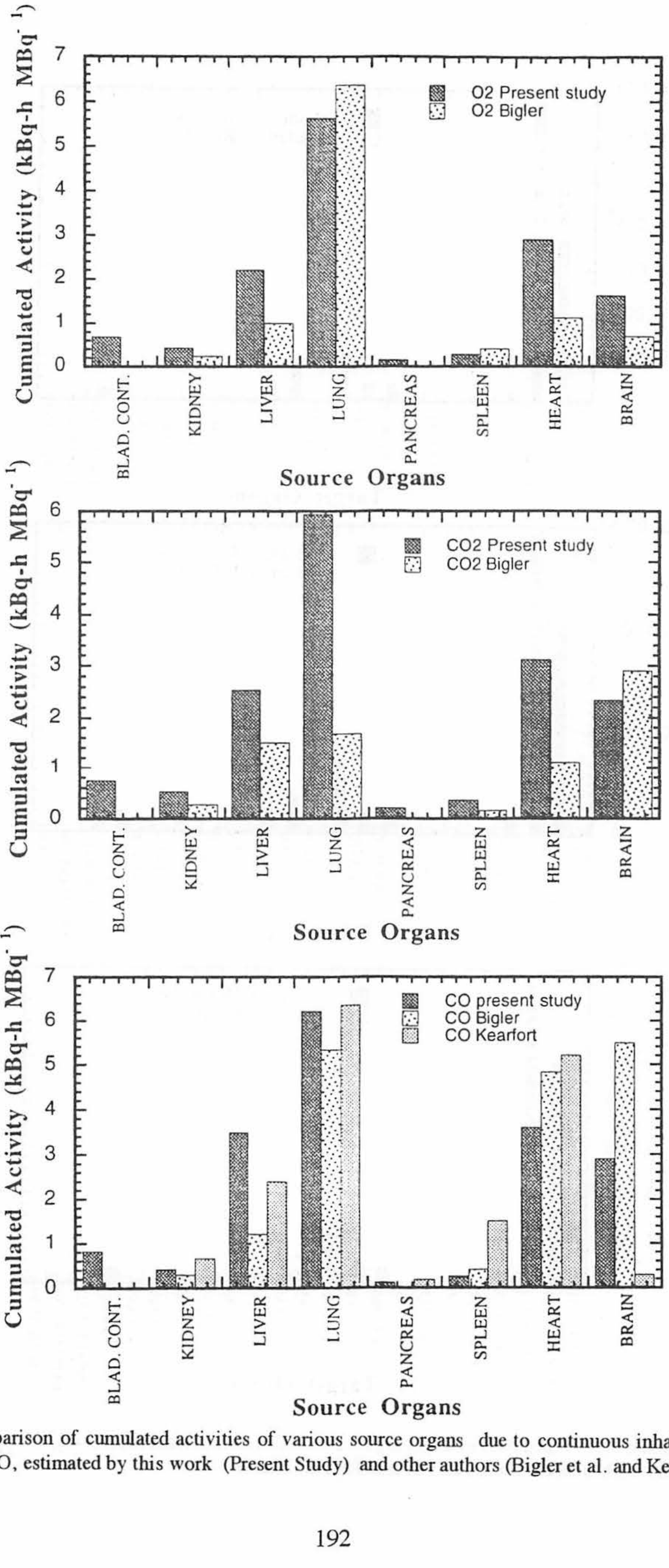

Fig. 1. Comparison of cumulated activities of various source organs due to continuous inhalation of O_2, $C^{15}O_2$ and $C^{15}O$, estimated by this work (Present Study) and other authors (Bigler et al. and Kearfort et al.)

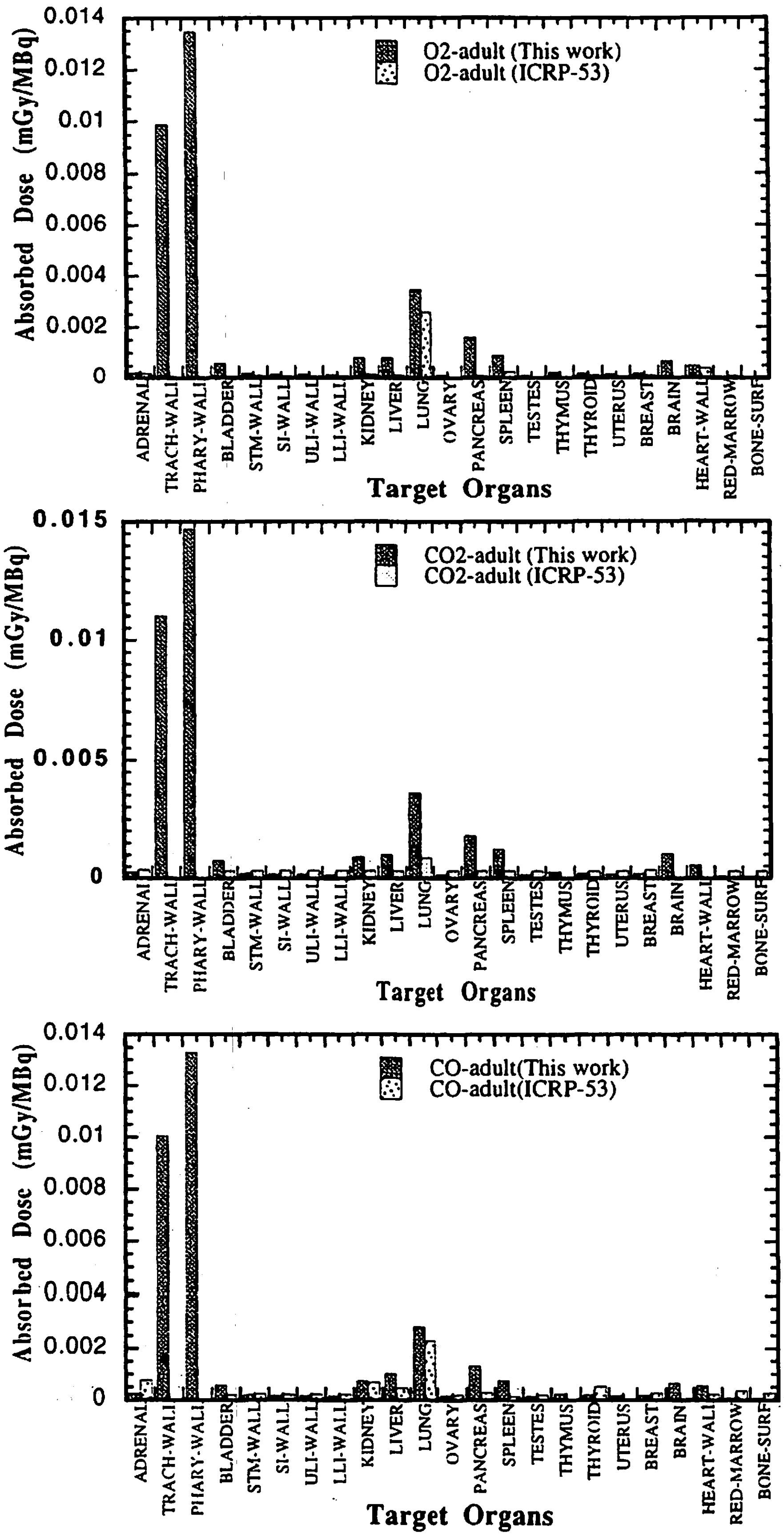

Fig. 2. Comparison of absorbed dose in target organs due to continuous inhalation of O_2, $C^{15}O_2$ and $C^{15}O$, estimated by this work (Present Study) and with ICRP Publ. No. 53.

V. 3. Radiation Protection and Management

Miyata T., Yamadera A., Nakamura T., Satake Y., and Watanabe N.**

Cyclotron and Radioisotope Center, Tohoku University
*Japan Radiation Protection Co., Ltd.**

(1) Unsealed radionuclides used in the center

The kinds and activities of unsealed radionuclides handled in the center in 1995 are shown in Table 1. The table includes the isotopes produced by the cyclotron, purchased from the Japan Isotope Association and took over from another RI institutes.

(2) Individual monitoring

The exposure doses of the workers in the center in 1995 is given in Table 2. They were less than the permissible doses.

(3) Monitoring of the workplace

Radiation dose rates inside and outside of the controlled areas were monitored periodically and as needed. They were below the legal permissible levels. Surface contamination levels of the floors inside the controlled areas were measured by smear method and with survey meters periodically and as needed. They also cleared under the legal regulation levels.

(4) Wastes management

The radioactive wastes delivered to the Japan Radioisotope Association in 1995 are shown in Table 3. The concentration of radioisotopes in the air released after filtration from the stack was monitored with stack gas monitors. The levels were less than the legal regulation levels. The radioactive water was storaged at the tanks at least for 3 days and then released to the sewerage after confirming that the concentration was less than permissible levels.

The treated volume of radioactive waste of organic scintillator was 1358 ℓ by the incinerator made by Fujikogyo Co., Ltd.

Table 1. Unsealed radionuclides used in the center in 1995.

(a)Cyclotron Building (kBq)	
2. ^{95m}Tc	1,000.000
total	1,000.000
3. ^{11}C	498,575,000.000
^{62}Cu	222,000.000
^{111}In	4,462,080.000
^{28}Mg	3,182.000
^{48}V	247,484.000
total	503,509,746.000
4. ^{18}F	442,751,080.000
total	442,751,080.000

(b) R I Building (kBq)	
2. ^{45}Ca	59,657.528
^{68}Ge	239,393.000
^{125}I	101,315.200
total	400,365.728
3. ^{11}C	2,521,000.000
^{131}I	43,253.300
^{62}Cu	777,000.000
^{67}Ga	10,400.000
^{111}In	181,810.000
^{28}Mg	1,942.500
^{32}P	1,018,250.684
^{35}S	462,814.000
^{48}V	19,198.000
total	5,035,668.484
4. ^{14}C	12,273.000
^{18}F	368,200,158.000
^{3}H	826,580.069
total	369,039,011.069

(c)Research Building (kBq)	
3. ^{11}C	6,277,050.000
total	6,277,050.000
4. ^{18}F	10,064,000.000
total	10,064,000.000

Table 2. Occupational radiation exposures at the center in 1995.

Dose range (mSv)	Number of individuals
No measurable exposure	32
Measurable exposure less than 1.0	7
1.0 to 2.5	4
2.5 to 5.0	2
Total persons monitored	45

Table 3. Radioactive wastes delivered to the Japan Radioisotope Association in 1995.

Wastes	Container	Number
solids		
Combustible Type Öü	50 ℓ drum	35
Combustible Type Ö†	50 ℓ drum	16
Incombustibles	50 ℓ drum	6
Annimal carcasses	50 ℓ drum	5
Filters	50 l /unity	58
liquids		
inorganic liquids	25 ℓ PE bottle	5

V. 4. Measurement of Heavy Ion Tracks Using Imaging Plate

*Yamadera A., Taniguti S., Nakamura T., and Fukumura A.**

Cyclotron and Radioisotope Center, Tohoku University
*National Institute of Radiological Sciences, Anakawa, Inage-ku, Chiba-shi, Japan**

Introduction

We have developed a new-type track-counting-method of high energy heavy ions penetrating through a matter by using imaging plate (IP) in order to estimate the deposited energy distributions of projectile and fragment particles.

Nuclear emulsion film and polycarbonate film such as CR-39 are widely used for counting of high energy particles. But, for obtaining accurate track information, it is necessary to develop or etch these detectors under highly controlled chemical conditions and with skilled technique. Their sensitivities are not so high the counting area is limited within the view range of microscope.

On the other hand, IP has many advantages; Tracks are analyzed automatically by using the Image Reader and we have no use for chemical treatment and skilled techniques. The counting efficiency of IP is over 100 times higher than the above two detectors, because we can set up the counting area freely with in the size of IP. The image data are stored in CPU and we can easily analyze these stored data.

Experiment and results

Imaging Plate and Image Reader

We used IP(BAS-'III) and BAS-2000 as a reader for measuring 290MeV/u Carbon particles and 400MeV/u Neon particles, and IP(BAS-UR) and BAS-3000 for α and β particles. These instrument are fabricated by Fuji Film Co. Ltd. The IP size of BAS-'III Land BAS-UR are 20cm × 40cm and 12.5cm × 12.5cm, respectively. The pixel sizes of BAS-2000 and BAS-3000 are 100 μm and 50μm, respectively.

Irradiation experiments

Fig. 1 shows the irradiation setup at the National Institute of Radiological Sciences. In order to irradiate the IPs with projectile particles having different energies at the same time, two sheets of 1cm thick acrylic moderators(moderator-2) were sandwiched between three IP detectors. This stack was set behind the another moderator(Moderator-1). The IPs were irradiated with uniformly dispersed 290MeV/u C or 400MeV/u Ne beam which was collimated to 4cm x 4cm. Number of particles was counted with a ΔE counter which was set in front of the Moderator-1, and the irradiation was stopped manually when the counts of the Δ E counter reached about 1000.

For observing track profiles along the direction of particle flights, we irradiated an IP which was set parallel to the beam line.

Photostimulated luminescence

Latent figure in imaging plate was read out by the BAS-2000 system. Fig. 2 shows a cross sectional track view of 290MeV/u Carbon particles. The large tracks are produced by high energy Carbon particles and small ones are due to gamma rays or electrons. From the track sizes, we could easily distinguish heavy ion tracks from the other light particles. The diameters of large tracks are 200~300μm (2~3pixels) and small ones are 100μm.

The cross sectional photostimulated luminescence(PSL) of every track was calculated. Fig. 3 shows the relation of the average PSL/track and the moderator thickness. The distribution of PSL/track corresponds to a Blagg curve. The PSL value at the Blagg peak and the corresponding absorber thickness are 2.8PSL/track and 143.9mm, respectively, for Carbon particles, and 3.4PSL/track and 129.9mm for Neon particles. These absorber thicknesses just correspond to the ranges of these two projectiles. Beyond the range, we can see the PSL/track distribution which may be due to the fragment particles.

Conclusion

We developed a new type track-counting-method by using imaging plate. The IP is very easy to treat with and does not need special technique such as chemical treatment. It gives not only an information of track density but also an information of projectile species and energies.

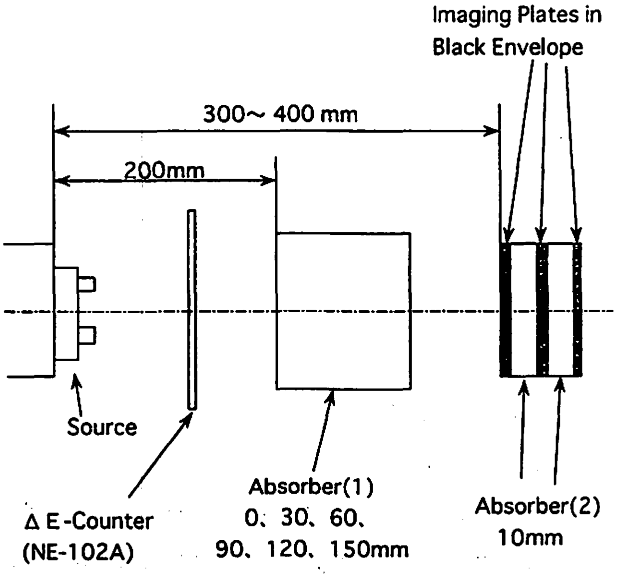

Fig. 1. Irradiation setup at the National Institute of Radiological Science.

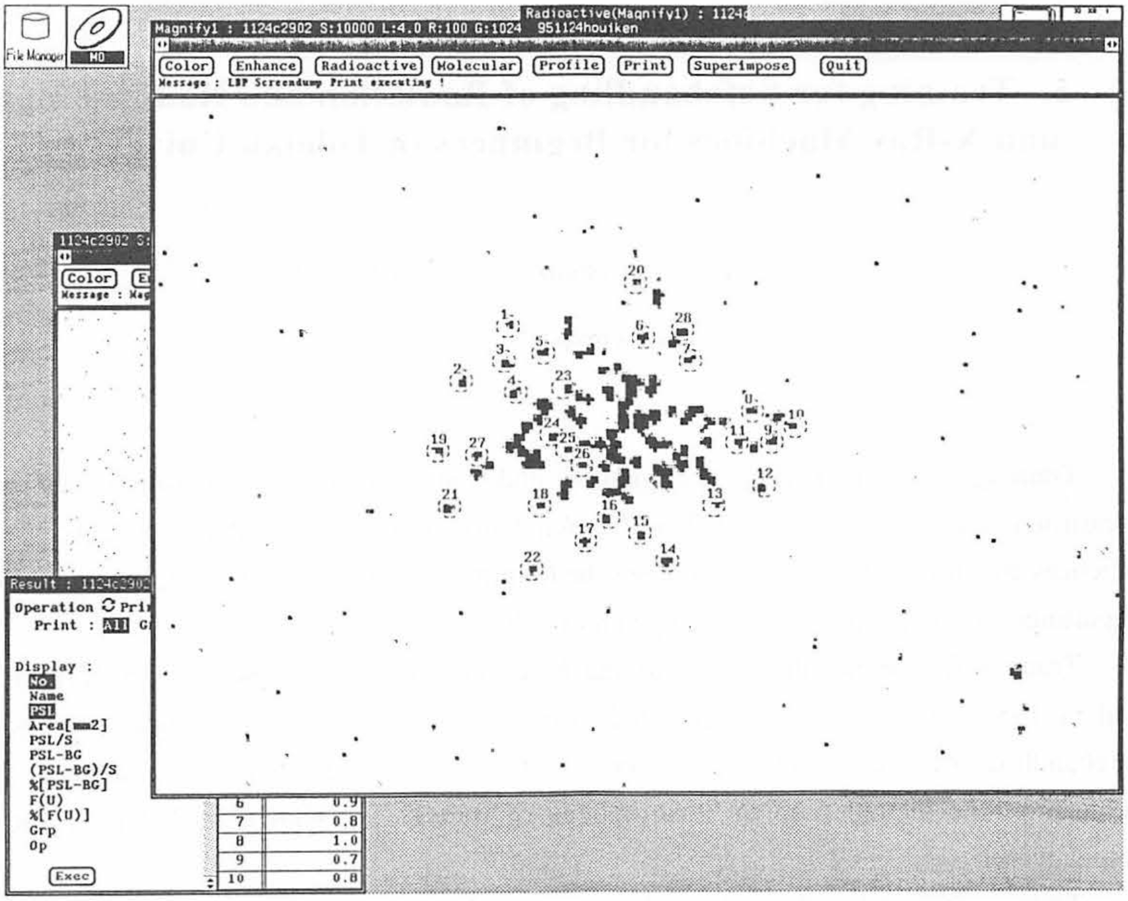

Magnify1 : 1124c2902 S:10000 L:4.0 R:100 G:1024 951124houiken

Message : LBP Screendump Print executing !

Print : All

6	0.9
7	0.8
8	1.0
9	0.7
10	0.8

Fig. 2. Cross sectional track view of 290MeV/u Carbon particles.

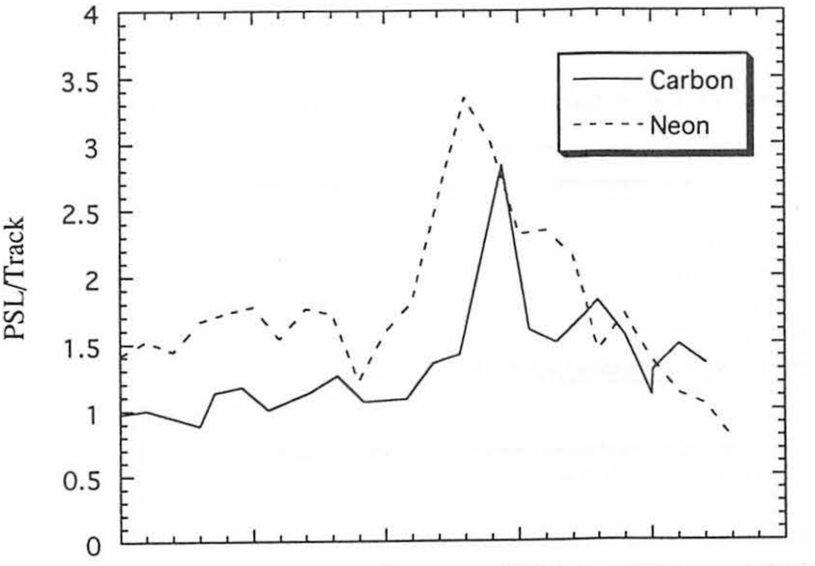

Fig. 3. Relation of the average PSL/track and the moderator thickness.

V. 5. Training for Safehandling of Radiation and Radioisotopes and X-Ray Machines for Beginners in Tohoku University

Nakamura T., Yamadera A. and Miyata T.

Cyclotron and Radioisotope Center, Tohoku University

Training for safehandling of radiation and radioisotopes for beginners has been conducted twice a year from 1977 in Tohoku University. The contents of lectures and practices are shown in Table 1. In 1995 the training was performed for 522 persons. The departments to which they belong are given in Table 2.

Training for safehandling of X-ray machines and electron microscopes began from the end of 1983. The training is scheduled to be held twice a year at the same time as the safehandling of radiation and radioisotopes. Only lectures are given and not practices. The contents of the lectures and the distributions of trainees are shown in Tables 3 and 4, respectively.

Training for safehandling of synchrotron radiation began from the end of 1995. The contents of the lectures are the same as safehandling of radiation and radioisotopes for beginners and not practices. In 1995 the training was performed for 38 persons.

Table 1. Contents of lectures and practices for safehandling of radiation and radioisotopes in 1995.

Lectures (one day)	
Radiation physics and measurements	1.5 (hours)
Chemistry of radioisotopes	1.0
Radiological protection ordinance	1.0
Effects of radiation on man	1.0
Safehandling of radioisotopes	1.5
VTR for safehandling of radiation and radioisotopes	2.0

Practices (one day)	
Treatment of unsealed radioactive solution (hours)	4.0
Measurements of surface contamination and decontamination	1.0
Measurements of gamma rays and beta rays	2.0

Table 2. Distribution of trainees for safehandling of radiation and radioisotopes in 1995.

Department	Staff	Student	Total
Faculties			
Medicine	22	88	110
Dentistry	0	5	5
Pharmacy	1	53	54
Science	7	110	117
Engineering	1	50	51
Agriculture	2	102	104
Research Institutes	11	68	79
The others	1	1	2
Total	45	477	522

Table 3. Contents of lectures for safehandling of X-ray machines and electron microscopes in 1995.

Safehandling of X-ray machines	1.5 (hours)
Radiological protection ordinance	1.0
VTR for safehandling of radiation and radioisotopes	1.0

Table 4. Distribution of trainees for safehandling of X-ray machines and electron microscopes in 1995.

Department	Staff	Student	Total
Faculties			
Medicine	0	0	0
Science	0	27	27
Engineering	10	90	100
Agriculture	0	1	1
Research Institutes	14	112	126
Total	24	230	254

Table 5. Distribution of trainees for synchrotron radiation in 1995.

Department	Staff	Student	Total
Faculties			
Science	1	7	8
Pharmacy	1	0	1
Engineering	1	10	11
Agriculture	1	1	2
Research Institutes	0	16	16
Total	4	34	38

VI. PUBLICATIONS

VI. PUBLICATIONS
(January 1995 ~ December 1995)

A

1. The $^{17,\,18}$O(p, n)$^{17,\,18}$F reaction at $E_p = 35$MeV
   Oura M. , Orihara H., Hosaka M., Jon G. C., Terakawa A., Ishii K., Narita A., Hosomi K., Nakagawa T., Miura K., Ohnuma H., Niizeki T., and Dehnhard D.
   Nuclear Physics **A586**(1995)20-34.

2. A permanent-magnet dipole with variable field strength and polarity
   Honma T., Fujioka M., Shinozuka T., and Matsumoto N.
   Nuclear Insturuments and Methods in Phsics Research **A361**(1995)13-20.

3. Column Extraction Method for Rapid Preparation of [^{11}C]Acetic and[^{11}C]Palmitic Acids
   Iwata R., Ido T. and Tada M.
   Appl. Radiat. Isot. **46-2**(1995)117-121.

4. On-column Preparation of 1-Aminocyclopentane-1-[^{11}C] Carboxylic Acid
   Iwata R., Ido T. and Tada M.
   Appl. Radiat. Isot. **46-9**(1995)899-905.

5. Validation of noninvasive quantification of rCBF compared with dynamic/integral method by using positron emission tomography and oxygen-15 labeled water
   Watabe H., Itoh M., Mejia M. R., Fujiwara T., Jones T., and Nakamura T.
   Annals of Nuclear Medicine **9-4**(1995)191-198.

6. Measurements of response function of organic liquid scintillator for neutron energy range up to 135 MeV
   Nakao N., Nakamura T., Baba M., Uwamino Y., Nakanishi N., Nakashima H., and Tanaka S-I.
   Nuclear Instruments and Methods in Physics Research **A362**(1995)454-465.

7. Development of Skin Surface Radiation Detector Systetm to Monitor Radioactivity in Arterial Blood Along with Positron Emission Tomography
   Watabe H., Miyake M., Narita Y., Nakamura T., and Itoh M.
   IEEE Transactions on Nuclear Science **42-4**(1995)1455-1459.

8. Linearized Method: A New Approach for Kinetic Analysis of Central Dopamine D2 Receptor Specific Binding
   Watabe H., Hatazawa J., Ishiwata K., Ido T., Iwata R., Takahashi T., Hatano K., and Nakamura T.
   IEEE Transaction on Medical Imaging **14-4**(1995)688-696.

B

9. Alteration of $[^3H]$hemicholinium-3 binding in the post-ischaemic gerbil brain
Araki T., Kato H., Fujiwara T., Kogure K., and Itoyama Y.
NeuroReport **6**(1995)561-564.

10. Methionine Uptake by Tumor Tissue: A Microautoradiographic Comparison with FDG
Kubota R., Kubota K., Yamada S., Tada M., Takahashi T., Iwata R., and Tamahashi N.
The Jounal of Nuclear Medicine **36-3**(1995)484-492.

11. Effects of Radiotherapy on the Cellular Uptake of Carbon-14 Labeled L-Methionine in Tumor Tissue
Kubota K., Kubota R., Yamada S., and Tada M.
Nucl. Med. Biol. **22-2**(1995)193-198.

12. Quantitative Double-Tracer Autoradiography with Tritium and Carbon-14 Using Imaging Plates: Application to Myocardial Metabolic Studies in Rats
Yamane Y., Ishide N.,Kagaya Y., Takeyama D., Shiba N., Chida M., Sekiguchi Y., Nozaki T., Ido T., and Shirato K.
The Journal of Nuclear Medicine **36-3**(1995)518-524.

13. Clinical application of ^{18}F-FUdR in glioma patients-PET study of nucleic acid metabolism
Kameyama M., Ishiwata K., Tsurumi Y., Itoh J., Sato K., Katakura R., Yoshimoto T., Hatazawa J., Ito M., and Ido T.
Journal of Neuro-Oncology **23**(1995)53-61.

14. Post-ischemic changes of $[^3H]$glycine binding in the gerbil brain after cerebral ischemia
Araki T., Kato H., Fujiwara T., Kogure K., Itoyama Y.
European Journal of Pharamacology **278**(1995)91-96.

15. Effects of chronic right ventricular pressure overload on myocardial glucose and free fatty acid metabolism in the conscious rat
Takeyama D., Kagaya Y., Yamane Y., Shiba N., Chida M., Takahashi T., Ido T., Ishide N., and Takishima T.
Cardiovascular Research **29**(1995)763-767.

16. Histamine H1 receptor occupancy in human brains after single oral doses of histamine H1 antagonists measured by positron emission tomography
Yanai K., Ryu J. H., Watanabe T., Iwata R., Ido T., Sawai Y., Ito K., and Itoh M.
British Journal of Pharmacology **116**(1995)1649-1655.

17. Clinical application of ^{18}F-FUdR in glioma patients-PET study of nucleic acid metabolism
Kameyama M., Ishiwata K., Tsurumi Y., Itoh J., Sato K., Katakura R., YoshimotoT. , Hatazawa J., Ito M., and Ido T.
Journal of Neuto-Oncology **23**(1995)53-61,

18. Mastoparan-induced phosphatidylcholine hydrolysis by phospholipase D activation in human astrocytoma cells
Mizuno K., Nakahata N.,and Ohizumi Y.
British Journal of Pharmacology **116**(1995)2090-2096.

19. Positron Emission Tomographic Study of Central Histamine H1-Receptor Occupancy in Human Subjects Treated with Epinastine, a Second-Generation Antihis tamine
Yanai K., Ryu J. H., Watanabe T., Iwata R., Ido T., Asakura M., Matsumura R., and Itoh M.
Meth. Find. Exp. Clin. Pharmacol. **17**(1995)64-69.

20. Age-related changes in bindings of second messengers in the rat brain
Araki T., Kato H., Fujiwara T., and Itoyama Y.
Brain Research **704**(1995)227-232

21. K-X Ray Production Cross Sections of Heavy Lanthanides Over the Energy Range of 3-40 MeV/amu
Sera K., Ishii K., Orihara H., and Morita S.
International Journal of PIXE **5-1**(1995)57-67

22. Positron Emission Tomographic Study of Central Histamine H1-Receptor Occupancy in Human Subjects Treated with Epinastine, a Second-Generation Antihistamine
Yanai K., Ryu J. H., Watanabe T., Iwata R., Ido T., Asakura M., Matsumura R., and Itoh M.
Meth. Find. Exp. Clin. Pharmacol. **17**(1995)64-69.

VII. MEMBERS OF COMMITTEES

VII. Members of Committees (as of Jan. 1, 1996)

General

(Chairman)	Hikonojo	Orihara	(CYRIC)
	Yasuo	Endo	(Faculty of Science)
	Hiroshi	Kudo	(Faculty of Science)
	Takashi	Yoshimoto	(School of Medicine)
	Tadashi	Yamada	(School of Dentistry)
	Akira	Naganuma	(Faculty of Pharmaceutical Sciences)
	Katsunori	Abe	(Faculty of Engineering)
	Shichiro	Sugawara	(Faculty of Agriculture)
	Reimon	Hanada	(Institute for Materials Research)
	Ken-ichi	Akiba	(Research Institute for Mineral Dressing and Metallurgy)
	Hiroshi	Fukuda	(Institute for Development, Aging and Cancer)
	Kiyohiko	Sakamoto	(School of Medicine)
	Masumi	Sugawara	(Faculty of Science)
	Manabu	Fujioka	(CYRIC)
	Tatsuo	Ido	(CYRIC)
	Takashi	Nakamura	(CYRIC)
	Masatoshi	Itoh	(CYRIC)
	Ren	Iwata	(CYRIC)
	Akira	Yamadera	(CYRIC)
	Keizo	Ishii	(Faculty of Engineering)
	Takeo	Fujino	(Research Institute for Mineral Dressing and Metallurgy)
	Takeo	Fujino	(Research Institute for Mineral Dressing and Metallurgy)

Research Program

(Chairman)	Takashi	Nakamura	(CYRIC)
	Takemi	Nakagawa	(Faculty of Science)
	Takashi	Yamaya	(Faculty of Science)

Tutomu	Sekine	(Faculty of Science)
Kazuyoshi	Masumoto	(Faculty of Science)
Mieko	Kawamura	(Faculty of Agriculture)
Takashi	Yoshimoto	(School of Medicine)
Hidetada	Sasaki	(School of Medicine)
Katsunori	Abe	(Faculty of Engineering)
Keizo	Ishii	(Faculty of Engineering)
Reimon	Hanada	(Institute for Materials Research)
Hiroshi	Fukuda	(Institute for Development, Aging and Cancer)
Masao	Tada	(Institute for Development, Aging and Cancer)
Manabu	Fujioka	(CYRIC)
Tatsuo	Ido	(CYRIC)
Masatoshi	Itoh	(CYRIC)

Cyclotron

(Chairman)	Manabu	Fujioka	(CYRIC)
	Takemi	Nakagawa	(Faculty of Science)
	Satoru	Kunii	(Faculty of Science)
	Tutomu	Sekine	(Faculty of Science)
	Takashi	Yamaya	(Faculty of Science)
	Kyuya	Kodajima	(Faculty of Engineering)
	Ken	Abe	(Faculty of Engineering)
	Keizo	Ishii	(Faculty of Engineering)
	Akira	Hasegawa	(Faculty of Engineering)
	Reimon	Hanada	(Institute for Materials Research)
	Ken-ichi	Akiba	(Research Institute for Mineral Dressing and Metallurgy)
	Tatsuo	Ido	(CYRIC)
	Takashi	Nakamura	(CYRIC)
	Keizo	Ishii	(CYRIC)
	Masatoshi	Itoh	(CYRIC)
	Ren	Iwata	(CYRIC)
	Tsutomu	Shinozuka	(CYRIC)
	Atuki	Terakawa	(CYRIC)

Radiation Protection and Training of Safe Handling

(Chairman)	Tadashi	Yamada	(School of Dentistry)
	Yoshiaki	Fujii	(Faculty of Science)
	Hiroshi	Kudo	(Faculty of Science)
	Tetsuya	Ono	(School of Medicine)
	Kiyohiko	Sakamoto	(School of Medicine)
	Kazuo	Ouchi	(Faculty of Pharmaceutical Sciences)
	Yasushi	Inoue	(Faculty of Engineering)
	Toshiyasu	Yamaguchi	(Faculty of Agriculture)
	Masayuki	Hasegawa	(Institute for Materials Research)
	Hiroshi	Fukuda	(Inute for Dstitevelopment, Aging and Cancer)
	Manabu	Fujioka	(CYRIC)
	Takashi	Nakamura	(CYRIC)
	Akira	Yamadera	(CYRIC)
	Kenichi	Akiba	(Research Institute for Mineral Dressing and Metallurgy)

Life Science

(Chairman)	Tatsuo	Ido	(CYRIC)
	Kazuo	Yamamoto	(Faculty of Science)
	Kiyohiko	Sakamoto	(School of Medicine)
	Yasuhito	Itoyama	(School of Medicine)
	Reizo	Shirane	(School of Medicine)
	Masahiko	Yamamoto	(School of Medicine)
	Kazuie	Iinuma	(School of Medicine)
	Michinao	Mizugaki	(University Hospital)
	Shin	Maruoka	(University Hospital)
	Kazuo	Ouchi	(Faculty of Pharmaceutical Sciences)
	Keizo	Ishii	(Faculty of Engineering)
	Mieko	Kawamura	(Faculty of Agriculture)
	Hiroshi	Fukuda	(Institute for Development, Aging and Cancer)
	Masao	Tada	(Institute for Development, Aging and Cancer)
	Kazuo	Kubota	(Institute for Development, Aging and Cancer)
	Manabu	Fujioka	(CYRIC)
	Takashi	Nakamura	(CYRIC)

	Masatoshi	Itoh	(CYRIC)
	Takehiko	Fujiwara	(CYRIC)
	Yoshihito	Funaki	(CYRIC)

Prevention of Radiation Hazards

(Chairman)	Takashi	Nakamura	(CYRIC)
	Takemi	Nakagawa	(Faculty of Science)
	Tutomu	Sekine	(Faculty of Science)
	Ken	Abe	(Faculty of Engineering)
	Manabu	Fujioka	(CYRIC)
	Tatsuo	Ido	(CYRIC)
	Akira	Yamadera	(CYRIC)
	Takehiko	Fujiwara	(CYRIC)
	Muneo	Aoyama	(CYRIC)
	Takamoto	Miyata	(CYRIC)

VIII. PERSONNEL

VIII. Personnel (as of Jan. 1, 1996)

Director Hikonojo Orihara

Division of Accelerator

Manabu Fujioka
Shogo Hayashibe1)
Takashi Yamaya1)
Tsutomu Shinozuka
Toshihiro Honma
Shizuo Kan6)
Shizuo Chiba6)
Naoto Takahashi6)
Yasuaki Omiya6)

Division of Instrumentations

Hikonojo Orihara
Keizo Ishii2)
Atuki Terakawa
Sho-ichi Watanuki
Tsutomu Ichikawa

Division of Radiopharmaceutical Chemistry

Tatsuo Ido
Masao Tada5)
Ren Iwata
Yoshihito Funaki
Hideo Takahashi
Yo-ichi Ishikawa7)
Yutaka Naitoh7)

Division of Cyclotron Nuclear Medicine

Masatoshi	Itoh
Takehiko	Fujiwara
Kazuhiko	Yanai4)
Shinya	Seo

Division of Radiation Protection and Safety Control

Takashi	Nakamura
Akira	Yamadera
Takamoto	Miyata
Yasuhiro	Satake7)
Hiroki	Mukai7)

Graduate Student and Researcher

Masahiro	Fujita (Graduate School, Division of Science)
Ai	Watanabe (Graduate School, Division of Science)
Yasumori	Kanai (Graduate School, Division of Science)
Toshio	Kouda (Graduate School, Division of Science)
Guan	Zhong (Graduate School, Division of Science)
Kazuya	Itoh (Graduate School, Division of Science)
Yohiko	Teramoto (Graduate School, Division of Science)
Asaki	Yamamoto (Graduate School, Division of Science)
Naoto	Matumura (Grduate Schaool, Division of Science)
Naoto	Nakagawa (Graduate School, Division of Pharmaceutical Sciences)
Masanobu	Mukoyoshi (Graduate School, Division of Pharmaceutical Sciences)
Tsuyoshi	Yamaguchi (Graduate School, Division of Pharmaceutical Sciences)
Kaori	Suzuki (Graduate School, Division of Pharmaceutical Sciences)
Shinji	Nagata (Graduate School, Division of Pharmaceutical Sciences)
Masato	Higuchi (Graduate School, Division of Medicine)
Marko	Mejia (Graduate School, Division of Medicine)
Masashi	Takada (Graduate School, Division of Engineering)
Yu-ichiro	Narita (Graduate School, Division of Engineering)
Hossain	Deloar (Graduate School, Division of Engineering)

Atuko Konno (Graduate School, Division of Engineering)
Masayasu Miyake (Graduate School, Division of Engineering)
Kim Eun Ju (Graduate School, Division of Engineering)
Ryutaro Izumi (Researcher)
Takashi Uehara (Researcher)
Syunji Takagi (Researcher)
Norio Tujimura (Researcher)

Office Staff

Muneo Aoyama
Ichiro Fukuda
Hashime Wako
Urara Saso
Kyoko Fujisawa
Satoshi Kawamura
Fumiko Mayama
Mitsuko Endo
Yu-ko Yamashita
Rie Yoshida
Yoshie Suzuki
Yuri Okumura
Miyuki Domon
Toshiyuki Watanabe7)

1) Faculty of Science
2) Faculty of Engineering
3) Institute for Materials Research
4) School of Medecine
5) Institute for Development, Aging and Cancer)
6) SUMI-JU Accelerator Service Ltd.
7) Japan Radiation Protection Co., Ltd.